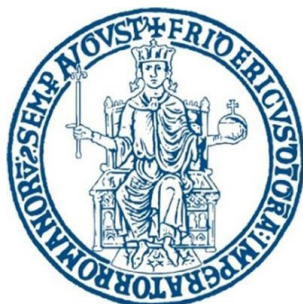


University of Naples Federico II



***Supramolecular chemistry:
realization of multifunctional nanoparticles***

Giovanni Dal Poggetto

PhD in Industrial Product and Process Engineering - XXXII cycle
Department of Chemical, Materials and Production Engineering

Tutor: Prof. Veronica Ambrogi

Co-tutor: Dr. Paola Laurienzo

Year 2020

Table of Contents

1 Introduction	3
1.1 Cancer therapy and Nanomedicine	3
1.2 Supramolecular Chemistry and Nanofabrication	4
1.3 Targeting	6
1.3.1 Passive targeting.....	6
1.3.2 Active targeting	7
1.3.2.1 Peptides.....	8
1.3.2.2 Folic acid.....	9
1.3.2.3 Cationic groups.....	9
1.3.2.4 Gene therapy.....	10
1.4 Chemistry behind the scene	11
1.4.1 Ring Opening Polymerization.....	11
1.4.2 “Click” Chemistry CuAAC (Copper(I)-catalyzed Azide-Alkyne Cycloaddition)	12
1.4.3 N ₃ -PEG-PCL Synthesis.....	13
1.4.4 Polyrotaxanes	14
1.4.5 Atom Transfer Radical Polymerization.....	16
1.5 Aim of the work	17
1.6 References	19
2 Shedding light on surface exposition of poly(ethylene glycol) and folate targeting units on nanoparticles of poly(ϵ-caprolactone) diblock copolymers: Beyond a paradigm	23
Introduction	23
Experimental section	24
Results and discussion	28
Conclusions	39
References	39
Supplementary Materials	43
3 Biodegradable nanoparticles exposing a short anti-FLT1 peptide as antiangiogenic platform to complement docetaxel anticancer activity	48
Introduction	48
Materials and methods	49
Results and discussion	54
Conclusions	65
References	65
Supplementary Materials	68
4 Improved outcome of docetaxel therapy using antiangiogenic folate-targeted biodegradable nanoparticles in in vitro and in vivo cancer models	74
Introduction	74
Methods	75

Results and discussion.....	78
Conclusions.....	81
References.....	82
<i>5 Nanoparticles decorated with folate based on a site-selective αCD-rotaxanated PEG-PCL copolymer for targeted cancer therapy.....</i>	<i>86</i>
Introduction.....	86
Experimental	87
Result and discussion.....	91
Conclusions.....	103
References.....	104
<i>6 Biodegradable nanoparticles based on an amine terminated polyester as a strategy to tune surface properties, protein interaction and accumulation in lung metastasis</i>	<i>108</i>
Introduction.....	108
Experimental	109
Results and discussion	113
Conclusions.....	120
References.....	120
Supplementary materials	123
<i>7 Surface Exposure of PEG and Amines on Biodegradable Nanoparticles as a Strategy to Tune Their Interaction with Protein-Rich Biological Media ⁴</i>	<i>127</i>
Introduction.....	127
Materials and Methods.....	128
Results and discussion	132
Conclusions.....	143
References.....	143
Supplementary materials	146
<i>8 Terpolymers for combined therapy of cancer.....</i>	<i>153</i>
Introduction.....	153
Experimental Section	154
Result and Discussion	158
Conclusions.....	166
Reference	166
<i>9 Conclusions.....</i>	<i>168</i>

1 Introduction

1.1 Cancer therapy and Nanomedicine

Molecular chemotherapeutics have often undesired physicochemical and pharmacological properties, such as low solubility and narrow therapeutic index (1). These drawbacks limit their applications for clinical cancer treatments. Two strategies have emerged over the past 2-3 decades to address these intrinsic drawbacks of chemotherapeutics (2). One approach is to design and develop new derivatives of chemotherapeutics with improved physicochemical and pharmacological properties so that they can be used to precisely and specifically modulate the molecular processes and pathways associated with tumor progression (3) The other one is to drive the existing chemotherapeutic agents using nanotechnology. (4)

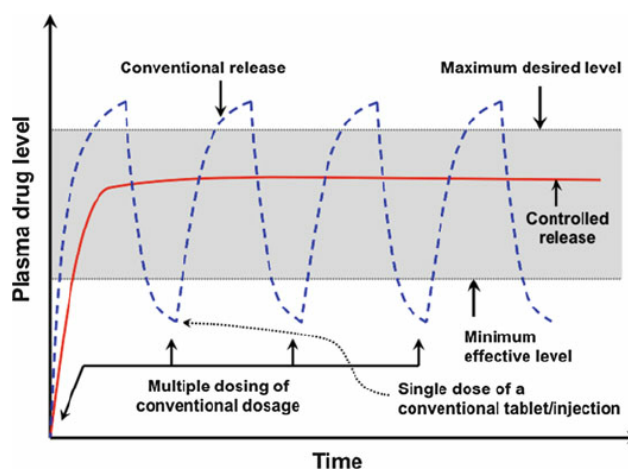
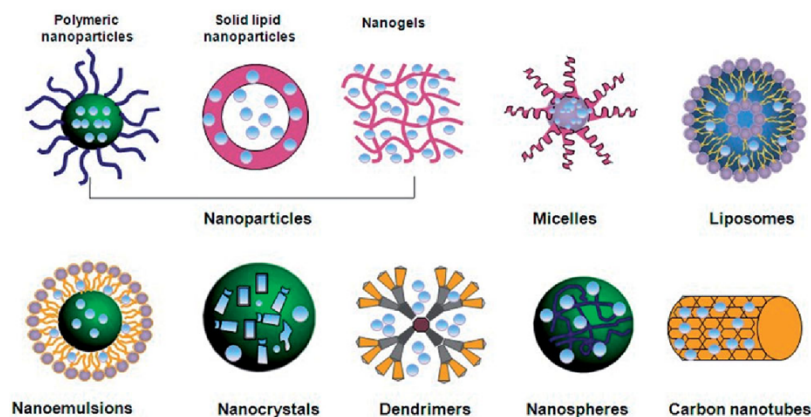


Figure 1 Conventional vs. Controlled release

In the field of nanotechnology significant advances, especially in material science and medicine, have been achieved. In particular, the application of nanotechnologies in medicine, the so-called nanomedicine has given an impulse to the development of various types of drug-loaded nanocarriers, usually ranging from 1 to 1000 nm. A wide variety of nanocarrier systems (**Scheme 1.1**), composed of different materials including lipids, polymers and inorganic materials have been proposed in the biomedical field (5), resulting in delivery systems that, depending on their physicochemical properties, will be suitable for different applications. In drug delivery, nanocarriers are designed (i) to protect a drug from in vivo degradation; (ii) to enhance drug absorption by facilitating diffusion through endothelium; (iii) to achieve a controlled and sustainable release over time (**Figure 1**); (iv) to improve intracellular penetration and subcellular distribution; (v) to impart or enhance particular capabilities thanks to surface modification. This last topic will be described in-depth in a later chapter.



Scheme 1.1 Lipid and polymer-based nanoparticulate systems used in the field of drug delivery and active targeting

1.2 Supramolecular Chemistry and Nanofabrication

Supramolecular chemistry is the discipline covering “the chemistry of molecular assemblies and of the intermolecular bond” and deals with “organized entities that result from the association of two or more chemical species held together by intermolecular forces.

From: Advances in Organometallic Chemistry, 2012

Supramolecular chemistry is described as the chemistry of the non-covalent bond. Self-assembly of molecular building blocks to bigger aggregates is the core of nanostructures, molecular materials, and more complex systems; the spark for bottom-up nanofabrication. The forces responsible for spatial organization of systems include hydrogen bonding, metal coordination, hydrophobic forces, Van der Waals forces, $\pi-\pi$ and electrostatic interaction.

In molecular self-assembly molecules are guided to assemble through non-covalent interactions. Self-assembly could be divided into *intermolecular* self-assembly (to form a supramolecular assembly), and *intramolecular* self-assembly (or folding). Molecular self-assembly allows the formation of larger structures such as nanocarriers, membranes, vesicles, and liquid crystals. Among several kinds of nanocarriers, this thesis focuses on polymeric NPs, in which polymeric matrix is based on amphiphilic block copolymers. Typically, the amphiphilic block copolymers are formed by covalently bonded hydrophobic and hydrophilic blocks. In water, amphiphilic block copolymers with soluble and insoluble blocks can self-assemble with various shapes and sizes. The NPs are formed above a critical micelle concentration (CMC) and/or critical micelle temperature (CMT) characteristic of the copolymers, where the insoluble blocks aggregate into dense micellar cores surrounded by shell composed by the soluble blocks extending into the solvent.

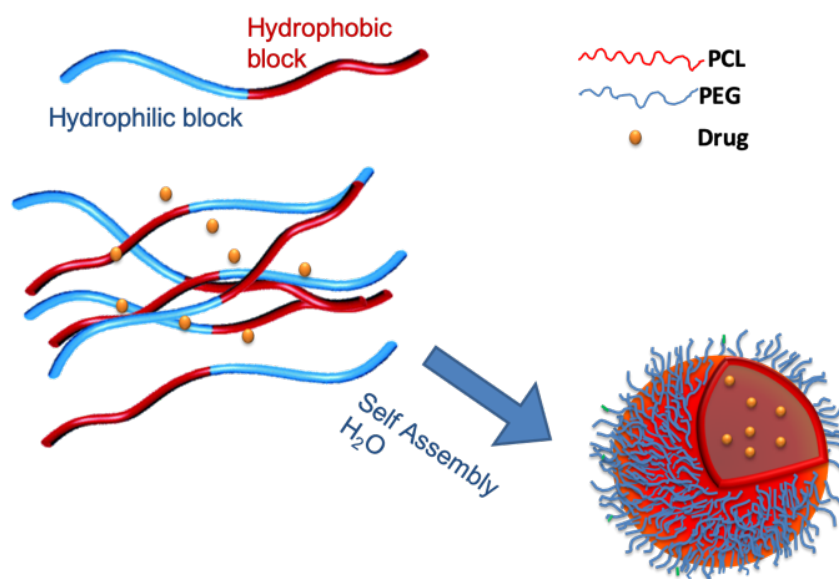


Figure 2 Self-assembly of amphiphilic block copolymers

NPs can be realized from a variety of materials such as proteins, polysaccharides and polymers, depending on several aspects such as i) size of the desired NPs, ii) properties of the drug to be encapsulated (solubility, stability, etc.), iii) surface characteristics and functionality, iv) degree of biodegradability and biocompatibility, and v) drug release profile of the final product.

In this thesis, NPs based on Poly(ethylene glycol) (PEG) as hydrophilic block and Poly(ϵ -caprolactone) (PCL) as hydrophobic block are presented.

PEG (**Figure 3**) is a hydrophilic biocompatible polyether. This polymer has the peculiarity of imparting a steric barrier to the surface of NPs and minimizes their protein interactions (opsonization). Absorption of plasma proteins onto NPs surface is the primary mechanism for the reticuloendothelial system (RES) to recognize the circulating nanoparticles and thus eliminate them, causing a major loss of the injected dose (ID) (>50%) within a few hours after injection.

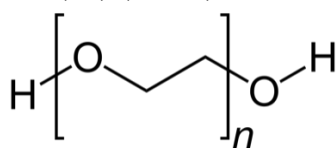


Figure 3 Poly(ethylene glycol)

PCL (**Figure 4**) is a biocompatible and biodegradable semi-crystalline, hydrophobic polyester. It's easily synthesized through Ring Opening Polymerization of ϵ -caprolactone. The main final product of PCL degradation is the 6-hydroxyhexanoic acid. The main advantage of PCL compared to other aliphatic polyesters, such as polylactic acid (PLA) and polyglycolic acid (PGA), is its high permeability to hydrophobic drugs

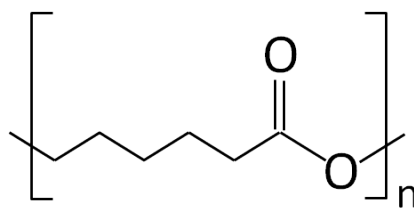


Figure 4 Poly(ε-caprolactone)

1.3 Targeting

One major challenge in nanomedicine is selectively deliver NPs to diseased tissues.

The ideal “smart” NPs should have specific targeting to pathologic tissues, which minimizes or avoids off-target effects of the chemotherapeutic agents on healthy tissues. Much research has been directed towards conjugation of targeting ligands, specific to cell surface receptors that are unique, or over-expressed, in dysplastic and pathologic tissues, to NPs surfaces. Furthermore, surface modification of NPs is normally used to control their biological fate in a desirable way. The aim of such modification includes: an increased stability and half-life of nanocarriers in the circulation, active targeting into the required pathological zone and responsiveness to local stimuli such as changes in local pH and/or temperature. These modifications concern several classes of targeting units: small molecules, peptides, protein domains, antibodies, nucleic acid-based aptamers and cationic groups.

1.3.1 Passive targeting

The longer blood circulation of the NPs also leads to an improvement in the second requirement for drug delivery systems in cancer therapy, since long circulating NPs were found to have increased accumulation in tumor tissue over healthy tissue.

Characteristics of many malignant tumors are their fast growth and need to form new blood vessels (angiogenesis). These newly formed blood vessels are often abnormal in their form and architecture with large fenestrations varying from 100-1200 nm (6), a pore size much larger than the ones found in normal vessels (around 6 nm). This leakiness combined with an ineffective lymphatic drainage make NPs passively accumulate in tumor tissue (7). This effect is named enhanced permeability and retention (EPR) (**Figure 5**). A large distribution of NPs in the interstitium surrounding the tumor cells is allowed due to a high interstitial pressure and a large interstitial space compared with healthy tissue. Not all solid tumors are suitable for treatment with passive accumulating NPs, as the tumor vasculature is highly heterogeneous in terms of density and distribution of vessels, depending on the size of the tumor as well as their location inside the tumor. Generally, peripheral regions have a higher vessel density than central parts, and the central parts have a higher interstitial pressure than the periphery. This leads to an irregular drug distribution throughout the solid tumor, resulting in larger tumors being more difficult to treat than smaller ones.

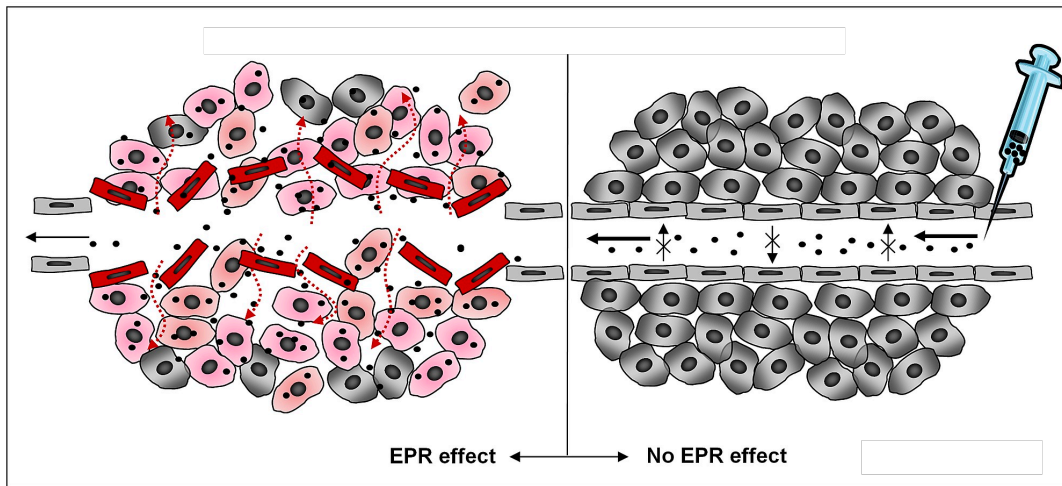


Figure 5 EPR effect

1.3.2 Active targeting

A way to maintain the NPs in the interstitial space of the tumor is to take advantage of specific surface receptors and antigens that are overexpressed on cancer cells or on endothelial cells in the blood vessels (8-9). The targeted NPs concentrate in the tumor site by the EPR effect like for the non-targeted NPs, but once there, they can actively be taken up by the tumor cells after binding to their target receptor or antigen. This is commonly referred to as active targeting (**Figure 6**).

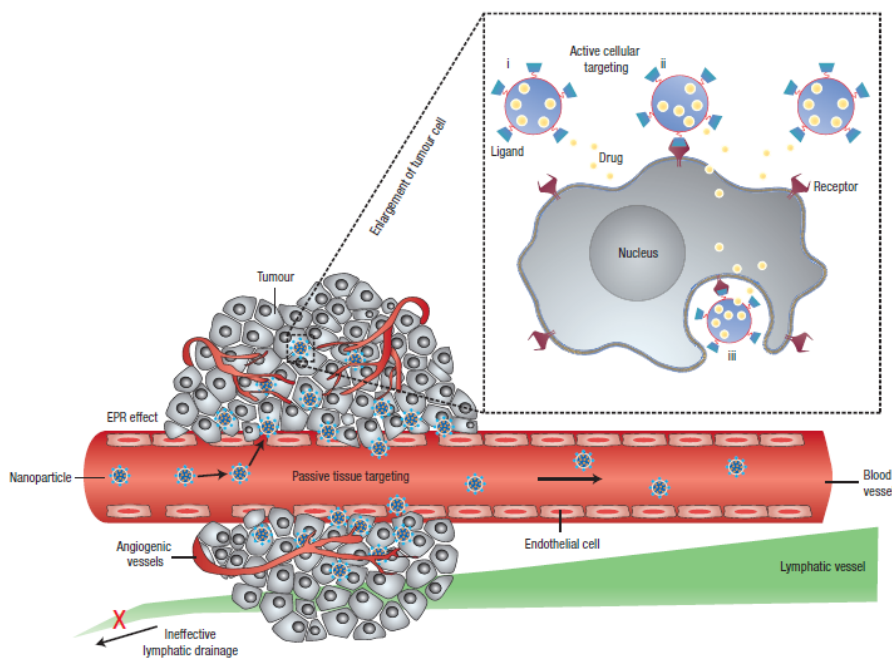


Figure 6 Active targeting

Targeting of endothelial cells in tumoral blood vessels is generally considered to be advantageous over tumor cell targeting as endothelial cells are generically stable and the risk of developing drug resistance is reduced (10). They are highly accessible for circulating NPs, and damage to a few tumor blood vessels may result in a strong growth inhibition of the surrounding tumor cells, which

are depending on nutrients and oxygen supply from these vessels. The special characteristics of proliferating endothelial cells in tumors are shared between a variety of tumor types which can be beneficial when trying to develop a wide-ranging chemotherapeutic formulation. Strategies, which target both tumor vasculature as well as tumor cells, have proved to be more effective than targeting of the two tissues individually.

Different approaches have been tested for attachment of the targeting ligand to the NPs surface. Targeting ligands have been conjugated directly to the phospholipid headgroups of non-PEGylated NPs (11). However, these NPs suffered from rapid blood clearance. A similar conjugation approach was used on PEGylated NPs, resulting in longer circulating NPs, but these NPs showed reduced targeting properties due to steric hindrance from the PEG chains. To minimize shielding of the targeting ligand by the PEG chains, the targeting ligand was moved to the end of the PEG chain, giving it opportunity to extend beyond the PEG coating and maximize its exposure to the targeted receptor (12).

A great number of different targeting ligands have been conjugated to the NPs surface including peptides, vitamins and antibodies using a variety of chemical methods.

1.3.2.1 Peptides

The use of peptide-targeted NPs as therapeutics has become highly interesting with the increasing knowledge of specific peptide sequences involved in cell to cell interactions as well as the improvement in synthesis of peptides that closely resemble the human ones. The peptide-targeted NPs can increase the delivery of drug to cancer cells by targeting overexpressed receptors or by using unspecific cell penetrating peptides.

G protein-coupled receptors (GPCR) are a diverse family of transmembrane proteins responsible for interacting with extracellular molecules and thus regulate various functions in the cell. A large number of GPCRs with known binding peptides are found to be overexpressed on the surface of cancer cells,

Cell-penetrating peptides (CPP) are a class of peptides which typically contain a large portion of highly charged amino acids such as arginine or lysine (13). When applying these sorts of peptide sequences, it is critical to have the right ratio between cell-penetrating peptide and a shielding PEG layer on the surface of the NPs. PEG needs to ensure long enough blood circulation time for the NPs to accumulate in the target site by the EPR effect and hinder that the cell-penetrating peptide has too much unspecific binding to healthy cells encountered on its way. However, PEG must not shield the cell-penetrating peptide too much, making it unable to interact with the target cell membrane.

Another approach possible through peptide surface modification is reduce and/or suppress angiogenesis.

Angiogenesis is the process through which new blood vessels are formed from pre-existing vessels, new growth in the vascular network is important since the proliferation, as well as metastatic spread, of cancer cells depends on an adequate supply of oxygen and nutrients and the removal of waste products. Angiogenesis is regulated by both activator and inhibitor molecules.

Antagonist peptides specific for the vascular endothelial growth factor receptor (VEGFR) have been investigated. The effects of the antagonists on the VEGF-induced endothelial cell functions and tumor progression have been reported as very promising for cancer treatment. (14)

1.3.2.2 Folic acid

NPs functionalized with the folic acid, B vitamin, have attracted much attention as the folate receptors are highly overexpressed in the majority of solid tumors. (15) Folic acid is internalized to a large extent in proliferating cells as is essential in the biosynthesis of nucleotides; consequently, fast dividing malignant cells need this nutrient. Normally, the folate receptors are expressed at the apical side of epithelial cells and not accessible to drug in the blood circulation. However, when the epithelial cell becomes malignant, the membrane loses its polarity and the folate receptor can be located at the basal surface of the membrane as well.

An interesting feature of folate-targeted NPs is that they have shown an ability to bypass the P-glycoprotein efflux pump (16). This is often involved in multi-drug resistance mechanisms and considered to be a major complication in cancer therapy. It is found that the ability is coupled to folate- NPs being taken up by receptor-mediated endocytosis (17).

Although the active targeting strategies can seem promising, obstacles still exist. Unfortunately, the use of targeted NPs does not necessary results in increased tumor accumulation and even if an increased accumulation is achieved, this does not guarantee an improved therapeutic outcome. Attaching a targeting ligand on the surface of NPs naturally decreases its blood circulation time as the ligand will increase unspecific binding to healthy cells and may trigger enhanced opsonization and removal by RES. When NPs with strong binding ligands bind to the first cancerous cells they meet, there is a risk that they will block the extravasation of more NPs to the tumor interstitial space (18). Moreover, their fast binding will prevent their diffusion through the tumor tissue and they will mainly be located in the blood vessel region. This is known as the binding-site barrier. Another challenge of active targeting via receptor-mediated uptake is release of the encapsulated drug once the NPs have been internalized. The harsh environment found in endosomes and especially lysosomes can degrade the encapsulated drug, if it does not succeed in escaping these vesicles.

1.3.2.3 Cationic groups

Surface charge of NPs is one of the most determinant property for cellular internalization, with charge-based uptake highly dependent on cell type.

In nonspecialized mammalian cells, clathrin-mediated endocytosis represents the classic mechanism governing uptake of NPs. (19)

The tumor microenvironment exhibits increased interstitial fluid pressure that is caused by leaky vasculature, poor lymphatic drainage and a high density of cells and extracellular matrix (20). Due to this nature, the distribution of NPs is limited to the tumor peripheral region, and NPs show superficial penetration in the interstitial space (21). To overcome these problems, drug carriers require enhanced cellular uptake and interstitial distribution, which can be achieved modifying the surface charge. Cationic NPs are able to pass through biological membranes with simplified uptake in cells, due to their strong interaction with negatively charged biological membranes. Another

important advantage is that they can mask the negative charge of anionic drugs to escape the mononuclear phagocytic system (MPS).

These NPs can also condense small nucleic acid (e.g. siRNA) or proteins to form polyplexes for intracellular gene/drug delivery.

As drawback, cationic NPs have several undesirable features including the aggregation of erythrocytes and platelets, some inflammatory effects and moreover exhibit a high cytotoxicity. There are several strategies to reduce these complications; for instance, adsorption of negative charged molecules to tune net positive charge.

1.3.2.4 Gene therapy

Gene therapy is a relatively new area of medicine for specific treatment of numerous gene-related diseases ranging from cancer to neurodegenerative and autoimmune diseases. This therapy introduces genes into the target cells altering the expression of the genes to cure or prevent the progression of the related disease (22). Bare genomic material cannot be internalized efficiently because of its serum nuclease susceptibility, phagocyte uptake and toxic effect by immune response stimulation, which restricts their medical application. To deliver genomic materials there are two main categories of methods:

- **Viral delivery:** viruses whose genomes have been edited deleting some areas so that their replication ability has been altered. This system has some problems, such as their marked immunogenicity that causes inflammatory response, toxin production and their limitation in capacity size
- **Non-Viral delivery:** includes all the methods not regarding viruses, ranging from well-designed polymers to ultrasound and gene-gun. Efficiency of these systems is less than that of viral ones, but it's compensated by cost/effectiveness, availability, and more importantly less induction of immune system and no limitation in size of genomic material.

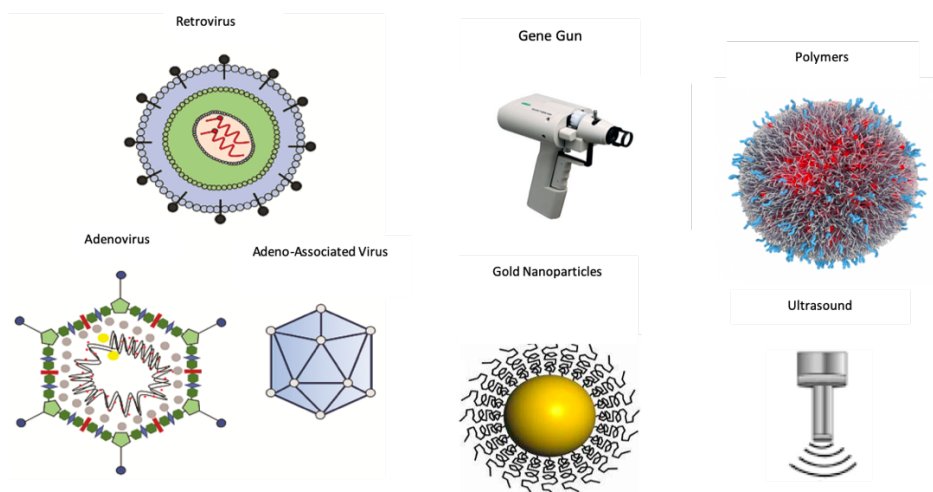


Figure 7 examples of gene vectors

1.4 Chemistry behind the scene

In this chapter the chemistry used to realize amphiphilic block copolymers and the strategies to achieve the surface modification of NPs is presented.

1.4.1 Ring Opening Polymerization

Ring-opening polymerization (ROP) is a procedure of chain-growth polymerization strongly used for the synthesis of biopolymers (23).

ROP has proved to be a suitable synthetic route to obtain technologically interesting polymers with specific and controllable properties (e.g., refractive index), for preparing synthetic variants to naturally occurring polymers or to optimize biodegradable polymers for agricultural, medicinal and pharmaceutical applications. ROP can be divided in Cationic, Radical and Anionic. These reactions have in common that the monomers are cyclic (**Figure 8**).

Name	Structure	Ring size	Mechanism
Ether		3–5,7	Cationic, anionic
Thioether		3,4	Cationic, anionic
Amine		3,4,7	Cationic
Lactone		4,6–8	Anionic, cationic
Thiolactone		4–8	Anionic, cationic
Lactam		≥4	Anionic, cationic

Figure 8 different ROP monomers

Monomers made up of 3–8 atoms may polymerize due to the loss of enthalpy associated with the loss of ring strain.

The driving force for most ROPs is the release of ring tension and associated steric hindrance.

ROP, used to synthesize PCL in this thesis, can be described as a nucleophilic attack of the initiator, the -OH group of PEG/mPEG, to a heterocyclic monomer (ϵ -caprolactone) followed by growing chain steps (**Figure 9**). Stannous octoate (SnOct_2) is preferred as catalyst for biomedical applications because of its low toxicity and has been approved as food additive (24).

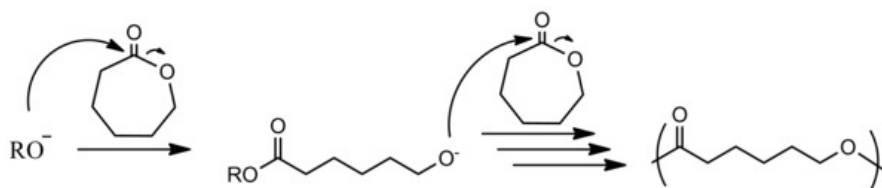


Figure 9 ROP reaction scheme

1.4.2 “Click” Chemistry CuAAC (Copper(I)-catalyzed Azide-Alkyne Cycloaddition)

The term "Click Chemistry" is used to describe reactions characterized by high yield and selectivity, which produce only byproducts that can be removed without intensive purifications, are stereospecific, simple to perform, and can be carried out under mild conditions. Several reactions have been identified that fulfill these parameters, thermodynamically favored reactions that achieve specifically to one product, such as formation of hydrazones and heterocycles, oxidative formation of epoxides, Michael additions, and cycloaddition reactions.

Among these last ones, a variant of the Huisgen 1,3-dipolar cycloaddition, catalyzed by copper(I), lead organic azides and terminal alkynes to afford 1,4-regioisomers of 1,2,3-triazoles as unique products. **Figure 10** (25). This reaction is usually named Copper(I)-catalyzed Azide-Alkyne Cycloaddition (CuAAC).

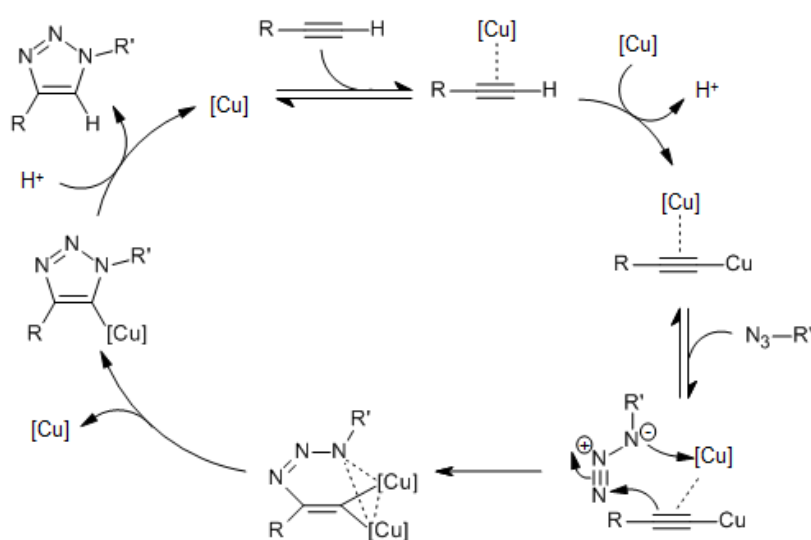


Figure 10 CuAAC catalytic cycle

The Cu species undergo to insertion reaction into the terminal alkynes. The Cu(I) species may be introduced in the reaction pot in several ways:

- As Cu²⁺ compound in presence of a reducing agent (e.g. sodium ascorbate) which reduces the Cu from the (+2) to the (+1) oxidation state. The advantage of generating the Cu(I) species in situ resides in tolerance for any oxygen which may be present into the system. Oxygen oxidizes Cu⁺ to Cu⁺² resulting in inhibition of reaction and low yields. On the other side, as drawback the presence of a reducing agent may affect, in case of complex reactants, reducing-susceptible reagents.
- Halides of Cu(I) are subject to solubility which sometimes could be an issue.
- Cu (0) metal that generate by comproportionation reaction Cu (I) has the advantage of an easy removal of catalyst (25)

In this thesis CuAAC is used to conjugate N₃-PEG-PCL copolymer to an opportune alkyne-modified target ligand, peptide or molecules in general.

1.4.3 N₃-PEG-PCL Synthesis

This synthesis route was designed to obtain N₃-PEG_{1,5k}-PCL_{4k} starting from commercial OH-PEG_{1,5k}-OH without the need of any tedious chromatographic purification. The key point of the reaction resides in the desymmetrization step, which lead to formation of highly pure di-hetero functional PEG (**Figure 11**).

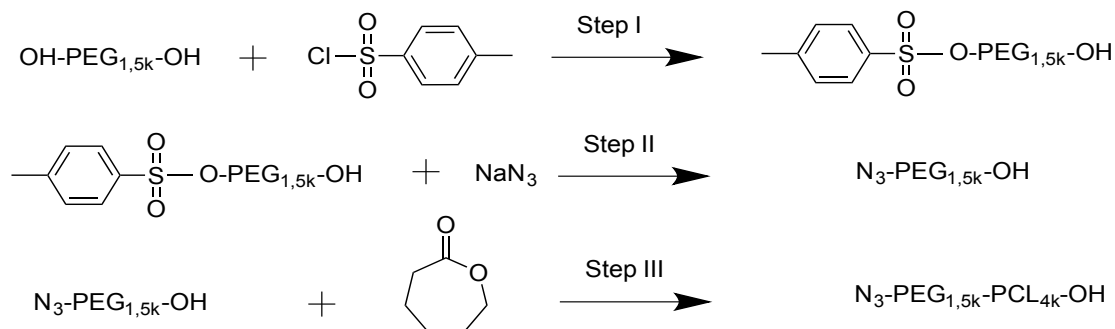


Figure 11 hetero terminated PEG reaction scheme

In the first step of synthesis only one -OH group of PEG was converted to tosyl group (OTs), using Ag₂O as catalyst. Several mechanisms are present in literature to explain this reaction (26-28) agreeing that yield and conversion are dependent of PEG chain length.

Success of reaction was confirmed through ¹H-NMR (**Figure 12**) in which integrals of to OTs (red and green), α -CH₂- to OTs (blue) and -OH (yellow) are in the desired ratio.

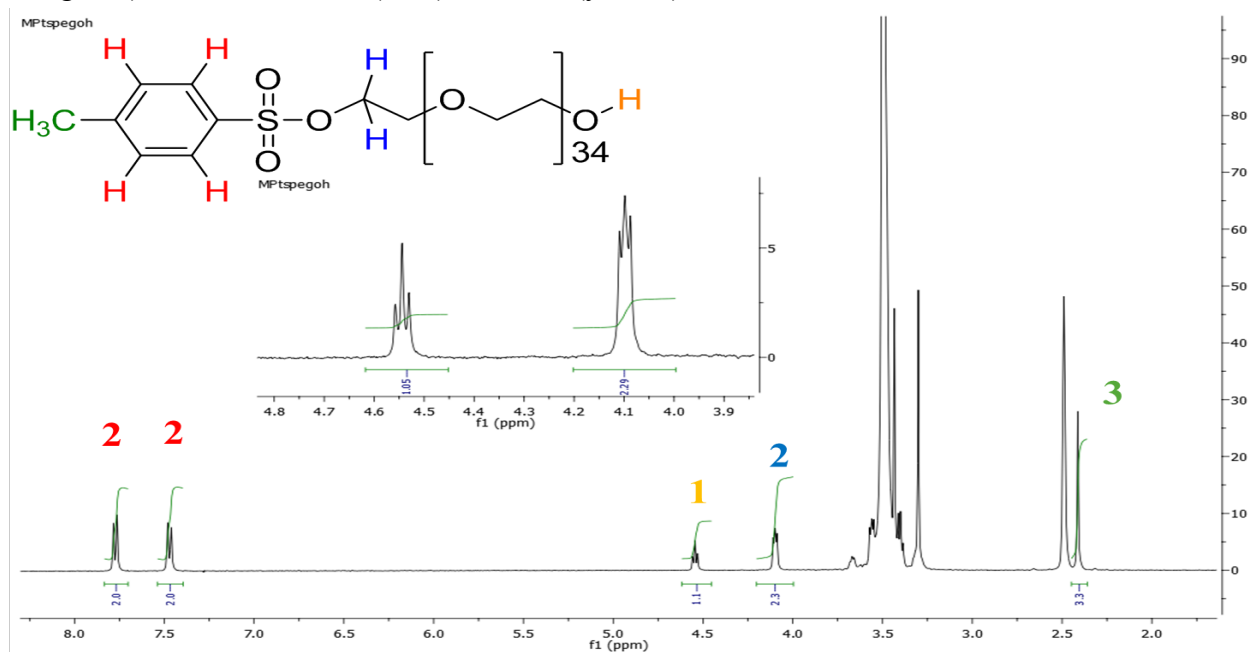


Figure 12 ¹H NMR TsO-PEG-OH

In the second step, -OTs was substituted by -N₃, achieving a N₃-PEG_{1,5k}-OH. The residual -OH group was used for ROP of ε-caprolactone to obtain N₃-PEG_{1,5k}-PCL_{4k}.

The aim of this route of synthesis is to obtain an amphiphilic block copolymer bearing an -N₃ group able to conjugate any opportunely alkyne-modified molecules to be exposed on NPs surface. Success of conjugation can be easily followed by IR spectroscopy, through the disappearance of the R-N₃ characteristic band around 2100cm⁻¹. (**Figure 13**).

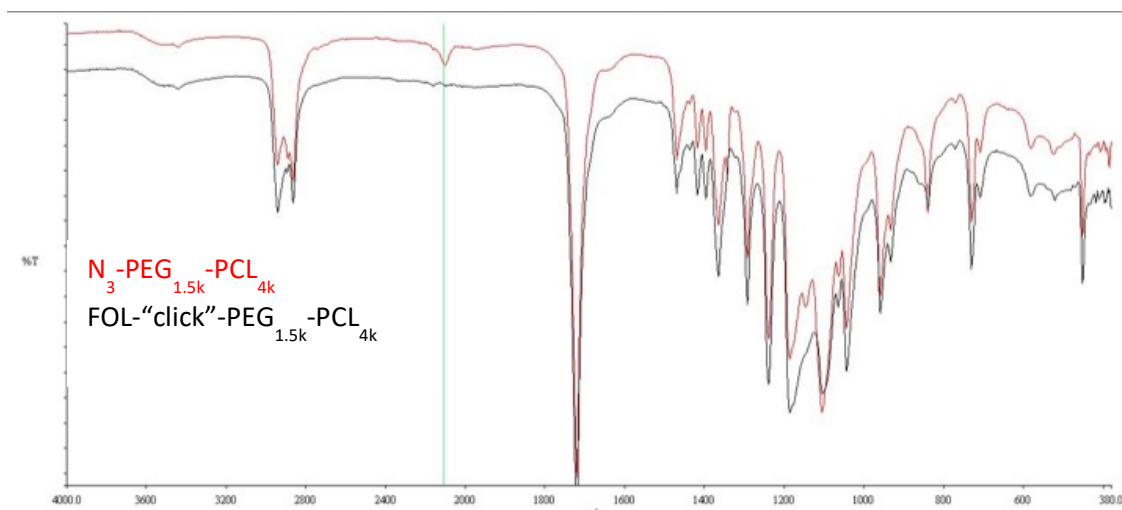


Figure 13 Superimposed FTIR spectra highlighting R-N₃ and its absence after CuAAC reaction

As an example, FTIR spectra of N₃-PEG-PCL and Fol-PEG-PCL obtained via CuACC are compared.

1.4.4 Polyrotaxanes

A polyrotaxane is a type of supramolecular complex consisting of multiple rings threaded onto a molecular “string” and end-conjugated with two bulky groups to prevent dethreading **Figure 14**. Usually these bulky groups are identical (29). As the cyclic molecules are mechanically locked to the string, polyrotaxane exhibit molecular mobility, in fact the cyclic molecules can freely slide or rotate along the chain. This particular feature can endow materials with dynamic functionalities. For instance, polyrotaxane-based hydrogels have been prepared by cross-linking between cyclic molecules. (30)

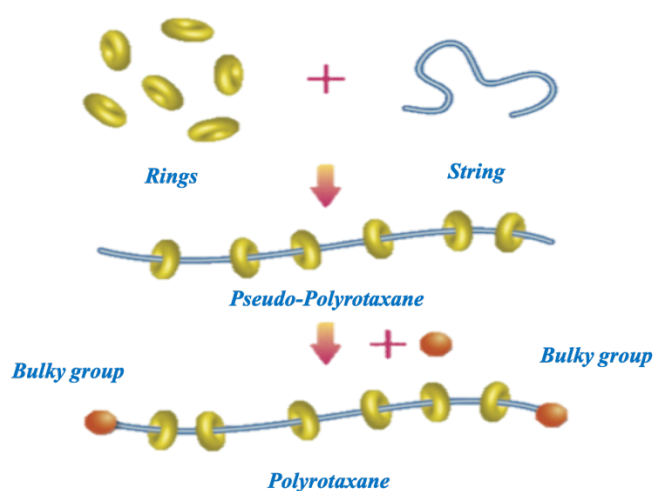


Figure 14 Schematic representation of general polyrotaxane

In this thesis an “asymmetrical” end-capped polyrotaxane composed by N₃-PEG-OTs as string threaded with α -cyclodextrin as rings having different end-capping groups was synthesized. on one side, PCL bearing an alkyne group for CuAAC reaction and on the other side, folic acid conjugated to PEG via -OTs substitution, act as stoppers to prevent α CD dethreading. **Figure 15**

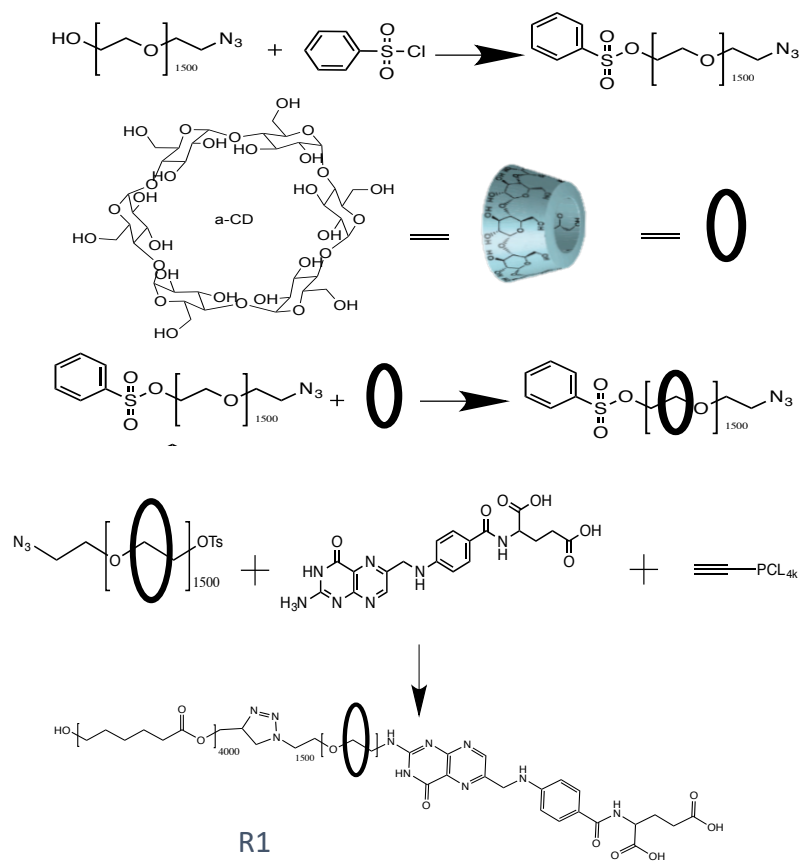


Figure 15 Reaction scheme of asymmetrical polyrotaxane

The purpose of this synthesis is to obtain an amphiphilic block copolymer able to impose an more extended conformation of PEG block on NPs surface, enhancing exposure of folic acid. PEG chains in the NPs shell, due to several factors as hydrophilic/hydrophobic ratio of copolymer and method of preparation, can assume two main opposite morphologies, respectively defined as “mushroom” and “brush” **Figure 16**. The first one is characterized by folding of PEG chains which overlap over themselves, hiding any end functionalities. The other one has PEG chains outstretched on NPs surface, improving functionalities exposure. This topic will be studied in depth in chapter 1 and 5.

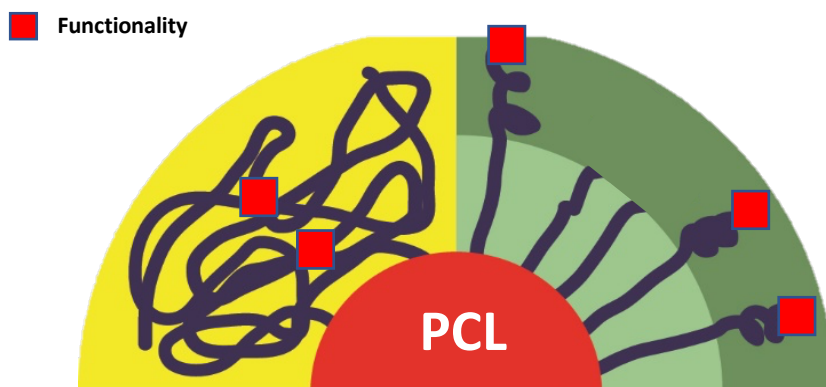


Figure 16 Different surface NPs morphology

1.4.5 Atom Transfer Radical Polymerization

Atom transfer radical polymerization (ATRP) is one of the most commonly used tool for living polymerization. ATRP allows the polymerization of a wide variety of monomers with different chemical groups and provides control of molecular weight, molecular architecture and polymer composition while assuring low polydispersity (31).

ATRP is a complex reaction, the polymerization process includes an initiator with one or more homolytic transferable atoms, one or more monomers (M) having functional groups able to stabilize radicals and a transition metal complex in two oxidation states, which can be made up of various counterions and ligands.

In general reaction starts through reversible homolytic halogen transfer between dormant species: an initiator (R-X) and a transition metal complex in the lower oxidation state (Mt^nY/ligand) to produce an active radical ($R\cdot$) and a higher oxidation state metal ($X-Mt^{n+1}Y/\text{ligand}$). **Figure 17**

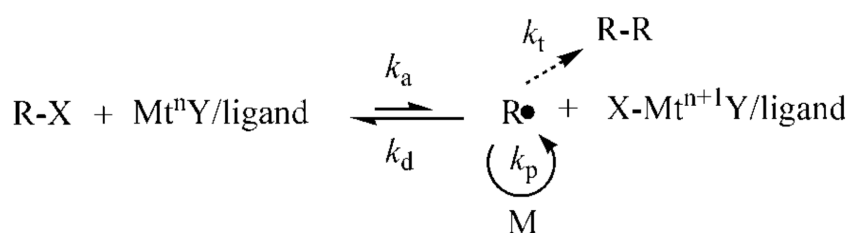


Figure 17 General reaction scheme

$R\cdot$ is formed with rate constant of activation k_a , consequently propagate with a rate constant k_p and reversibly deactivated k_d , but, because is a radical process, the active species can even terminate with a rate constant k_t .

As the reaction progresses radical termination is reduced as a result of the Persistent Radical Effect (PRE) (32), increased chain length, as well as conversion. Consequently, the equilibrium is strongly shifted towards the dormant species ($k_a \ll k_d$).

At the end of the polymerization in real living polymerizations, the chain ends should be able to start a new polymerization. This is possible by the reversible halogen end-capping. Once the polymerization has reached completion, polymer chains have a halogen atom at the chain end, so

can then be utilized as macroinitiators for block copolymers synthesis, end-chain substitution or, in case of multifunctional initiators, synthesis of star/branched polymers.

1.5 Aim of the work

This work focused on synthesis and characterization of self-assembling amphiphilic *di*block copolymers for fabrication of nanoparticles (NPs). Characterization of NPs surface properties was done in collaboration with Department of Pharmacy, University of Naples Federico II (prof. F. Quaglia). The biological properties of NPs were evaluated in collaboration with Department of Biology, University of Padova (prof. Elena Reddi).

Particular attention was given to the realization of well-defined block copolymers based on PCL and PEG bearing functionalities able to improve or to impart specific properties to NPs (targeting, trafficking, antiangiogenic activity...).

Chapter 2 focuses on PEG-PCL NPs and their folate-targeted version to encourage accumulation in cancer cells overexpressing folate receptor α . NPs were prepared with mixtures of PEG-PCL with different PEG length (short 1.0 kDa, long 2.0 kDa,) and a folate-functionalized PEG-PCL (PEG 1.5 kDa). Characterization of NPs surface by $^1\text{H-NMR}$, fluorescence and photon correlation spectroscopy evidenced a PEGylation extent below 7% with PEG in a mushroom conformation and the presence of folate more exposed to water pool in the case of copolymer with short PEG. Uptake of NPs exposing folate prepared with short PEG was high in KB cells, occurred via FR-receptor and involved lipid rafts-dependent endocytosis. Results demonstrate that PEG length critically affects protein interaction and folate exposure with a logical impact on receptor-mediated cell uptake.

Chapter 3 concerns combination of antiangiogenic molecules with chemotherapeutics, which is considered a valuable strategy to increase the efficacy of a cancer treatment. Multifunctional core-shell NPs bearing an antiangiogenic anti-FLT1 hexapeptide (aFLT1) on the surface and entrapping the poorly water-soluble chemotherapeutic docetaxel (DTX) in lipophilic core were prepared, with the aim to enhance anticancer activity. Amphiphilic PEG-PCL copolymer conjugated with aFLT1 (aFLT1-PEG_{1.5k}-PCL_{4k}) and a monomethoxy-PEG-PCL (mPEG_{1k}-PCL_{4k}) were synthesized, fully characterized and mixed in appropriate ratios to form core-shell NPs by nanoprecipitation. The presence of aFLT1 on NP surface affected the conformation of the external PEG shell, modifying the interaction with blood proteins and resulting in satisfactory stability in human plasma. NPs were internalized in human umbilical endothelial cells (HUVEC) and showed much higher antiangiogenic activities in comparison to equivalent doses of free aFLT1, and when loaded with DTX almost completely abolished tube formation. On the contrary, *in vivo* studies carried out in MDA-MB-231 cells implanted in chicken embryo chorioallantoic membranes (CAMs) evidenced a stronger antitumor efficacy of DTX entrapped in NPs with respect to the free drug, further potentiated by the presence of aFLT1. The delivery approach proposed here can be suited for other chemotherapeutics which can take advantage of complementary antiangiogenic properties and finally improve their pharmacological profile.

Chapter 4 explore the combination of NPs based on PEG-PCL conjugated either with the antiangiogenic hexapeptide aFLT1 or Fol. The aim is to improve the overall antitumor effect

combining chemotherapeutic and antiangiogenic effects with selective delivery of NPs to cancer cells via folate receptor mediated endocytosis. In FR-positive KB carcinoma cells in vitro, the antitumor effects of both ligands on NPs were not significantly higher than standard DTX, while in zebrafish embryos xenografted with KB cells the antiangiogenic Fol-targeted NPs reduced DTX systemic toxicity and inhibited the growth of the tumor and associated vasculature thanks to aFLT1 antiangiogenic effect.

Chapter 5 focuses on a new strategy to enhance exposure of Fol on NPs through supramolecular complex: polyrotaxanes. Fol-PEG_{1.5k}-PCL_{4k} copolymer was synthesized with the PEG segment threaded with α -cyclodextrins (α CDs). Threatening α CDs onto PEG block should impose a more extended conformation to PEG block which, thanks to the hydrophilic nature of α CDs, can self-organize in a brush conformation on NPs outer shell, enhancing in this way exposure of Fol. Success of realization of inclusion complex (IC) was confirmed through 2D DOSY spectroscopy, wide-angle RX, TGA and Polarized Optical Microscopy. NPs fabricated with this rotaxanated polymer showed, as preliminary result, promising internalization values and a good active targeting effect.

Chapter 6 investigates NPs with a cationic charge as a powerful nanotool, due to their unique ability to penetrate deeply inside tumor tissue and to interact preferentially with plasma membrane of cancer cells. Cationic NPs based on an amine terminated PCL (NH₂-PCL_{4.2k}) or its mixture with mPEG_{1k}-PCL_{4k} were obtained. Zeta potential values were changed to negative through adsorption of low molecular weight hyaluronate (HA). NPs exposing both amines and PEG on the surface showed a larger Fixed Aqueous Layer Thickness as compared to fully PEGylated NPs, suggesting that PEG conformation/localization is affected by the presence of amino groups. Interaction with human plasma protein pool indicated a time-dependent protein corona formation imparting an overall negative charge. NPs induced hemolysis was low while cytotoxicity against lung cancer cell lines was cell-specific as well as dose and time-dependent. The presence of amino groups greatly changed in vivo biodistribution of NPs in tumor-bearing mice (allowing amine/PEGylated NPs to accumulate mainly at target organ).

Chapter 7 focuses on NPs based on a diamino-terminated PCL and its mixture with PEG-PCL copolymers with different PEG length. The presence of an amine resulted in NPs with a net positive charge and a zeta potential dependent on the length of PEG in the copolymer. Amine/PEG-NPs had a larger fixed aqueous layer thickness as compared to PEG-NPs, suggesting that PEG conformation is affected by the presence of positive charges. In general, amine-bearing NPs promptly interacted with the dysopsonic protein HSA, due to electrostatic interactions, and lose stability, thereby undergoing time-related aggregation. On the other hand, amine/PEG-NPs interaction with mucin induced switching to a negative surface charge. The transport kinetics of NPs through a layer of artificial mucus and tumor extracellular matrix was studied by means of fluorescent NPs based upon FRET. Amine/PEG-NPs did not cross the ECM, but they were promptly transported through the AM, with swifter transport noted at increasing length of PEG block in the copolymer. All the different NPs types developed in this study were internalized by human monocytes and, despite the positive charge, they did not induce a measurable inflammatory effect.

Chapter 8 discusses on the synthesis and characterization of triblock copolymers composed by mPEG-pDMAEMA-PCL. These triblock copolymers were realized since pDMAEMA (2-(N,N-Dimethylamino)ethyl methacrylate) has received a lot of attention for gene delivery because it can be easily synthesized through ATRP. The presence of DMAEMA block imparts a positive charge to the surface of NPs able to complex small interfering RNA (siRNA).

Moreover, the formation of NPs loaded with docetaxel (DTX) and complexate with siRNA was investigated.

1.6 References

1 Hoelder, Swen & Clarke, Paul & Workman, Paul. (2012). Discovery of small molecule cancer drugs: Successes, challenges and opportunities. *Molecular oncology*. 6. 155-76. 10.1016/j.molonc.2012.02.004.

2 Li, Xiaoyu & Wu, Meiyong & Pan, Limin & Shi, Jianlin. (2015). Tumor vascular-targeted co-delivery of anti-angiogenesis and chemotherapeutic agents by mesoporous silica nanoparticle-based drug delivery system for synergetic therapy of tumor. *International Journal of Nanomedicine*. 11. 93. 10.2147/IJN.S81156.

3 Cohen, Zoya & Maimon, Yair & Yoeli-Lerner, Merav & Yang, Peiyong & Samuels, Noah & Berger, Raanan. (2014). Selective anticancer effects and protection from chemotherapy by the botanical compound LCS101: Implications for cancer treatment. *International journal of oncology*. 46. 10.3892/ijo.2014.2711.

4 Zhao, Chen-Yang & Cheng, Rui & Yang, Zhe & Tian, Zhong-Min. (2018). Nanotechnology for Cancer Therapy Based on Chemotherapy. *Molecules (Basel, Switzerland)*. 23. 10.3390/molecules23040826.

5 Rhee, Yun & Mansour, Heidi. (2011). Nanopharmaceuticals I: Nanocarrier systems in drug delivery. *International Journal of Nanotechnology - INT J NANOTECHNOL*. 8. 10.1504/IJNT.2011.037172.

6 Nagy, Janice & Chang, S-H & Dvorak, A & Dvorak, Harold. (2009). Why are tumour blood vessels abnormal and why is it important to know?. *British journal of cancer*. 100. 865-9. 10.1038/sj.bjc.6604929.

7 Jie Kai, Tee & Yip, Li Xian & Tan, Eveline & Santitewagun, Supawan & Prasath, Arun & Ke, Pu & Ho, Han & Leong, David. (2019). Nanoparticles' interactions with vasculature in diseases. *CHEM SOC REV 2019. Chemical Society Reviews*. 48. 5381-5407. 10.1039/C9CS00309F.

8 Orentas, Rimantas & Sindiri, Sivasish & Duris, Christine & Wen, Xinyu & He, Jianbin & Wei, Jun & Jarzembowski, Jason & Khan, Javed. (2017). Paired Expression Analysis of Tumor Cell Surface Antigens. *Frontiers in Oncology*. 7. 173. 10.3389/fonc.2017.00173.

- 9 Hong, Yourae & Park, Choa & Kim, Nayoung & Cho, Juyeon & Moon, Sung Ung & Kim, Jongmin & Jeong, Euna & Yoon, Sukjoon. (2018). QSurface: Fast identification of surface expression markers in cancers. *BMC systems biology*. 12. 17. 10.1186/s12918-018-0541-6.
- 10 Mansoori, Behzad & Mohammadi, Ali & Davudian, Sadaf & Shirjang, Solmaz & Baradaran, Behzad. (2017). The Different Mechanisms of Cancer Drug Resistance: A Brief Review. *Advanced Pharmaceutical Bulletin*. 7. 339-348. 10.15171/apb.2017.041.
- 11 Sawant, Rupa & Torchilin, Vladimir. (2012). Challenges in Development of Targeted Liposomal Therapeutics. *The AAPS journal*. 14. 303-15. 10.1208/s12248-012-9330-0.
- 12 Suk, Jung & Xu, Qingguo & Kim, Namho & Hanes, Justin & Ensign, Laura. (2015). PEGylation as a strategy for improving nanoparticle-based drug and gene delivery. *Advanced drug delivery reviews*. 99. 10.1016/j.addr.2015.09.012.
- 13 Räägel, Helin & Pooga, Margus. (2011). Peptide and Protein Delivery with Cell-penetrating Peptides. 10.1016/B978-0-12-384935-9.10010-0.
- 14 Bae, Dong-Goo & Kim, Tae-Dong & Li, Ge & Yoon, Wan-Hee & Chae, Chi-Bom. (2005). Anti-Flt1 Peptide, a Vascular Endothelial Growth Factor Receptor 1-Specific Hexapeptide, Inhibits Tumor Growth and Metastasis. *Clinical cancer research : an official journal of the American Association for Cancer Research*. 11. 2651-61. 10.1158/1078-0432.CCR-04-1564.
- 15 Soe, Zar & Ou, Wenquan & Gautam, Milan & Poudel, Kishwor & Kim, Bo & Le Minh, Pham & Cao Dai, Phung & Jeong, Jee-Heon & Jin, Sung & Choi, Han-Gon & Ku, Sae & Yong, Chul & Kim, Jong. (2019). Development of Folate-Functionalized PEGylated Zein Nanoparticles for Ligand-Directed Delivery of Paclitaxel. *Pharmaceutics*. 11. 562. 10.3390/pharmaceutics11110562.
- 16 Goren, D & Horowitz, A & Tzemach, D & Tarshish, M & Zalipsky, Samuel & Gabizon, Alberto. (2000). Nuclear delivery of doxorubicin via folate-targeted liposomes with bypass of multidrug-resistance efflux pump. *Clinical cancer research : an official journal of the American Association for Cancer Research*. 6. 1949-57.
- 17 Behzadi, Shahed & Serpooshan, Vahid & Tao, Wei & Hamaly, Majd & Alkawareek, Mahmoud & Dreaden, Erik & Brown, Dennis & Alkilany, Alaaldin & Farokhzad, Omid & Mahmoudi, Morteza. (2017). Cellular uptake of nanoparticles: Journey inside the cell. *Chem. Soc. Rev.*. 46. 10.1039/C6CS00636A.
- 18 Yoo, Jihye & Park, Changhee & Yi, Gawon & Lee, Donghyun & Koo, Heebeom. (2019). Active Targeting Strategies Using Biological Ligands for Nanoparticle Drug Delivery Systems. *Cancers*. 11. 640. 10.3390/cancers11050640.
- 19 Foroozandeh, Parisa & Abdul Aziz, Azlan. (2018). Insight into Cellular Uptake and Intracellular Trafficking of Nanoparticles. *Nanoscale Research Letters*. 13. 10.1186/s11671-018-2728-6.

- 20 Swartz, Melody & Lund, Amanda. (2012). Lymphatic and interstitial flow in the tumour microenvironment: Linking mechanobiology with immunity. *Nature reviews. Cancer*. 12. 210-9. 10.1038/nrc3186.
- 21 Barua, Sutapa & Mitragotri, Samir. (2014). Challenges associated with Penetration of Nanoparticles across Cell and Tissue Barriers: A Review of Current Status and Future Prospects. *Nano today*. 9. 10.1016/j.nantod.2014.04.008.
- 22 Kumar, Sandeep & Markusic, David & Biswas, Moanaro & High, Katherine & Herzog, Roland. (2016). Clinical development of gene therapy: results and lessons from recent successes. *Molecular therapy. Methods & clinical development*. 3. 16034. 10.1038/mtm.2016.34.
- 23 Kamber, Nahrain & Jeong, Wonhee & Waymouth, Robert & Pratt, Russell & Lohmeijer, Bas & Hedrick, James. (2008). Organocatalytic Ring-Opening Polymerization. *Chemical reviews*. 107. 5813-40. 10.1021/cr068415b.
- 24 Labet, Marianne & Thielemans, Wim. (2009). Synthesis of polycaprolactone: A review. *Chemical Society reviews*. 38. 3484-504. 10.1039/b820162p.
- 25 Pérez, Pedro & Haldón, Estela & Nicasio, M. Carmen. (2015). Copper-catalysed azide-alkyne cycloadditions (CuAAC): An update. *Org. Biomol. Chem.*. 13. 10.1039/C5OB01457C.
- 26 Mahou, Redouan & Wandrey, Christine. (2012). Versatile Route to Synthesize Heterobifunctional Poly(ethylene glycol) of Variable Functionality for Subsequent Pegylation. *Polymers*. 4. 561-589. 10.3390/polym4010561.
- 27 Bouzide, Abderrahim & Sauvé, Gilles. (2010). ChemInform Abstract: Silver(I) Oxide Mediated Highly Selective Monotosylation of Symmetrical Diols. Application to the Synthesis of Polysubstituted Cyclic Ethers. *Cheminform*. 33. 10.1002/chin.200248051.
- 28 Pohlit, Hannah & Worm, Matthias & Langhanki, Jens & Berger-Nicoletti, Elena & Opatz, Till & Frey, Holger. (2017). Silver Oxide Mediated Monotosylation of Poly(ethylene glycol) (PEG): Heterobifunctional PEG via Polymer Desymmetrization. *Macromolecules*. 50. 10.1021/acs.macromol.7b01787.
- 29 Takata, Toshikazu. (2006). Polyrotaxane and Polyrotaxane Network: Supramolecular Architectures Based on the Concept of Dynamic Covalent Bond Chemistry. *Polymer Journal*. 38. 1-20. 10.1295/polymj.38.1.
- 30 Arisaka, Yoshinori & Yui, Nobuhiko. (2019). Polyrotaxane-based biointerfaces with dynamic biomaterial functions. *Journal of Materials Chemistry B*. 7. 10.1039/C9TB00256A.
- 31 Matyjaszewski, Krzysztof. (2012). Atom Transfer Radical Polymerization (ATRP): Current Status and Future Perspectives. *Macromolecules*. 45. 4015-4039. 10.1021/ma3001719.

32 Fischer, Hanns. (2002). The Persistent Radical Effect: A Principle for Selective Radical Reactions and Living Radical Polymerizations. *Chemical reviews*. 101. 3581-610. 10.1021/cr990124y.

2 Shedding light on surface exposition of poly(ethylene glycol) and folate targeting units on nanoparticles of poly(ϵ -caprolactone) diblock copolymers: Beyond a paradigm ¹

Introduction

Polymeric nanoparticles (NPs) are in the limelight in cancer nanotechnology due to the advantages of prompt manipulation of the overall features (size, surface hydrophilicity/charge, release rate, biodegradability) through appropriate tailoring of the chemistry of building blocks (Grossen et al., 2017). Amid the huge amount of biomaterials developed so far, poly(ϵ -caprolactone)-poly(ethylene glycol) PEG-PCL copolymers with different hydrophilic/lipophilic balance and architectures have been synthesized resulting in a wide arsenal for drug delivery application (Li and Tan, 2014). In the context of cancer therapies, NPs of PEG-PCL block copolymers have gained attention in preclinical studies and in clinical settings with the promise to ameliorate chemotherapy outcome and decrease treatment toxicity. As far as PEG-PCL NPs for intravenous injection are concerned, a PEGylated surface can help to escape Mononuclear Phagocyte System (MPS), to attain long-circulation and to promote extravasation in inflamed tissues with a typical dysfunctional capillary bed such as in tumors (Bertrand and Leroux, 2012). While demonstrating excellent stability in PBS, PEG-PCL NPs were even found to aggregate in the presence of serum (Gao et al., 2014).

Surface modification of PEGylated NPs with covalently-linked small ligands is a further strategy followed to increase drug level in cancer cells. To this purpose, the design of folate-decorated NPs carrying a chemotherapeutic and internalizing in cancer cells through FR α -mediated endocytosis has become a hot topic (Cheung et al., 2016). FR α expression level is a marker of tumor aggressiveness, plays a role in the low response rate to chemotherapeutics resistance and is insensitive to chemotherapy regimen (Cheung et al., 2016), thus strengthening the potential utility of FR-mediated delivery. Folate decoration of PEG-PCL NPs has been attempted by us and other authors by synthesizing all-in-one amphiphilic block copolymers bearing folate at PEG hydroxyl-end group and able to form core-shell NPs (Grossen et al., 2017). When the amphiphilic diblock polymers self-assemble into NPs in an aqueous phase, the PEG segments are expected to form the outer corona allowing the conjugated folic acid to become fully accessible on the surface. In contrast to this paradigm, we observed that for highly PEGylated micelle-like NPs, folate exposition in the presence of serum is highly dependent by the formation of a protein corona (Conte et al., 2016).

Another aspect to consider when fabricating PEG-PCL NPs refers to the mode of copolymer assembly. While dialysis has been largely employed to prepare PEG-PCL micelles/NPs, scale-up of production as well as in-process sterilization is feasible with microfluidics which takes after solvent

¹ The work presented in this paragraph has been published as: Shedding light on surface exposition of poly(ethylene glycol) and folate targeting units on nanoparticles of poly(ϵ -caprolactone) diblock copolymers: Beyond a paradigm

Alessandro Venuta, Francesca Moret, Giovanni Dal Poggetto, Diletta Esposito, Fraixd, Concetta Avitabile, Francesca Ungaro, Mario Malinconico, Salvatore Sortino, Alessandra Romanelli, Paola Laurienzo, Elena Reddi, Fabiana Quaglia.

European Journal of Pharmaceutical Sciences, Volume 111, 1 January 2018, Pages 177-185
<https://doi.org/10.1016/j.ejps.2017.09.048>

displacement (nanoprecipitation) techniques. Importantly, mode of assembly of PEG-PCL copolymers can highly affect the amount of PEG on the surface (Quaglia et al., 2006) while its impact on protein adsorption and targeting features has been poorly considered.

On this basis, it is evident that PEG coverage plays a crucial role in controlling the biological fate of PEGylated NPs with a huge impact on the processes driven by protein interactions (immune system recognition, biodistribution), transport through biological matrices (tumor extracellular matrix, mucus, bacteria biofilm), and target recognition and docking (cell uptake) (Rabanel et al., 2014). Despite the extensive use of PEG, there is no consensus on the target product profile in term of PEG density, molecular weight and conformation when developing PEGylated NPs intended for a specific application, in cancer as well (Owens and Peppas, 2006). Thus, surface of NPs should be characterized in depth through complimentary techniques in view of a full optimization of the nanocarrier and following clinical application (Rabanel et al., 2014).

In this study, we tried to shed light on the surface exposition of PEG and folate targeting units on NPs of PEG-PCL diblock copolymers prepared by solvent displacement technique and to relate shell features to uptake in human cells. To this purpose, we synthesized PEG-PCL copolymers with either 1 kDa or 2 kDa PEG chains and a Fol-PEG-PCL copolymer with 1.5 kDa PEG segment. Shell properties of untargeted and folate-targeted NPs were fully characterized through complementary techniques, such as ¹H NMR, fluorescence, photon correlation spectroscopy and ζ potential. The impact of shell features on NPs interaction with human serum albumin, stability in biologically-relevant media as well as internalization in human macrophages and cancer cells overexpressing folate receptor were investigated.

Experimental section

Materials

Poly(ethylene glycol) (PEG) with Mn 1.5 kDa (PEG1.5k, Sigma-Aldrich, Milan, Italy), monomethoxy-poly(ethylene glycol) with Mn 2.0 kDa (mPEGL, Sigma-Aldrich, Italy) and monomethoxy-poly(ethylene glycol) with Mn 1.0 kDa (mPEGS, Nanocs Inc., USA) were dehydrated by azeotropic distillation with dry toluene in a Dean-Stark trap. ϵ -Caprolactone (CL, Sigma-Aldrich, Italy) was distilled over CaH₂ under vacuum. Stannous-(2-ethylhexanoate)₂ (Sn(oct)₂), N-hydroxysuccinimide (NHS), N,N'-dicyclohexylcarbodiimide (DCC), triethylamine (TEA), dimethylaminopyridine (DMAP), tosyl chloride (TsCl), folic acid (Fol), propargylamine, triphenylphosphine (PPh₃), silver(I) oxide, potassium iodide and sodium azide were used without further purification. Copper wires (Carlo Erba, Italy) were treated with H₂SO₄ for 3 min, washed with water and methanol, and finally dried under vacuum in an oven for 30 min at 60 °C. 1,4-Butandiol, 1-hexanol, N,N-dimethylformamide (DMF) and dichloromethane (DCM) were dried before use according to standard procedures. All the other solvents (analytical grade) were purchased from Sigma-Aldrich and used as received. (2-Hydroxypropyl)- β -cyclodextrin (HP β CD, DS 0.9), Nile Red (NR) and Human Serum Albumin (HSA) were from Sigma (Italy).

Copolymer characterization

FTIR analysis was performed with a Perkin-Elmer spectrometer (Paragon 500) equipped with a ZnSe attenuated total reflectance (ATR) crystal accessory. Samples were placed in direct contact with the ATR crystal and pressed with a pressure clamp positioned over the crystal/sample area to

allow intimate contact between the material and the crystal. Spectra were acquired in the 4000–400 cm^{-1} range, at a resolution of 2 cm^{-1} (average of 20 scans). ^1H NMR analysis, spectra were recorded with a Bruker Avance DPX400 apparatus operating at 400 MHz. For GPC analysis, samples were dissolved in THF and passed through a 0.22 μm PTFE membrane filter. Measurements were performed on an injected volume of 100 μL by using a Malvern-Viscotek GPC MAX/TDA 305 quadruple detector array equipped with a precolumn and two Phenogel columns (Phenomenex) with exclusion limits 106 and 103 respectively. The GPC instrument was used at a flow rate of 0.8 mL/min and at columns and system temperature of 35 $^{\circ}\text{C}$. Triple detectors calibration was based on a standard of polystyrene with molecular weight 104,959 Da. Residual copper content was estimated by Microwave Plasma-Atomic Emission Spectrometry (MP-AES) with a Agilent 4100 spectrometer. A microwave digestion system Milestone Ethos Touch Control was used for digestion of sample. The finely ground sample (0.1 g) was transferred in a teflon microwave digestion vessel and treated with 6 mL of HNO_3 , 3 mL of HCl and 1 mL of H_2O_2 (Ultrapure Reagents, trace metal grade $< 1 \mu\text{g/L}$). The samples were processed by microwave digestion as follows: ramp to 200 $^{\circ}\text{C}$ over 10 min, then hold at 200 $^{\circ}\text{C}$ for 20 min. After digestion, the samples were cooled to room temperature, filtered, transferred in a 50 mL volumetric flask and adjusted to 50 mL with distilled water for spectrometric analysis. The amount of Fol linked to the copolymer was quantified by UV-vis spectroscopy on DMSO polymer solutions (0.2–2 mg/mL), using Fol standard solutions in DMSO to construct calibration curves. The absorbance of the sample was evaluated at 360 nm on a Shimadzu 1800 spectrophotometer.

Synthesis of mPEG_S-PCL and mPEG_L-PCL

Linear diblock copolymers were prepared by ring-opening polymerization (ROP) of CL at 120 $^{\circ}\text{C}$ for 24 h using mPEG_L or mPEG_S as initiator and $\text{Sn}(\text{Oct})_2$ as catalyst (20%). CL/initiator molar ratio = 36. ^1H NMR (CDCl_3 , δ in ppm), PCL block: 1.29–1.78 (m), 2.19–2.43 (t) 3.20 (m); 3.92–4.21 (t), 4.31(t); PEG block: 4.10 (t), 3.64 (s), 3.38, (t).

Synthesis of Fol-PEG-PCL

Synthesis of azido-PEG-PCL copolymer (N₃-PEG-PCL)

Step 1. Synthesis of monotosyl-PEG (Ts-PEG-OH).

PEG (5.00 g, 3.34 mmol) was dissolved in 50 mL of dry toluene. Ag_2O (1.161 g, 5.01 mmol) and KI (110 mg, 0.668 mmol) were finely dispersed in the solution by stirring, then TsCl (2.76 g, 14.5 mmol) was added. The reaction mixture was kept at room temperature under stirring and nitrogen atmosphere for 12 h. The solution was filtered and solvent removed by rotary evaporation. The polymer was dissolved in 10 mL of DCM and precipitated in cold diethyl ether (yield 95%). ^1H NMR (d_6 -DMSO, δ in ppm): 7.79 (2H, d), 7.49 (2H, d), 4.56 (1H, t), 4.11 (2H, t), 3.49 (128H, s), 2.43 (3H, s).

Step 2. Synthesis of monoazido-PEG (N₃-PEG-OH).

Ts-PEG-OH (1.00 g, 0.66 mmol) was dissolved in 15 mL of dry DMF, then NaN_3 (214 mg, 3.3 mmol) was added and the mixture was stirred at 90 $^{\circ}\text{C}$ overnight under nitrogen atmosphere. The reaction mixture was cooled to room temperature, filtered, and DMF removed under vacuum. The product was dissolved in 10 mL of DCM and the solution was extracted twice with brine and twice

with water in a separating funnel. The organic phase was dried over anhydrous Na_2SO_4 , concentrated and poured in cold diethyl ether. Polymer was collected by filtration (yield 81%). ^1H NMR (d^6 -DMSO, δ in ppm): 4.56 (1H, t), 3.6 (2H, t), 3.5 (127H, s, PEG backbone), 3.4 (2H, t). FTIR diagnostic band: 2107 cm^{-1} (N_3 stretching).

Step 3. Synthesis of N_3 -PEG-PCL copolymer.

N_3 -PEG-OH (600 mg, 0.393 mmol), CL (1.572 g, 13.77 mmol) and $\text{Sn}(\text{Oct})_2$ (31 mg, 0.078 mmol) were charged in a flask under dry nitrogen. The polymerization was carried out at $120\text{ }^\circ\text{C}$ for 24 h under stirring. The copolymer was dissolved in 10 mL of DCM, precipitated in cold hexane, recovered by filtration and finally dried (yield 91%). ^1H NMR (CDCl_3 , δ in ppm): 3.6 (2H, t), 3.5 (127H, s, PEG backbone), 3.4 (2H, t), 1.29–1.78 (139H, m); 2.19–2.43 (82H, m), 3.92–4.21 (82H, t), 4.31 (2H, t); M_n of PCL evaluated by ^1H NMR = 4,6 kDa.

Synthesis of propargylfolate

Fol (500 mg, 1.13 mmol) was charged in a flask under dry nitrogen and dissolved by stirring in 20 mL of DMSO over mild heating, then DCC (446 mg, 2.16 mmol) and NHS (260 mg, 2.26 mmol) were added. Reaction was carried out in the dark at room temperature for 17 h, the solution was filtered to remove the side product (dicyclohexylurea, DCU), then propargylamine (124 mg, 2.25 mmol) and TEA (228 mg, 2.25 mmol) were added. The reaction was left overnight. The product was precipitated with a diethylether/acetone 80/20 mixture, repeatedly washed first with acetone and then with diethylether, and finally dried under vacuum overnight. A yellow powder was obtained and analyzed by LC-MS (Agilent Technologies, 6230 ESI-TOF) on a Phenomenex Jupiter column (C18, $3\text{ }\mu\text{m}$, $150 \times 2.0\text{ mm}$) with a gradient of acetonitrile (0.1% TFA) in water (0.1% TFA), from 5 to 50% in 15 min at a flow rate of 0.2 mL/min.

Click conjugation of propargylfolate with N_3 -PEG-PCL (Fol-PEG-PCL)

N_3 -PEG-PCL (800 mg, 0.12 mmol) dissolved in 15 mL of DMSO was charged in a flask under dry nitrogen, then propargylfolate (86 mg, corresponding to a propargyl/ N_3 molar ratio of 1.1) and copper wires (120 mg) were added; the reaction was carried out under stirring at room temperature overnight. The solution was filtered to remove copper and then dialyzed against DMSO with a 2000 cut-off dialysis tube for 4 days, in order to eliminate free propargylfolate and other side products. Finally, DMSO was evaporated under nitrogen stream. The occurrence of reaction was confirmed by FTIR through the complete disappearance of 2097 cm^{-1} N_3 stretching band (yield 95%). Fol content = 6.5% by wt, functionalization degree = 90%.

Preparation and characterization of nanoparticles

Non-targeted NPs were prepared from $m\text{PEG}_S$ -PCL and $m\text{PEG}_L$ -PCL while folate-decorated NPs were prepared from a mixture of $m\text{PEG}_S$ -PCL or $m\text{PEG}_L$ -PCL with Fol-PEG-PCL. NPs were formed by solvent diffusion of an organic phase (10 mg of copolymer in 1 mL of acetone) added dropwise in water (2 mL) under magnetic stirring (500 rpm). After solvent evaporation, NPs were filtered through $0,45\text{ }\mu\text{m}$ Phenex® filters (Phenomenex, USA). NPs could be freeze-dried (Modulyo Edwards) after the addition of HP β CD as cryoprotectant (polymer: HP β CD 1:10 wt. ratio, sample frozen in liquid N_2 , condenser temperature $-55\text{ }^\circ\text{C}$) and stored at $4\text{ }^\circ\text{C}$. Recovery yield of the production process was evaluated on an aliquot of NPs without cryoprotectant by weighing the solid residue after freeze-drying. To evaluate cell uptake, the lipophilic dye NR was physically entrapped

(0.2% of copolymer weight). The hydrodynamic diameter (DH), polydispersity index (PI) and zeta potential (ζ) of NPs were determined on a Zetasizer Nano Z (Malvern Instruments Ltd).

Fixed aqueous layer thickness (FALT) of NPs was measured by monitoring the influence of ionic strength on ζ . Different amounts of NaCl stock solutions were added to NPs dispersed in water (5 mg/mL, 100 μ L) and zeta potential of the samples measured. A plot of $\ln \zeta$ against $3.33[\text{NaCl}]^{0.5}$ gives a straight line where the slope represents the thickness of the shell in nm. (Endres et al., 2011) ^1H NMR was carried out on NPs dispersions to evaluate the amount of PEG on the surface. Spectra were recorded for either NPs prepared in D₂O or NPs freeze-dried without cryoprotectant dissolved in d₆-DMSO (5 mg/mL). Steady state fluorescence spectra were carried out with a RF6000 spectrofluorimeter (Shimadzu, Japan). Fluorescence lifetimes were recorded with Fluorolog-2 spectrofluorimeter (Model F111, Horiba) equipped with a TCSPC Triple Illuminator. The samples were irradiated by pulsed diode excitation source Nanoled at 370 nm. The kinetics were monitored at 450 nm and each solution was used to register the prompt at the excitation wavelength. The system allowed measurement of fluorescence lifetimes from 200 ps. The multiexponential fit of the fluorescence decay was obtained using the following equations:

$$I = \alpha_1 \exp(-t/\tau_1) + \alpha_2 \exp(-t/\tau_2).$$

All measurements were performed in a thermostated quartz cell (1 cm path length, 3 mL capacity).

Stability of NPs in the presence of HSA (1–500 μ M) was evaluated by placing a NPs sample (0.05 mg/mL) in the HSA water solution and monitoring immediately the size distribution by PCS.

Intracellular uptake of NPs in cancer cells

KB carcinoma cells (American Type Culture Collection, ATCC, Rockville, USA) over-expressing FR (FR α) were selected to study the specific internalization of Fol-decorated NPs vs. non-targeted NPs. The cells were grown in Eagle's medium (MEM) (Life Technologies) supplemented with 10% fetal bovine serum (FBS) (Gibco), 100 U/mL Penicillin G and 100 μ g/mL Streptomycin and maintained at 37 °C in a humidified atmosphere containing 5% CO₂. Flow cytometry measurements of the uptake of DBLS, DBLS/DBL-Fol, DBLL, DBLL/DBL-Fol were performed using fluorescent NR-loaded NPs. For all the experiments mentioned above, cells were seeded in 24 wells/plate (40,000 cells/well) in folate-deficient RPMI medium (Life Technologies) supplemented with 10% FBS. After 24 h of growth at 37 °C, the cells were incubated for 1 h with 20 μ g/mL of NR-loaded NPs, freshly re-suspended in milliQ water and diluted in RPMI medium with or without 10% of FBS. After incubation with NPs, the cells were washed, detached from the plates with trypsin (Life Technologies), centrifuged and re-suspended in Versene before measuring NR fluorescence using a BD FACSCanto™ II instrument (Becton Dickinson). The blue laser at 488 nm was used as excitation source and the PerCP channel (670–735 nm) was selected for the detection of NR fluorescence. 104 events/sample were acquired and analyzed with the FACSDiva Software. Competition experiments with 1 mM free Fol were carried out incubating the cells for 1 h prior to the addition of NPs in order to saturate FRs exposed on cell surface. The intracellular uptake of NR loaded DBL_S and DBL_S/DBL-Fol was measured also in A549 cells (ATCC), negative for FR expression. The cells were grown in F12-K medium (Life Technologies) supplemented with 10% FBS, 100 U/mL Penicillin G and 100 μ g/mL Streptomycin. For the uptake experiments, cells were seeded as described above for KB cells and incubated for 1 h with NP formulations in the absence of serum in the incubation medium.

To assess the endocytosis mechanism of DBLs/DBL-Fol NPs, KB cells were incubated 30 min before and during NP incubation (1 h) with specific molecules (all from Sigma) able to inhibit clathrin-mediated endocytosis (chlorpromazine hydrochloride, 5 $\mu\text{g}/\text{mL}$), caveolae-independent lipid-raft-dependent endocytosis (methyl- β -cyclodextrin, M β CD, 1 mM), caveolae-dependent endocytosis (Genistein 54 $\mu\text{g}/\text{mL}$ and Filipin III 5 $\mu\text{g}/\text{mL}$).

The internalization of NPs in KB cells pre-incubated or not with 1 mM free Fol was assessed also by confocal microscopy using a SP5 laser scanning microscope (Leica Microsystems). 6×10^4 cells were seeded in special tissue culture dishes for fluorescence microscopy (μ -Dish 35 mm, high, Ibidi GmbH), were allowed to grow for 24 h and then incubated for 1 h with 20 $\mu\text{g}/\text{mL}$ NPs in medium added with 10% FBS. After incubation, the cells were washed twice with PBS with Ca²⁺ + and Mg²⁺ + and immediately visualized under the microscope.

Capture of NPs by human macrophages

The capture by human macrophage of NPs decorated or not with Fol and pre-incubated in human serum (HS) was measured in order to assess their stealth properties. A positive control of non-PEGylated NPs (PCL) was tested too. Macrophages were derived from monocytes isolated from buffy coats of healthy donors by centrifugation over a Ficoll-Hypaque step gradient and subsequent Percoll gradient (Sigma-Aldrich). 2×10^6 isolated monocytes/well were seeded in 24 wells/plate and cultured for 7 days in RPMI 1640 medium (Life Technologies) supplemented with 20% FBS and 100 ng/mL of human macrophage colony-stimulating factor (PeproTech) to promote macrophage differentiation. On day 4 from the seed, the macrophage colony-stimulating factor was added again. For the uptake experiment, macrophages were incubated for 3 h in RPMI added with 10% FBS and 20 $\mu\text{g}/\text{mL}$ fluorescent NPs previously incubated at 37 °C in human serum type AB (Sigma-Aldrich) for 0, 10 or 30 min. Macrophages were then washed and detached from the plates using PBS with 5 mM EDTA, centrifuged, re-suspended in PBS + 1% BSA and analyzed by flow cytometry for fluorescence as described previously. Propidium Iodide (1 $\mu\text{g}/\text{mL}$) staining of the samples during flow cytometry acquisition was used to measure the macrophage viability, which was higher than 95%.

Statistical analysis

The Primer software for biostatistics (McGraw-Hill, Columbus, USA) was used for statistical analysis of the data. The data are expressed as means \pm SD of at least 3 independent experiments. The difference between groups was evaluated using the Student's t-test considered significant for $p < 0.05$.

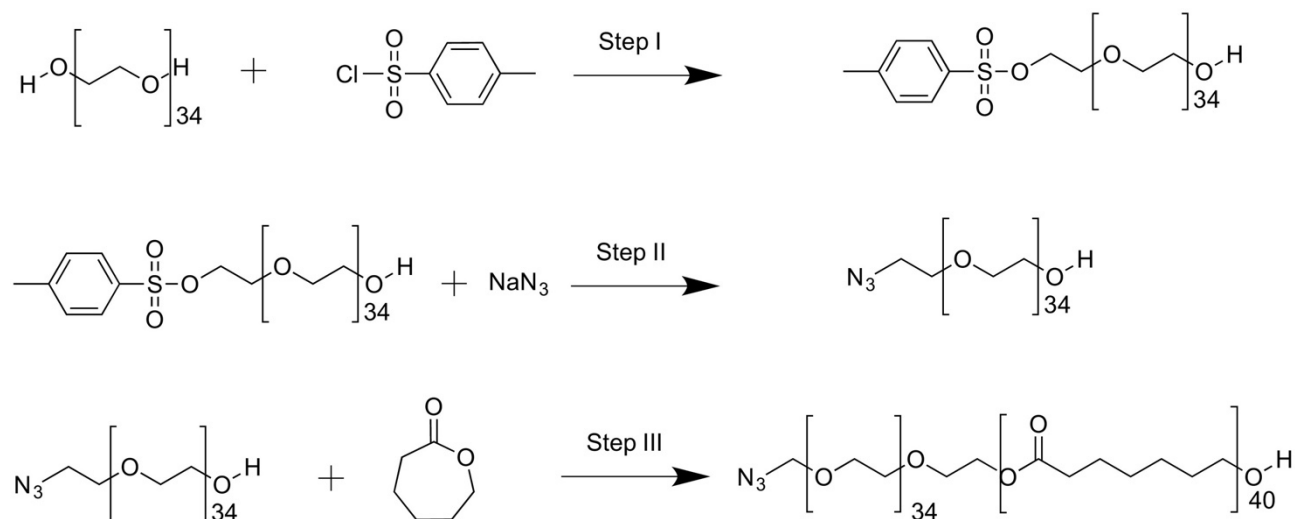
Results and discussion

Synthetic strategy

The following PEG-PCL diblock copolymers with different PEG lengths were synthesized: i) Fol-PEG-PCL copolymer (PEG MW = 1.5 kDa); ii) mPEG-PCL with a PEG MW = 1.0 kDa (mPEGS-PCL); iii) mPEG-PCL with a PEG MW = 2.0 kDa (mPEGL-PCL). Copolymers were synthesized by typical ROP polymerization of ϵ -caprolactone using a mono-hydroxyl PEG as initiator. The molecular weight of PCL block was controlled by the CL/initiator molar ratio in the feed. A value

of around 4.0 kDa was fixed for PCL on the basis of previous works (Conte et al., 2016, Tirino et al., 2014, Ungaro et al., 2012).

To prepare Fol-PEG-PCL copolymer, Cu(I)-catalyzed 1,3-Huisgen cycloaddition (“click” reaction) was chosen to conjugate folate to PEG-PCL (Himo et al., 2005). 1,3-Huisgen cycloaddition is the addition of alkynes to azides, with formation of highly stable 1,2,3-triazoles. The reaction is high yielding, stereospecific, does not create any byproduct, and can be conducted in mild conditions. PEG was first modified by introduction of an azide on one terminal group (**Scheme 1**).



Scheme 1. Synthetic pathway for synthesis of N₃-PEG-PCL diblock copolymer. Monofunctionalization of PEG was checked by ¹H NMR analysis through the ratios between the integrals of OH (4.56 δ) and CH₂OTs (4.11 δ) protons of PEG, and aromatic (7.79, 7.49 δ) and CH₃ (2.43 δ) protons of tosyl group (step 1).

Synthetic strategies aimed to asymmetrically modify PEG are largely explored in the literature. In general, the reported methods suffer from a complex chemistry and/or low purity of the final product (Li and Chau, 2010, Szekely et al., 2014). The most common way to synthesize heterotelechelic PEG remains polymerization of ethylene oxide from different initiators (Cammass et al., 1995, Hiki and Kataoka, 2007, Ishii et al., 2005, Raynaud et al., 2009, Thompson et al., 2008). To achieve monofunctionalization, the use of a large excess of PEG has been reported too (El-Gogary et al., 2014) although separation of non-modified from modified polymer requires tedious chromatography and yields are generally low. In the present paper, we used a method recently reported (Mahou and Wandrey, 2012) to achieve asymmetric activation of low molecular weight alcohols to low molecular weight PEG, so that it becomes possible to selectively link a biomolecule of interest to one end of PEG, and use the residual OH for copolymerization.

N₃-PEG-OH is used as initiator for ring-opening polymerization of CL, leading to a PEG-azido functionalized copolymer. Azide is stable at the temperature required by ROP (120 °C), as confirmed through FTIR analysis, where no change of diagnostic band of azide at 2097 cm⁻¹ is detected in the copolymer spectrum. Mn of PCL block in the copolymers was calculated by the ratio between intensities of the resonance associated to CH₂OH methylene protons at 3.64 δ and CH₂CO units in the PCL chain at 2.31 δ of ¹H NMR spectrum. A good agreement between theoretical and experimental values is found (**Table 1**).

Table 1. Theoretical and experimental molecular weights of copolymers.

Sample	Mn (Da) ^a	Mn (Da) ^b	Mn (Da) ^c	Mw (Da) ^c	PDI ^d (Mw/Mn)
N ₃ -PEG-PCL	5547	6203	5943	8049	1.36
mPEG _S -PCL	5047	5446	5059	6737	1.33
mPEG _L -PCL	6047	6579	6594	8720	1.35

^aTheoretical number-average molecular weight. ^bNumber-average molecular weight evaluated by ¹H NMR. ^cMolecular weight obtained by GPC. ^dMolecular weight polydispersity index obtained by GPC.

In order to introduce the complementary alkyne group for successive coupling to N₃-PEG-PCL, folic acid was conjugated with propargylamine through carbodiimide chemistry. It is known from the literature that only γ -folate conjugates retain affinity towards the receptor (Chen et al., 2013). Remarkably, γ -conjugates are intrinsically obtained as the major product in reactions with carbodiimide (Viola-Villegas et al., 2008); nevertheless, a clean product is hard to obtain, as separation of γ -conjugate from α - and bis-conjugates and unreacted folic acid is troublesome. For this reason, it is critical to find reaction conditions under which formation of “clickable” α - and bis-conjugates is minimized. In this case, the crude product can be used as such for coupling with N₃-PEG-PCL, then the final Fol-PEG-PCL copolymer will be easily separated from non-conjugated folic acid and other byproducts (i.e., activated folic acid, Fol-NHS) by dialysis (Liu et al., 2012). For purposes of optimization, a screening at different reaction conditions (type and amount of catalyst and propargylamine/catalyst molar ratio) was preliminary carried out, and products were characterized by LC-MS (**Table S1**, **Figure S1**). Identification of α - and γ -conjugate peaks was made according to literature (Trindade et al., 2014). Conditions for γ -propargylfolate synthesis were set so that only a negligible amount of α -conjugate and no bis-conjugate are formed (see **Entry 1 of Table S1**).

In the click reaction, copper in form of wires was preferred as catalyst, since concentration of Cu(I) ions in solution is very low with respect to other catalysts type (Nahrwold et al., 2013), avoiding long purification steps. The total amount of crude propargylfolate was calculated in order to have a propargyl/N₃ molar ratio corresponding to 1.1. Finally, the copolymer was easily purified by extensive dialysis to remove non-conjugated molecules. Reaction was followed by FTIR; the absence of azide band in the spectrum of Fol-PEG-PCL accounts for a 100% conversion (**Figure S2**). For sake of accuracy, Fol-PEG-PCL was analyzed by GPC-UV. The chromatogram shows a single peak at a retention time corresponding to that of pristine N₃-PEG-PCL copolymer, confirming the absence of free folic acid and/or derivatives (**Figure S3**). As a final check, the amount of residual copper in the copolymer, determined by MP-AES analysis, was as low as 12 ppm, allowing to exclude any possible cytotoxic effect (Cao et al., 2012).

Influence of PEG length on nanoparticle shell

We aimed at studying the effect of PEG length on the shell properties of folate-decorated NPs. To this purpose, NPs based on mixtures of Fol-PEG-PCL with either mPEG_S-PCL (DBL_S/DBL-Fol), where PEG is 1.0 kDa, or mPEG_L-PCL (DBL_L/DBL-Fol), where PEG is 2.0 kDa, were prepared (**Figure 1**). We fixed Fol-PEG-PCL amount in the composition at 20% by wt based on the results obtained in a previous paper (Conte et al., 2016). Corresponding non-targeted NPs were prepared

from mPEGL-PCL (DBL_L) and mPEGS-PCL (DBL_S). Solvent diffusion method, currently indicated as nanoprecipitation, was selected since it is very popular for preparing biodegradable NPs. Furthermore, solvent diffusion is a working principle in microfluidics, a process useful to increase the scale of NP production.

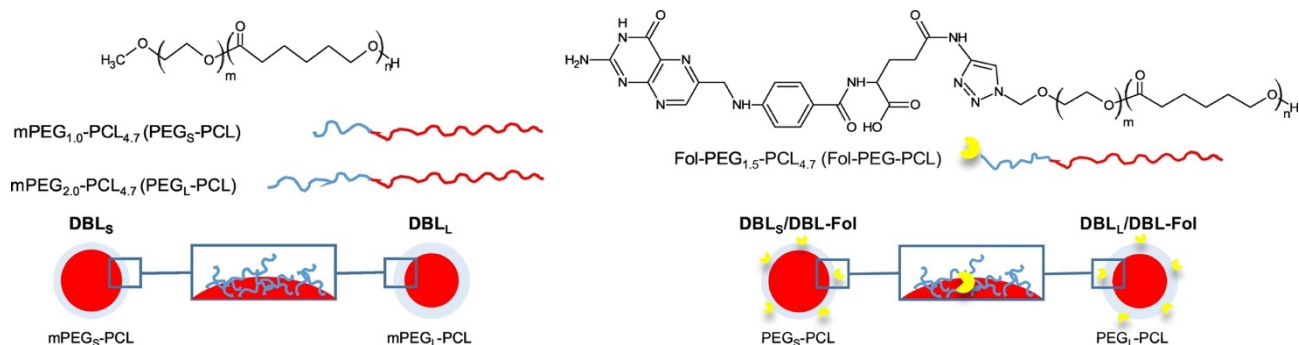


Figure 1. Design of untargeted and targeted NPs prepared from PEG-PCL diblock copolymers with different PEG length.

As can be seen in **Table 2**, monodispersed NPs spontaneously form in good yield (around 60%) without the help of any surfactant. DBL_L are smaller than DBL_S likely due to higher hydrophilicity of mPEGL-PCL. A size lower than 100 nm as determined by dynamic light scattering and comprised in a narrow size range (PI < 0.22) makes this formulation suitable for intravenous injection. ζ is slightly negative as commonly found for PEGylated NPs and slightly decreased for DBL_S/DBL-Fol. NPs exhibit spherical morphology and preserve their shape once freeze-dried in the presence of HP β CD (**Figure S4**, Supplementary material).

Table 2. Properties of NPs prepared from short (DBL_S) and long (DBL_L) MPEGPCL copolymers without and with Fol-PEG-PCL (DBL-Fol).

Formulation	D _H ^a (nm)	PI	ζ (mV)	Surface PEG ^b (wt%)	[Γ] ^c (chains/100 nm ²)	[Γ]/[Γ^*] ^d
DBL _S	78 ± 1	0.12	- 13 ± 2	7.1	2.3	0.10
DBL _S /DBL-Fol 20	82 ± 4	0.11	- 18 ± 2	4.2	1.4	0.07
DBL _L	34 ± 2	0.16	- 15 ± 1	3.5	0.6	0.06
DBL _L /DBL-Fol 20	59 ± 5	0.22	- 17 ± 3	2.0	0.6	0.05

Values lower than 1 suggest a mushroom conformation. [Γ^*] represents the theoretical number of unconstrained PEG chains that would occupy the nanoparticle surface.

^aThe results are reported as mean of three separate measurements on three different batches ± SD.

^bSurface PEG was measured by ¹H NMR integrals of PEG signals in copolymer solution and in NPs.

^c[Γ] is the number of PEG chains per 100 nm² of nanoparticle surface area.

^dThe ratio [Γ]/[Γ^*] indicates packing extent of PEG on the surface.

The amount of PEG on NPs surface was evaluated by ¹H NMR and the packing extent of PEG on the surface calculated (Auguste et al., 2006, Xu et al., 2015). Results are reported in **Table 2**. For all the samples, the experimental amount of PEG on the surface is much lower than the theoretical value, suggesting that, in the conditions adopted to produce non-targeted and folate-targeted NPs, PEG is located inside NP core and partly confined to the surface. The amount of PEG on the surface decreases for DBL_L (despite their low size) and more in general upon addition of folate copolymer. Furthermore, [Γ]/[Γ^*] values well below the cut-off value of 1 indicate that PEG chains are in the mushroom-like conformation. These data demonstrate that, although NPs are prepared from

PEGylated copolymers, the amount of PEG on the surface is below 7% in line with our previous results on triblock and star-shaped PEG-PCL copolymers (Ungaro et al., 2012). Similar degree of PEG coverage has been found preparing NPs by emulsion-solvent evaporation from mixtures of non-PEGylated and PEGylated copolymers (Xu et al., 2015).

The thickness of the external shell of NPs was evaluated by FALT, measuring the values of NPs ζ in NaCl solutions at different concentrations and fitting the data to a regression line ($r > 0.980$) (**Figure 2A**). The slope of these lines in absolute value represents FALT in nm. FALT is lower for NPs prepared from DBLS with short PEG (2.51 ± 0.20 nm) and higher for NPs prepared from DBLL with long PEG (3.84 ± 0.15 nm). In folate-decorated NPs, however, FALT increases for DBLS/DBL-Fol (2.72 ± 0.11 nm) and decreases for DBLL/DBL-Fol (3.58 ± 0.29 nm) suggesting a different arrangement of folate in the shell. Folate folding in PEG chains on the surface is likely occurring for DBLL/DBL-Fol, which could hide targeting ligand on the surface and prevent receptor recognition.

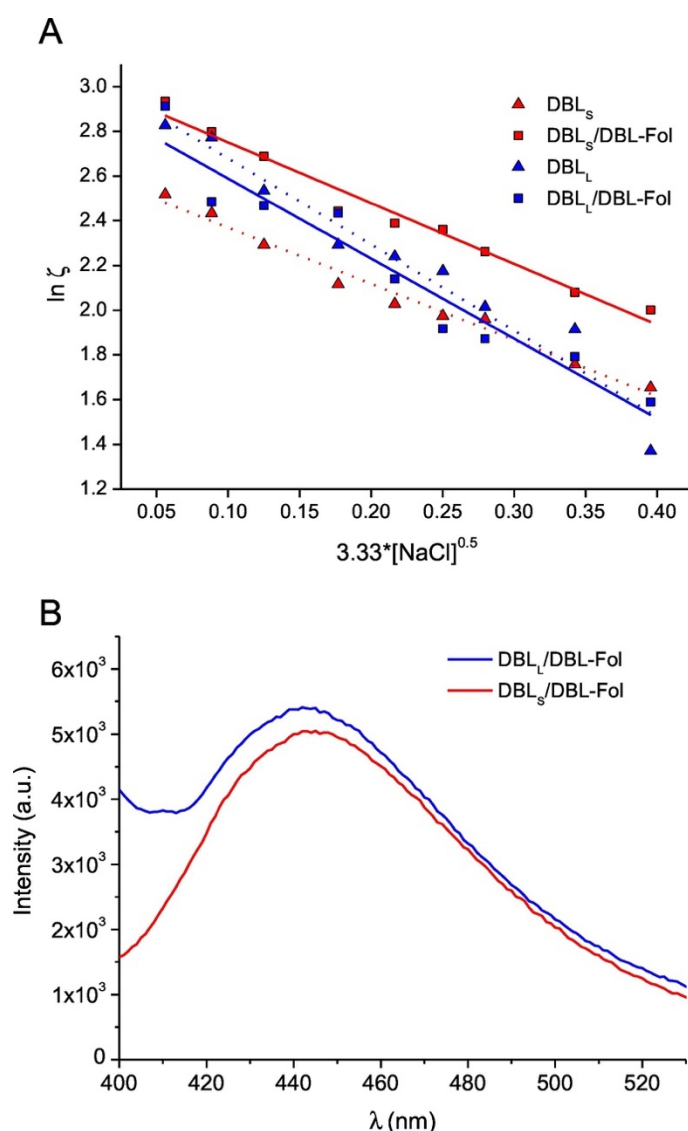


Figure 2. Properties of the NPs shell. A) Thickness of the outer shell of non-targeted NPs (DBL_S and DBL_L) and targeted NPs (DBL_S/DBL-Fol and DBL_L/DBL-Fol). Shell thickness (in nm) can be derived from the absolute value of the slope in the regression lines. For clarity purpose, results of a single experiment are reported. B) Emission spectra of folate-decorated NPs (5 mg/mL) in water ($\lambda_{ex} = 370$).

To gain insights into the environment experienced by folate moieties in the NPs, the emission behaviour of DBL_S/DBL-Fol and DBL_L/DBL-Fol was investigated by steady-state and time-resolved fluorescence spectroscopy. In fact, folate is a fluorescent molecule emitting in the visible range with an emission maximum at 450 nm. **Figure 2B** shows the typical fluorescence emission of the folic acid, which is slightly more intense for DBL_L/DBL-Fol. Inasmuch the two samples contain the same number of fluorogenic units, these slight but reproducible differences account for a larger fluorescence quantum yield for DBL_L/DBL-Fol. In principle, this can be the result of i) self-quenching effects occurring in DBL_S/DBL-Fol, ii) the different polarity experienced by the folate groups, or both. The dynamic behavior of the fluorescence is in line with the former hypothesis. As shown in **Table 3**, the fluorescence decay was bi-exponential in both cases. However, we observed a more pronounced contribution of the longer component in the case of DBL_L/DBL-Fol. These findings are in fairly good agreement with a picture involving the folate group of DBL_S/DBL-Fol more exposed to water pool instead of being extended in the PEG shell.

Table 3. Lifetimes (in ns) and amplitudes ($\Sigma\alpha = 1$) obtained by the biexponential fitting of the fluorescence decay for the different samples ($\lambda_{\text{ex}} = 370$ nm $\lambda_{\text{em}} = 450$ nm).

Sample	τ_1	α_1	τ_2	α_2
DBL_S/DBL-Fol 20	0.50	0.30	7.71	0.70
DBL_L/DBL-Fol 20	0.63	0.22	8.00	0.78

Interaction of nanoparticles with HSA

Conformation of PEG on NPs surface can drive interactions with proteins. Here we focused on HSA, the most abundant protein in the blood pool. Interaction of NPs with HSA was clearly demonstrated by fluorescence spectroscopy. **Figure 3A** shows the fluorescence spectra of HSA in the absence and in the presence of NPs upon excitation at 278 nm. This wavelength allows the selective excitation of HSA over folate. The black spectrum shows the typical dual band fluorescence spectrum of HSA, which reflects the contribution of the tyrosine (λ_{em} ca 310 nm) and tryptophan (λ_{em} ca 340 nm) fluorogenic centres. This strong emission is quenched by more than one order of magnitude upon addition of NPs. In contrast, the fluorescence of folate is basically unaffected in the presence of HSA (data not shown).

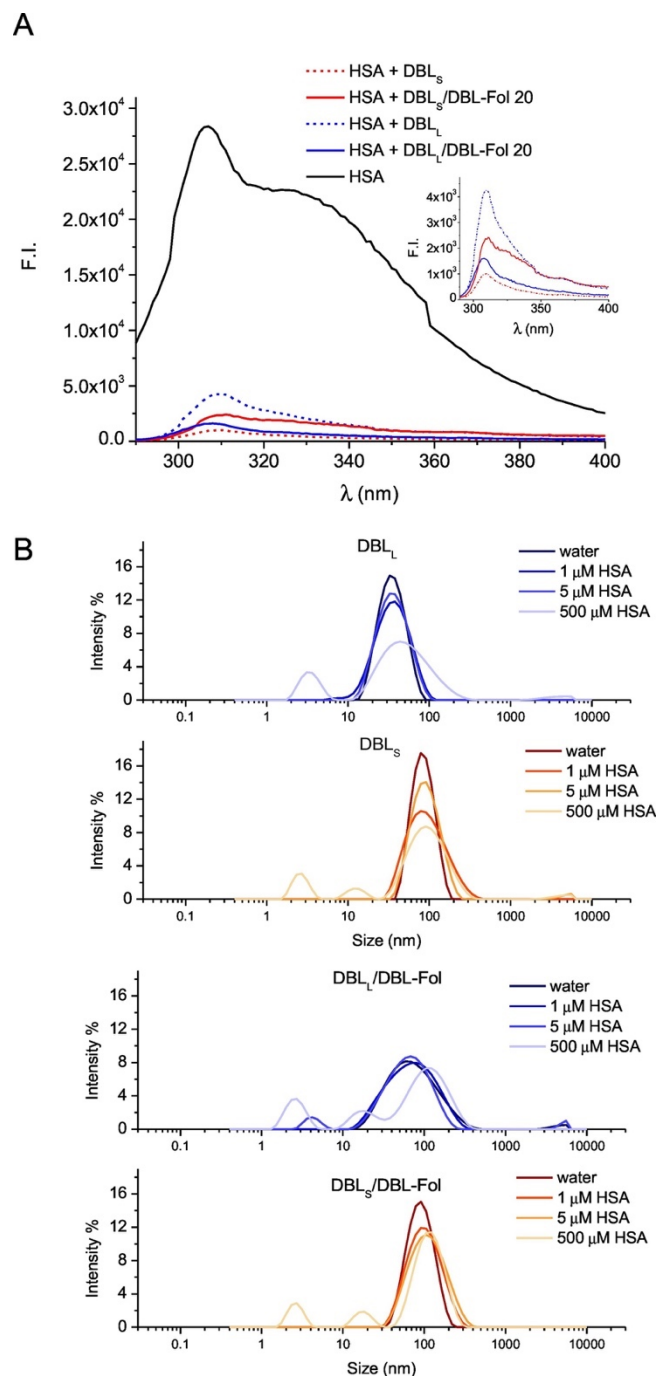


Figure 3. Behaviour of NPs in the presence of HSA. A) Emission spectra of folate-decorated NPs (5 mg/mL) in the presence of HSA (3 μ M). A reference curve of a HSA solution (0.3 μ M) is reported for comparison. Excitation wavelength was 278 nm. B) Size distribution curves of NPs (0.05 mg/mL) in the presence of HSA (1–500 μ M).

Since the emission of HSA fluorescent aminoacids well overlaps with the absorption spectrum of the folate, one could explain the quenching observed as a result of a photoinduced energy transfer via FRET mechanism. However, this is not the case since no emission of the folate was in fact observed concurrently to the quenching. Rather, the fluorescence behaviour might be simply due to static quenching effects arising by the massive aggregation of HSA on the NPs.

Formation of a HSA corona was evidenced also by evaluating size distribution curves of NPs at increasing HSA concentration (**Figure 3B**). As compared to water, addition of HSA up to 5 μ M does not change greatly the shape of the size curves, while at physiologically relevant HSA concentrations (500 μ M) NPs mean size is increased for NPs of DBL_L series and is unaltered for

DBLS. The appearance of the peaks at 3 and 11 nm corresponding to free HSA monomers/tetramers/hexamers, indicate that in these adopted conditions, the surface of NPs is fully occupied by HSA. Remarkably, these results highlight that despite PEGylation, NPs developed here adsorb HSA forming a soft corona without inducing their aggregation.

Interaction of nanoparticles with human macrophages

To predict NPs in vivo capture by MPS once NPs are intravenously injected, we studied in vitro their uptake in human macrophages differentiated from monocytes and isolated from human buffy coats. Untargeted and folate-targeted NPs were not pre-incubated (time 0) or pre-incubated with human serum for 10 or 30 min at 37 °C before the addition and 3 h incubation with macrophages. A positive control of PCL NPs (non-PEGylated) was employed. Pre-incubation of NPs with human serum significantly increases their time-dependent uptake by macrophages for non-PEGylated NPs only (**Figure 4**), while the uptake of all the PEGylated NPs is unaffected or shows the opposite trend. Confirming a general paradigm, non-PEGylated NPs demonstrate the highest capture level by macrophages. The uptake of untargeted NPs increases when shortening the PEG length from 2.0 kDa to 1.0 kDa. In any case, the presence of folate on the surface does not affect significantly NPs phagocytosis. These results are in line with the general observation that the presence of a PEG shell on NPs surface limits the adsorption of serum proteins largely preventing NPs capture by phagocytes as macrophages (Walkey et al., 2012).

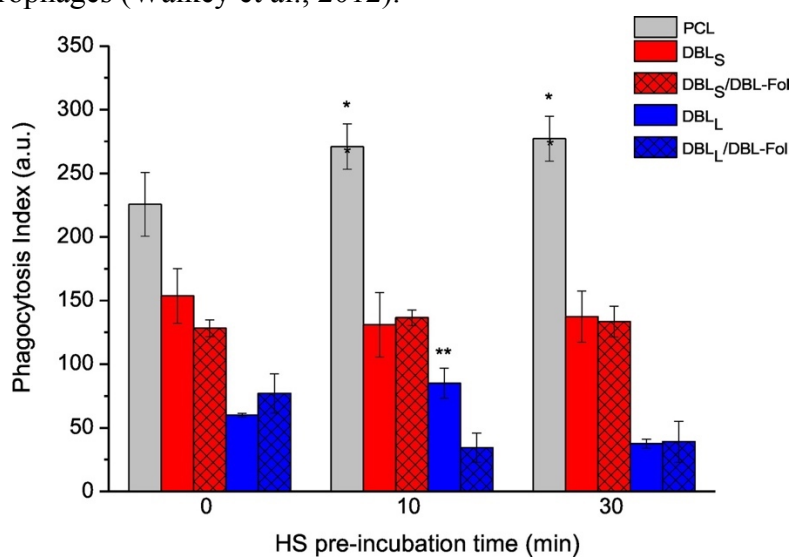


Figure 4. NPs capture by macrophages. NPs were pre-incubated in human serum (HS) for 10 or 30 min before a 3 h incubation with macrophages at 37 °C. Phagocytosis Index represents the median total fluorescence intensity measured per macrophage by FACS. * $p < 0.005$, ** $p < 0.001$, with respect to NPs not pre-incubated with human serum (Student's t-test).

Cellular uptake of nanoparticles in KB cancer cells

To assess if the exposition of folate over the PEGylated surface increased the specific uptake of NPs in cells over-expressing FRs, we measured the uptake of targeted and non-targeted NPs in KB cells by flow cytometry. The uptake was measured in the absence and in the presence of 10% serum in the cell incubation medium to highlight the impact of NPs interaction with serum proteins. As reported in **Figure 5A**, the uptake of DBL_S/DBL-Fol occurs at least in part through FR-mediated endocytosis. In fact, pre-incubation of cells with 1 mM free Fol for 1 h to saturate FRs prior to NPs addition significantly decreases internalization. The extent of FR-mediated endocytosis of

DBLS/DBL-Fol is higher without serum in the medium, probably due to partial ‘masking effect’ exerted by protein association to NPs shell (Conte et al., 2016). On the contrary, although PEGylation degree is low and PEG is in a mushroom conformation for both DBL_S/DBL-Fol and DBL_L/DBL-Fol, only DBL_S/DBL-Fol allows the recognition of folate moieties by FR in the presence of serum. For DBL_L/DBL-Fol, folate amount is lower than expected on the basis of fluorescence lifetimes, and is probably unable to extend over the NPs surface because of the presence of a serum proteins corona. Flow cytometry (**Figure 5A**) and confocal microscopy analysis (**Figure 5B, C**) confirm the capability of DBL_S/DBL-Fol to be taken up by KB cells with some selectivity, especially in the absence of serum. Microscopy images highlight a cytoplasmic and more in particular a perinuclear localization of DBL_S/DBL-Fol with a clear decrease of fluorescence signal in the case of cells pre-incubated with free folate.

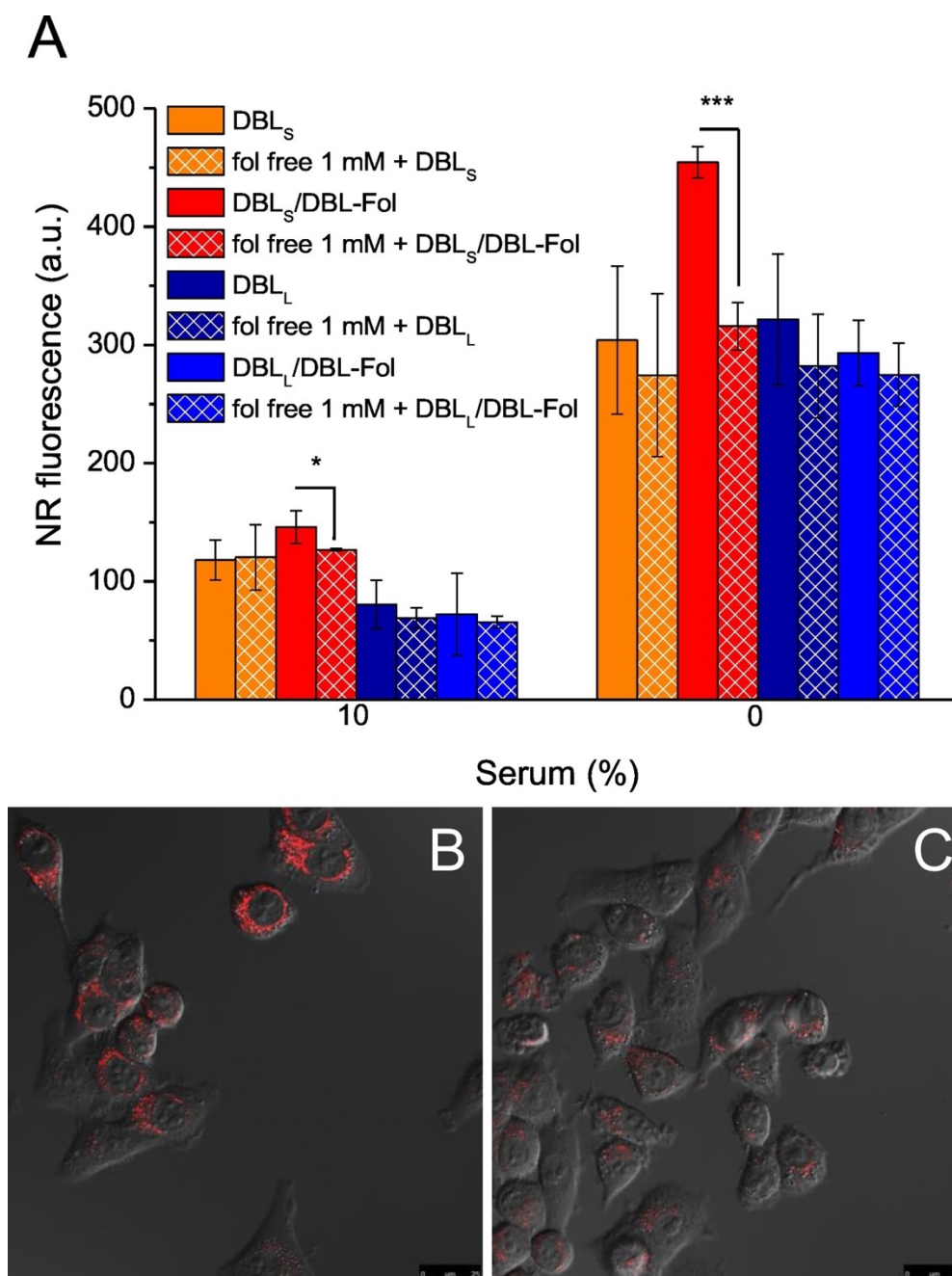


Figure 5. Intracellular uptake of NPs in KB cells over-expressing FRs. Flow cytometry measurements of the uptake of 20 $\mu\text{g}/\text{mL}$ of Nile Red-loaded NPs (A). Cells were incubated with NPs for 1 h with or without 10%

serum in the medium and in the absence or the presence of 1 mM free folate (competition experiment). Significant different for * $p < 0.05$, *** $p < 0.001$, Student's t-test. Confocal images of cells incubated with DBLS/DBL-Fol in the absence (B) or in the presence (C) of 1 mM free folate. (For interpretation of the references to color in this figure legend, the reader is referred to the web version of this article.)

On the contrary, in A549 cells negative for FR expression, flow cytometry experiments (**Figure S5**) showed that the uptake of DBLS vs. DBLS/DBL-Fol was not significantly different ($p > 0.05$, t-test) even in the absence of serum in the incubation medium. Accordingly, in spite of a slight decreased NP uptake observed in competition experiments with an excess of free folate, this decreased uptake was not statistically relevant comparing DBLS and DBLS/DBL-Fol ($p > 0.05$, t-test).

To gain more insight into the mechanism of DBLS/DBL-Fol uptake in KB cells we used drugs widely employed as inhibitors of specific endocytic pathways as clathrin-mediated endocytosis (chlorpromazine hydrochloride, CHL), lipid-raft-dependent endocytosis (methyl- β -cyclodextrin, Me β CD) and caveolae-dependent endocytosis (Genistein, GEN and Filipin III, FIL). As reported in **Figure S6**, Me β CD significantly lowered NP uptake ($\sim 80\%$), indicating that also the majority of NPs which did not enter the cells via FRs ($\sim 30\%$) were taken up exploiting lipid raft-dependent endocytosis. On the other hand, neither chlorpromazine nor Genistein nor Filipin were able to inhibit DBLS/DBL-Fol NP uptake, indicating that clathrin-mediated and caveolae-dependent endocytosis were not involved in the cell internalization process.

Modulating degree of valency in folate-decorated nanoparticles based on mPEG₅-PCL

As a final experiment, we prepared DBLS/DBL-Fol at different folate copolymer percentage (0–50% by wt of total copolymer) to understand if the amount of folate copolymer affected uptake in KB cells. Size distribution curves indicate that all the formulations are monodispersed (**Figure 6A**) with a size below 100 nm up to 30% of folate copolymer. A trend towards an increase of mean size and PI is observed for NPs at 50% Fol-PEG-PCL. All the NPs show a negative surface (ζ potential from -13 to -18 mV) as generally found for PEGylated NPs. As it can be seen in **Figure 6B**, emission intensity of NPs is increased when increasing folate content whereas NPs of PEG₅-PCL (without folic acid) do not exhibit any fluorescence signal. Furthermore, increase of Fol-PEG-PCL to 50% does not increase significantly NPs fluorescence, confirming that a fluorescence quenching is observed when the surface is more populated by folate moieties. Uptake studies in KB cells incubated with DBLS/DBL-Fol containing 10%, 20% or 30% DBL-Fol polymers (**Figure 6C**) demonstrated that, even in the presence of serum all the folate targeted formulations are taken up by cells via FR α -mediated endocytosis. Nevertheless, the extent of NPs accumulation through FR α -mediated endocytosis was comparable for all the formulations suggesting that an increase of folate amount in the NPs does not improve the extent of NPs intracellular accumulation.

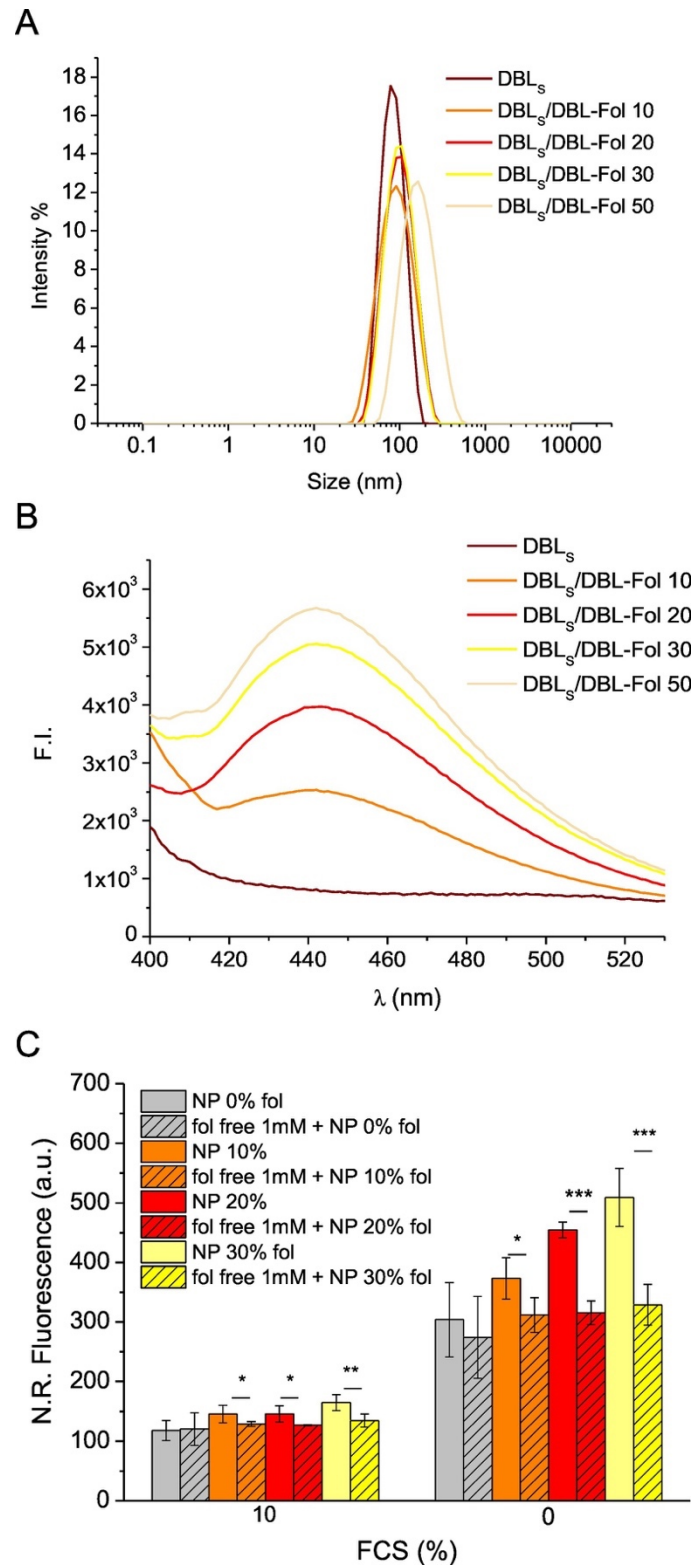


Figure 6. Properties of DBL_s/DBL-Fol NPs with different percentages of Fol-PEG-PCL. A) Size distribution curves. B) Emission spectra at λ_{ex} 278 nm (NPs concentration was 5 mg/mL). C) Uptake of NR-loaded NPs (20 μ g/mL) in KB cells after 1 h incubation in the presence and absence of FCS.

Conclusions

Our study highlights that the too simplistic view of PEGylated NPs, both untargeted and targeted, is out to be close to the actual situation and needs to be elucidated if one wishes to correlate appropriately NPs properties to biological behaviour. We demonstrate that NPs prepared from diblock PEG-PCL copolymers by the widely employed solvent displacement method show a degree of PEGylation much lower than expected which depends on the length of PEG block. PEG acquires a mushroom conformation on NPs surface and its length affects the thickness of the hydrophilic shell as well as folate amount and exposition. HSA interacts with all NPs forming a protein corona which is not detrimental for stability. While all NPs show limited uptake in human macrophages, only the presence of short PEG (1.0 kDa) in the copolymer ensures that folate-bearing NPs are accumulated in KB cancer cells via FR α -mediated endocytosis.

This study offers a proof on how complimentary and simple techniques such as light scattering, fluorescence and NMR, can be employed to finely characterize the shell of targeted NPs with a PEGylated surface in the attempt to drive downstream effect such as NPs internalization in sub-set cell populations.

Acknowledgments

This work was supported by Italian Association for Cancer Research (IG2014 #15764). The authors thank Mrs. D. Melck (NMR Service of Institute of Biomolecular Chemistry, CNR, Pozzuoli, Italy) for technical assistance. The authors are indebted to Prof. M. Trifuoggi (ACE Laboratory, University of Naples Federico II, Italy) for MP-AES analysis.

References

- Auguste et al., 2006 D.T. Auguste, S.P. Armes, K.R. Brzezinska, T.J. Deming, J. Kohn, R.K. Prud'homme
pH triggered release of protective poly(ethylene glycol)-b-polycation copolymers from liposomes
Biomaterials, 27 (2006), pp. 2599-2608
- Bertrand and Leroux, 2012 N. Bertrand, J.C. Leroux
The journey of a drug-carrier in the body: an anatomo-physiological perspective
J. Control. Release, 161 (2012), pp. 152-163
- Cammas et al., 1995 S. Cammas, Y. Nagasaki, K. Kataoka
Heterobifunctional poly(ethylene oxide): synthesis of alpha-methoxy-omega-amino and alpha-hydroxy-omega-amino PEOs with the same molecular weights
Bioconjug. Chem., 6 (1995), pp. 226-230
- Cao et al., 2012 B. Cao, Y. Zheng, T. Xi, C. Zhang, W. Song, K. Burugapalli, H. Yang, Y. Ma
Concentration-dependent cytotoxicity of copper ions on mouse fibroblasts in vitro: effects of copper ion release from TCu380A vs TCu220C intra-uterine devices
Biomed. Microdevices, 14 (2012), pp. 709-720

- Chen et al., 2013 C. Chen, J. Ke, X.E. Zhou, W. Yi, J.S. Brunzelle, J. Li, E.-L. Yong, H.E. Xu, K. Melcher
Structural basis for molecular recognition of folic acid by folate receptors
Nature, 500 (2013), pp. 486-489
- Cheung et al., 2016 A. Cheung, H.J. Bax, D.H. Josephs, K.M. Ilieva, G. Pellizzari, J. Opzoomer, J. Bloomfield, M. Fittall, A. Grigoriadis, M. Figini, S. Canevari, J.F. Spicer, A.N. Tutt, S.N. Karagiannis
Targeting folate receptor alpha for cancer treatment
Oncotarget (2016)
- Conte et al., 2016 C. Conte, I. Fotticchia, P. Tirino, F. Moret, B. Pagano, R. Gref, F. Ungaro, E. Reddi, C. Giancola, F. Quaglia
Cyclodextrin-assisted assembly of PEGylated polyester nanoparticles decorated with folate
Colloids Surf. B: Biointerfaces, 141 (2016), pp. 148-157
- El-Gogary et al., 2014 R.I. El-Gogary, N. Rubio, J.T.-W. Wang, W.T. Al-Jamal, M. Bourgognon, H. Kafa, M. Naeem, R. Klippstein, V. Abbate, F. Leroux, S. Bals, G. Van Tendeloo, A.O. Kamel, G.A.S. Awad, N.D. Mortada, K.T. Al-Jamal
Polyethylene glycol conjugated polymeric nanocapsules for targeted delivery of quercetin to folate-expressing cancer cells in vitro and in vivo
ACS Nano, 8 (2014), pp. 1384-1401
- Endres et al., 2011 T.K. Endres, M. Beck-Broichsitter, O. Samsonova, T. Renette, T.H. Kissel
Self-assembled biodegradable amphiphilic PEG–PCL–IPEI triblock copolymers at the borderline between micelles and nanoparticles designed for drug and gene delivery
Biomaterials, 32 (2011), pp. 7721-7731
- Gao et al., 2014 H. Gao, Z. Yang, S. Zhang, Z. Pang, X. Jiang
Internalization and subcellular fate of aptamer and peptide dual-functioned nanoparticles
J. Drug Target., 22 (2014), pp. 450-459
- Grossen et al., 2017 P. Grossen, D. Witzigmann, S. Sieber, J. Huwyler
PEG-PCL-based nanomedicines: a biodegradable drug delivery system and its application
J. Control. Release, 260 (2017), pp. 46-60
- Hiki and Kataoka, 2007 S. Hiki, K. Kataoka
A facile synthesis of azido-terminated heterobifunctional poly(ethylene glycol)s for “Click” conjugation
Bioconjug. Chem., 18 (2007), pp. 2191-2196
- Himo et al., 2005 F. Himo, T. Lovell, R. Hilgraf, V.V. Rostovtsev, L. Noodleman, K.B. Sharpless, V.V. Fokin
Copper(I)-catalyzed synthesis of azoles. DFT study predicts unprecedented reactivity and intermediates

J. Am. Chem. Soc., 127 (2005), pp. 210-216

Ishii et al., 2005 T. Ishii, M. Yamada, T. Hirase, Y. Nagasaki
New synthesis of heterobifunctional poly(ethylene glycol) possessing a pyridyl disulfide at one end and a carboxylic acid at the other end
Polym. J., 37 (2005), pp. 221-228

Li and Chau, 2010 Z. Li, Y. Chau
Synthesis of heterobifunctional poly(ethylene glycol)s by an acetal protection method
Polym. Chem., 1 (2010), pp. 1599-1601

Li and Tan, 2014 Z. Li, B.H. Tan
Towards the development of polycaprolactone based amphiphilic block copolymers: molecular design, self-assembly and biomedical applications
Mater. Sci. Eng. C, 45 (2014), pp. 620-634

Liu et al., 2012 L. Liu, M. Zheng, T. Renette, T. Kissel
Modular synthesis of folate conjugated ternary copolymers: polyethylenimine-graft-polycaprolactone-block-poly(ethylene glycol)-folate for targeted gene delivery
Bioconjug. Chem., 23 (2012), pp. 1211-1220

Mahou and Wandrey, 2012 R. Mahou, C. Wandrey
Versatile route to synthesize heterobifunctional poly(ethylene glycol) of variable functionality for subsequent pegylation
Polymer, 4 (2012), p. 561

Nahrwold et al., 2013 M. Nahrwold, C. Weiß, T. Bogner, F. Mertink, J. Conradi, B. Sammet, R. Palmisano, S. Royo Gracia, T. Preuße, N. Sewald
Conjugates of modified cryptophycins and RGD-peptides enter target cells by endocytosis
J. Med. Chem., 56 (2013), pp. 1853-1864

Owens and Peppas, 2006 D.E. Owens 3rd, N.A. Peppas
Opsonization, biodistribution, and pharmacokinetics of polymeric nanoparticles
Int. J. Pharm., 307 (2006), pp. 93-102

Quaglia et al., 2006 F. Quaglia, L. Ostacolo, G. De Rosa, M.I. La Rotonda, M. Ammendola, G. Nese, G. Maglio, R. Palumbo, C. Vauthier
Nanosopic core-shell drug carriers made of amphiphilic triblock and star-diblock copolymers
Int. J. Pharm., 324 (2006), pp. 56-66

Rabanel et al., 2014 J.M. Rabanel, P. Hildgen, X. Banquy
Assessment of PEG on polymeric particles surface, a key step in drug carrier translation
J. Control. Release, 185 (2014), pp. 71-87

Raynaud et al., 2009 J. Raynaud, C. Absalon, Y. Gnanou, D. Taton

- N-Heterocyclic carbene-induced zwitterionic ring-opening polymerization of ethylene oxide and direct synthesis of α,ω -difunctionalized poly(ethylene oxide)s and poly(ethylene oxide)-b-poly(ϵ -caprolactone) block copolymers
J. Am. Chem. Soc., 131 (2009), pp. 3201-3209
- Szekely et al., 2014 G. Szekely, M. Schaepertoens, P.R.J. Gaffney, A.G. Livingston
Iterative synthesis of monodisperse PEG homostars and linear heterobifunctional PEG
Polym. Chem., 5 (2014), pp. 694-697
- Thompson et al., 2008 M.S. Thompson, T.P. Vadala, M.L. Vadala, Y. Lin, J.S. Riffle
Synthesis and applications of heterobifunctional poly(ethylene oxide) oligomers
Polymer, 49 (2008), pp. 345-373
- Tirino et al., 2014 P. Tirino, C. Conte, M. Ordegno, R. Palumbo, F. Ungaro, F. Quaglia, G. Maglio
Y- and H-shaped amphiphilic PEG-PCL block copolymers synthesized combining ring-opening polymerization and click chemistry: characterization and self-assembly behavior
Macromol. Chem. Phys., 215 (2014), pp. 1218-1229
- Trindade et al., 2014 A.F. Trindade, R.F.M. Frade, E.M.S. Macoas, C. Graca, C.A.B. Rodrigues, J.M.G. Martinho, C.A.M. Afonso
“Click and go”: simple and fast folic acid conjugation
Org. Biomol. Chem., 12 (2014), pp. 3181-3190
- Ungaro et al., 2012 F. Ungaro, C. Conte, L. Ostacolo, G. Maglio, A. Barbieri, C. Arra, G. Misso, A. Abbruzzese, M. Caraglia, F. Quaglia
Core-shell biodegradable nanoassemblies for the passive targeting of docetaxel: features, antiproliferative activity and in vivo toxicity
Nanomedicine, 8 (2012), pp. 637-646
- Viola-Villegas et al., 2008 N. Viola-Villegas, A.E. Rabideau, J. Cesnavicious, J. Zubieta, R.P. Doyle
Targeting the folate receptor (FR): imaging and cytotoxicity of ReI conjugates in FR-overexpressing cancer cells
ChemMedChem, 3 (2008), pp. 1387-1394
- Walkey et al., 2012 C.D. Walkey, J.B. Olsen, H. Guo, A. Emili, W.C. Chan
Nanoparticle size and surface chemistry determine serum protein adsorption and macrophage uptake
J. Am. Chem. Soc., 134 (2012), pp. 2139-2147
- Xu et al., 2015 Q. Xu, L.M. Ensign, N.J. Boylan, A. Schon, X. Gong, J.C. Yang, N.W. Lamb, S. Cai, T. Yu, E. Freire, J. Hanes
Impact of surface polyethylene glycol (PEG) density on biodegradable nanoparticle transport in mucus ex vivo and distribution in vivo
ACS Nano, 9 (2015), pp. 9217-9227

Supplementary Materials

Table S1. Examples for the optimization of folic acid γ -conjugation. Equivalents (eq) refer to initial folic acid. Attribution of peaks was made on the basis of corresponding MS analysis.

Entry	Propargyl-amine (eq)	Base (eq)	Bis-propargyl-folate (wt %)	Fol-NHS (wt%)	Folate (wt %)	(α + γ)-propargyl-folate (wt %)
1	2	TEA (2)	--	27.4	14.9	57.7
2	5	TEA (5)	22.3	--	27.1	50.6
3	5	--	35.8	--	10.5	53.6
4	3	--	56.6	--	9.8	33.5
5	3	TEA (3)	42.5	--	9.2	48.1
6	3	DMAP (3)	56.3	--	9.8	33.8
7	3	Pyridine (3)	66.2	--	10.5	23.2
8	2.5	TEA (2.5)	51.6	--	8.6	39.7
9	1	TEA (1)	--	20.5	34.0	44.7
10	1	--	--	27.0	30	42.5

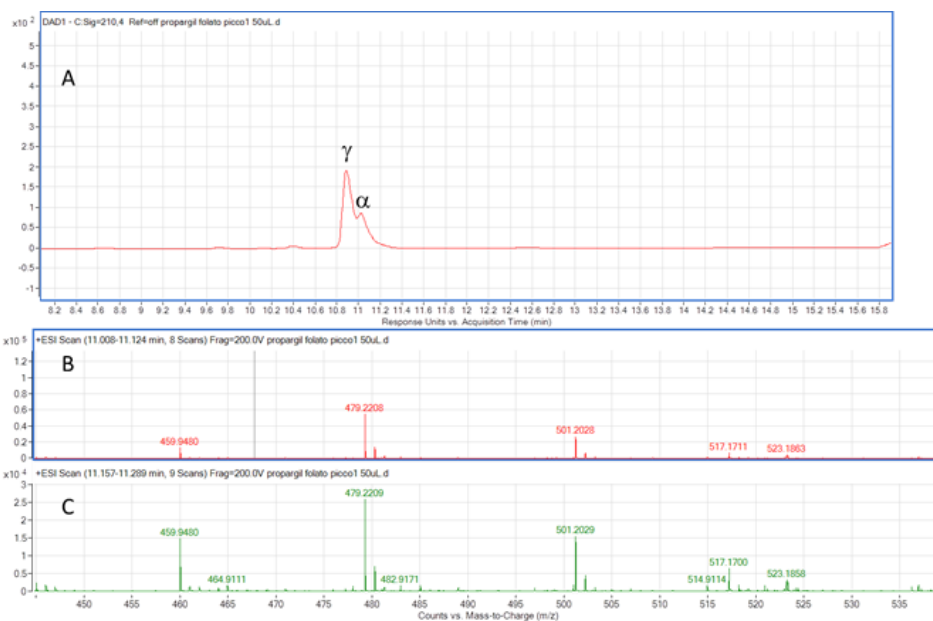


Figure S1. HPLC profile of the purified propargyl folate from Entry 1 (A); mass spectrum of the γ -propargyl folate derivative (B); mass spectrum of the α -propargyl folate derivative (C).

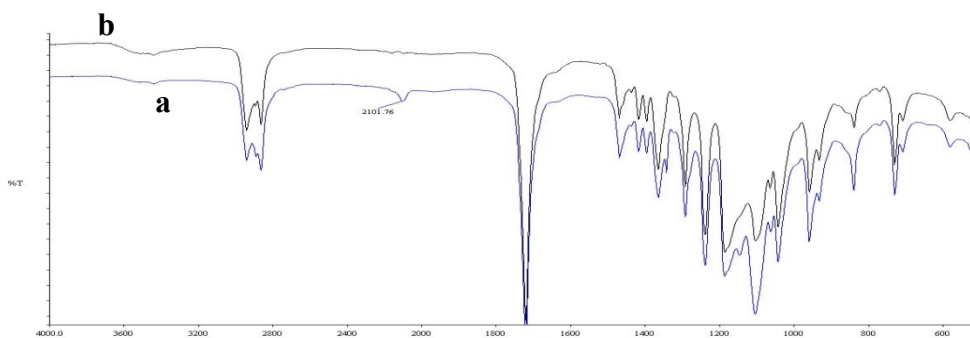


Figure S2. IR spectra of **a** = PCL-PEG-N₃ and **b** = PCL-PEG-Fol.

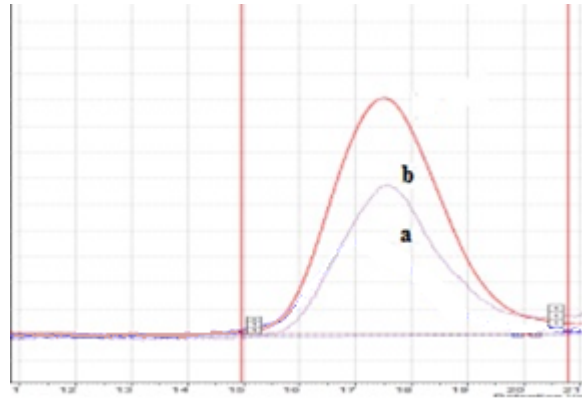


Figure S3. GPC chromatogram of PCL-PEG-Fol (**a** = UV detector; **b** = refractive index detector). The regular profile of GPC-UV curve supported a homogeneous functionalization of macromolecules.

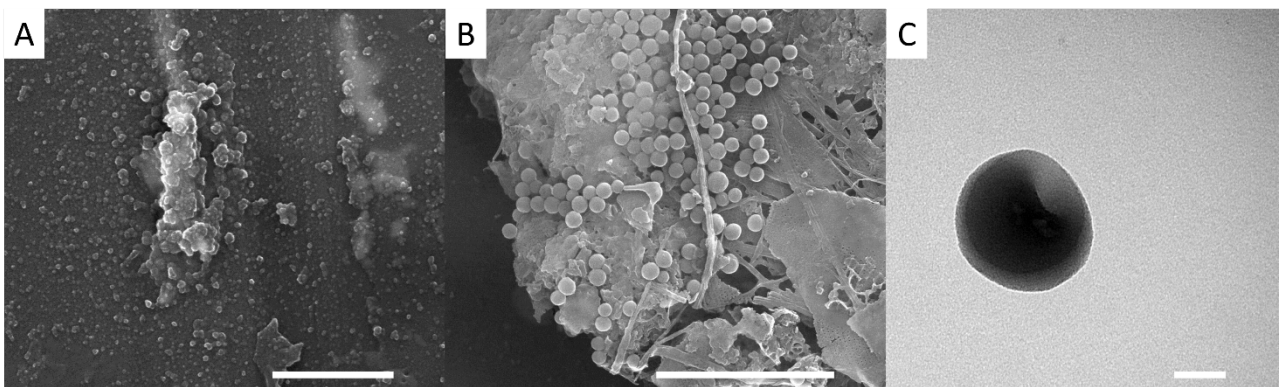


Figure S4. SEM images (FEI Quanta 200 FEG) of DBL_S/DBL-Fol freeze-dried without (A) and with (B) HPβCD as cryoprotectant (polymer : HPβCD 1:10 by wt). NPs were frozen in liquid N₂ and dried in a Modulyo Edwards apparatus (condenser temperature 55°C) for 24 h. (C) TEM image (CM 12 Philips) of DBL_S/DBL-Fol after staining with a 2% w/v phosphotungstic acid solution. Scale bars: 1 μm (A), 3 μm (B), 50 nm (C).

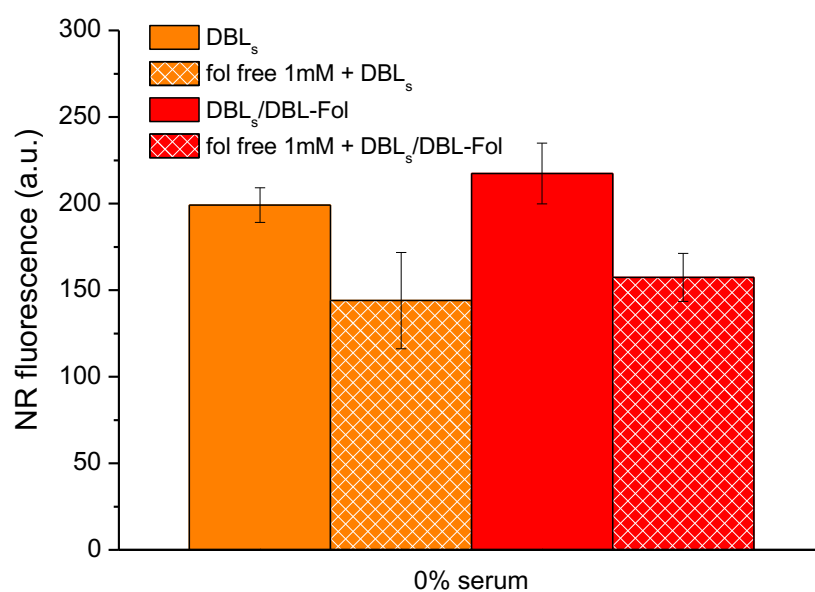


Figure S5. Intracellular uptake of NPs in A549 cells not expressing FRs. Flow cytometry measurements of the uptake of 20 $\mu\text{g}/\text{mL}$ of Nile Red-loaded NPs. Cells were incubated with NPs for 1 h without serum in the medium and in the absence or the presence of 1 mM free folate (competition experiment).

DBLs vs. DBLs/DBL-Fol: $p > 0.05$, Student's t-test; Fol free 1mM + DBLs vs. Fol free 1mM + DBLs/DBL-Fol: $p > 0.05$, Student's t-test.

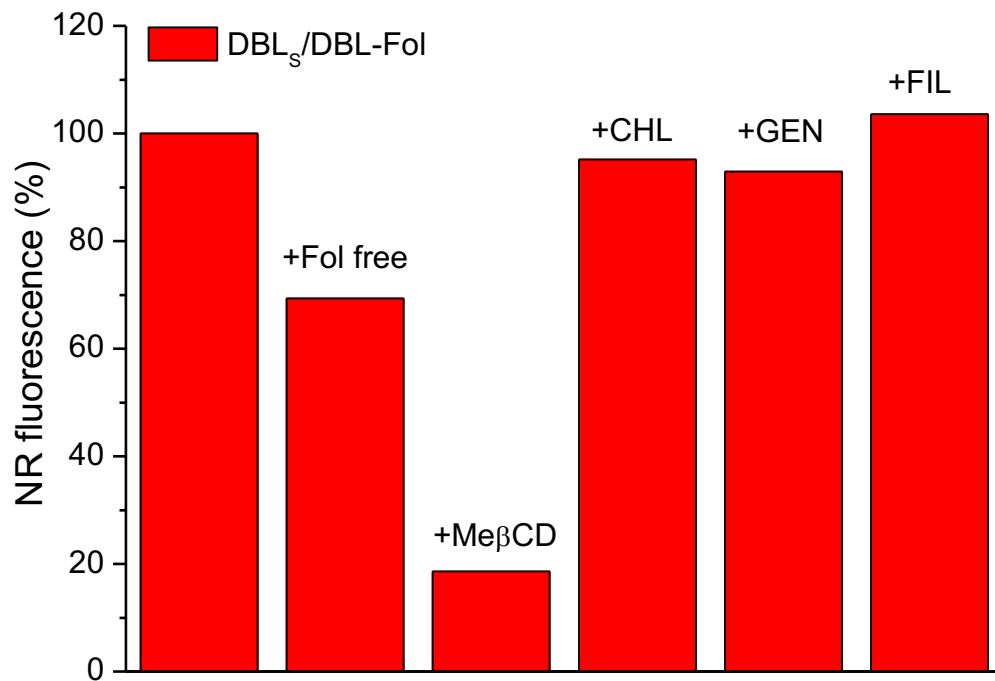


Figure S6. Effects of inhibitors of specific endocytic pathways on the uptake of DBL_S/DBL-Fol in KB cells. Clathrin-mediated endocytosis (chlorpromazine hydrochloride, CHL), lipid-raft-dependent endocytosis (methyl-β-cyclodextrin, MeβCD) and caveolae-dependent endocytosis (Genistein, GEN and Filipin III, FIL). The cells were incubated or not incubated (control) with the inhibitors (for 30 min before and as well as during the 1 h incubation with NPs).

3 Biodegradable nanoparticles exposing a short anti-FLT1 peptide as antiangiogenic platform to complement docetaxel anticancer activity²

Introduction

Angiogenesis is essential for the supply of nutrients and oxygen to cancer cells and greatly contributes to tumor growth, invasion and metastasis (1,2). Rapid cancer cell proliferation creates hypoxic, glucose-deprived environments that activate the so called “angiogenic switch”. In these conditions, tumor cells begin to secrete a variety of diffusible pro-angiogenic factors, including Vascular Endothelial Growth Factors (VEGFs), which play a crucial role in stimulating neovascularization. VEGF is a potent mitogen for endothelial cells that binds its high affinity tyrosine kinase receptors (VEGFRs), triggering various intracellular signals promoting survival, division and migration of endothelial cells. In response, several other growth factors are secreted in the proximity of the newly formed capillaries finally stimulating the proliferation of cancer cells (3). While VEGFR2 (known as Flk-1/KDR) is considered a major player in angiogenesis (4), VEGFR1 (also known as Fms-like tyrosine kinase, FLT1) acts as a regulator of angiogenesis (decoy protein for VEGF-A, the main ligand of VEGFR2) and is upregulated in endothelial cells undergoing growth and remodeling (5,6). VEGFR1 stimulation promotes pathological angiogenesis and triggers activation of protumoral M2 macrophages, which induce tumor cell proliferation and metastasis (7). Furthermore, FLT1 is expressed in different cancer cell lines and upon stimulation with VEGF family members, tumor progression and spreading are activated (7).

The evidence that VEGFR1-related signaling pathway participates in the “angiogenic switch” in tumors paved the way to targeting this receptor in anticancer therapies (8). Indeed, some anti-VEGFR1 antibodies or inhibitory peptides have been proposed to arrest tumor growth and metastasis spreading in various cancer models (8,9,10). Nevertheless, only anti-angiogenic therapies interfering with the VEGF pathway mediated by both VEGFR2 and VEGFR1 have become a relevant and widely accepted approach for the treatment of cancer. A number of preclinical/clinical studies have confirmed that the inhibition of angiogenesis causes an arrest of the tumor growth and formation of metastasis. The approval of several antiangiogenic drugs acting as i) VEGF decoy (bevacizumab and other anti-VEGF antibodies), ii) tyrosine kinase inhibitors inactivating all VEGFRs, and iii) “vascular-disrupting agents” has thus followed (3,11,12). However, their clinical use has faced severe limitations such as direct and indirect acquired resistance of cancer cells through induction of escape mechanisms and impaired oxygenation level, respectively. Cancer cell invasion, toxicity in normal organs, high blood pressure and bleeding are other drawbacks to consider during an antiangiogenic treatment (13-16).

The delivery of antiangiogenic molecules through nanoparticulate systems may be considered a valuable strategy to overcome some of their main therapeutic limitations and confine antiangiogenic effects at tumor level. However, the development of antiangiogenic nanoplatforms for cancer

² The work presented in this paragraph has been published as: Biodegradable nanoparticles exposing a short anti-FLT1 peptide as antiangiogenic platform to complement docetaxel anticancer activity
Claudia Conte, Francesca Moret, Diletta Esposito, Giovanni Dal Poggetto, Concetta Avitabile, Francesca Ungaro, Alessandra Romanelli, Paola Laurienzo, Elena Reddi, Fabiana Quaglia.
Materials Science and Engineering: C Volume 102, September 2019, Pages 876-886
<https://doi.org/10.1016/j.msec.2019.04.054>

therapy has been reported in a limited number of studies (17,18,19) while the delivery of single anti-angiogenic molecules or their combination with chemotherapeutics has been mainly attempted to improve pharmacokinetics and avoid undesired effects in healthy organs (20-23).

In the context of combination therapies for cancer, polymeric nanoparticles (NPs) with core-shell architectures offer the advantage of easy manipulation of their overall features (size, surface hydrophilicity/charge, release rate, biodegradability) through appropriate tailoring of the chemistry of polymer building blocks (24-27). Furthermore, NPs can be logically designed to incorporate multiple drugs with different physical-chemical properties in the core or in the shell and deliver them at different release rates, which can be crucial to attain desired synergic/additive effects (28-31). NPs made of amphiphilic block copolymers of poly(ethylene glycol) and poly(ϵ -caprolactone) (PEG-PCL) with different hydrophilic/lipophilic balance and architecture have been proposed to home poorly water-soluble chemotherapeutics to solid tumors due to their stability, sustained release features and degradability (27,32,33). Furthermore, surface functionalization of PEG-PCL NPs with specific ligands, thus providing multifunctional NPs, has been proposed as a strategy to target drug cargo to specific cancer cells populations (32).

Herein, we propose a novel approach to impart antiangiogenic properties to PEG-PCL NPs and provide a proof of concept of their therapeutic potential in delivering the poorly water-soluble chemotherapeutic docetaxel (DTX) in triple negative breast cancer cells. NPs with a hydrophobic core of PCL accommodating DTX and a hydrophilic shell of PEG exposing an anti-angiogenic short peptide sequence have been constructed. The peptide GNQWFI (aFLT1), selectively binding VEGFR1 isoform in vitro and inhibiting tumor growth and metastasis in a mice xenograft of VEGF-secreting cancer cells (9), was covalently linked through click chemistry to the PEG -OH end to give an aFLT1-PEG-PCL copolymer. NPs were prepared from a mixture of PEG-PCL, with PEG molecular weight of 1000 Da, and aFLT1-PEG-PCL with PEG molecular weight of 1500 Da to promote aFLT1 exposition on NPs surface at appropriate ratios. NPs <100 nm entrapping DTX were obtained by nanoprecipitation. After an in-depth characterization aimed to assess shell properties, NPs were tested in human umbilical vein endothelial (HUVEC) and breast cancer cell (MDA-MB-231) models as well as in chicken embryo chorioallantoic membranes (CAMs) xenografted with MDA-MB-231 cells to investigate the impact of DTX delivery through anti-angiogenic NPs on its anticancer activity.

Materials and methods

Chemicals and reagents

Poly(ethyleneglycol) with Mn 1.5 kDa (PEG1.5k, Sigma-Aldrich, Milan, Italy) and monomethoxy-poly(ethyleneglycol) with Mn 1.0 kDa (mPEG1k, Nanocs Inc., USA) were dehydrated by azeotropic distillation with dry toluene in a Dean-Stark trap. ϵ -caprolactone (CL, Sigma-Aldrich, Italy) was distilled at reduced pressure over CaH₂. Trifluoroethanol (TFE) was purified as described in Purification of Laboratory Chemicals Armarego. Cu wires (Carlo Erba, Italy) were treated with H₂SO₄ for 10 min, washed twice with distilled water, methanol, and dried under reduced pressure at 60 °C for 30 min.

Docetaxel (DTX, MW = 807.88) was purchased from LC laboratories (USA). Triisopropylsilane (TIS), N-methylmorpholine (NMM), N,N dimethylformamide (DMF), sodium chloride, potassium phosphate dibasic and potassium phosphate monobasic, sodium azide, Rhodamine B isothiocyanate (Rhod), dicyclohexylcarbodiimide (DCC), 4-(dimethylamino)pyridine (DMAP), Tin(II) 2-

ethylhexanoate (Sn(Oct)₂), potassium chloride, sodium phosphate dibasic, sucrose, glucose, threose, poloxamer 188 (P188), mannitol, sorbitol, human serum albumin (HSA), human plasma and (2-Hydroxypropyl)- β -cyclodextrin (HP β CD, DS 0.6) were used as received (Sigma-Aldrich, Italy). All the other chemicals were of analytical grade.

Peptide synthesis

Peptides aFLT1 (GNQWFI-NH₂), Pra-Ahx-aFLT1 (Pra-Ahx-GNQWFI), Reverse aFLT1 (IFWQNG-NH₂), Reverse Pra-Ahx-aFLT1 (Pra-Ahx-IFWQNG) (Pra: propargyl glycine, Ahx: amino hexanoic acid) were obtained by solid phase synthesis following standard protocols (34) on the Rink amide MBHA resin (0.54 mmol g⁻¹). Peptides were cleaved off the resin and deprotected by treatment of the resin with a solution of TFA/TIS/H₂O 95/2.5/2.5 v/v/v, 90 min. TFA was concentrated and peptides were precipitated in cold ethylic ether. Analysis of the peptides was performed by LC-MS ESI-TOF on a Agilent Technologies 6230 ESI-TOF instrument using a Phenomenex Jupiter 3 C18 (150 \times 2.0 mm) column with a flow rate of 0.2 mL min⁻¹. Analysis of the crudes was performed by LC-MS using a gradient of acetonitrile (0.1% TFA) in water (0.1% TFA) from 5 to 70% in 15 min. Peptides were purified by RP-HPLC on a Phenomenex Jupiter 10 μ Proteo 90 Å (250 \times 10 mm) using a gradient of acetonitrile (0.1% TFA) in water (0.1% TFA) from 5 to 70% in 20 min.

The peptide derivatized with rhodamine, named Rhod-Ahx-aFLT1 (Rhod-Ahx-GNQWFI) and reverse Rhod-Ahx-aFLT1 were obtained as follows. To the resin bound a peptide, the Fmoc-Ahx-OH linker was coupled and Fmoc deprotected following standard procedures for peptide synthesis. Rhod (10 Eq) was dissolved in DMF, NMM (14 Eq) was added; the solution was reacted with the peptide 3 h at r.t. and another coupling was performed overnight. Peptides were cleaved off the resin and deprotected by treatment of the resin with a solution of TFA/TIS/H₂O 95/2.5/2.5 v/v/v, 90 min. TFA was concentrated and peptides were precipitated in cold ethylic ether. Analysis of the crudes was performed by LC-MS ESI-TOF using a gradient of acetonitrile (0.1% TFA) in water (0.1% TFA) from 5 to 80% in 15 min. Peptides were purified by RP-HPLC using a gradient of acetonitrile (0.1% TFA) in water (0.1% TFA) from 5 to 80% in 20 min.

aFLT1 sequence: GNQWFI-NH₂. Calculated mass (Da): 762.83; found: [M + 2H]²⁺ = 382.68.

Reverse aFLT1 sequence: IFWQNG-NH₂. Calculated mass (Da): 762.83; found: [M + 2H]²⁺ = 382.27.

Pra-Ahx-aFLT1: Pra-Ahx-GNQWFI. Calculated mass (Da): 970.43; [M + 2H]²⁺ = 486.21; found: 970.25; [M + 2H]²⁺ = 486.09;

Rhod-Ahx-aFLT1: Rhod-Ahx-GNQWFI. Calculated mass (Da): 1374.80; found: [M + 2H]²⁺ = 688.33

Reverse Rhod-Ahx-aFLT1: Rhod-Ahx-IFWQNG. Calculated mass (Da): 1374.80; found: [M + 2H]²⁺ = 688.33

Copolymer synthesis

Synthesis of mPEG-PCL-Rhod diblock copolymer.

mPEG-PCL (500 mg) was dissolved in 10 mL of dry chloroform, then DCC (41.6 mg, 0.2 mmol), DMAP (24.4 mg, 0.2 mmol) and Rhod (95.8 mg, 0.2 mmol) were added and the solution was left under stirring at room temperature overnight. The polymer was precipitated in diethylether and repeatedly washed (yield 92%). Washing solvent was analyzed by UV–vis absorption to exclude residual free Rhod ($\lambda = 360$ nm). The amount of Rhod on the copolymer was quantified by UV–vis spectroscopy on DMSO solutions, using Rhod standard solutions as calibration curve (Rhod: 5% by wt, functionalization degree: 74%).

Synthesis of aFLT1-copolymer conjugate (aFLT1-PEG-PCL).

Azido-PEG-PCL copolymer (N₃-PEG-PCL) was prepared starting from PEG1.5k according to a procedure reported elsewhere (35).

In a flask equipped with N₂ inlet, N₃-PEG-PCL (0.02 mmol, 144 mg) and Pra-Ahx-aFLT1 (0.031 mmol, 30 mg) were dissolved in 2 mL of TFE/DMF (30/70 v/v) under nitrogen stream. Cu wires (100 mg) were added and the reaction was carried out at 40 °C for 48 h under mechanical stirring. The reaction mixture was protected from light by aluminum foil. After removal of Cu wires and evaporation of solvent, the product was dissolved in THF and the solution was filtered with a screw filter 0.22 μ m PTFE. The insoluble fraction, consisting of unreacted aFLT1, was weighed (7.56 mg, corresponding to 25% of the total peptide; conjugation degree: 75%). The THF solution containing aFLT1-PEG-PCL conjugate was finally purified by passing over neutral alumina to remove copper. The conjugate was recovered by THF evaporation at reduced pressure (yield 83%). FTIR diagnostic bands (cm⁻¹): 2097 (N₃ stretching), 1736 (CO stretching), 1650 (amide I band), 1540 (amide II band).

NPs preparation

aFLT1-decorated NPs were prepared from a mixture of mPEG-PCL with aFLT1-PEG-PCL (mPEG-PCL/aFLT1-PEG-PCL weight ratio 9:1) (DBLaFLT1) whereas NPs without aFLT1 (DBL) were prepared from mPEG-PCL. NPs were formed by solvent diffusion of an organic phase (10 mg of copolymer mixture in 1 mL of acetone) added dropwise in water (2 mL) under magnetic stirring (500 rpm). After solvent evaporation, NPs were filtered through 0.45 μ m Phenex® filters (Phenomenex, USA). NPs were freeze-dried after the addition of HP β CD as cryoprotectant (polymer: HP β CD 1:10 wt. ratio) and subsequent 1:10 dilution in water. NPs loaded with DTX were prepared according to the procedure reported above by co-dissolving DTX with the copolymer(s) (10% w/w) in the organic phase. To evaluate cellular uptake, fluorescent NPs were prepared according to the procedure reported above by using a mixture of mPEG-PCL, mPEG-PCL-Rhod and aFLT1-PEG-PCL (weight ratio 8:1:1).

NPs characterization

Hydrodynamic diameter (DH), polydispersity index (PI) and zeta potential (ζ) of NPs were determined on a Zetasizer Nano Z (Malvern Instruments Ltd). Results are reported as mean DH of three separate measurements of three different batches (n = 9) \pm standard deviation (SD). Yield of

NP production process was evaluated on an aliquot of NP dispersion by weighting the solid residue after freeze-drying. Results are expressed as the ratio of the actual NP weight to the theoretical polymer weight $\times 100$.

Fixed aqueous layer thickness (FALT) of NPs was measured by monitoring the influence of ionic strength on zeta potential (ζ). Different amounts of NaCl stock solutions were added to NPs dispersed in water ($500 \mu\text{g mL}^{-1}$) and ζ of the samples measured. The plot of $\ln \zeta$ against $3.33[\text{NaCl}]^{0.5}$ gives a straight line where the slope represents the thickness of the shell in nm (35). The exposition of aFLT1 on the surface of DTX-DBLaFLT1 was evaluated using LavaPep™ Peptide and Protein Quantification Kit (Gel Company). A serial dilution of aFLT1 free in water was prepared ($2\text{--}200 \mu\text{g mL}^{-1}$) and the samples were incubated with working solution in the dark for 60 min at r.t. Using fluorescence microlitre plate reader (Glomax Explorer, Promega, Italy), the fluorescence was evaluated with the $540 \pm 10 \text{ nm}$ excitation and $630 \pm 10 \text{ nm}$ emission filters. The same protocol was used to quantify the amount of aFLT1 on NP surface directly using NP dispersion. The results are expressed as % exposition \pm SD of three experiments.

In order to evaluate the interaction of NPs with HSA, DBL and DBLaFLT1 were placed in a HSA solution with different concentrations of HSA in water and then analyzed by fluorescence spectroscopy and size measurements. The fluorescence emission spectra of HSA ($500 \mu\text{M}$), in the absence and in the presence of NPs (5 mg mL^{-1}) upon excitation at 278 nm, were collected in order to explore the fluorescence behavior of NPs and the possible static quenching effects by the massive aggregation of HSA on NPs (RF6000 spectrofluorimeter, Shimadzu, Japan). Similarly, 1.5 mg of NPs (in $500 \mu\text{L}$ of water) were diluted with a HSA solution ($1\text{--}500 \mu\text{M}$) or $250 \mu\text{L}$ of human plasma and incubated at 37°C for different times. Hydrodynamic diameter (DH), polydispersity index (PI) and zeta potential (ζ) of NPs were determined on a Zetasizer Nano Z (Malvern Instruments Ltd).

DTX actual loading and release

DTX loading inside NPs was assessed by placing 1 mg of freeze-dried NPs (without cryoprotectant) in $500 \mu\text{L}$ of acetonitrile, adding $500 \mu\text{L}$ of water and filtering the samples through a $0.45 \mu\text{m}$ filter (Phenomenex, USA). DTX was analyzed by HPLC using a Shimadzu (Japan) apparatus equipped with a LC-10ADvp pump, a SIL-10ADvp autoinjector, a SPD-10Avp UV–Vis detector and a C-R6 integrator. The analysis was performed using a Juppiter $5 \mu\text{m}$, C18 column ($250 \times 4.6 \text{ mm}$, Å) (Phenomenex, USA). The mobile phase was a 55:45 (v/v) mixture of water with 0.1% TFA and acetonitrile pumped at a flow rate of 1 mL min^{-1} . The UV detector was set at 227 nm. A calibration curve for DTX in ethanol was plotted in the concentration range of $2\text{--}200 \mu\text{g mL}^{-1}$.

The release of DTX was determined on 0.5 mg NPs dispersed in 0.5 mL of 10 mM phosphate buffer containing NaCl (137 mM) and KCl (2.7 mM) at pH 7.4 (PBS) at 37°C in a dialysis bag immersed in an external phase (5 mL) of the same medium. Dialysis membranes (MWCO 3500, regenerated cellulose, Spectra/Por(R)) were conditioned in water for 15 min before use. At predetermined times, 1 mL aliquots of the sample were collected and then analyzed by HPLC to evaluate the actual loading of DTX in NPs. The results are expressed as % release \pm SD of three experiments.

Cell lines

All cell lines were obtained from American Type Culture Collection (ATCC, Rockville, USA). HUVEC (human umbilical vein endothelial cells) were cultured in Medium-200 supplemented with antibiotics (100 U mL^{-1} Penicillin G and $100 \mu\text{g mL}^{-1}$ Streptomycin) and with the Low Serum Supplement Kit (Life Technologies) having a final fetal bovine serum (FBS) concentration of 2%. MDA-MB-231 cells were grown in DMEM supplemented with 10% FBS and antibiotics. All cell

lines were maintained at 37 °C in a humidified atmosphere containing 5% CO₂. All the in vitro studies were performed with NP dispersions immediately after preparation.

Tube formation assay

Geltrex® Matrix (Geltrex® LDEV-Free Reduced Growth Factor Basement Membrane Matrix, Life Technologies) was thawed at 4 °C overnight. Each well of pre-chilled 24-well/plates was coated with 100 µL of matrix, incubated and solidified at 37 °C for at least 30 min. Meanwhile, HUVEC (cultured for maximum 4 passages from thawing) were harvested from flasks and seeded (4.8×10^4 cells/well) in M200 medium supplemented with LVES (Large Vessel Endothelial Supplement, Gibco) for 18 h. During cell seeding, in each well, free peptides (100 µM), unloaded or DTX-loaded NPs (NPs=50 µg mL⁻¹; DTX=5 µg mL⁻¹) or free DTX (5 µg mL⁻¹) were added. Wells containing untreated HUVEC were used as negative controls of tube forming cells while HUVEC incubated with 0.01% DMSO were employed as positive control. After 18 h of incubation, the cells were washed with PBS with Ca²⁺ and Mg²⁺, incubated at 37 °C with Calcein AM 2 µM (Molecular Probes) for 15 min, washed again and maintained in M200 medium until the end of the image acquisition. Tube formation was analyzed using an inverted fluorescence microscope (DMI4000, Leica) at $\times 5$ or $\times 10$ magnification. Image analysis was performed from randomly selected fields using a dedicated plug-in (Angiogenesis Analyzer) for Image J and the percentage of inhibition in treated cells vs control cells was reported for the formed numbers of junctions, master segments and meshes.

Cytotoxicity

The viability of HUVEC and MDA-MB-231 cells incubated with increasing concentrations of free DTX dissolved in standard solution (DMSO) or loaded in DBL or DBLaFLT1 NPs was measured with the MTS assay (CellTiter 96® AQueous One Solution Cell Proliferation Assay, Promega Co., Madison, USA). The viability was measured also in cells incubated with empty DBL or DBLaFLT1 NPs to check the safety of the delivery system. For MTS assay, cells (8×10^3 MDA-MB-231 or 7×10^3 HUVEC) were seeded in 96-well plates and, after 24 h of growth, incubated with the various formulations diluted in cell medium added with 10% FBS. Cell viability was measured after 48 and 72 h of incubation. For the MTS assay the culture medium was replaced with 100 µL of serum-free medium and 20 µL of the CellTiter 96® reagent and the plates were incubated for 1 h at 37 °C. The absorbance at 492 nm was measured using a Multiskan Go (Thermo Fischer Scientific, Waltham, USA) plate reader and the viability of treated cells was expressed as percentage of the absorbance of control cells that was taken as 100% viability. The Primer software for biostatistics (McGraw-Hill, Columbus, USA) was used for statistical analysis of the data. The data are expressed as means \pm standard deviations (SD) for at least 3 independent experiments. The difference between groups was evaluated with the Student's t-test and was considered significant for $p < 0.05$.

Chicken embryo chorioallantoic membrane (CAM) assay

The CAM model was used to evaluate anti-angiogenic effects, tumor growth delay, metastasis inhibition and toxicity induced by DTX-loaded DBL and DBLaFLT1 NPs. Fertilized chicken eggs were incubated at 37.5 °C with 50% relative humidity for 9 days. At this time (E9), the CAMs were dropped by drilling a small hole through the eggshell into the air sac and a 1 cm² window was cut in the eggshell above the CAM. Thereafter, MDA-MB-231 cells (90% confluence, passage 12), cultured as indicated above, were re-suspended in graft medium and inoculated (106 cells) onto the

CAM of each egg. Twenty-one eggs were used for each condition and randomized into 5 groups. The day after induction (E10), the tumors began to be detectable and the treatment started once a day for a total of 5 consecutive days (days E10–E14). Freeze-dried HP β CD-NPs (without or with DTX) were dispersed in PBS while free DTX was solubilized in a 1% DMSO in PBS, achieving a final DTX concentration of 1 μ M (100 μ L of tested samples were employed). The daily doses of DTX and NPs were, respectively, 0.083 and 0.83 μ g. Negative control samples were inoculated with 100 μ L of PBS.

For evaluating the anti-angiogenic effects, images (8–12 upper CAMs per group) of tumors with associated vessels were taken at E15. On these images, the number of vessels arriving on tumors was counted (3 different counts for each sample). A one-way ANOVA analysis with post-tests was applied on data. For measuring the tumor size, the upper portion of the CAM with tumors was removed at E16, washed in PBS and immediately fixed in paraformaldehyde for 48 h. The normal CAM tissue around the tumors was carefully removed and the tumors were weighed. A one-way ANOVA analysis with post-tests has been done on these data. At E16, a 1 cm² portion of the lower CAM, distant from the site of tumor cells implantation, was also collected to evaluate the number of metastatic cells (invasion analysis). Genomic DNA was extracted from the CAM, and analyzed by qPCR with specific primers for the human specific Alu sequences (36). Statistical analysis was directly performed on data from the Bio-Rad CFX Maestro software.

The toxicity of the different treatments on embryo viability was monitored at E16 by counting the dead embryos as well as observing eventual visible macroscopic abnormalities.

Results and discussion

Synthesis and characterization of aFLT1-PEG-PCL conjugate

aFLT1 peptides were obtained in highly pure form in two different variants: the free peptide (GNQWFI) and the alkyne derivatized peptide (Pra-Ahx-GNQWFI). The propargyl glycine (Pra), needed for the click reaction with the azide-functionalized polymer was separated from the peptide by an amino hexanoic acid linker so that the alkyne was less sterically hindered and therefore available for the click reaction. As a control, we also prepared GNQWFI conjugated with Rhod and a peptide with reverse sequence (IFWQNG).

Copper(I)-catalyzed alkyne-azide 1,3-dipolar cycloaddition (CuAAC) “click” reaction was used to conjugate the peptide to N₃-PEG-PCL copolymer (**Figure 1**). This reaction has been widely used for conjugation of peptides, drugs and other biological molecules to synthetic azide/alkyne-functionalized polymers, and particularly to PEG (37). The reaction can be performed by using different Copper sources (Cu(I) salts, Cu(II) salts, solid Cu(0)). For peptide conjugation, the catalyst is better prepared in situ by reduction of Cu(II) salts, which are often purer than Cu(I) salts, in presence of a reducing agent. The Cu(SO₄)/ascorbate system is often reported for peptides conjugation in aqueous medium. In the case of water insoluble copolymers such as PEG-PCL, Cu(0) in form of wires, turnings, powder or colloidal particles has been used as source of Cu(I) catalyst, with or without addition of Cu(II) salts, base or ligand (38).

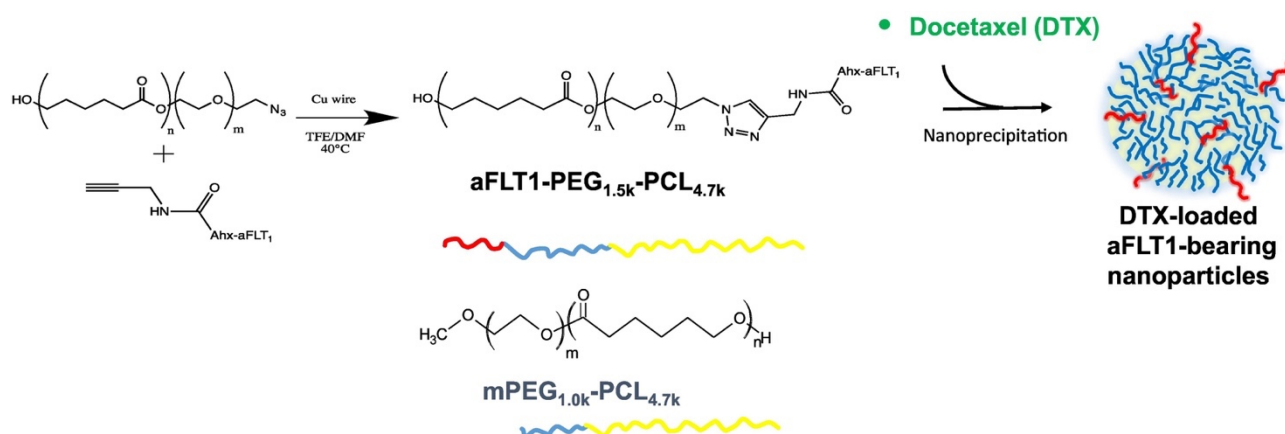


Figure 1. Synthesis of aFLT1-PEG-PCL and structure of antiangiogenic NPs.

For aFLT1 coupling, the reaction was carried out in a TFE/DMF mixture to promote unfolding of the peptide and to promote the exposition of alkyne group for click reaction. As a matter of fact, preliminary tests confirmed that addition of TFE increases the final conjugation ratio. At the end of the reaction, after solvent and Cu wires removal, the product was dissolved in THF and separated from the unreacted peptide (insoluble) by filtration. The formation of the conjugate was confirmed by FTIR spectroscopy, which showed a significant decrease of the azide band at 2097 cm^{-1} in comparison to that of the initial copolymer, and the appearance of the characteristic amide I and amide II bands, attributed to peptide bonds (**Figure S1**). The substitution degree was estimated from FTIR spectra comparing the ratio between the absorbance intensities of azide peak and PCL carbonyl peak (1736 cm^{-1}) of peptide-copolymer conjugate to corresponding ratio of N_3 -PEG-PCL copolymer. The conjugation efficiency was $\sim 70\%$ in good agreement with the value calculated through gravimetric measurement of unreacted peptide ($\sim 75\%$).

Properties of aFLT1-decorated NPs

Anti-angiogenic NPs were prepared from a mixture of mPEG-PCL with aFLT1-PEG-PCL (DBLaFLT1) and their properties compared to those of NPs prepared from mPEG-PCL (DBL). Solvent diffusion method, currently indicated as nanoprecipitation, was selected since it is suggested as valid option to produce NPs in an industrial setting and thus to increase the scale of NP production. Colloidal properties of NPs in terms of size (DH), polydispersity index (PI), zeta potential (ζ) and entrapment efficiency of DTX are reported in **Table 1**.

Table 1. Overall properties of unloaded and DTX-loaded NPs. SD are calculated on three different batches.

NPs formulation	D_H^a (nm)	PI ^b	ζ^c (mV)	Yield ^d (%)	DTX Act. Load. ^e (%)	DTX Entr. Eff. ^f (%)	aFLT1 exposition ^g (%)
DBL	78±2	0.1	-12±0.1	68±4	-	-	-
DBL _{aFLT1}	78±5	0.1	-10±2.0	60±2	-	-	19±1.9
DTX-DBL	92±7	0.2	- 9.8±0.3	72±6	8.8±0.9	96±2.3	-
DTX-DBL _{aFLT1}	78±4	0.1	- 9.4±1.5	75±3	8.5±0.6	95±1.7	20±1.3

^aHydrodynamic diameter. ^bPolydispersity index. ^cZeta potential. ^dYield of the preparation process.

^eActual loading is reported as the amount (mg) of drug encapsulated per 100 mg of nanoparticles.

^fRatio between experimental and theoretical loading $\times 100$. ^gRatio between experimental and theoretical amount of aFLT1 $\times 100$.

We obtained NPs formulations in high yield without the help of any surfactant with a size below 100 nm and low PI (<0.2). The ζ was slightly negative as commonly found for PEGylated NPs and unaffected by the incorporation of the aFLT1-modified copolymer. To guarantee long term stability of the formulations, we attempted to freeze-dry NPs in the presence of HP β CD as cryoprotectant, as previously reported (39). However, due to the limited shielding of short PEG chain length on particle-particle interactions, previous conditions were not successful and detailed freeze-drying studies were needed. Different cryoprotectants at different weight ratio with the NPs and different NPs concentration were tested (**Table S1**). The screening allowed identification of the best freeze-drying conditions when using HP β CD in the ratio 1:10 to NPs and successive 1:10 NP sample dilution, since on these conditions no significant size and PI changes were observed after NP re-suspension. Furthermore, the covalent linkage between the diblock copolymer and the aFLT1 did not modify the colloidal properties of NPs after redispersion. Preliminary stability studies on freeze-dried powders stored at 4 °C (**Table S2**) demonstrated that the key parameters of NPs were unchanged after one month.

The amount of aFLT1 exposed on NPs surface was evaluated through a fluorimetric assay. Independently on DTX encapsulation, the amount of aFLT1 on the surface was much lower than expected (~20%), suggesting that, in the conditions adopted to produce NPs, the peptide is partly localized inside the NP core or is in the surface layer but buried in the PEG chains. Nevertheless, the thickness of the external hydrophilic shell of NPs, as evaluated by FALT (**Figure 2A**), was 4.9 nm for DBLaFLT1 and much lower for DBL (2.5 nm) in line with previously reported results (35). These data suggest that a different arrangement of PEG chains on NP surface due to the presence of the peptide is achieved.

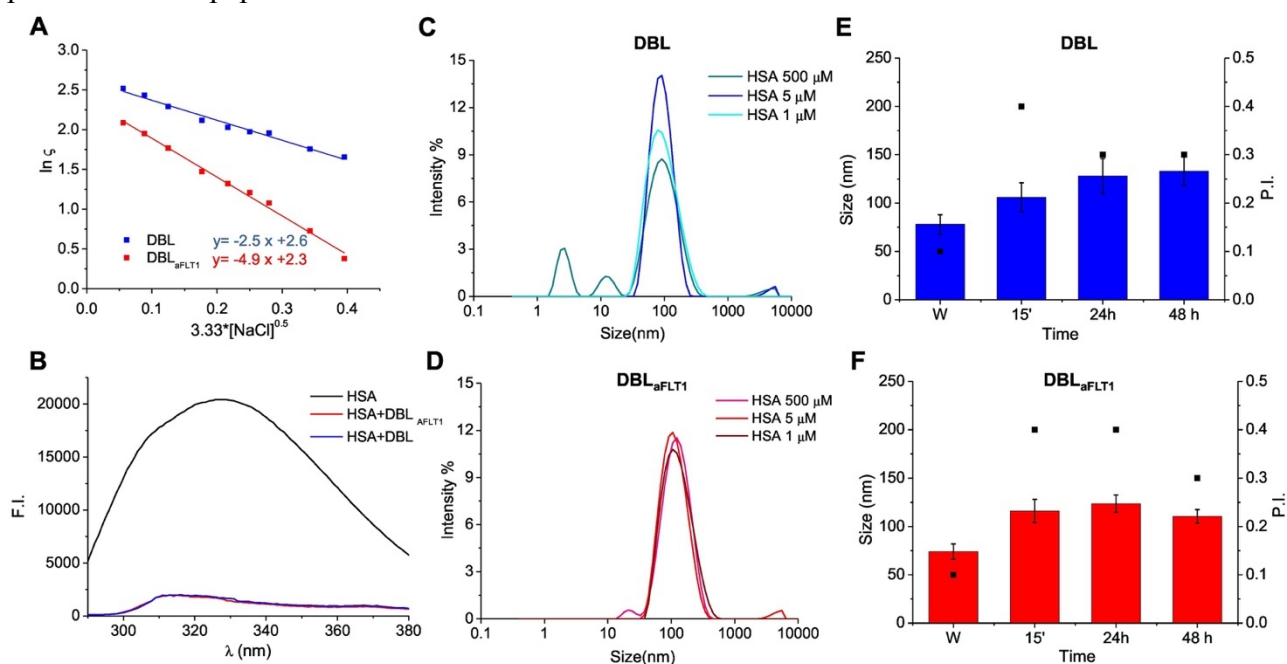


Figure 2. Properties of NPs. A) FALT measurements: the slope of the straight line represents the thickness of the outer hydrophilic shell in nm; B) fluorescence emission spectra of 500 μM HSA in the absence and in the presence of 5 mg mL^{-1} NPs; size distribution of DBL (C) and DBLaFLT1(D) in the presence of increasing concentration of HSA; mean size (bar) and PI (square) of DBL (E) and DBLaFLT1 (F) after incubation for different times in human whole plasma at 37 °C.

Interaction of aFLT1-decorated NPs with protein-rich media

It is well known that the conformation of PEG on NP surface can drive the interactions with serum proteins profoundly affecting NP biodistribution and interaction with different cell populations (40,41). The impact of aFLT1 on the interaction of NPs with human serum albumin (HSA), the most abundant plasma protein, as well as whole human plasma was thus investigated. To this purpose, the fluorescence emission spectra of HSA in the absence and presence of NPs were collected upon excitation at 278 nm, which reflect the contribution of the tyrosine (λ_{em} ca 310 nm) and tryptophan (λ_{em} ca 340 nm) fluorogenic centers (**Figure 2B**). The strong HSA emission was quenched by more than one order of magnitude upon addition of both kind of NPs formulations, thus suggesting a massive interaction between NPs and the protein. The formation of a HSA corona on NPs was confirmed by the changes of the size distribution curves of NPs at increasing HSA concentration (**Figure 2C and D**).

However, through this experiment, we observed a different behavior between DBL and DBLaFLT1 NPs. In the case of DBL, addition of HSA up to 5 μ M did not change greatly the shape of the size curves, while at physiologically relevant HSA concentration (500 μ M) NP size intensity was reduced. In particular, the appearance of the peaks at 3 and 11 nm corresponding to free HSA monomers/tetramers/hexamers, indicates that in these conditions, the surface of NPs is fully occupied by HSA. In contrast, size curve distribution of DBLaFLT1 NPs did not change significantly in the presence of HSA, thus suggesting the formation of a soft protein corona on NP surface without inducing their aggregation, probably due to different thickness of the hydrophilic shell and organization of hydrophilic PEG/aFLT1 chains as previously suggested.

To reproduce the biological conditions encountered by NPs during i.v. injection, their stability in human plasma until 48 h of incubation was evaluated. As shown in **Figure 2E and F**, both DBL and DBLaFLT1 NPs showed a slight increase of size (which was however below 150 nm) and a slight increase of PI, thus demonstrating adequate stability in simulated biological conditions. These results are in line with further stability studies carried out by dispersing NPs in different media, including PBS at pH 7.4 and DMEM with 10% FBS (**Figure S2**).

Effect of aFLT1-decorated NPs on HUVEC tube formation

The capability of the synthesized aFLT1 peptide to bind VEGFR1 was first assessed in HUVEC cells, which are known to overexpress this receptor (42). As confirmed in **Figure S3A**, in the adopted experimental conditions, VEGFR1 was highly expressed by HUVEC as documented by specific antibody recognition and flow cytometry analyses. A significantly higher interaction of the Rhod-conjugated aFLT1 peptide (Rhod-Ahx- aFLT1) compared to the reverse peptide (Rhod-Ahx-reverse aFLT1) was observed in HUVEC cells (**Figure S3B**). The results of competition experiments carried out using the VEGFR1 and VEGFR2 specific ligand VEGF165, showed a significant ($p < 0.005$, t-test) inhibition of aFLT1 interaction after co-incubation of HUVEC with 50 ng mL⁻¹ VEGF165, indicating that aFLT1 peptide and VEGF165 competed for the binding to VEGFR1. On the contrary, no significant inhibition in peptide interaction was measured for the peptide with reverse sequence, confirming its inability to interact with VEGFR1 and to affect VEGFR ligands interaction. Overall, our results are in agreement with those reported by Bae and coworkers (9), who verified the VEGFR1-specific character of the aFLT1 peptide with purified recombinant proteins and measured a 60% inhibition of VEGF165 binding to VEGFR1 in the

presence of aFLT1 peptide in HUVEC. Furthermore, aFLT1-decorated NPs were internalized by HUVEC as shown by confocal microscopy on rhodamine-labeled DBLaFLT1 (**Figure S3D**). To assess whether the covalent binding of aFLT1 on NPs surface could alter its antiangiogenic activity, we performed an in vitro endothelial tube formation assay in HUVEC. **Figure 3A** shows representative images of the tubes formed in the presence of different antiangiogenic agents and **Figure 3B** summarizes the results obtained from the analysis of the images with the ImageJ dedicated plugin (Angiogenesis Analyzer).

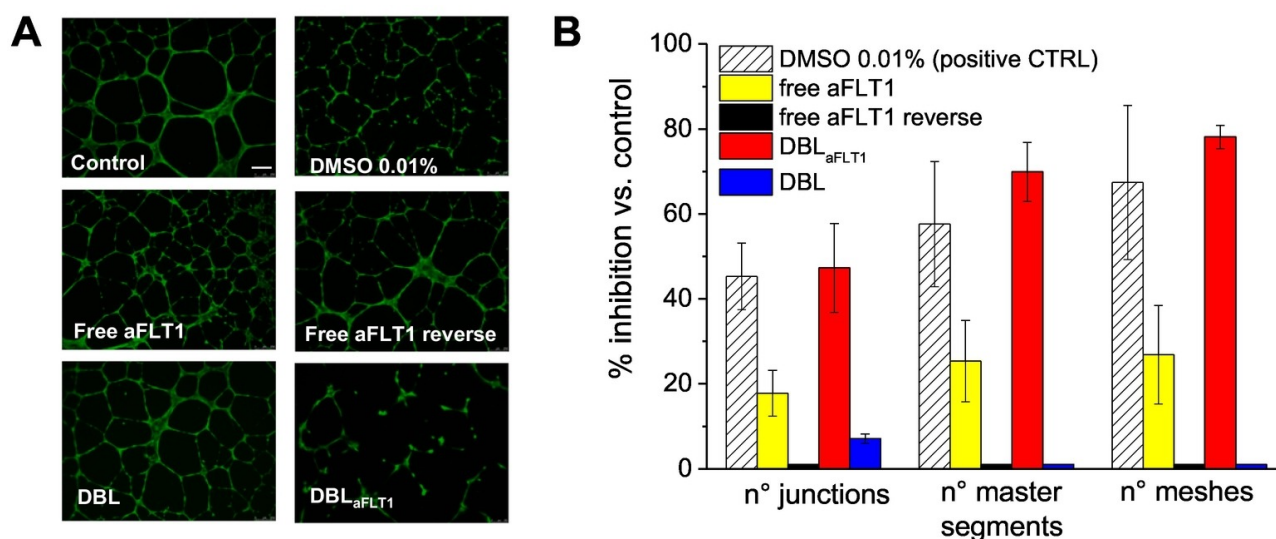


Figure 3. In vitro endothelial tube formation assay in HUVEC. A) Representative fluorescence images of tubes and B) summary of results on percent inhibition of tube formation with the different treatments. Inhibition caused by cell incubation for 18 h with $50 \mu\text{g mL}^{-1}$ of DBL or DBLaFLT1 or with the corresponding dose of free aFLT1 or reverse sequence peptide ($100 \mu\text{M}$). Cell incubation with 0.01% DMSO was used as inhibitor of tube formation. Scale bars: $250 \mu\text{m}$.

The number of junctions, master segments and meshes were reported in **Figure 3B** as the most significant parameters. Surprisingly, the aFLT1 peptide conjugated to NPs (DBLaFLT1 at $50 \mu\text{g mL}^{-1}$) demonstrated significantly higher anti-angiogenic activity (at least two times) than the free peptide in reducing all the three parameters considered for evaluating the antiangiogenic activity (in both cases aFLT1 was $100 \mu\text{M}$). As expected, no effects on tube formation were detected for the free reverse peptide. Similarly, DBL caused only a slight ($\sim 10\%$) reduction of the number of junctions but did not affect the number of master segments and meshes of the endothelial tubes. It is worth noting that NPs were not cytotoxic for HUVEC until 72 h at the tested concentration ($50 \mu\text{g mL}^{-1}$) (**Figure S4**). Thus, it appears clear that the anti-angiogenic activity of the DBLaFLT1 can be attributed exclusively to the presence of aFLT1 peptide on NP surface, even though only 20% of the peptide was exposed.

Properties of DTX-loaded NPs and cytotoxicity on MDA-MB-231 and HUVEC

DTX was loaded in the core of NPs after dissolution in the polymer mixture. Some properties of drug-loaded NPs are reported in **Table 1**. The size of DTX-DBL was slightly larger as compared to the other formulations while ζ remained negative. The amount of aFLT1 on NPs surface was unchanged upon drug encapsulation and NPs were stable in both water and PBS (**Figure 4A**). The release of DTX from NPs was evaluated in 10 mM PBS, pH 7.4 at 37°C through the dialysis

method. DTX entrapped at 10% theoretical loading was almost completely associated to NPs, without any significant difference for copolymer material employed (**Table 1**).

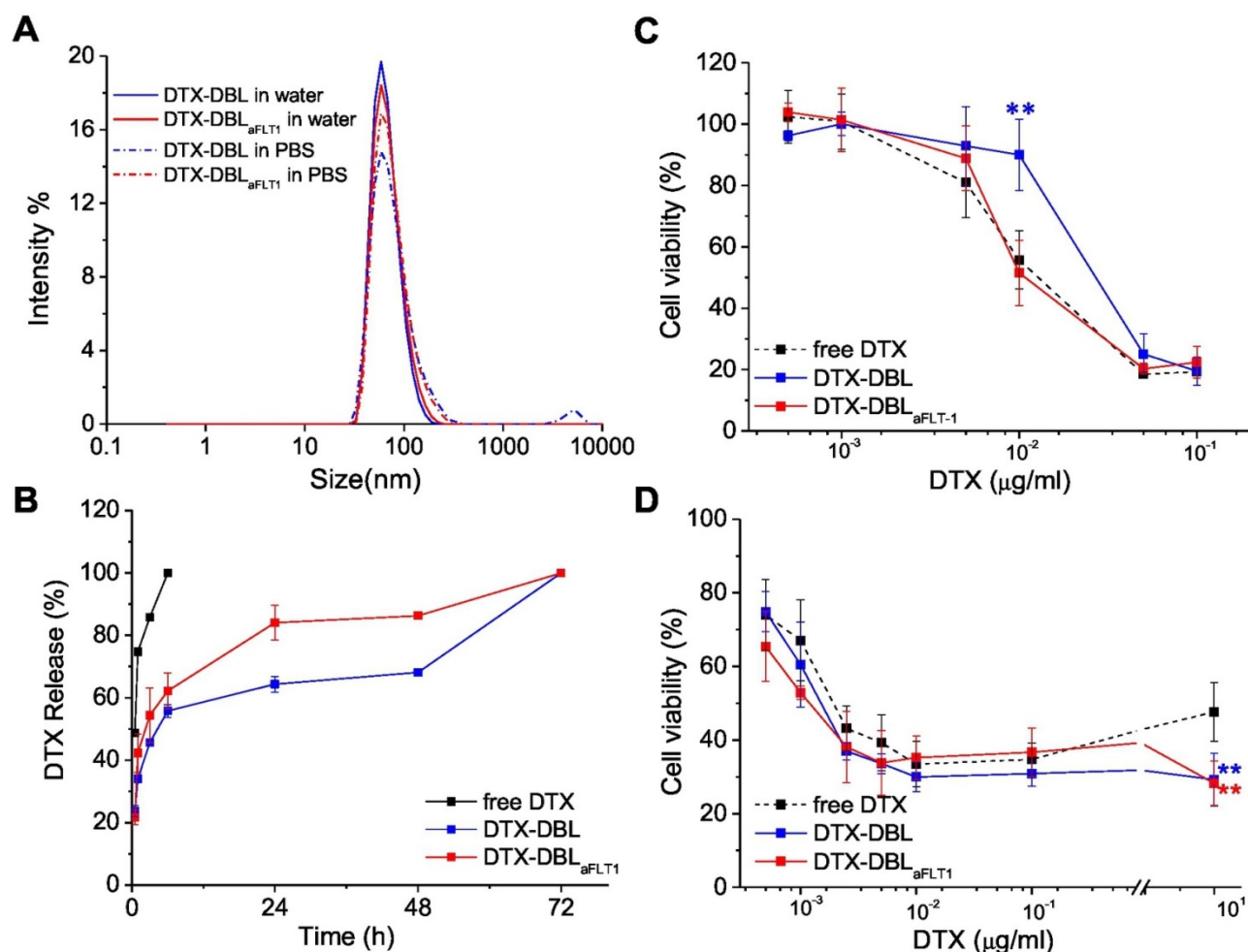


Figure 4. Properties and cytotoxicity of DTX-loaded NPs. A) Size distribution of DTX-loaded NPs in water and PBS pH 7.4; B) DTX release from NPs in PBS 10 mM pH 7.4, at 37 °C evaluated by dialysis method. Results are the means \pm SD of three measurements obtained on three different NPs batches. Cytotoxicity in C) MDA-MB-231 cells and D) HUVEC of DTX delivered in DMSO or loaded in DBL or DBLaFLT1. Cell viability was measured with the MTS assay after 72 h of cell incubation. Data are mean values \pm SD of at least three independent experiments carried out in triplicate. *p value<0.005, vs. free DTX; **p value<0.001, vs. free DTX (Student's t-test).

Due to its good compatibility with PCL phase, DTX is assumed to localize in NPs lipophilic core. As evident in **Figure 4B**, in both DTX-DBL and DTX-DBLaFLT1 NPs we observed a fast release of about 50% of the drug during the first 6 h followed by a slow release rate indicating that NPs are able to sustain drug release along time as compared to free drug (100% release in 6 h). The overall results are in line with our previous studies on DBL demonstrating that DTX was released slowly as typical for a sustained-release nanosystem (39). Furthermore, the presence of aFLT1 on NP surface does not affect greatly the overall release rate of the hydrophobic drug entrapped in the internal core.

MTS assay was employed to measure viability reduction in triple negative MDA-MB-231 breast cancer cells (**Figure 4C**) and HUVEC (**Figure 4D**) incubated for up to 72 h with free DTX or loaded in DBL or DBLaFLT1. The viability curves in MDA-MB-231 cancer cells showed a clear dose-dependent cell mortality, that was >80% after 72 h of treatment at the highest DTX dose tested

($0.1 \mu\text{g mL}^{-1}$) for all the formulations. In some cases (e.g. $0.01 \mu\text{g mL}^{-1}$ DTX), DTX-DBL were significantly less cytotoxic than free DTX or DTX-DBLaFLT1 NPs also after 48 h (**Figure S5**). Since MDA-MB-231 do not express full-length surface FLT1 it is plausible that both the slower release of DTX from DBL and the different amount of NPs uptaken play a role. Some contributions of the delivery system in determining cell toxicity was excluded by measuring the viability of MDA-MB-231 cells incubated with empty DBL or DBLaFLT1 up to $100 \mu\text{g mL}^{-1}$ NPs, corresponding to the highest DTX tested dose (**Figure S4**). Overall, the results show that DTX-DBL and DTX-DBLaFLT1 NPs exert similar cytotoxic activity toward MDA-MB-231 cells and, importantly, not lower than that of free DTX.

The shape of the viability curves in HUVEC was completely different and comparable cytotoxicity after 72 h of incubation for all the tested concentrations was observed, with the exclusion of the highest concentration (e.g. $10 \mu\text{g mL}^{-1}$) at which DTX-loaded NPs were significantly more effective with respect to the free chemotherapeutic. This behavior was observed also after 48 h incubation (**Figure S5A**). Notably, the viability curves of HUVEC showed a clear plateau around 50% and 40% viability after 48 and 72 h of incubation, respectively, for DTX doses ranging from 0.005 to $10 \mu\text{g mL}^{-1}$, indicating that a fraction of these cells are not sensitive to DTX.

It is well known that DTX exerts its antineoplastic activity by inhibition of microtubule depolymerization in different cancer cell lines blocking proliferation. Obviously, these effects are not limited to transformed cells and endothelial dysfunction and apoptosis has been reported for DTX at nM concentration in HUVEC and related to both an analogous mechanism (43) and upregulation of oxidative stress (44). In the attempt to explore the impact of DTX or DTX-loaded NPs on antiangiogenic activity at a concentration cytotoxic for MDA-MB231 ($5 \mu\text{g mL}^{-1}$), the endothelial tube formation assay was performed. In the experimental conditions adopted, free DTX or NPs formulations showed no cytotoxicity in HUVEC after 24 h (**Figure 5A**). DTX-DBLaFLT1 gave the highest antiangiogenic effect and was able to completely abolish mesh formation (**Figure 5B**). Free DTX demonstrated an antiangiogenic activity comparable or slightly increased with respect to that of free aFLT1 peptide (**Figure 3A and B**), while its encapsulation in DBL resulted in a significant reduction of activity ($p < 0.001$, t-test for all the three considered parameters).

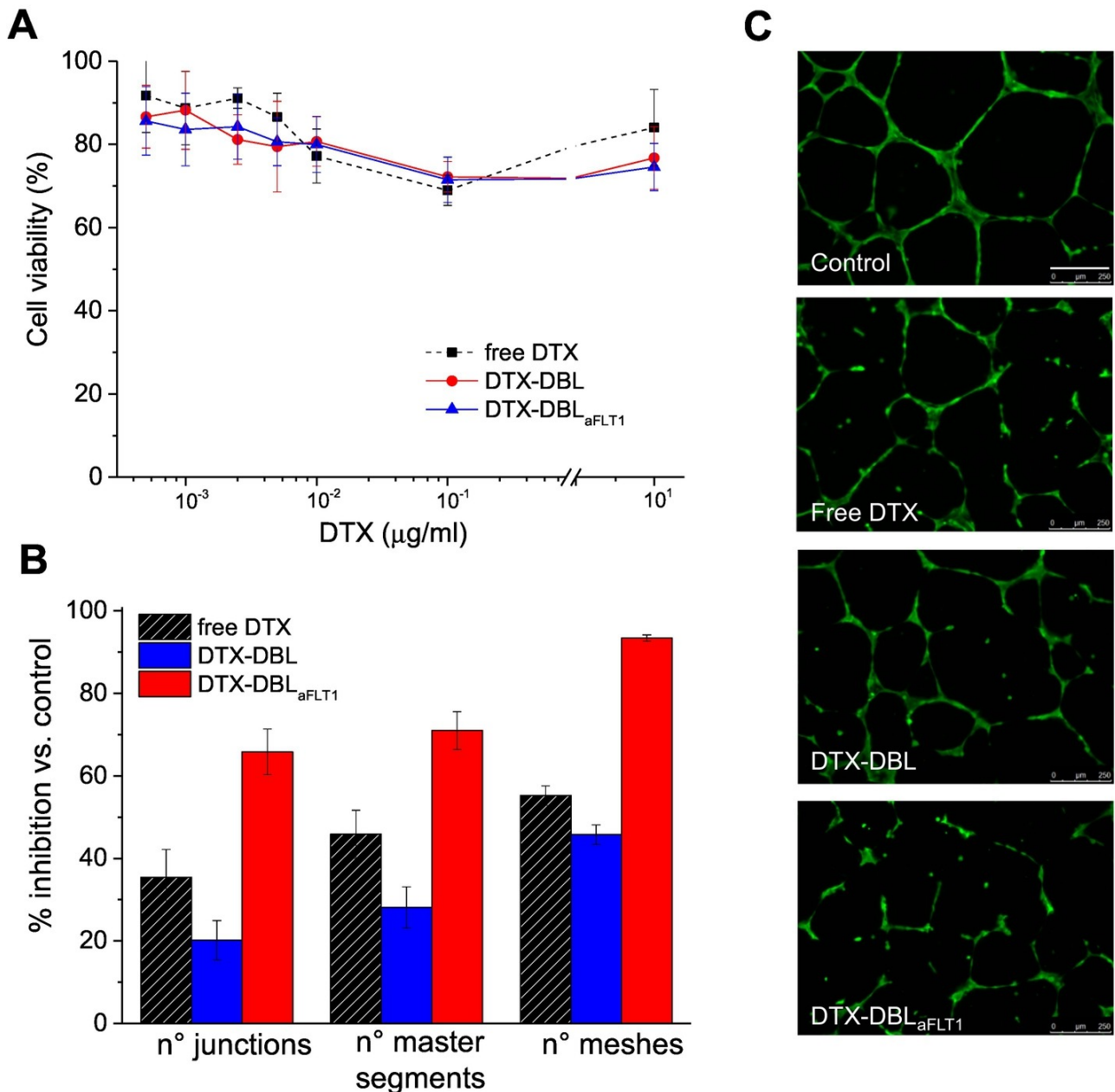


Figure 5. Cytotoxicity and endothelial tube formation assay in HUVEC cells of DTX and DTX-loaded NPs. A) Cytotoxicity of DTX delivered in the standard solvent or loaded in DBL or DBLaFLT1 NPs in HUVEC cells. Cell viability was measured with the MTS assay after 24 h of cell incubation. Data are mean values \pm standard deviation of at least three independent experiments carried out in triplicate. B) Summary of results on percent inhibition of tube formation with the different treatments and C) representative fluorescence images of tubes. Inhibition caused by cell incubation for 18 h with $50 \mu\text{g mL}^{-1}$ of DBL or DBLaFLT1 or with the corresponding dose of free DTX ($5 \mu\text{g mL}^{-1}$). Scale bars: $250 \mu\text{m}$.

In any case, the inhibition of the number of junctions and meshes with DTX-DBLaFLT1 was significantly potentiated compared to unloaded DBLaFLT1 ($p < 0.001$, t-test), while the number of master segments was not ($p > 0.05$, t-test).

Overall, the results confirmed that NPs decorated with aFLT1 are more anti-angiogenic with respect to the free peptide and the loading of NPs with the chemotherapeutic drug potentiates the inhibition of formation of properly conformed tubes (e.g. no meshes formed at all with DTX-DBLaFLT1) at least in the in vitro assay. Remarkably, the covalent binding of aFLT1 on NP surface does not

decrease the cytotoxicity of the transported drug but it is expected to enhance the chemotherapeutic effect through its anti-angiogenic activity in more complex models.

In vivo anti-angiogenic potential and anticancer activity of NPs on a CAM model

Based on the promising *in vitro* results, we translated our investigations on MDA-MB-231 cells xenografted on CAMs. MDA-MB-231 tumors were implanted on 9-days old CAMs (E9) and the day after (E10) treatment started once a day, for a total of five days, with free DTX in DMSO or loaded in DBL or DBLaFLT1 (0.083 μ g DTX/day). Additional embryos were injected with the corresponding dose of empty DBL (0.83 μ g/day) to exclude any cytotoxicity or effect on tumor growth caused by the vehicle.

The systemic toxicity of the different treatments on the chicken embryos was evaluated by counting the numbers of dead/surviving embryos at day 7 after beginning the treatments (E16). As shown in **Figure S6**, none of the treatments caused an embryos death higher than 15%, a value which was comparable with that of the negative controls (8%), namely embryos treated with PBS solution.

The anti-angiogenic effects were evaluated by counting the number of vessels arriving on the tumors on CAMs images (**Figure 6A**) taken on the day after the end of the treatments (E15, 6 days after tumor induction). The analysis (**Figure 6B and C**) showed that the number of vessels per tumor was significantly reduced with respect to the negative control in all the CAMs treated with DTX-loaded NPs (p values vs negative control: 0.0077, 0.0003 and <0.0001 for free DTX, DTX-DBL and DTX-DBLaFLT1, respectively). As expected, DBL did not reduce significantly tumor angiogenesis (p = 0.8505 DBL vs negative control).

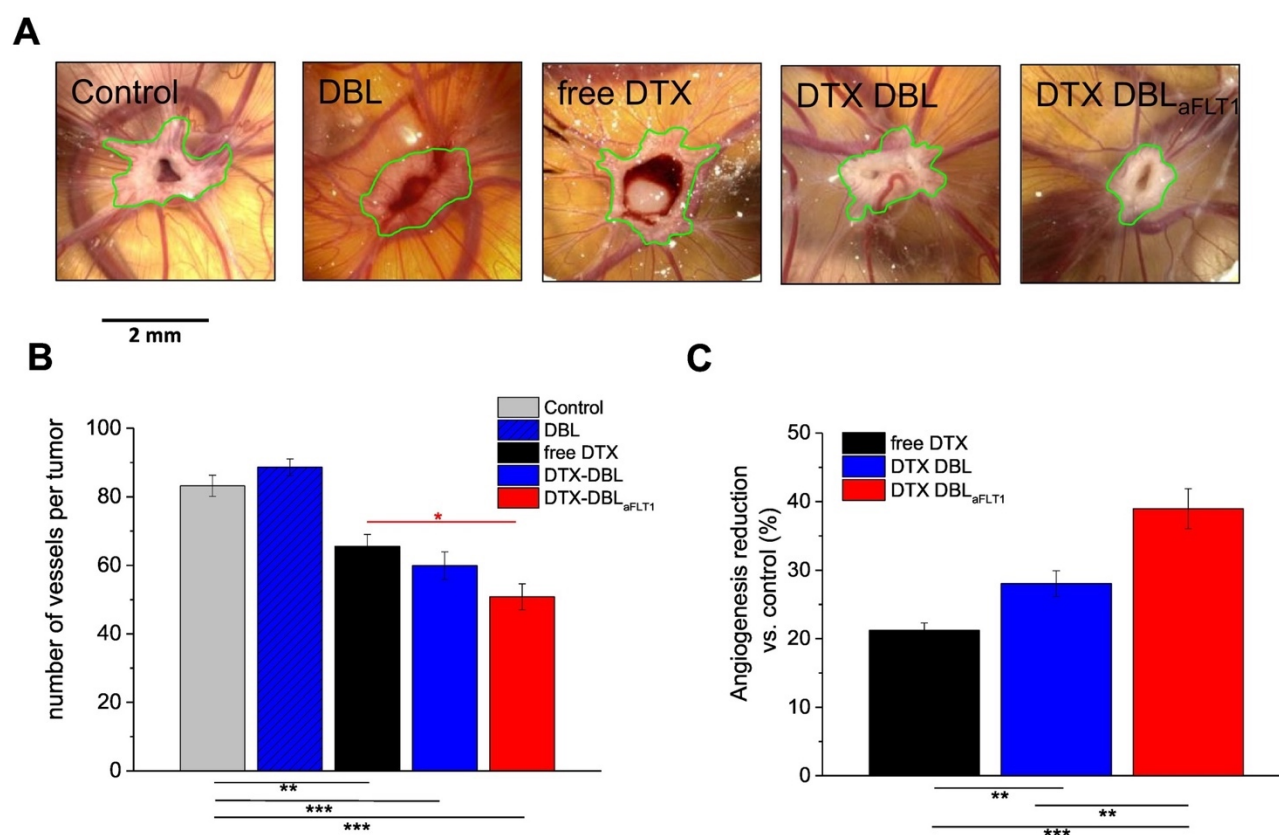


Figure 6. Anti-angiogenic effects of free DTX or DTX-NPs (DTX dose 0.083 μ g, NPs dose 0.83 μ g) on MDA-MB-231 cells xenografted on CAMs (unloaded DBL are used as control). A) Representative images of tumors and associated blood vessels. The tumor borders are highlighted in green. B) Numbers of vessels per tumor counted on

samples at E15 and reported as means \pm SEM for each experimental group. C) Extent of angiogenesis reduction versus negative control. * 0.05 > p value > 0.01; ** 0.01 > p value > 0.001; *** p value < 0.001, One-way ANOVA with post-tests. (For interpretation of the references to colour in this figure legend, the reader is referred to the web version of this article.)

Interestingly, DTX-DBLaFLT1 were significantly more potent in reducing the numbers of tumor-associated blood vessels with respect to free DTX (p values of 0.0301) while DTX-DBL were not (p value of 0.7694), suggesting an important role of the anti-angiogenic aFLT1 peptide on DTX-DBLaFLT1. Overall, the data of the counts of vessels per tumor showed that the treatments of CAMs with free DTX, DTX-DBL and DTX-DBLaFLT1 reduced tumor angiogenesis by 21, 28 and 39%, respectively (**Figure 6B**), and clearly indicated the improved efficacy of DTX nanodelivery in combination with aFLT1 peptide-based anti-angiogenic therapy with respect to the standard chemotherapy. From the analyses of the images of tumors and associated vessels it was also evident some tumor shrinkage especially in the group treated with DTX-DBLaFLT1 (**Figure 6A**).

In fact, the evaluation of the weight of the tumors removed from the CAM (E16, 7 days after tumor induction) demonstrated a significant reduction of tumor growth with all DTX formulations considered (p value < 0.001) compared to negative controls (**Figure 7A**). No inhibitory effects on tumor growth were observed with DBL vs. negative control (p = 0.336). In agreement with the angiogenesis reduction, the most prominent effect on the inhibition of tumor growth was observed with DTX-DBLaFLT1, followed by DTX-DBL and free DTX. The reduction of tumor weight caused by both DTX-DBLaFLT1 and DTX-DBL was significantly higher than that of free DTX (p < 0.01 and p < 0.001, respectively) (**Figure 7A**). Accordingly, the percentages of tumor regression associated to CAM treatments with free DTX, DTX-DBL and DTX-DBLaFLT1 calculated versus the negative control were 32, 46 and 60%, respectively (**Figure 7B**), and was significantly higher for both types of NPs with respect to free DTX (p < 0.001).

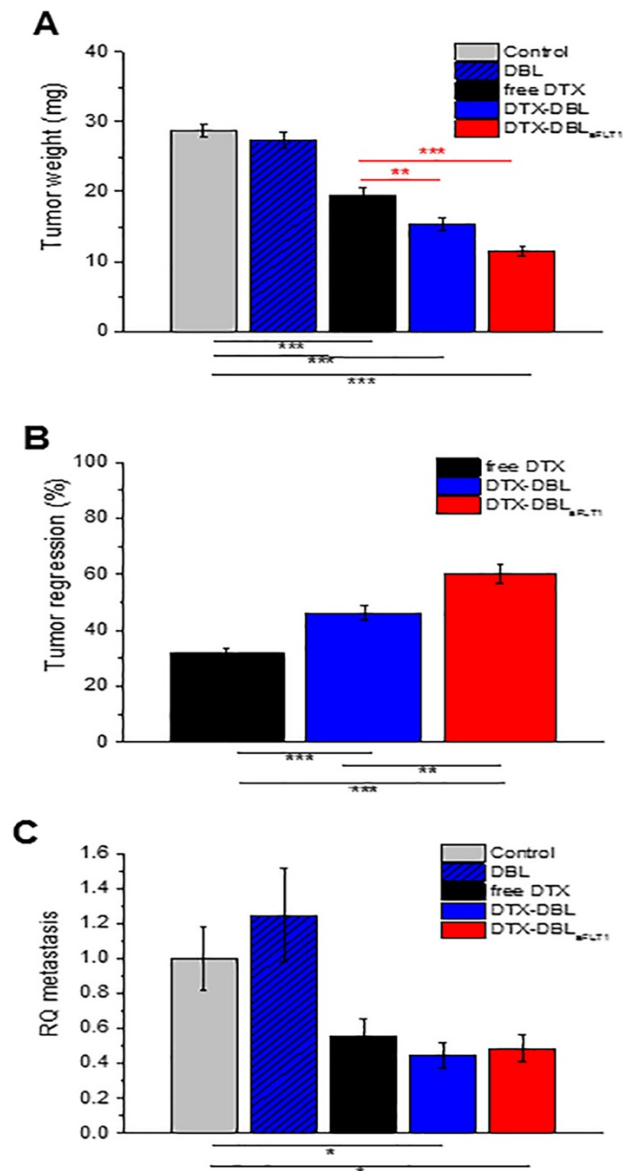


Figure 7. Tumor growth and metastasis analysis on MDA-MB-231 cells xenografted on CAMs. Tumor weight (A) and regression percentage (B) were measured by removing the tumor from normal CAM tissue at E16 and weighting them. The data are means \pm SEM for each experimental group. * 0.05 > p value > 0.01; ** 0.01 > p value > 0.001; *** p value < 0.001, One-way ANOVA with post-tests. C) Relative quantity of MDA-MB-231 metastasis (RQ). Invasion was measured by qPCR for Alu sequences in the lower part of CAMs. The arbitrary value for metastasis is 1 (negative control) and data are means \pm SEM for each experimental group.

It is repeatedly reported that the neovascularization of tumors promotes the spread of cancer cells and the formation of metastasis. Thus, we assessed if the proposed anti-angiogenic NPs were able to reduce the metastatic potential of MDA-MB-231 cells xenografted on CAMs. Toward this aim, on E16 the genomic DNA of a distal portion of each CAM (lower portion) was extracted and analyzed by quantitative PCR (qPCR) with specific primers for human Alu sequences, widely recognized as a reliable method to evaluate the anti-metastatic potential of drugs in xenograft models (45). As one can see in **Figure 7C**, showing the relative amount of metastatic cells, DTX NPs significantly decreased the MDA-MB-231 metastatic cells in the lower portion of the CAMs compared to negative controls (p values vs negative control: 0.0134 and 0.0388 for DTX-DBL and DTX-DBL_{LaFLT1}, respectively). On the contrary, the metastasis reduction with free DTX was not

statistically relevant (p value vs negative controls: 0.0507). The latter results did not show a positive role of aFLT1 conjugated on DBL on reducing the formation of metastases potential, at least on xenografted CAM models, but the presence of the peptide does not have any negative effect on the overall performance of the DTX NPs (p = 0.7325 DTX-DBLaFLT1 vs. DTX-DBL), which was able to reduce by 50% the extent of tumor metastasis.

Conclusions

In summary, we have reported the successful preparation of NPs made of PCL-PEG copolymers conjugated with an anti-FLT1 hexapeptide with anti-angiogenic properties and carrying the chemotherapeutic DTX in the internal core. The presence of the peptide on the NP surface did not interfere with the DTX loading capacity of NPs nor on their stability in biologically-relevant media as whole human plasma. The conjugation with aFLT1 imparted to NPs the ability to inhibit angiogenesis in vitro much more efficiently than the equivalent dose of free peptide, indicating that conjugation somehow strengthens the interaction of the peptide with its specific receptor VEGFR1 involved in the regulation of new vessels formation. In vitro cytotoxicity studies showed that aFLT1-conjugated NPs did not affect the viability of HUVEC and MDA-MB 231 cells, but they became highly cytotoxic, especially to tumor cells, when DTX is entrapped in the internal hydrophobic core. The in vitro studies did not highlight significantly higher cytotoxic effects of the DTX-loaded aFLT1 conjugated NPs with respect to their unconjugated counterpart or free DTX while the in vivo model of MDA-MB 231 tumor xenografted in the CAM indicated higher antitumoral effects. In fact, DTX-loaded aFLT1 conjugated NPs induced significantly higher reduction of tumor weight and regression with respect to un-conjugated NPs and it is reasonable to assume that these effects come from the combination of improved antiangiogenic and cytotoxic activity of the NPs. Overall, the results reinforce the hypothesis that the combination of chemotherapeutics and antiangiogenic agents is a useful approach for fighting tumors and in this context a well-designed nanoplatform may represent an unprecedented tool for their combined delivery.

Acknowledgements

This work was supported by Italian Association for Cancer Research (IG2014 #15764).

References

- 1 A.M. Al-Abd, A.J. Alamoudi, A.B. Abdel-Naim, T.A. Neamatallah, O.M. Ashour J. Adv. Res., 8 (2017), pp. 591-605
- 2 L.C. Roudsari, J.L. West Adv Drug Deliver Rev, 97 (2016), pp. 250-259
- 3 G.C. Jayson, R. Kerbel, L.M. Ellis, A.L. Harris Lancet, 388 (2016), pp. 518-529
- 4 L.M. Ellis, D.J. Hicklin Nat. Rev. Cancer, 8 (2008), pp. 579-591
- 5 G.H. Fong, J. Rossant, M. Gertsenstein, M.L. Breitman Nature, 376 (1995), pp. 66-70

- 6 K.H. Plate, G. Breier, B. Millauer, A. Ullrich, W. Risau *Cancer Res.*, 53 (1993), pp. 5822-5827
- 7 P.M. Laca, G. Graziani *Pharmacol. Res.*, 136 (2018), pp. 97-107
- 8 C. Fischer, M. Mazzone, B. Jonckx, P. Carmeliet *Nat. Rev. Cancer*, 8 (2008), pp. 942-956
- 9 D.G. Bae, T.D. Kim, G. Li, W.H. Yoon, C.B. Chae *Clin. Cancer Res.*, 11 (2005), pp. 2651-2661
- 10 E.V. Rosca, J.E. Koskimaki, C.G. Rivera, N.B. Pandey, A.P. Tamiz, A.S. Popel *Curr. Pharm. Biotechnol.*, 12 (2011), pp. 1101-1116
- 11 M.M. Mita, L. Sargsyan, A.C. Mita, M. Spear *Expert Opin. Investig. Drugs*, 22 (2013), pp. 317-328
- 12 N. Ferrara, K.J. Hillan, H.P. Gerber, W. Novotny *Nat. Rev. Drug Discov.*, 3 (2004), pp. 391-400
- 13 G.W. Prager, M. Poettler, M. Unseld, C.C. Zielinski *Translational Lung Cancer Research*, 1 (2012), pp. 14-25
- 14 L. Moserle, G. Jimenez-Valerio, O. Casanovas *Cancer Discov.*, 4 (2014), pp. 31-41
- 15 G. Bergers, D. Hanahan *Nat. Rev. Cancer*, 8 (2008), pp. 592-603
- 16 F. Collinson, M. Hutchinson, R.A. Craven, D.A. Cairns, A. Zougman, T.C. Wind, N. Gahir, M.P. Messenger, S. Jackson, D. Thompson, C. Adusei, J.A. Ledermann, G. Hall, G.C. Jayson, P.J. Selby, R.E. Banks *Clin. Cancer Res.*, 19 (2013), pp. 5227-5239
- 17 D. Banerjee, R. Harfouche, S. Sengupta *Vascular Cell*, 3 (2011), p. 3
- 18 S. Mukherjee, C.R. Patra *Nanoscale*, 8 (2016), pp. 12444-12470
- 19 K. Yoncheva, G. Momekov *Expert Opinion on Drug Delivery*, 8 (2011), pp. 1041-1056
- 20 S. Huang, K. Shao, Y. Liu, Y. Kuang, J. Li, S. An, Y. Guo, H. Ma, C. Jiang *ACS Nano*, 7 (2013), pp. 2860-2871
- 21 R. Jahanban-Esfahlan, K. Seidi, B. Banimohamad-Shotorbani, A. Jahanban-Esfahlan, B. Yousefi *J. Cell. Physiol.*, 233 (2018), pp. 2982-2992
- 22 P. Bhattarai, S. Hameed, Z. Dai *Nanoscale*, 10 (2018), pp. 5393-5423
- 23 G. Gu, Q. Hu, X. Feng, X. Gao, J. Menglin, T. Kang, D. Jiang, Q. Song, H. Chen, J. Chen *Biomaterials*, 35 (2014), pp. 8215-8226

- 24 A. Wicki, D. Witzigmann, V. Balasubramanian, J. Huwyler *J. Control. Release*, 200 (2015), pp. 138-157
- 25 E. Blanco, H. Shen, M. Ferrari *Nat. Biotechnol.*, 33 (2015), pp. 941-951
- 26 I. d'Angelo, C. Conte, A. Miro, F. Quaglia, F. Ungaro *Expert Opinion on Drug Delivery*, 11 (2014), pp. 283-297
- 27 S. Parveen, S.K. Sahoo *J. Drug Target.*, 16 (2008), pp. 108-123
- 28 G. Shim, M.G. Kim, D. Kim, J.Y. Park, Y.K. Oh *Adv. Drug Deliv. Rev.*, 115 (2017), pp. 57-81
- 29 S.S. Qi, J.H. Sun, H.H. Yu, S.Q. Yu *Drug Delivery*, 24 (2017), pp. 1909-1926
- 30 J.A. Kemp, M.S. Shim, C.Y. Heo, Y.J. Kwon *Adv. Drug Deliv. Rev.*, 98 (2016), pp. 3-18
- 31 Q. Hu, W. Sun, C. Wang, Z. Gu *Adv. Drug Deliv. Rev.*, 98 (2016), pp. 19-34
- 32 P. Grossen, D. Witzigmann, S. Sieber, J. Huwyler *J. Control. Release*, 260 (2017), pp. 46-60
- 33 C. Conte, I. d'Angelo, A. Miro, F. Ungaro, F. Quaglia *Curr. Top. Med. Chem.*, 14 (2014), pp. 1097-1114
- 34 C. Avitabile, F. Netti, G. Orefice, M. Palmieri, N. Nocerino, G. Malgieri, L.D. D'Andrea, R. Capparelli, R. Fattorusso, A. Romanelli *Bba-Gen Subjects*, 1830 (2013), pp. 3767-3775
- 35 A. Venuta, F. Moret, G. Dal Poggetto, D. Esposito, A. Fraix, C. Avitabile, F. Ungaro, M. Malinconico, S. Sortino, A. Romanelli, P. Laurienzo, E. Reddi, F. Quaglia *Eur. J. Pharm. Sci.*, 111 (2018), pp. 177-185
- 36 T.D. Palmer, J. Lewis, A. Zijlstra *J. Vis. Exp.*, 51 (2011), p. e2815
- 37 H.C. Kolb, K.B. Sharpless *Drug Discov. Today*, 8 (2003), pp. 1128-1137
- 38 T.Y. Liu, W.M. Hussein, Z.F. Jia, Z.M. Ziora, N.A.J. McMillan, M.J. Monteiro, I. Toth, M. Skwarczynski *Biomacromolecules*, 14 (2013), pp. 2798-2806
- 39 C. Conte, F. Ungaro, G. Maglio, P. Tirino, G. Siracusano, M.T. Sciortino, N. Leone, G. Palma, A. Barbieri, C. Arra, A. Mazzaglia, F. Quaglia *Journal of Controlled Release: Official Journal of the Controlled Release Society*, 167 (2013), pp. 40-52
- 40 P. Aggarwal, J.B. Hall, C.B. McLeland, M.A. Dobrovolskaia, S.E. McNeil *Adv. Drug Deliv. Rev.*, 61 (2009), pp. 428-437
- 41 C.C. Fleischer, C.K. Payne *Acc. Chem. Res.*, 47 (2014), pp. 2651-2659

42 M.J. Cudmore, P.W. Hewett, S. Ahmad, K.Q. Wang, M. Cai, B. Al-Ani, T. Fujisawa, B. Ma, S. Sissaoui, W. Ramma, M.R. Miller, D.E. Newby, Y. Gu, B. Barleon, H. Weich, A. Ahmed Nat. Commun., 3 (2012), p. 972

43 K.A. Hotchkiss, A.W. Ashton, R. Mahmood, R.G. Russell, J.A. Sparano, E.L. Schwartz Mol. Cancer Ther., 1 (2002), pp. 1191-1200

44 C.H. Hung, S.H. Chan, P.M. Chu, K.L. Tsai Toxicological Sciences: An Official Journal of the Society of Toxicology, 145 (2015), pp. 59-67

45 T. Schneider, F. Osl, T. Friess, H. Stockinger, W.V. Scheuer Clinical & Experimental Metastasis, 19 (2002), pp. 571-582

Supplementary Materials

Table S1. Freeze drying studies of nanoparticles

Sample	Sample dilution	Hydrodynamic diameter (nm±SD)	PI	Cryoprotectant (ratio to polymer weight)	Freezing method
DBL before freeze drying	-	75	0.116	-	-
	-	955	0.254		
	1/5	605	0.411	P188	
	1/10	557	0.394		
	-	900	0.401		
	1/5	509	0.351	P188 1/10-Trehalose 1/10	
	1/10	320	0.294		
	-	758	0.404		-40 °C
	1/5	693	0.493	P188 1/5-Trehalose 1/10	
	1/10	668	0.436		
	-	1326	1		
	1/5	2309	1	Glucose 1/10	
	1/10	2762	1		

-	4689	0.471	
1/5	1041	0.751	Sucrose 1/10
1/10	3350	1	
-	1590	0.369	
1/5	447	0.437	Mannitol 1/10
1/10	5399	1	
-	382	1	
1/5	497	0.744	HP β CD 1/10
1/10	81 \pm 7	0.257	
-	1973	0.120	
1/5	1842	1	Sorbitol 1/10
1/10	1753	1	

Table S2. Long-term stability of freeze-dried nanoparticles in HPBCD dispersed in PBS pH 7.4 after one month of storage at 4 °C.

Sample	H_D (nm\pmSD)	PI	DTX Entrapment Eff. (%)
DTX-DBL	95 \pm 9	0.2	97 \pm 1.5
DTX-DBL_{aFLT1}	87 \pm 10	0.1	96 \pm 2.8

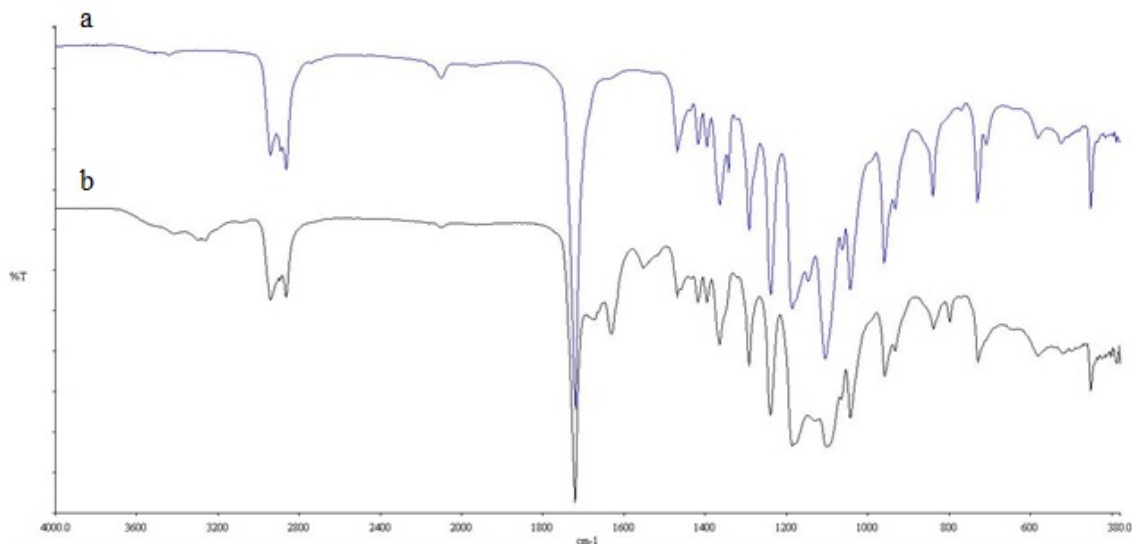


Figure S1. FTIR spectra of N₃-PEG-PCL (a) and aFLT1-PEG-PCL (b). Amide I and amide II bands of peptide bonds are clearly visible in the range 1650-1540 cm⁻¹ of conjugate spectrum.

S2. NP stability in cell culture medium and in DMEM+FBS

The stability of NPs was evaluated in phosphate buffered saline (PBS, 10 mM phosphate, 137 mM NaCl, 2.7 mM KCl) at pH 7.4 and in DMEM with 10% Fetal Bovine Serum (FBS). NPs (0.75 mg) were diluted in the selected media, incubated at 37 °C and measurements of the NPs size were taken after 15, 45, 60 minutes and 24 h of incubation. Hydrodynamic diameter (D_H) and polydispersity index (PI) were determined on a Zetasizer Nano Z (Malvern Instruments Ltd).

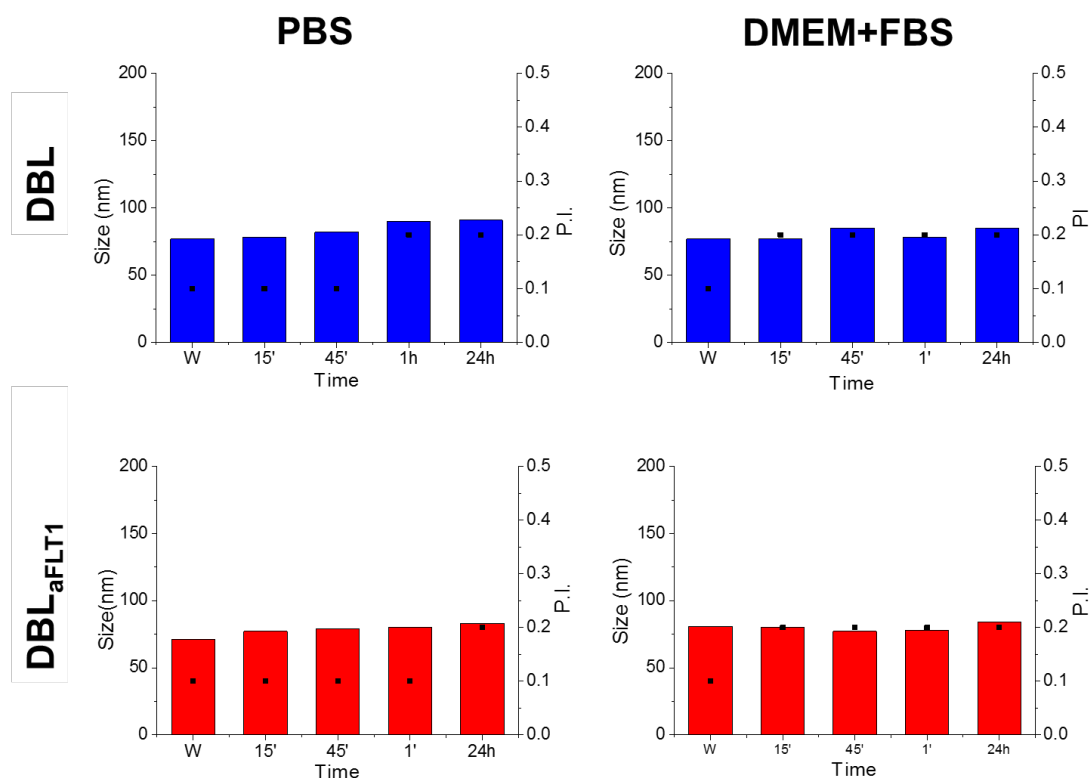


Figure S2. Mean size (bars) and PI (squares) of NPs in the presence of PBS 10 mM pH 7.4 (A) and DMEM + FBS 10% (B) at 37 °C measured along 24 h of incubation.

S3. Expression of FLT-1 receptor on HUVEC cell surface and NP uptake

The expression of FLT1 receptor on HUVEC cell surface was evaluated by flow cytometry (BD FACSCanto™ II instrument from Becton Dickinson, San Jose, USA) after cell staining with the anti-human VEGFR1/FLT1 FITC-conjugated antibody (Sino Biological, cat. Number 10136-R-111-F). 0.5×10^6 cells were collected from flasks, transferred in flow cytometry tubes and kept on ice for the entire duration of the experiment. Before incubation with the antibody, the cells were washed twice with 1 ml of cold PBS and centrifuged ($156 \times g$) for 7 min at 4 °C. After the second wash, PBS was completely removed and 1 μg of anti-FLT1 antibody was added to the cell pellet that after vortexing was incubated in ice for 1 h. Afterward, the samples were washed twice with 1 ml of cold PBS and re-suspended in 1 ml of PBS. A blue laser at 488 nm was used for excitation and the FITC channel (515-545 nm) was selected for the detection of the anti-FLT1 antibody fluorescence. 2×10^5 events were acquired and analyzed using the FACSDiva software.

The cell association/internalization of the free aFLT1 peptide and the reverse peptide conjugated to rhod was measured by flow cytometry. 5×10^4 HUVEC were seeded in 24-well/plates with 500 μL of complete medium. After 24 h, the cells were incubated for 1 h with 0.05 μM peptides. Competition experiments were carried out i) pre-incubating the cells for 1 h, before the rhod-peptide conjugates addition, with 5 μM un-conjugated aFLT1 peptide or 50 or 500 ng mL^{-1} VEGF₁₆₅ (Peprotech) or ii) co-incubating the cells with the peptides and 50 ng mL^{-1} VEGF₁₆₅. At the end of the incubation, the cells were washed, detached from the plates with trypsin (Life Technologies), centrifuged and re-suspended in Versene before measuring rhod fluorescence by flow cytometry. The blue laser at 488 nm was used as excitation source and the PE channel (564-606 nm) was selected for the detection of rhod fluorescence. 10^4 events/sample were acquired and analysed with the FACSDiva Software.

The internalization of aFLT1-conjugated and rhod -labeled NPs in HUVEC was evaluated by confocal microscopy using a SP5 laser-scanning microscope (Leica Microsystems). 9×10^4 cells were seeded in special tissue culture dishes for fluorescence microscopy (μ -Dish 35 mm, high, Ibidi GmbH), were allowed to growth for 24 h and then incubated for 1 h with 50 $\mu\text{g mL}^{-1}$ NPs in M200 culture medium. After incubation, the cells were washed twice with PBS with Ca^{2+} and Mg^{2+} and immediately inspected under the microscope using the 514 nm Argon laser as excitation source and detecting Rhod fluorescence in the range 560-600 nm. The acquired images were analysed using Image J software.

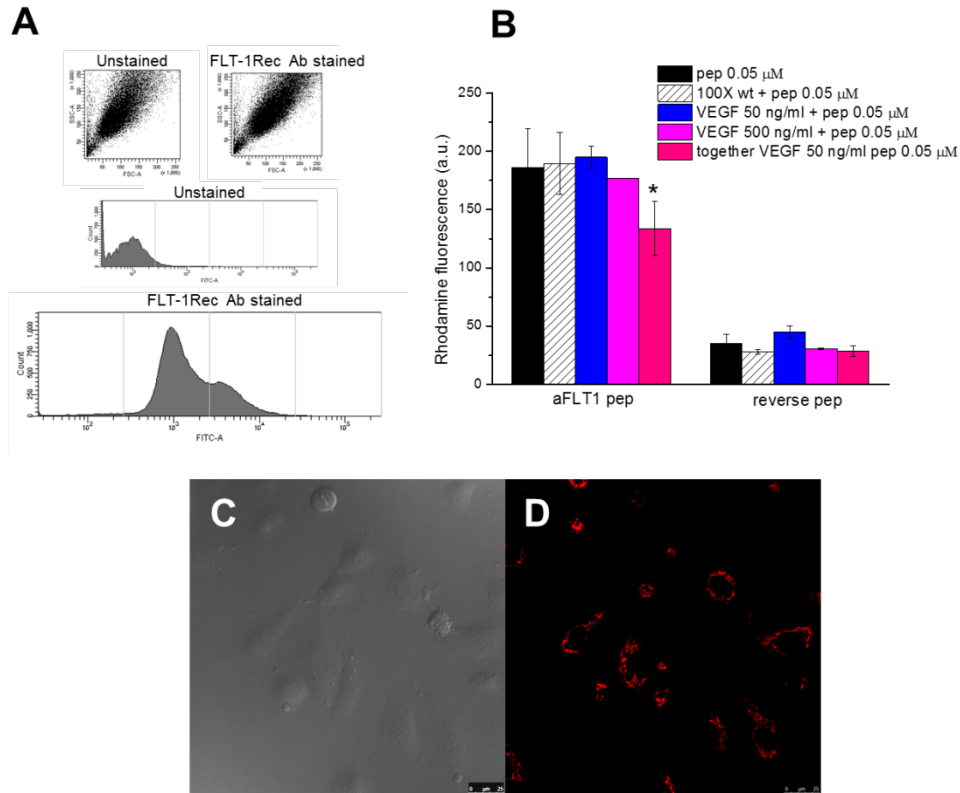


Figure S3. A) Expression of FLT-1 receptor on HUVEC cell surface measured by antibody recognition and flow cytometry. An anti FLT1 receptor specific antibody conjugated with FITC was used. B) Flow cytometry measurements of binding/uptake of rhodamine b-conjugated aFLT1 peptide and reverse-sequence of aFLT1 peptide in HUVEC cells after 1 h of cell incubation (black bars). For competition experiments cell were pre-incubated for 1 h before the addition of the rhodamine-peptide conjugates with: i) an excess of unlabeled aFLT1 peptide (white bars); ii) VEGF₁₆₅ 50 ng mL⁻¹ (blue bars); iii) 500 ng mL⁻¹ VEGF₁₆₅ (pink bars); or co-incubated with peptides and VEGF₁₆₅ 50 ng mL⁻¹ for 1 h (violet bars). **p*<0.005, *t* test vs. aFLT1 peptide alone. C-D) Confocal microscopy images of HUVEC cells incubated for 1 h with DBL_{aFLT1} NPs labeled with Rhod. C) Bright field D) NPs were clearly internalized in HUVEC as visible by Rhodamine red fluorescence inside the cells. Scale bars: 250 μ m.

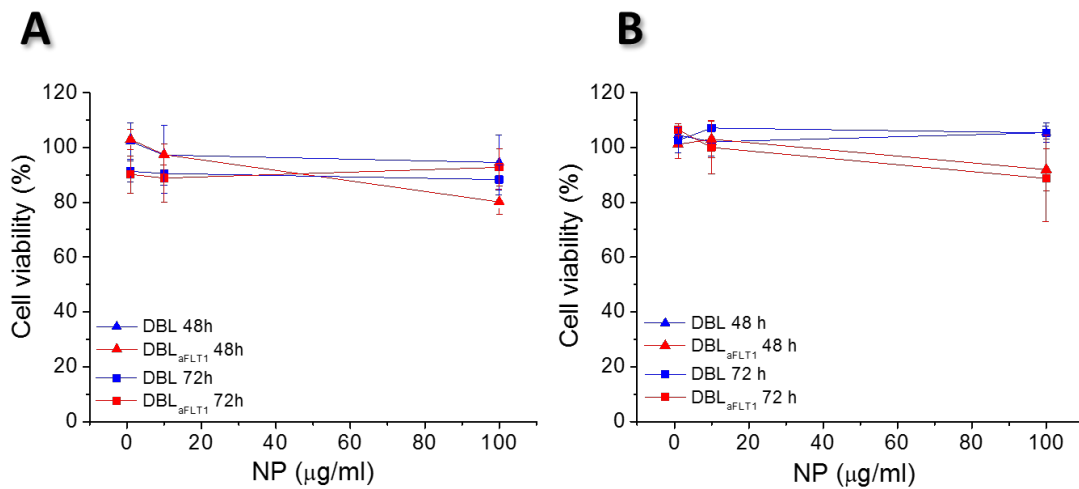


Figure S4. Cytotoxicity of empty DBL and DBL_{aFLT1} NPs toward HUVEC (A) and MDA-MB231 (B) cells measured by MTS assay after 48 or 72 h of incubation. Data are mean values \pm SD of at least two independent experiments carried out in triplicate.

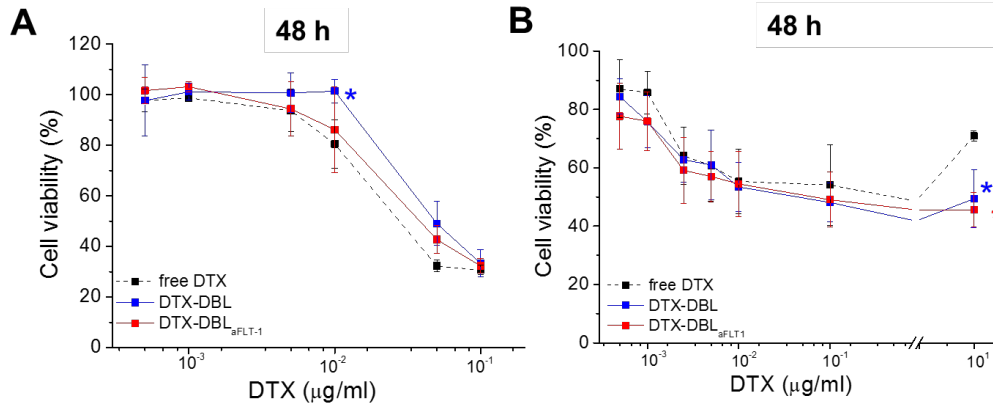


Figure S5. Cytotoxicity of DTX-DBL and DTX-DBL_{aFLT1} toward MDA-MB231 (A) and HUVEC (B) cells measured by MTS assay after 48 h of incubation. Data are mean values ± SD of at least two independent experiments carried out in triplicate.

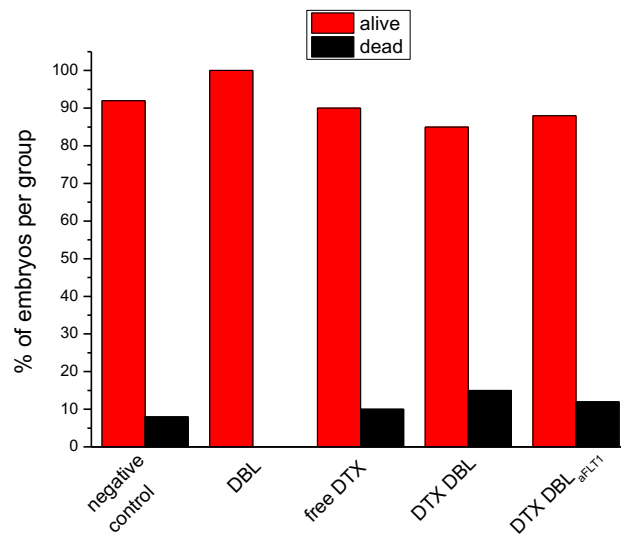


Figure S6. Percentages of surviving and dead chicken embryos for the different treatment group measured at E16, namely, 7 days after the beginning of the treatment

4 Improved outcome of docetaxel therapy using antiangiogenic folate-targeted biodegradable nanoparticles in *in vitro* and *in vivo* cancer models

Introduction

In the context of innovative nanomedicines for cancer treatment, multifunctional nanoparticles (NPs) delivering multiple drugs or exposing targeting moieties selective for a particular tumor recognition motif, have been deeply explored in order to: i) improve their accumulation in the desired pathological area, ii) reduce the systemic cytotoxicity of the delivered drugs, iii) attain synergic/additive effects, and iv) increase pharmacological response (1-3). Pharmacological effectiveness of the drug transported in NPs highly depends on the capability of NPs to reach the target site, thus overcoming the biological barriers encountered after administration (4,5). NP surfaces that expose specific motifs (folate, transferrin, RGD, albumin or hyaluronic acid) recognized by receptors overexpressed on cancer cells/vessels can aid NP accumulation in tumor, thus improving drug selectivity (6-9).

Amphiphilic block copolymers of poly(ethylene glycol) and poly(ϵ -caprolactone) (PEG-PCL), due to their high versatility, have shown an excellent capability to form a wide range of polymeric NPs, able to deliver in a sustained manner multiple drugs in combination, as well as to reach solid tumors through different targeting strategies (10-14). We have recently developed folate (Fol)-targeted core-shell NPs based on diblock PEG-PCL copolymers modified with Fol at the end of the PEG chain, able to selectively accumulate in cancer cells via folate receptor \square (FR) -mediated endocytosis (6,14).

The administration of conventional chemotherapeutic regimens in association with novel antiangiogenic drugs is considered an effective clinical strategy to potentiate therapeutic response, cancer patient outcome and survival (15,16), limiting the role of angiogenesis in tumor growth, invasion and metastasis (17,18). Nowadays, several anti-angiogenic drugs have been FDA-approved for cancer treatment, or are currently in preclinical/clinical evaluation (15,19), even if their efficacy is often limited by unfavorable pharmacokinetic, low tumor accumulation, and undesired immunological interaction. Thus, the delivery of antiangiogenic drugs with other chemotherapeutics through combined NPs represents a promising tool in the advanced anticancer therapies. We have recently reported the successful preparation of NPs made of PCL-PEG copolymers conjugated with an anti-FLT1 hexapeptide (GNQWFI) with anti-angiogenic properties (selectively binding VEGFR1 isoform) (aFLT1) (20,21), and carrying the poorly water-soluble antimitotic docetaxel (DTX) in the internal core. We have demonstrated that the presence of aFLT1 on NP surface inhibits angiogenesis *in vitro* as well as in chicken embryo chorioallantoic membranes (CAM) xenografted with triple negative breast cancer cells (11).

Here we propose a multifunctional nanosystem exposing both Fol as well as aFLT1 peptide to increase selectivity toward FR-positive cancer cells and to attain antiangiogenic activity in parallel. In particular, a combination of unmodified PEG-PCL and two derivatives modified with aFLT1 and Fol at PEG end group (aFLT1-PEG-PCL, Fol-PEG-PCL, respectively) were assembled into core-shell NPs through nanoprecipitation and DTX entrapped in the NP core. NPs were characterized in terms of colloidal and shell properties, and their antitumoral and anti-angiogenic efficacy was tested

in vitro in FR over-expressing KB cells and in *in vivo* zebrafish embryos xenografted with the same cancer cells.

Methods

Preparation of NPs

The anti-angiogenic peptide anti-FLT1 (aFLT1) was synthesized as previously described (11). Untargeted NPs (DBL) were prepared from mPEG-PCL co-polymer, folate-targeted NPs (DBL_{Fol}) were prepared from a mixture of mPEG-PCL and Fol-PEG-PCL (mPEG-PCL/Fol-PEG-PCL weight ratio 8:2), while aFLT1-decorated targeted NPs (DBL_{Fol/aFLT1}) were prepared from a mixture of mPEG-PCL with Fol-PEG-PCL and aFLT1-PEG-PCL (mPEG-PCL/Fol-PEG-PCL/aFLT1-PEG-PCL weight ratio 7:2:1). For the detailed synthesis and characterization of each co-polymers referred to(14,22). NPs were formed by solvent diffusion of an organic phase (10 mg of copolymers mixture in 1 mL of acetone) added dropwise in water (2 mL) under magnetic stirring (500 rpm). Addition of surfactant was not required. After solvent evaporation, NPs were filtered through 0.45 μm Phenex® filters (Phenomenex, USA). NPs loaded with DTX were prepared according to the procedure reported above and DTX was added in organic phase (10% w/w). Fluorescent NPs loaded with DiO for uptake studies were prepared with the same procedure and DiO was added in organic phase (1% w/w).

NP characterization

The hydrodynamic diameter (D_H), polydispersity index (PI) and zeta potential (ζ) of NPs were determined on a Zetasizer Nano ZS (Malvern Instruments Ltd). Results are reported as mean of three separate measurements of three different batches ($n = 9$) \pm standard deviation (SD).

The yield of NP production process was evaluated on an aliquot of NP dispersion by weighting the solid residue after freeze-drying. Results are expressed as the ratio of the actual NP weight to the theoretical polymer weight $\times 100 \pm \text{SD}$ ($n = 3$).

DTX loading inside NPs was assessed by placing 1 mg of NPs in 500 μL of acetonitrile under stirring and then 500 μL of water were added and the sample was filtered through a 0.45 μm filter (RC, Chemtek, Italy). DTX was analyzed by HPLC as reported in the ESI. The release of DTX was determined on 0.5 mg NPs dispersed in 0.5 mL of 10 mM phosphate buffer containing NaCl (137 mM) and KCl (2.7 mM) at pH 7.4 (PBS) at 37°C in a dialysis bag immersed in an external phase (5 mL) of the same medium. At predetermined times, 1 mL aliquots of the sample were collected and then analyzed by HPLC.

Fixed aqueous layer thickness (FALT) of NPs was measured by monitoring the influence of ionic strength on ζ . Different amounts of NaCl stock solutions were added to NPs dispersed in water (250 μg) and zeta potential of the samples measured. A plot of $\ln \zeta$ against $3.33 * [\text{NaCl}]^{0.5}$ gives a straight line where the slope represents the thickness of the shell in nm(23).

Cytotoxicity on monolayer cell cultures

Cell lines were obtained from American Type Culture Collection (ATCC, USA). HUVEC were cultured in Medium-200 supplemented with antibiotics (100 U/mL Penicillin G and 100 $\mu\text{g}/\text{mL}$ Streptomycin) and Low Serum Supplement Kit (Life Technologies) KB cells were grown in MEM supplemented with 10% FBS, while during the experiments with NPs were seeded in RPMI medium Fol-deficient. The viability of cells treated with increasing concentrations of DTX formulations was measured with the MTS assay, as explained in the supplementary methods.

Generation of spheroids and cytotoxicity measurements

Multicellular spheroids of KB cells were generated using the liquid overlay method, as previously reported (24). After 3 days of growth the spheroids had reached a diameter of about 500 μm and were used for the following experiments.

For cytotoxicity, spheroids were incubated for 48 or 72 h with 100 μL of fresh medium containing 10 % FBS and increasing concentration of free DTX or DTX-loaded NPs. At the end of incubation times, cell viability was measured using the CellTiter-Glo® 3D Cell Viability Assay (Promega) as previously reported (25). During the experiment, the spheroid morphological changes were monitored with a bright field microscope (DMI6000B, Leica) equipped with a DCF365FX camera.

NP penetration in spheroids

Three-days old KB spheroids were treated for 48 h with 50 $\mu\text{g}/\text{mL}$ of DiO-loaded NPs. The localization/penetration of NPs was evaluated by confocal microscopy (Leica SP5) by transferring the spheroids from 96-well plates to 35 mm cell imaging dishes and washing them twice with PBS before visualization. Images of about 20 different focal planes (z-stack 10 μm) were acquired from the top to the bottom of the spheroid using a 10X objective. DiO fluorescence was revealed using a 488 nm laser as excitation source and emission filters set from 505 to 550 nm. Maximum projection images were obtained with the software LAS AF Lite by superimposing the images of the 20 acquired focal planes. Furthermore, a 3D reconstruction of the distribution of the fluorescence signal in the equatorial plane of spheroids was obtained using the software ImageJ.

Zebrafish handling and xenotransplantation

Experiments were performed at the Zebrafish Facility of the University of Padova, under ethical authorization 407/2015-PR. Embryos were obtained from natural spawning of *casper* mutants (*a9-w2* double mutant line; ZFIN IDs: ZDB-ALT-980203-444, ZDB-ALT-990423-22) and *fli1a:EGFP* transgenic adults (ZFIN ID: ZDB-ALT-011017-8), raised according to standard protocols (26) and staged according to Kimmel et al. (26). For xenotransplantation, embryos were mechanically dechorionated at 2 dpf (days post-fertilization), anesthetized with 0.16 mg/ml tricaine and placed along the lanes of a microinjection mold, immersed in 2% methylcellulose/fish-water. KB cells were suspended at a density of $1 \times 10^6/\text{mL}$ and stained with 5 $\mu\text{g}/\text{ml}$ of DiI Vybrant Cell-Labeling Solution (Molecular Probes) for 20 minutes at 37 °C. Stained cells were loaded into a glass capillary needle and microinjected into the yolk (about 100 cells/embryo), using a WPI PicoPump apparatus. 24 h after tumor transplantation (3 dpf), embryos were microinjected using the same procedures described above with aqueous solution of phenol red (control), free DTX, DTX nanoformulations (DTX-DBL, DBL_{Fol} , $\text{DBL}_{\text{Fol/aFLT1}}$), empty $\text{DBL}_{\text{Fol/aFLT1}}$. Each embryo was injected with a DTX dose of about 2.5 ng; each experimental group of treatment was constituted of 25 embryos. Xenotransplanted embryos were grown at 33 °C and monitored daily starting from the injection day up to 1-week post-injection (experimental endpoint, 9 dpf). As important controls, embryos not injected with KB cells but only with DTX formulations were observed in parallel. Analyses included mortality rate, *in situ* (yolk) or metastatic (extra yolk) cancer cell location, and tumor size reduction evaluation, performed by cell counting/signal quantification using ImageJ software. Imaging was performed using a Leica MZFLIII fluorescence-dissecting microscope equipped with a Leica DFC7000T camera. For the analysis of neo-angiogenesis, the *fli1a:EGFP* transgenic line was used, having blood vessels and micro-vessels visible in green fluorescence. The

embryos (2 dpf) were injected with KB cells and 1 h later with DTX nanoformulations and tumor and blood vessels analyzed by fluorescence microscopy 48 h later

Results and discussion

NP preparation and characterization

We employed a mixture of PCL-PEG copolymers modified at the PEG end chain with either aFLT1 or Fol to produce multifunctional NPs with double decoration (DBL_{Fol/aFLT1}) (**Figure 1A**). For comparison purposes, NPs were prepared with PEG-PCL (DBL), with aFLT1-PEG-PCL/PEG-PCL (DBL_{aFLT1}) or Fol-PEG-PCL/PEG-PCL (DBL_{Fol}). NPs loaded or not with DTX were formed by solvent diffusion/evaporation method and DTX was encapsulated in the hydrophobic PCL core. Overall properties of the NPs are reported in **Table 1**.

Table 1. Properties of unloaded and DTX-loaded NPs

Formulation	D _H (nm ± SD ^a)	PI	ζ (mV ± SD)	Yield (%± SD)	DTX Actual loading (mg DTX/100 mg NPs)	DTX Entrapment Eff. (%)
DBL	78±2	0.1	-12±0.1	68±4	-	-
DBL _{Fol}	84±5	0.1	-18±6	52±3	-	-
DBL _{Fol/aFLT1}	101±8	0.2	-10±3	54±1	-	-
DTX-DBL	92±5	0.2	-10±1	72±6	8.8±0.9	98 ± 4
DTX-DBL _{Fol}	84±8	0.1	-19±4	61±4	8.7±1.5	98 ± 10
DTX-DBL _{Fol/aFLT1}	101±5	0.1	-9±2	55±3	8.5±0.6	96 ± 6

All the formulations showed a D_H between 78 and 101 nm, a low polydispersity index and a negative ζ. DTX entrapment in NPs at 10% theoretical loading was almost complete, without any significant difference based on the copolymer material employed and, highlighting the capability of these NPs to encapsulate lipophilic drugs in the hydrophobic PCL core despite the presence of decoration motifs.

The thickness of the external hydrophilic PEG shell of NPs was evaluated by FALT, measuring the values of ζ in NaCl solutions at different concentrations. The shell thickness was lower for untargeted NPs (~2.5 nm), compared to DBL_{Fol} (~2.7 nm) and DBL_{Fol/aFLT1} NPs (~3.1 nm), thus suggesting that the presence of surface modifiers only slightly impact the conformation of the PEG shell (**Figure 1B**).

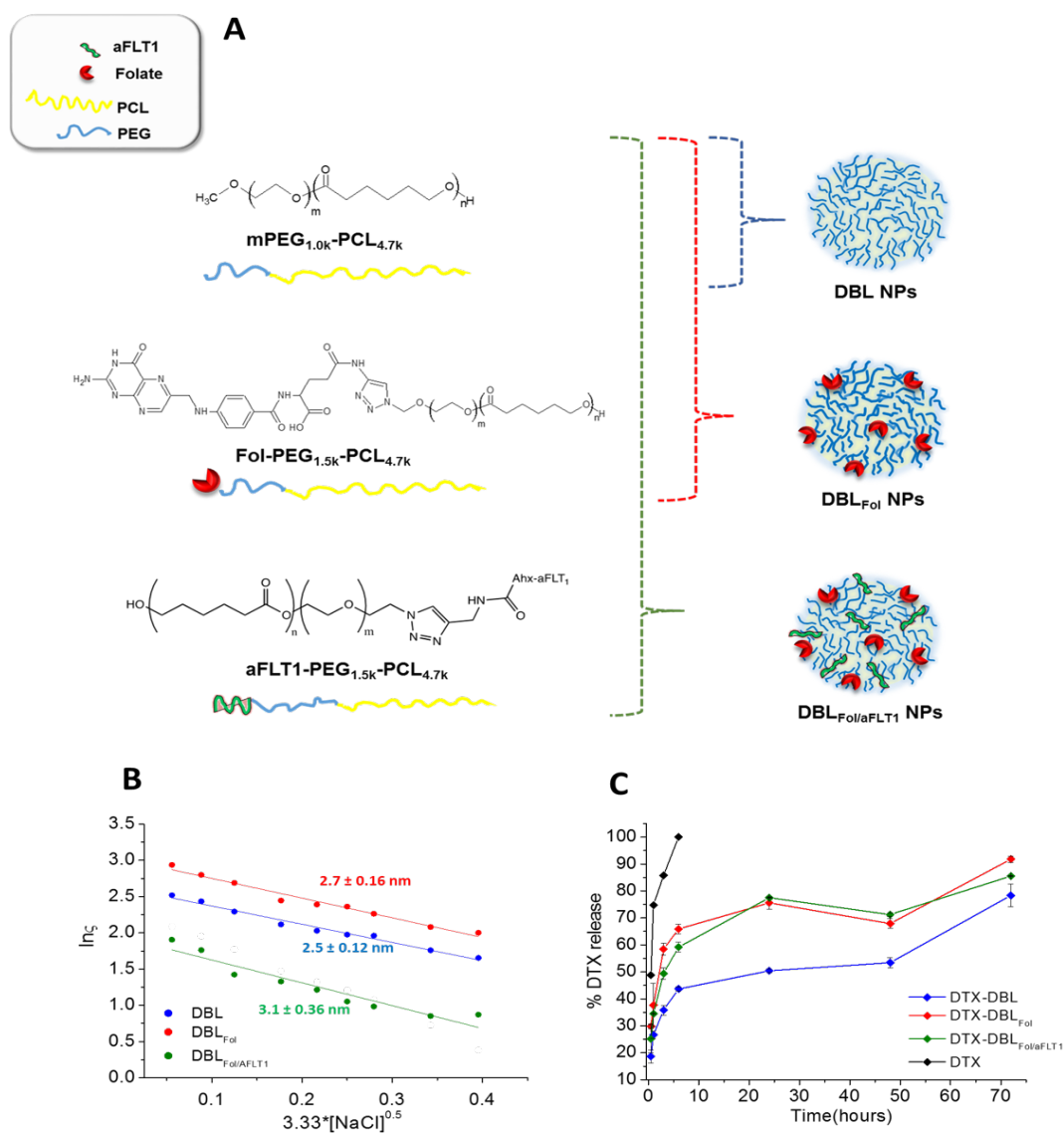


Figure 1. A) NPs composition; B) Representative FALD measurements: the slope of the straight line represents the thickness of the outer hydrophilic shell expressed in nm; C) DTX release from NPs in PBS 10 mM pH 7.4, at 37 °C evaluated by dialysis method. Results are the means \pm SD of three measurements obtained on three different NPs batches.

The release of DTX from NPs was evaluated in 10 mM PBS, at pH 7.4 and 37 °C, through the dialysis method (**Figure 1C**). In the case of untargeted NPs (DBL), we observed a fast release of about 40% of the drug in the first 6 h followed by a slow release rate indicating that NPs are able to sustain drug release along time as compared to free drug (100% release in 6 h) (10,12). NPs modified with Fol or Fol/aFLT1 showed a fast initial DTX release which was again sustained until 70 h. Finally, NPs showed an excellent stability in simulated physiological media (PBS, RPMI cell culture medium added with 10% FBS and human plasma) (**Figure S1**) until 48 h of incubation, with only a tendency to a slight increase of size along time.

Anti-angiogenic and cytotoxic activity of NPs in monolayer cell culture

In vitro endothelial tube formation assay in HUVEC cells was assessed to confirm that the antiangiogenic effect of NPs previously demonstrated (11). As shown in **Figure 2A-B**, the presence of Fol on

DBL_{Fol/aFLT1} did not alter the capability of the peptide to reduce the number of formed endothelial junctions and master segments and to abolish mesh formation in HUVEC cells. No anti-angiogenic effect was observed for DBL_{Fol}, confirming that the observed activity is completely ascribed to aFLT1.

Empty DBL_{Fol} and DBL_{Fol/aFLT1} NPs were not cytotoxic toward HUVEC and KB cells up to 100 $\mu\text{g/mL}$ and 72 h of incubation as measured by MTS assay (data not shown). On the contrary, when DTX was loaded inside NPs (**Figure 2C-D**) a concentration- and time-dependent cell viability reduction was measured in both cell lines, despite they showed different DTX sensitivity especially in the first 48 h of cell incubation. For instance, the IC₅₀ value for free DTX in KB cells was 0.0031 $\mu\text{g/mL}$ while that in HUVEC was almost 100-times higher (0.4863 $\mu\text{g/mL}$). Focusing on the presence of Fol on NP surface, cell viability curves of DTX-DBL_{Fol} and DTX-DBL_{Fol/aFLT1} vs. DTX-DBL indicated that the cytotoxicity of DTX was not modified by surface decoration, probably due to the poor contribution of FR-mediated NP endocytosis with respect to aspecific endocytosis, as we previously reported for monolayer cell cultures (14).

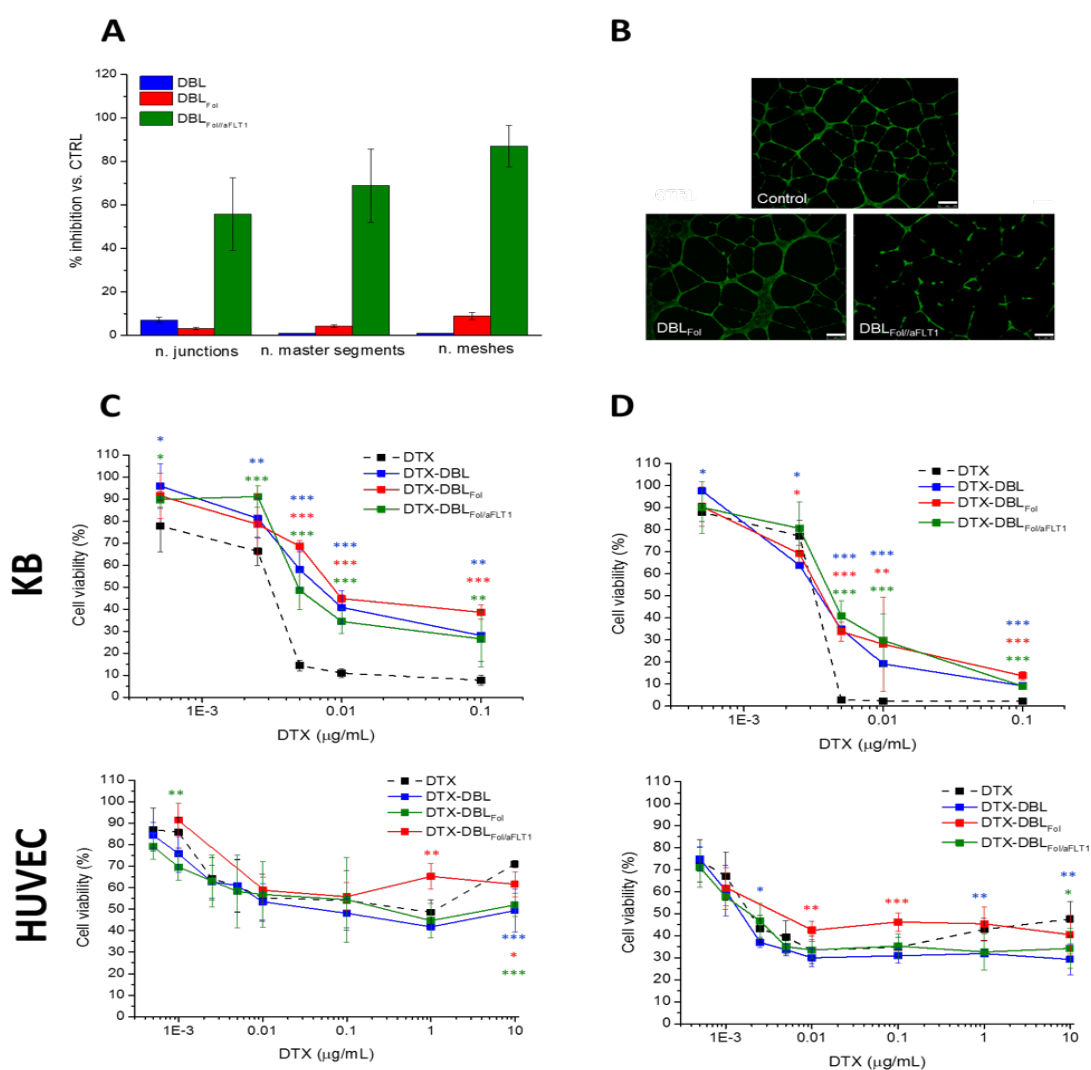


Figure 2. *In vitro* endothelial tube formation assay in HUVEC: A) Inhibition of tube formation caused by incubation for 18 h with 50 $\mu\text{g mL}^{-1}$ of NPs and B) representative fluorescence images of tubes. Scale bars: 250 μm .

Cytotoxicity of DTX-NPs vs free DTX in KB and HUVEC cells after C) 48 h or D) 72 h of incubation. Data are mean values \pm SD of at least three independent experiments carried out in triplicate. *p value<0.05, vs. free DTX; **p value<0.01, ***p<0.001, vs. free DTX (*Student's t-test*).

Conclusions

In recent years, there has been an explosive development of innovative nanomedicines, considered as revolutionary tools in cancer diagnosis and therapy (30), in order to avoid unspecific drug biodistribution and reduce the systemic cytotoxicity exerted by the majority of chemotherapeutics. Among the so called 'actively targeted NPs', able to specifically accumulate in malignancies, NPs decorated with Fol demonstrated high capacity of selective delivery of chemotherapeutics both *in vitro* as well as *in vivo* (31). For instance, we have demonstrated that core-shell NPs based on diblock PEG-PCL copolymers modified with Fol are able to selectively accumulate in cancer cells *via* FR-mediated endocytosis (6,14). The versatility of PEG-PCL block copolymers allowed us to propose different NPs for mono- or combined cancer therapy (12,13). We have recently prepared NPs conjugated with the anti-angiogenic anti-FLT1 peptide and transporting DTX in the PCL core. These NPs (DTX DBL_{aFLT1}) showed increased antitumoral effects in an *in vivo* model of breast tumor (11). Thus, herein we aim at further strength DTX DBL_{aFLT1} NP potential by engrafting Fol on their surface to promote the selective uptake in FR-positive cancer cells. DTX-DBL_{Fol/aFLT1} colloidal properties and stability in biological fluids, did not significantly differ with respect to NPs decorated with only Fol or aFLT1, thus highlighting that the synthesized copolymers, despite chemical modifications, were well prone to form homogeneous mixtures in organic solvent, without affecting NP structure and surface exposition of the functional moieties during nanoprecipitation. Importantly, the impressive capacity of impairing *in vitro* endothelial tube formation observed with DBL_{aFLT1} (11) was not affected by the addition of Fol on DBL_{Fol/aFLT1} NPs (**Figure 2A, B**), confirming again the high anti-angiogenic potential of aFLT1-decorated NPs. The *in vitro* cytotoxicity of DTX formulations was assessed, not only in FR positive cells cultured as monolayer but also in avascular spheroids, in order to mimic more closely the *in vivo* tridimensional tumor architecture and the enrichment in extracellular matrix components, which may affect drug distribution and efficacy (<https://www.ncbi.nlm.nih.gov/pubmed/29184400>). Unlike expectations, the targeting moiety on DTX-DBL_{Fol/aFLT1} NPs did not bring significant improvements on KB cell killing compared to DTX or DTX-untargeted NPs, nor in monolayers nor in tridimensional cultures (**Figure 2, 3**). Nonetheless, studies on NP uptake and distribution in spheroids indicated a different pattern of penetration driven by the surface moieties, and a significantly increased accumulation for Fol-NPs with respect to the unmodified counterpart (**Figure 4**). The unimproved cytotoxicity despite the increased uptake of Fol-decorated NPs was in accord with our previous results (14), which indicated that FR-mediated endocytosis is not the unique and prevalent mechanism of NP/drug internalization. Thus, even if a different pattern of NP internalization was observed in spheroids, this did not very likely correlate with a different extent of internalized drug and thus different overall cytotoxic profile, at least in our *in vitro* models.

The choice of using *Danio rerio* embryos xenotransplanted with KB cells as a preliminary *in vivo* models to study tumor regression and angiogenesis determined by our DTX formulations was dictated by several factors: i) the transparency of the embryo which allows easy observation of tumor development, angiogenesis, metastasis in real time; ii) high physiologic and genetic similarity to mammals (32); iii) low cost of maintenance and easy of manipulation with respect to rodents; iv) immature immune system up to 11 dpf thus avoiding the rejection of the xenotransplant (33); v) the availability of transgenic models

over-expressing fluorescent proteins (e.g. vascular proteins) offering a tool to monitor neo-angiogenesis(34,35). Differently from the *in vitro* observations, cytotoxicity and tumor regression studies in zebrafish highlighted improvements of DTX-DBL_{Fol/aFLT1} NP-based therapy with respect to free DTX with a significant increased capacity of tumor reduction (**Figure 5**) and decreased systemic toxicity of DTX (**Figure S3**). Importantly, we demonstrated that the improved antitumor effects of DTX-DBL_{Fol/aFLT1} is determined by DTX cytotoxicity combined with a significant anti-angiogenic capacity, documented by inhibition of formation of tumor blood vessels in the SIV region, by the presence of aFLT1 on NP surface (**Figure 6**). Of note, the treatment with free DTX had dramatic consequences on embryo survival (**Figure S3**) and correct vessel development (**Figure 6C**), thus demonstrating that the presence of the delivery system, besides improving drug solubility, limits the systemic toxicity very likely by changing the drug release profile. Importantly, while with the *in vitro* models we were unable to measure any active role of the Fol moiety, the *in vivo* experiments highlighted a decreased spread of metastasis when DTX DBL_{Fol} NPs were administered to xenografted zebrafish (**Figure S4**). The latter observation stress the importance of the *in vivo* studies to test NP efficacy, even using experimental models alternative to rodents as zebrafish, since also tridimensional *in vitro* models as spheroids, are sometimes only poorly predictive of *in vivo* NP/drug behaviors.

In conclusions, we have herein reported the successful production of PEGylated NPs engrafted with Fol and aFLT1 and defined their antitumor and antiangiogenic potential *in vitro* and *in vivo*. Overall, the significant antiangiogenic activity of aFLT1 engrafted on DBL_{Fol/aFLT1}, observed *in vitro* but also in xenografted zebrafish embryos, potentiated the antitumor effect of DTX, and the nanocarrier with the associated Fol moiety limited DTX systemic cytotoxicity and metastasis spread, respectively.

References

- 1 J. Kydd, R. Jadia, P. Velpurisiva, A. Gad, S. Paliwal, P. Rai, Targeting Strategies for the Combination Treatment of Cancer Using Drug Delivery Systems, *Pharmaceutics*, 9 (2017).
- 2 J.A. Kemp, M.S. Shim, C.Y. Heo, Y.J. Kwon, "Combo" nanomedicine: Co-delivery of multi-modal therapeutics for efficient, targeted, and safe cancer therapy, *Advanced drug delivery reviews*, 98 (2016) 3-18.
- 3 G. Seeta Rama Raju, L. Benton, E. Pavitra, J.S. Yu, Multifunctional nanoparticles: recent progress in cancer therapeutics, *Chemical communications*, 51 (2015) 13248-13259.
- 4 F. Danhier, O. Feron, V. Preat, To exploit the tumor microenvironment: Passive and active tumor targeting of nanocarriers for anti-cancer drug delivery, *Journal of controlled release : official journal of the Controlled Release Society*, 148 (2010) 135-146.
- 5 E. Blanco, H. Shen, M. Ferrari, Principles of nanoparticle design for overcoming biological barriers to drug delivery, *Nature biotechnology*, 33 (2015) 941-951.
- 6 S.A. Kularatne, P.S. Low, Targeting of nanoparticles: folate receptor, *Methods in molecular biology*, 624 (2010) 249-265.

- 7 Y. Zhong, F. Meng, C. Deng, Z. Zhong, Ligand-directed active tumor-targeting polymeric nanoparticles for cancer chemotherapy, *Biomacromolecules*, 15 (2014) 1955-1969.
- 8 Q. Tu, Y. Zhang, R. Liu, J.C. Wang, L. Li, N. Nie, A. Liu, L. Wang, W. Liu, L. Ren, X. Wang, J. Wang, Active drug targeting of disease by nanoparticles functionalized with ligand to folate receptor, *Current medicinal chemistry*, 19 (2012) 3152-3162.
- 9 A.K. Pearce, R.K. O'Reilly, Insights into Active Targeting of Nanoparticles in Drug Delivery: Advances in Clinical Studies and Design Considerations for Cancer Nanomedicine, *Bioconjugate chemistry*, 30 (2019) 2300-2311.
- 10 F. Ungaro, C. Conte, L. Ostacolo, G. Maglio, A. Barbieri, C. Arra, G. Misso, A. Abbruzzese, M. Caraglia, F. Quaglia, Core-shell biodegradable nanoassemblies for the passive targeting of docetaxel: features, antiproliferative activity and in vivo toxicity, *Nanomedicine : nanotechnology, biology, and medicine*, 8 (2012) 637-646.
- 11 C. Conte, F. Moret, D. Esposito, G. Dal Poggetto, C. Avitabile, F. Ungaro, A. Romanelli, P. Laurienzo, E. Reddi, F. Quaglia, Biodegradable nanoparticles exposing a short anti-FLT1 peptide as antiangiogenic platform to complement docetaxel anticancer activity, *Materials science & engineering. C, Materials for biological applications*, 102 (2019) 876-886.
- 12 C. Conte, F. Ungaro, G. Maglio, P. Tirino, G. Siracusano, M.T. Sciortino, N. Leone, G. Palma, A. Barbieri, C. Arra, A. Mazzaglia, F. Quaglia, Biodegradable core-shell nanoassemblies for the delivery of docetaxel and Zn(II)-phthalocyanine inspired by combination therapy for cancer, *Journal of controlled release : official journal of the Controlled Release Society*, 167 (2013) 40-52.
- 13 G. Palma, C. Conte, A. Barbieri, S. Bimonte, A. Luciano, D. Rea, F. Ungaro, P. Tirino, F. Quaglia, C. Arra, Antitumor activity of PEGylated biodegradable nanoparticles for sustained release of docetaxel in triple-negative breast cancer, *International journal of pharmaceutics*, 473 (2014) 55-63.
- 14 A. Venuta, F. Moret, G. Dal Poggetto, D. Esposito, A. Fraix, C. Avitabile, F. Ungaro, M. Malinconico, S. Sortino, A. Romanelli, P. Laurienzo, E. Reddi, F. Quaglia, Shedding light on surface exposition of poly(ethylene glycol) and folate targeting units on nanoparticles of poly(epsilon-caprolactone) diblock copolymers: Beyond a paradigm, *European journal of pharmaceutical sciences : official journal of the European Federation for Pharmaceutical Sciences*, 111 (2018) 177-185.
- 15 F. Shojaei, Anti-angiogenesis therapy in cancer: current challenges and future perspectives, *Cancer letters*, 320 (2012) 130-137.
- 16 A.M.E. Abdalla, L. Xiao, M.W. Ullah, M. Yu, C. Ouyang, G. Yang, Current Challenges of Cancer Anti-angiogenic Therapy and the Promise of Nanotherapeutics, *Theranostics*, 8 (2018) 533-548.
- 17 L.M. Ellis, W. Liu, F. Fan, N. Reinmuth, R.M. Shaheen, Y.D. Jung, S. Ahmad, Role of angiogenesis inhibitors in cancer treatment, *Oncology*, 15 (2001) 39-46.

- 18 M. Rajabi, S.A. Mousa, The Role of Angiogenesis in Cancer Treatment, *Biomedicines*, 5 (2017).
- 19 J.M. Ebos, R.S. Kerbel, Antiangiogenic therapy: impact on invasion, disease progression, and metastasis, *Nature reviews. Clinical oncology*, 8 (2011) 210-221.
- 20 D.G. Bae, T.D. Kim, G. Li, W.H. Yoon, C.B. Chae, Anti-flt1 peptide, a vascular endothelial growth factor receptor 1-specific hexapeptide, inhibits tumor growth and metastasis, *Clinical cancer research : an official journal of the American Association for Cancer Research*, 11 (2005) 2651-2661.
- 21 C. Fischer, M. Mazzone, B. Jonckx, P. Carmeliet, FLT1 and its ligands VEGFB and PlGF: drug targets for anti-angiogenic therapy?, *Nature reviews. Cancer*, 8 (2008) 942-956.
- 22 L. Castelani, J.R.P. Arcaro, J.E.P. Braga, A.S. Bosso, Q. Moura, F. Esposito, I.P. Sauter, M. Cortez, N. Lincopan, Short communication: Activity of nisin, lipid bilayer fragments and cationic nisin-lipid nanoparticles against multidrug-resistant *Staphylococcus* spp. isolated from bovine mastitis, *Journal of dairy science*, 102 (2019) 678-683.
- 23 T.K. Endres, M. Beck-Broichsitter, O. Samsonova, T. Renette, T.H. Kissel, Self-assembled biodegradable amphiphilic PEG-PCL-IPEI triblock copolymers at the borderline between micelles and nanoparticles designed for drug and gene delivery, *Biomaterials*, 32 (2011) 7721-7731.
- 24 E. Gaio, D. Scheglmann, E. Reddi, F. Moret, Uptake and photo-toxicity of Foscan(R), Foslip(R) and Fospeg(R) in multicellular tumor spheroids, *Journal of photochemistry and photobiology. B, Biology*, 161 (2016) 244-252.
- 25 E. Gaio, A. Guerrini, M. Ballestri, G. Varchi, C. Ferroni, E. Martella, M. Columbaro, F. Moret, E. Reddi, Keratin nanoparticles co-delivering Docetaxel and Chlorin e6 promote synergic interaction between chemo- and photo-dynamic therapies, *Journal of photochemistry and photobiology. B, Biology*, 199 (2019) 111598.
- 26 M. Westerfield, *The zebrafish book. A guide for the laboratory use of zebrafish (Danio rerio)*, 4th ed ed., Univ. of Oregon Press, Eugene., 2000.
- 27 C.B. Kimmel, W.W. Ballard, S.R. Kimmel, B. Ullmann, T.F. Schilling, Stages of embryonic development of the zebrafish, *Developmental dynamics : an official publication of the American Association of Anatomists*, 203 (1995) 253-310.
- 28 G. Gaudenzi, M. Albertelli, A. Dicitore, R. Wurth, F. Gatto, F. Barbieri, F. Cotelli, T. Florio, D. Ferone, L. Persani, G. Vitale, Patient-derived xenograft in zebrafish embryos: a new platform for translational research in neuroendocrine tumors, *Endocrine*, 57 (2017) 214-219.

- 29 J.Q. Wu, J. Zhai, C.Y. Li, A.M. Tan, P. Wei, L.Z. Shen, M.F. He, Patient-derived xenograft in zebrafish embryos: a new platform for translational research in gastric cancer, *Journal of experimental & clinical cancer research* : CR, 36 (2017) 160.
- 30 M. Chidambaram, R. Manavalan, K. Kathiresan, Nanotherapeutics to overcome conventional cancer chemotherapy limitations, *Journal of pharmacy & pharmaceutical sciences* : a publication of the Canadian Society for Pharmaceutical Sciences, Societe canadienne des sciences pharmaceutiques, 14 (2011) 67-77.
- 31 B. Bahrami, M. Mohammadnia-Afrouzi, P. Bakhshaei, Y. Yazdani, G. Ghalamfarsa, M. Yousefi, S. Sadreddini, F. Jadidi-Niaragh, M. Hojjat-Farsangi, Folate-conjugated nanoparticles as a potent therapeutic approach in targeted cancer therapy, *Tumor Biol*, 36 (2015) 5727-5742.
- 32 T.P. Barros, W.K. Alderton, H.M. Reynolds, A.G. Roach, S. Berghmans, Zebrafish: an emerging technology for in vivo pharmacological assessment to identify potential safety liabilities in early drug discovery, *British journal of pharmacology*, 154 (2008) 1400-1413.
- 33 M. Mimeault, S.K. Batra, Emergence of zebrafish models in oncology for validating novel anticancer drug targets and nanomaterials, *Drug discovery today*, 18 (2013) 128-140.
- 34 C. Zhao, H. Yang, H. Shi, X. Wang, X. Chen, Y. Yuan, S. Lin, Y. Wei, Distinct contributions of angiogenesis and vascular co-option during the initiation of primary microtumors and micrometastases, *Carcinogenesis*, 32 (2011) 1143-1150.
- 35 K. Stoletov, H. Kato, E. Zardouzian, J. Kelber, J. Yang, S. Shattil, R. Klemke, Visualizing extravasation dynamics of metastatic tumor cells, *Journal of cell science*, 123 (2010) 2332-2341.

5 Nanoparticles decorated with folate based on a site-selective α CD-rotaxanated PEG-PCL copolymer for targeted cancer therapy

Introduction

Nanoparticles (NPs) made up of biodegradable block copolymers have attracted significant attention in the field of innovative anticancer therapies. The most common approach to improve their accumulation in tumor cells remains surface decoration with targeting ligands recognizing specific receptors that are over-expressed on cancer cell membrane. Nevertheless, a great challenge remains the effective exposition of targeting molecule on NPs surface (1, 2).

In a previous work (3), we focused on poly(ethylenglycol)-poly(ϵ -caprolactone) (mPEG-PCL) NPs and their folate-targeted version (Fol-PEG-PCL) to encourage accumulation in cancer cells overexpressing folate receptor (FR) α . We demonstrated that NPs prepared with a mixture of mPEG-PCL with 1 kDa PEG chains and Fol-PEG-PCL with 1.5 kDa PEG segment ensure that folate-bearing NPs are accumulated in KB cancer cells via FR α -mediated endocytosis. The different length of PEG segment in Fol-PEG-PCL enhances folate exposition on NPs surface. In the present work, we prepared a Fol-PEG_{1.5k}-PCL_{4k} copolymer in which the PEG segment is threaded with α -cyclodextrins (α CDs) to further promote surface exposition of folate. Supramolecular structures consisting in macrocycles as CDs threaded on a linear polymer and blocked at the ends by bulky groups are called polyrotaxanes (4). Conversely, in absence of end stoppers, they are referred to as pseudo-polyrotaxanes. The specific nomenclature is based on the number of CD per polymer chain, when note, which is reported in square brackets (i.e., [2]rotaxane with one macrocycle and one axis, [3]rotaxane with two macrocycles per axis, and so on up to 5) (5). When the number of macrocycles is higher or unknown, they are simply termed polyrotaxanes. The term “inclusion complex” (IC) is referred to the polymer chain included not covalently within the macrocycle cavity.

A pioneering study by Harada and Kamachi discovered an inclusion complex consisting of many α CDs and PEG that resulted in the formation of polypseudorotaxanes (6). Since then, CD-based polyrotaxanes derived from the biocompatible PEG have been developed to encompass a broad range of diverse medical applications, from erodible hydrogels to drug nanocarriers (7,8). NPs for drug delivery were fabricated from self-assembling amphiphilic polyrotaxanes, obtained by conjugating hydrophobic moieties to PEG terminal groups (9). Targeting moieties as ligands were conjugated to the hydroxyl groups of CDs to enhance ligand-receptor recognition. It was reported that the flexible motion of CDs, which could slide along and rotate around the PEG chains, avoided the mismatch of ligand-receptor interaction (10). In our approach, we based on the hypothesis that, since α CDs locked on the PEG block impart a more extended conformation to chains, NPs fabricated with rotaxanated copolymers will expose Fol-functionalized PEG brushes on their surface, favoring Fol exposition. To date, α CD-threaded PEG polyrotaxanes (PEG α CD) have been prepared directly from PEG diol or by first converting the hydroxyl end groups to more reactive functional groups. Hence, PEG polyrotaxanes bearing identical bulky terminal groups were obtained. Here, we have developed a new strategy to convert a α,ω -heterobifunctional-PEG(α CD)

pseudo-rotaxane to a Fol-PEG(α CD)-PCL polyrotaxane, taking advantage of the different terminal functional groups of-PEG.

PCL with 4 kDa molecular weight, able to act as a bulky stopper, was bonded via “click” chemistry on one side, whereas Fol was bonded via a classical nucleophilic substitution on the other side.

Rotaxanated copolymers were analyzed by solubility tests, Fourier Transform Infrared (FTIR), ^1H NMR and 2D Diffusion Ordered (DOSY) spectroscopies, Gel Permeation Chromatography (GPC), Differential Scanning Calorimetry (DSC), Wide Angle X-ray diffraction (WAXD), Thermogravimetric analysis (TGA), and polarized optical microscopy. The composition was determined by elemental analysis. NPs were prepared by nanoprecipitation and characterized for size, polydispersity, surface charge and PEG shell thickness. The extent of PEG and α CD on NPs surface was calculated through ^1H NMR. Finally, uptake studies on KB cancer cells overexpressing FR α were carried out to verify the occurrence folate-mediated endocytosis of NPs.

Experimental

Materials

Poly(ethyleneglycole), HO-PEG-OH, with Mn 1,5 kDa (PEG_{1,5k} Sigma-Aldrich, Milan, Italy) and monomethoxy-poly(ethyleneglycole), CH₃O-PEG-OH, with Mn 1,0 kDa (mPEG_{1,0k}, Nanocs Inc., New York, USA) were dehydrated by azeotropic distillation with dry toluene in a Dean-Stark trap. α -cyclodextrine (α CD) and all reagents were purchased from Sigma-Aldrich (Milan, Italy). ϵ -caprolactone (CL) was distilled over CaH₂ under vacuum. Tin(II) bis(2-ethylhexanoate) (Sn(Oct)₂), tosyl chloride (TsCl), folic acid (Fol), sodium hydride and sodium azide were used without further purification. 3-butyn-1-ol was anhydridified through silica gel. Copper wires (Carlo Erba, Milan, Italy) were treated with H₂SO₄ for 3 minutes just before reaction, repeatedly washed with water and methanol, and finally dried under vacuum in an oven for 30 minutes at 60°C.

Synthesis of TsO-PEG_{1,5k}-N₃

Monoazido-PEG_{1,5k} (N₃-PEG_{1,5k}-OH) was prepared as described in a previous paper (Venuta et al. 2018). In a round flask under argon stream, 1.2 g (0.8 mmol) of N₃-PEG_{1,5k}-OH were dissolved under stirring in 15 mL of dry THF. 274 μL (2.0 mmol) of *N,N*-diethylethanamine (NEt₃) and 375 mg (2.0 mmol) of TsCl were added. The reaction was carried out at 25°C under vigorous stirring for 24 h. The solution was first filtered on paper, concentrated by rotovapor and then precipitated in cold n-hexane. After hexane removal, the product was dried under vacuum overnight (yield: 87.5%). ^1H NMR (d₆-DMSO, δ in ppm), 3.1-3.48 (m); 4,1-4.2 (t); 5.5-7.8(t).

Synthesis of Fol-targeted PEG-PCL copolymer (Fol-PEG_{1,5k}-PCL_{4k})

Folic acid was treated with NaH before reaction. 97.6 mg (0.22 mmol) of Fol and 8 mg (0.33 mmol) of dry NaH were dissolved in 3 mL of DMSO under Ar stream at T 45°C. The reaction was let to go on until complete H₂ evolution. In a second flask, 40 mg of TsO-PEG_{1,5k}-N₃ were dissolved in 3 mL of DMSO under Ar stream at T 45°C. 92 mg of Cu and 121.6 mg (0.03 mmol) of butynyl-PCL were then added under stirring. The folic acid solution was added dropwise. The reaction was carried out at T 45°C under vigorous stirring for 48 h. The solution was poured in 60 mL of acetone. After filtration, solvent was removed under vacuum to recover the product. Yield: 94%. Fol functionalization degree: 93%. ^1H NMR

(CDCl₃, δ in ppm): 3.6 (2H, t), 3.5 (127H, s, PEG backbone), 3.4 (2H, t), 1.29–1.78 (139H, m); 2.19–2.43 (82H, m), 3.92–4.21 (82H, t), 4.31 (2H, t); Mn of PCL evaluated by ¹H NMR = 4,6 kDa. Elemental analysis. Theoretical: C% 59.99; H% 8.55; (O+N)% 31.44. Found: C%56.8; H%8.8; (O+N)% 34.4

Preparation of TsO-PEG_{1.5k}(α CD)-N₃ pseudo-rotaxane

In a round flask, 10.2 g (10.5mmol) of α CD were dissolved in 80 mL of H₂O (milliQ) at room temperature in N₂ atmosphere under vigorous magnetic stirring for 20 min. The α CD solution was poured in a second flask containing a solution of 1.0 g (0.618 mmol) of TsO-PEG-N₃ in 40 mL of H₂O (milliQ) and then stirred overnight at room temperature (α CD concentration in the final solution: 8% w/v). White precipitate (IC formed between PEG and α CD) appeared after around 30 min. Water was removed at T 40°C under air stream for around 4 h, and the recovered product was put in a vacuum oven at T 40°C to remove residual water.

Synthesis of Fol-PEG_{1.5k}(α CD)-PCL_{4k} rotaxane

Two different protocols are reported. In the first case, the end-capping reagents were added simultaneously to the pseudo-rotaxane; in the second case, the end-capping reactions were performed in two separate steps. Since the pseudorotaxane was not purified from α CD excess, the number of α CD per PEG chain is unknown; as a consequence, the reagent/PEG stoichiometric ratio was set hypothesizing a full α CD coverage (which corresponds to α CD/PEG molar ratio: 17/1).

Synthesis of Fol-PEG_{1.5k}(α CD)-PCL_{4k} rotaxane by “one-step” endcapping (R1)

100 mg of TsO-PEG_{1.5k}(α CD)-N₃ pseudopolyrotaxane were dissolved in 3 mL of DMSO under Ar stream at T 45°C. 230 mg of Cu wires and 304 mg (0.08 mmol) of butynyl-PCL were then added under stirring. After complete dissolution, a solution of Fol (244 mg, 0.66 mmol) pretreated with NaH in 3 mL of DMSO as previously described was added dropwise. The reaction was carried out at T 45°C under vigorous stirring for 48 h. After mechanical removal of Cu wires, the solution was dialyzed against DMSO (membrane cut-off: 2000 Da) during two weeks. DMSO was removed and replaced by fresh solvent every day. The solution was then recovered from the dialysis tube, the solvent evaporated under N₂ stream, and the recovered product was finally dried under vacuum overnight. Yield 58.3%.Fol functionalization degree=94%. Elemental analysis: Theoretical (number of α CD calculated by NMR): C% 61.99; H% 8.79; (O+N) % 29.2; Found: C% 60.7, H% 8.7, (O+N)% 30.06. ¹H-NMR (d₆-DMSO, T 40°C, δ in ppm); PCL block: 1.3-1.5(t), 2.2(t),4.1(t); PEG block: 3.25(s) 3.51(s); α CD: 5.5(d), 5.35(s), 5.1(s), 4.6(m), 3.8(m), 3.65(m), 3.55(m), 3.39(m)

Synthesis of Fol-PEG_{1.5k}(α CD)-PCL_{4k} rotaxane by “two-steps” endcapping (R2)

100 mg of TsO-PEG_{1.5k}(α CD)-N₃ pseudorotaxane were dissolved in 5 mL of DMSO at T 45°C under Ar atmosphere. 230 mg of Cu wires and 304 mg (0.07 mmol) of butynyl-PCL were added, and the reaction was carried out for 48 h. The solution was first concentrated by rotovapor and finally dried under vacuum overnight. Before continuing, completeness of click reaction was checked by FTIR. Tos-PEG_{1.5k}(α CD)-PCL_{4k} (100 mg) was then dissolved in DMSO (3 mL) at T 45°C under Ar atmosphere. 3 mL of a DMSO solution containing 244 mg (0.55 mmol) of Fol, pre-treated with 20 mg (0.87 mmol) of NaH as described above, were added dropwise. The reaction was let to go on for 48h at T 45°C. The final rotaxane was purified by dialysis following the same procedure described for R1 synthesis. Yield =57.3%. Fol

functionalization degree=19%. Elemental analysis: Theoretical (number of α CD calculated by NMR): C% 62.02, H% 8.80, (O+N)% 29.18; Found: C% 62.9; H% 9.1; (O+N)% 28. $^1\text{H-NMR}$ (d_6 -DMSO, α -CD): PCL block: 1.29(t), 1.58(t), 2.24(m), 3.98(t); PEG block: 2.49(s), 3.23(s), 3.51(m); α CD: 5.5(d), 5.35(s), 5.1(s), 4.6(m), 3.8(m), 3.65(m), 3.55(m), 3.39(m).

Copolymer characterization

Elemental analysis was performed with a LECO ITALY Mod 840 analyzer.

Fourier Transform Infrared (FTIR) analysis was performed with a Perkin-Elmer spectrometer (Paragon 500) equipped with a ZnSe attenuated total reflectance (ATR) crystal accessory. Samples were placed in direct contact with the ATR crystal and pressed with a pressure clamp positioned over the crystal/sample area to allow intimate contact between the material and the crystal. Spectra were acquired in the 4000–400 cm^{-1} range, at a resolution of 2 cm^{-1} (average of 20 scans).

Gel Permeation Chromatography (GPC) analyses were performed in THF at 35°C and flow rate of 0.8 mL/min with a Malvern-Viscotek GPC MAX/TDA 305 quadruple detector array, using a precolumn and two Phenogel columns (Phenomenex, USA) with exclusion limits 106 and 103, respectively. Samples (100 μL) were filtered through a 0.22 μm PTFE membrane filter before injection. Triple detectors calibration was based on a standard of polystyrene with molecular weight 104,959 Da.

^1H NMR spectra were obtained on a Bruker DRX-400 spectrometer using 5 mm tubes. Sample concentrations were about 0.7% (w/v). All spectra were measured with 16 accumulations and a 10 s recycle delay.

Diffusion-ordered NMR spectroscopy (DOSY) experiments were carried out at 298°K for R2 and 313°K for R1 on a Bruker 600 DRX equipped with a cryo-probe. The concentration of the samples was about 0.7% (w/v) in d_6 DMSO. The ledbpgp2s pulse sequence from Bruker library, incorporating bipolar gradient pulse pair and 2 spoil gradients, with a longitudinal eddy current delay, was run with linear gradient (5.35 G cm^{-1}) stepped between 2.0% and 95.0%, incremented in 32 steps. The gradient duration was held constant at 2 ms and the echo delay (Δ) at 200 ms. After Fourier transformation and baseline correction of 1D ^1H spectra (F2 dimension), the diffusion dimension (F1) of the 2-dimensional DOSY was processed by using TopSpin software (version 2.1)

Differential Scanning Calorimetry (DSC) analysis (Q2000 TA Instruments) was performed under nitrogen flow with a 2°C min^{-1} scanning rate. Sample (about 4 mg) sealed in an aluminum crucible was heated from -20 to 90 °C, cooled at -20 °C and finally heated again to 90 °C.

X-ray powder diffraction profiles were obtained at room temperature with Ni filtered CuK α radiation using an automatic diffractometer X-Pert by Panalytical.

Thermogravimetric (TGA) analysis was carried out on a Perkin-Elmer Pyris Diamond TG-DTA apparatus from 25 to 500°C under nitrogen flow (50 ml/min) at 10 °C/min heating rates.

Polarized optical microscopy was performed on an Axioscop-Zeiss instrument equipped with a THMS 600 hot stage and a Linkam TMS 91 temperature programmer.

The amount of Fol linked to the copolymer was quantified by UV–vis spectroscopy on DMSO polymer solutions (0.2–2 mg/mL), using Fol standard solutions in DMSO to construct calibration curves. The absorbance of the sample was evaluated at 360 nm on a Shimadzu 1800 spectrophotometer.

Preparation and characterization of nanoparticles

Non-targeted NPs were prepared from mPEG_{1k}-PCL_{4k} whereas folate-decorated NPs were prepared from a mixture of mPEG_{1k}-PCL_{4k} either with Fol-PEG_{1.5k}-PCL_{4k} (Fol-NPs) or with R1 (R1-NPs) (10 and 20% by wt). NPs were formed by solvent diffusion of an organic phase (5 mg of copolymer in 1 mL of acetone for NPs; 5 mg of copolymers mixture in 1 mL of acetone for Fol-NPs; 5 mg of copolymers mixture in 1 mL of THF/DMSO 1/1 v/v for R1-NPs) added dropwise in water (4 mL) under magnetic stirring (300 rpm). After solvent evaporation, NPs were filtered through 0,45 µm Phenex® filters (Phenomenex, USA). In case of Fol-NPs, THF was evaporated whereas DMSO was removed by dialysis against water before filtration. NPs could be freeze-dried (Christ Alpha 2–4 LSCplus, Martin Christ Freeze Dryers, Germany, sample frozen in liquid N₂) after the addition of HPβCD as cryoprotectant (polymer/HPβCD 1/10 wt ratio), whereas Fol-NPs could be freeze-dried without the help of any cryoprotector. Recovered nanoparticles were stored at 4°C. Recovery yield was evaluated by weighing the solid residue after freeze-drying (yield > 99% for all formulations). The hydrodynamic diameter (DH), polydispersity index (PI) and zeta potential (ζ) of NPs were determined on a Zetasizer Nano Z (Malvern Instruments Ltd). ¹H NMR was carried out on NPs and Fol-NPs aqueous dispersions to evaluate the amount of, respectively, PEG and PEG/αCD on the surface. Spectra were recorded for either nanoparticles dispersed in D₂O or nanoparticles dissolved in d₆-DMSO/d₈-THF 1/1 v/v (5 mg/mL). Fixed aqueous layer thickness (FALT) was measured by monitoring the influence of ionic strength on ζ. Different amounts of NaCl stock solutions were added to NPs dispersed in water (250 µg) and zeta potential of the samples measured. A plot of ln ζ against 3.33*[NaCl]^{0.5} gives a straight line where the slope represents the thickness of the shell in nm (11)

Cell cultures and NP uptake studies

KB carcinoma cells (American Type Culture Collection, ATCC, Rockville, USA) over-expressing FRα were grown in Eagle's medium (MEM) (Life Technologies) supplemented with 10% fetal bovine serum (FBS), 100 U/mL Penicillin G and 100 µg/mL Streptomycin and maintained at 37 °C in a humidified atmosphere containing 5% CO₂. Flow cytometry (FACS) experiments were performed in order to study the uptake of NR-loaded NP formulations. For the experiments, cells were seeded in 24 wells/plate (50,000 cells/well) in folate-deficient RPMI medium (Life Technologies) supplemented with 10% FBS. After 24 h of growth at 37 °C, the cells were incubated for 1 h with 100 µg/mL of NPs diluted in RPMI medium. At the end of NP incubation time, the cells were washed, detached from the plates with 0.25% trypsin (Life Technologies), centrifuged and resuspended in Versene™ before measuring NR fluorescence using a BD FACSCanto™ II instrument (Becton Dickinson). The blue laser at 488 nm was used as excitation source and the PE channel (585/42 nm) was selected for the detection of NR fluorescence. 10⁴ events/sample were acquired and analyzed with the FACSDiva Software. The competition experiments were carried out incubating the cells with 1 mM free Fol 1 h prior to the addition of NPs in order to saturate FRs present on cell surface.

Result and discussion

Synthesis and FTIR characterization of copolymers

mPEG_{1k}-PCL_{4k} copolymer was synthesized by typical ROP polymerization of CL using mono-hydroxyl PEG_{1k} as initiator and stannous octoate as catalyst. The molecular weight of PCL block was controlled by the CL/initiator molar ratio in the feed, and calculated by the ratio between the intensities of the resonance associated to -CH₂-OH methylene protons at 3.64 δ and -CH₂-CO- units in the PCL chain at 2.31 δ of ¹H NMR spectrum. Butynyl-PCL with Mn ~4 kDa was synthesized analogously using 3-butyn-1-ol as initiator. Fol-PEG_{1.5k}-PCL_{4k} copolymer and its rotaxane derivatives were prepared following a multi-step procedure. First, tailoring of PEG was performed through a method that allows selective introduction of different α,ω - moieties (12,13), as described in **Scheme 1**. The key step of the reaction is the desymmetrization of PEG diol, achieved using the method of Bouzide and Sauve (14) Tosylate group and azide were introduced for successive reactions with Fol and butynyl-PCL, respectively.

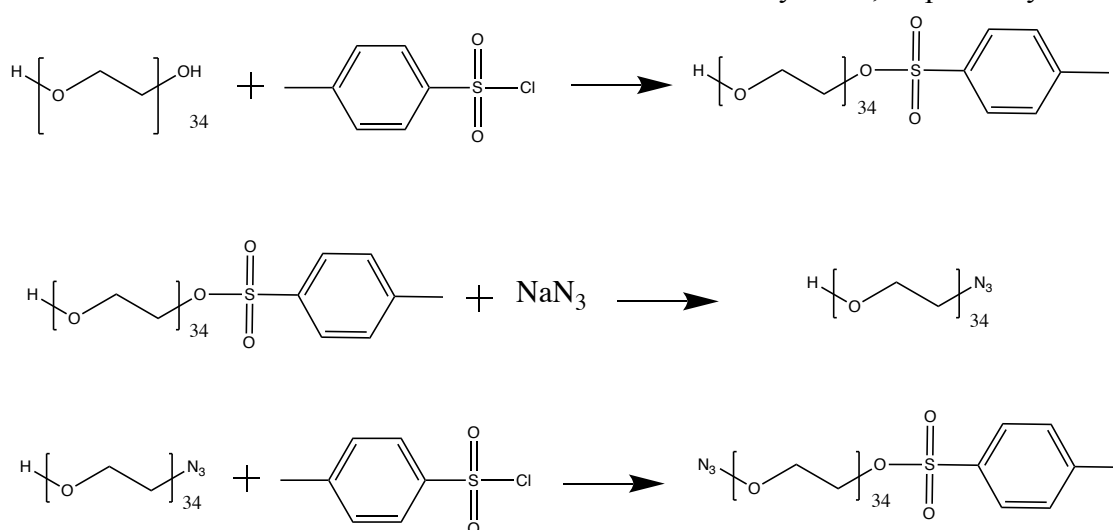


Figure 1. Synthesis pathway to TsO-PEG-N₃ derivative

The molecular structure of all intermediates was confirmed by the presence of corresponding peaks and peak integration in ¹H NMR spectrum. The azide group was identified by the characteristic band at 2105 cm⁻¹ in the FTIR spectrum.

TsO-PEG_{1.5k}-N₃ / α CD inclusion complex was formed by simple mixing in water of components, giving a pseudo-rotaxane. Rotaxane derivatives were prepared following a “two-poth” procedure, i. e., TsO-PEG_{1.5k}(α CD)-N₃ pseudo-rotaxane was first isolated and successively re-dissolved in DMSO for end-capping reactions. Purification steps were performed directly on final rotaxane since removal of unthreaded α CDs from pseudo-rotaxane is troublesome.

Different capping reactions are reported in literature to prevent CDs unthreading from PEG chains (15). All of them use a α,ω -homo-bifunctional pseudo-polyrotaxane PEG as precursor. Then, identical bulky groups, acting as physical stoppers, are coupled to the functional end groups of rotaxanated PEG through a variety of reactions, such as nucleophilic substitution or condensation (16; 17; 18). In the present work, end-capping was realized for the first time using two different stoppers, starting from a α,ω - hetero-bifunctional PEG pseudo-rotaxane. On one side, folate was coupled to the α -tosyl terminal group of PEG via nucleophilic substitution, after activating the amine functionality of Fol with sodium hydride. On the other side, butynyl-PCL_{4k} was coupled to the ω -azido terminal group via Cu(I)-catalyzed Huisgen [2 + 3]

dipolar cycloaddition (“click” reaction), described in literature to be an ideal and versatile solution to the problem of efficiently end-capping α CD-based polyrotaxanes (5) Since PCL chain is thin enough to fit within α CD, a possible involvement of PCL in complex formation could be envisaged. Nevertheless, PCL is reported to form inclusion complexes only for molecular weight up to 3 kDa under similar preparation conditions (4). Furthermore, for extremely hydrophobic polymers such as PCL, slow CD threading kinetics makes complexation unlikely. Hence, a PCL block with M_n of 4 kDa was expected to be an enough efficient stopper. As regards folate, it was already described in literature as an efficient cap to prevent unthreading of CD from PEG. (19) Besides, Fol conjugation through the amine functionality was preferred, since other possible reactions involving the γ -carboxylic group of Fol may concern also the α -carboxyl, negatively affecting the folate receptor-mediated endocytosis (20).

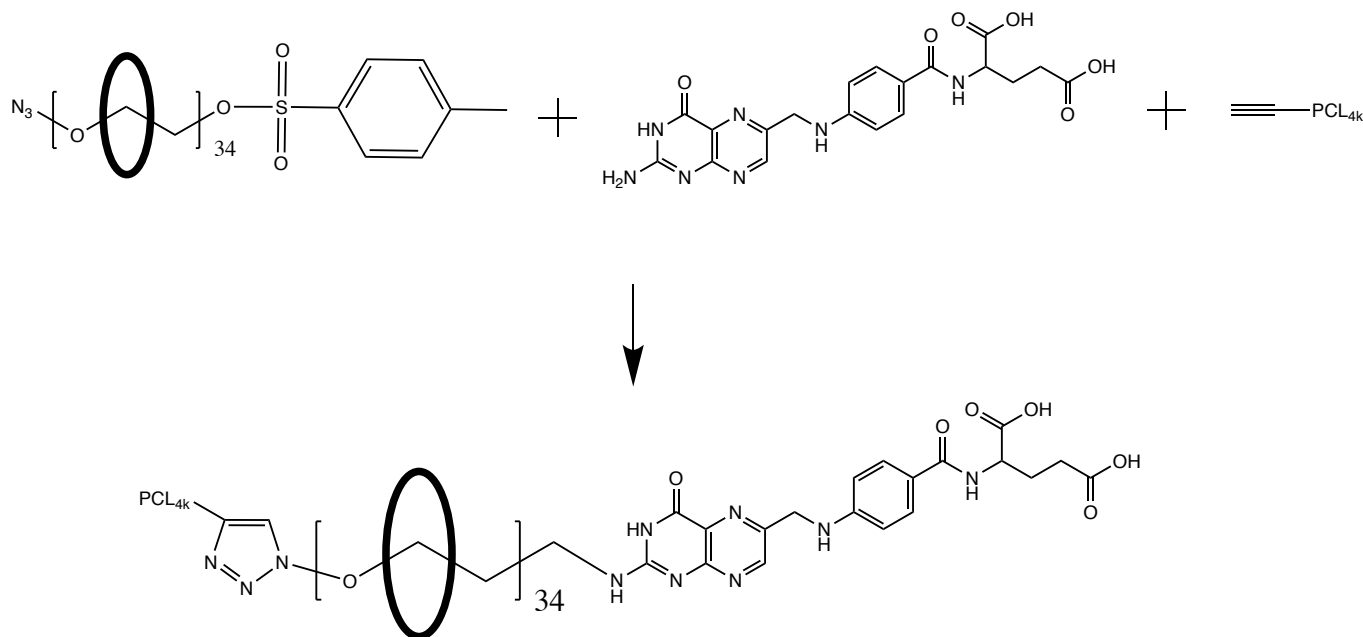


Figure 2. End-capping reactions of TsO-PEG_{1.5k}-N₃ pseudo-rotaxane (“two-steps” method)

A selectively threaded copolymer was finally obtained (so-called “site-selective complexation”). (21) Selective complexation of block copolymers is usually based on different binding affinity of the two blocks towards a certain ring size. In the case of triblock copolymers of PCL and PEG, it was found that both blocks were complexed by α CD because there is no preference for one block (22). Hence, the strategy here described allows a selective α CD-complexation of PEG block in PEG-PCL copolymers not obtainable otherwise. Two slightly different pathways were pursued and compared. The difference just consisted in the timeline. Capping was carried out simultaneously on both ends in the “one-step” approach, whereas the two reactions were carried out in sequence with the “two-steps” method (**Figure 2**). Particularly worth of note is the good yield obtained in both cases (>50%), significantly higher with respect to what reported in literature for most PEG polyrotaxanes (<10%) (23).

FTIR analysis of both rotaxanated copolymers evidenced the complete disappearance of the peak at 2105 cm^{-1} , corresponding to specific vibration of the azide group, suggesting that all PEG-N₃ groups were reacted (**Figure 3**). Peaks attributable to α CD (3350 and 1640 cm^{-1}) were visible in the FTIR spectra, although their low intensity suggests a low rotaxanation degree.

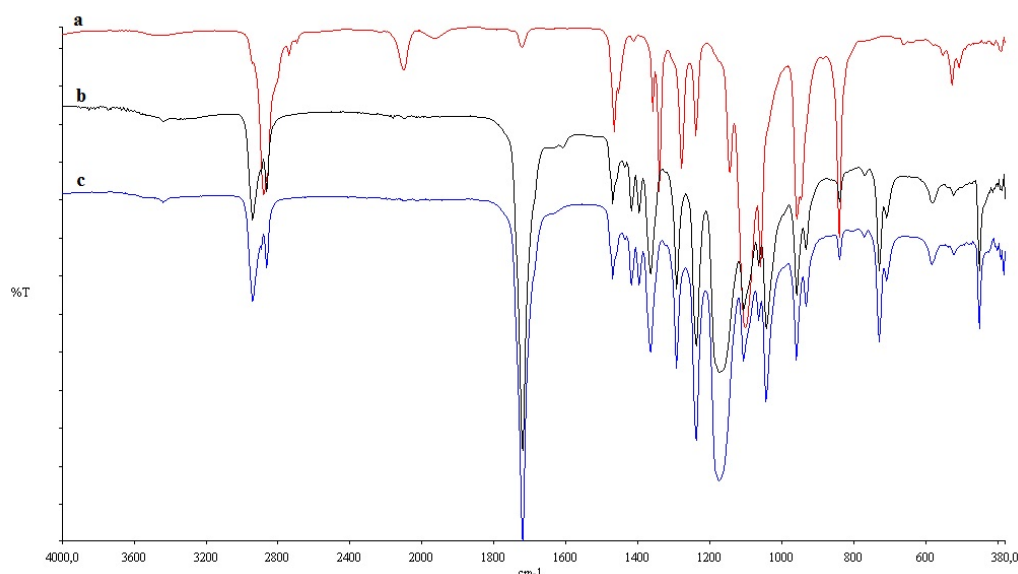


Figure 3 FTIR spectra of (a) TsO-PEG1.5k-N₃, (b) R1, and (c) R2.

Functionalization degree of Fol as determined by UV-vis spectroscopy was found to be very different between R1 and R2 (respectively, 94 and 19%). The difference can be ascribed to different reactivity of tosyl-end group on PEG. In fact, when the capping reactions were carried out in sequence, nucleophilic substitution of tosyl with folate has a reduced efficiency, since the tosyl group of TsO-PEG-PCL copolymer is likely less accessible. On the contrary, a high functionalization degree was obtained with the one-step capping since substitution of tosyl group with folate involves mainly free TsO-PEG-N₃.

Fol content has a big impact on solubility properties. R1 is insoluble in THF and CHCl₃ and barely soluble in DMSO at room temperature, whereas easily dissolves in DMSO at $T > 40^{\circ}\text{C}$ and in a THF/DMSO 1/1 v/v mixture at room temperature. On the contrary, R2 retains the good solubility of the precursor copolymer in various organic solvents.

GPC analysis

GPC analysis can definitively distinguish between polyrotaxane and a pseudo-polyrotaxane (which unthreads in solution to give the retention times of polymer and CD). Results on Fol-PEG_{1.5k}-PCL_{4k} and R2 are reported in **Table 1**. As a matter of fact, the poor solubility of R1 prevented a reliable analysis.

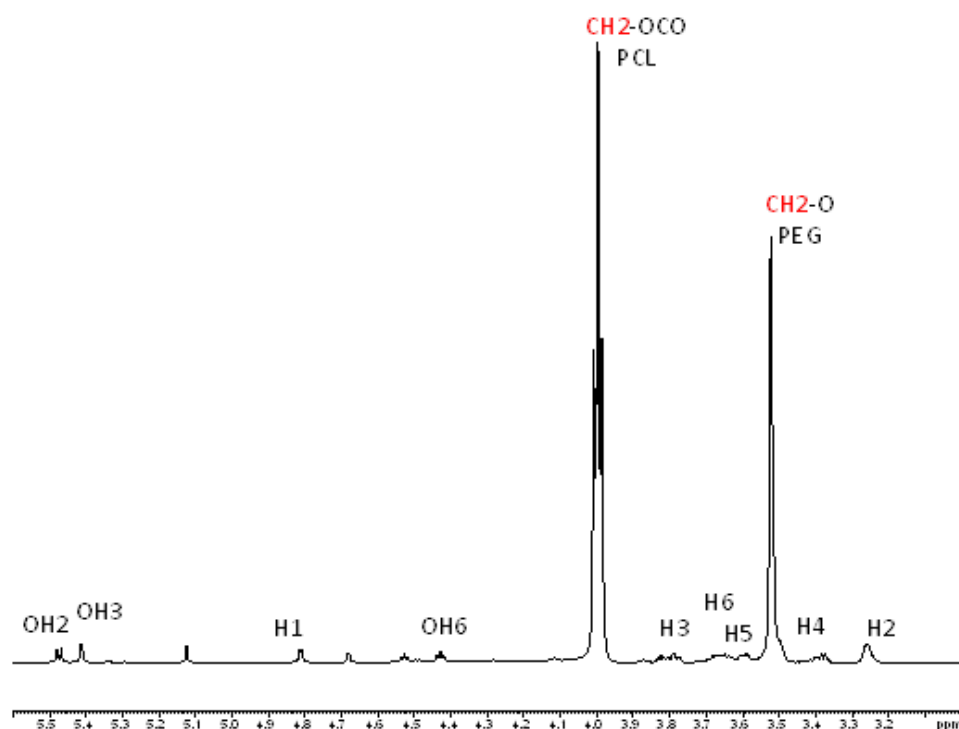
GPC confirmed that α CDs are threaded on PEG in R2, since only one peak was detected in correspondence of copolymer. Moreover, the increase of the Mark-Howink constant α was accounted for a semi-rigid conformation of PEG chains in the inclusion complex. An increase of M_w , in line with the presence of CDs on PEG, was found. Nevertheless, it must be kept in mind that, according to literature, molecular weight of polyrotaxanes cannot be rightly determined by GPC since polyrotaxanes behave unlike any commercial standard, due to their rod-like morphology (5)

Table 1. GPC parameters (in THF)

Sample	α	Mw (Da)	Mn (Da)	PDI
Fol-PEG _{1.5k} - PCL _{4k}	0.55	6737	5987	1.12
R2	0.66	8696	6354	1.36

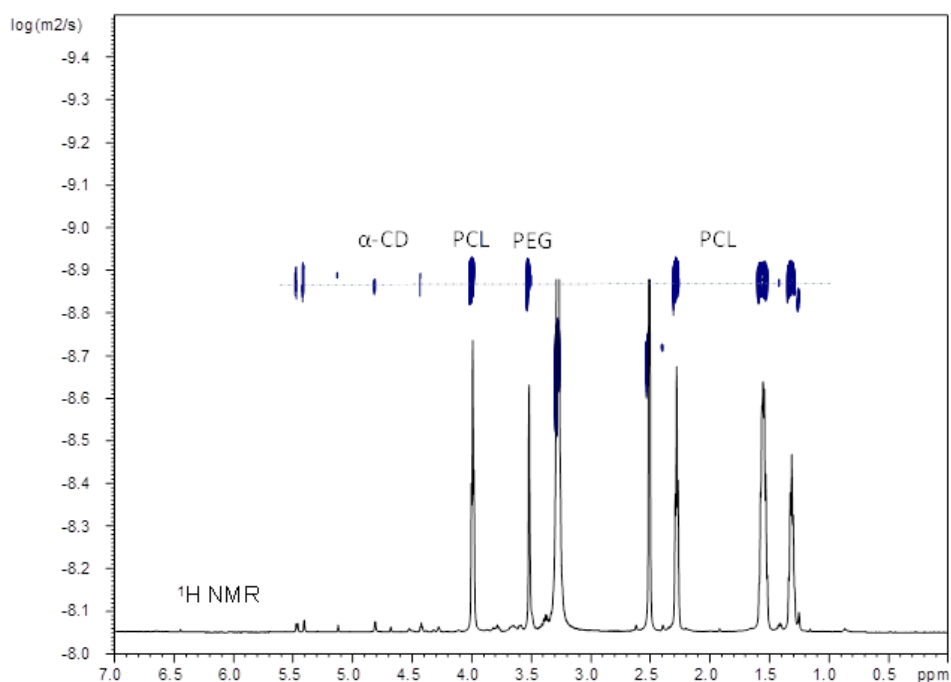
¹H NMR analysis and 2D-DOSY spectroscopy

¹H NMR was used to determine the PEG/ α CD ratio, although it is unable to establish whether or not PEG is included in the macrocycle. Signals of copolymer and α CD are clearly visible in both R1 and R2 spectra; peak designation of α CD protons is reported in **Figure 4** for R1. From the ratio between the integrals of the signal of protons of CH₂ unit of PEG chain at 3.4 ppm and the signal of the anomeric proton H1 of α CD at 4.8 ppm, the number of α CD associated or threaded per PEG chain was calculated. Coverage percentage was estimated by assuming that 100% complexation corresponds to aCD/PEG_{units} ratio = 1/2, as found in literature, which is exactly the ratio in the originating (or threading) solution. A value of around 2 aCD per PEG chain was obtained, corresponding to around 9% coverage. This value is far below what reported with traditional stoppers, such as 3,5-dimethylphenol (~70%) (23). The coverage ratio was not calculated for R2, since formation of α CD/PEG inclusion complex was not confirmed by DOSY spectroscopy (as reported below).

**Figure 4.** ¹H NMR spectrum in d₆-DMSO of R1 with designation of α CD peaks

The threading level in a polyrotaxane is limited by competition between the end-capping reaction and unthreading of pseudo-rotaxane precursor. In fact, threading complexation is generally a reversible process (24). Since DMSO is a good solvent for the α CD/PEG inclusion complex and for free α CD as

well, it is assumed that unthreading prevails, thus explaining the low coverage ratio. As a matter of fact, formation of rotaxane in DMSO solution is a quite difficult task to carry out, and lower inclusion ratio or even failure to trap α CD on a polymeric backbone in DMSO have been described (25). Furthermore, a limited coverage is often reported in case of polymer molecular weight higher than 1kDa, since threaded segments aggregate and precipitate before full coverage has been achieved. It is worth to underline, however, that formation of polyrotaxanes with a low coverage is a desired goal for applications as “sliding” materials (26). Some authors have resorted to use α -hydroxypropyl-CD instead of native α CD to avoid hydrogen bonds between adjacent CD and minimize the CD number on polymer chains (27) DOSY is a very sensitive method for discriminating threaded from unthreaded macrocycles in rotaxanated polymers (28). In a pseudo-2D “DOSY spectrum, the chemical shifts are displayed along the horizontal axis, while the diffusion coefficients are reported along the F1 dimension. Thus, from the diffusion-ordered two-dimensional NMR spectroscopy of R1 it was clearly observed that the diffusion coefficient of the PEG axis was coincident with that of the α CD rings, providing strong evidence of rotaxanation (**Figure 5a**). Instead, the two horizontal lines in R2 spectrum (**Figure 5b**) marking the diffusion coefficients for α CD and PEG-PCL copolymer indicate that the material exists as two separate components and not as a threaded structure. This result is apparently in contrast with GPC analysis. A possible interpretation is that R2 inclusion complex is actually a pseudo-rotaxane, due the low capping % of Fol, and rapidly unthreads upon dissolution in DMSO. On the other hand, the poor solubility of free α CDs in THF might be responsible for a tendency of α CDs to be retained on PEG chain, giving rise to a single peak in GPC chromatogram.



a

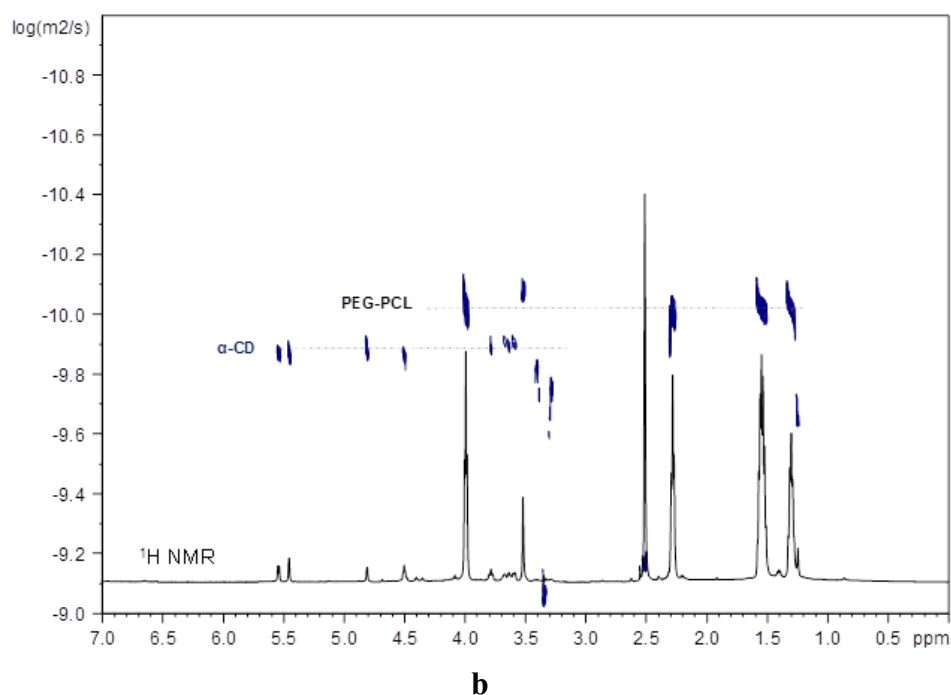


Figure 5: Superimposition of ^1H NMR and 2D DOSY spectra in d_6 -DMSO of R1 at 313°K (a) and R2 at 298°K (b)

DSC analysis

DSC analysis was performed in order to study the influence of the inclusion complex on the crystallinity of PEG and PCL blocks. Since PEG and PCL have close melting temperatures, a low scanning rate was chosen to promote the formation of well-separate exo/endotherms for the two different blocks. Thermal properties of Fol-PEG-PCL copolymer, rotaxanes and the precursors (butynyl-PCL, PEG diol and azido-PEG-PCL) are reported in **Table 2**. Melting peaks of PEG and PCL are distinguished in N_3 -PEG $_{1.5\text{k}}$ -PCL $_{4\text{k}}$ copolymer, indicating phase segregation of blocks. Since the PEG block is shorter than the side PCL block, the crystallization of PCL is dominant, leading to imperfect crystallization of PEG. (29). As a matter of fact, both T_m and ΔH_m of PEG decrease significantly in the copolymer with respect to free PEG. The melting endotherm of PEG in the 30-40°C range, instead, was completely absent in the thermogram of Fol-PEG $_{1.5\text{k}}$ -PCL $_{4\text{k}}$. This result can be ascribed to the effect originating from terminal folate group, which significantly affects crystallinity and melting temperature of PEG (30). Similarly to unthreaded Fol-PEG-PCL, also rotaxanes did not show a separate PEG melting endotherm; therefore, the influence of αCD ringing on PEG crystallinity cannot be deduced by DSC analysis.

The presence of PCL melting endotherm around 55°C in rotaxanes confirms that PCL chains are not involved in inclusion complexation. Interestingly, the high value of ΔH_m found for Fol-PEG $_{1.5\text{k}}$ -PCL $_{4\text{k}}$ and rotaxanated copolymers, both in first and second run, suggests that the endotherm cannot be ascribed to PCL melting alone (whose ΔH_m° corresponds to 139.5 J/g), but there is a contribution from PEG. This hypothesis is in line with literature reports on rotaxanated PEGs, which show complete absence of crystallinity only starting from 70% coverage ratio. It is believed that crystallization and melting temperatures of the two blocks approached up to overlap, due to the reduced mobility of PEG chain in the Fol terminated copolymers which causes an increase of PEG crystallization temperature.

The melting temperature of PCL is not influenced by its covalent connection with PEG in rotaxanated copolymers, whereas a decrease was noted in the case of N_3 -PEG-PCL and Fol-PEG-PCL, both in first and second heating run. As known, T_m is related to crystallites size and structure, considering that

crystallinity degree does not influence T_m value. Since the semicrystalline nature of PCL and its higher hydrophobicity can likely give micelles with greater kinetic stability and lower rates of disassembly (31), the finding that PCL block retains its crystalline structure unchanged in the rotaxanated copolymers might be a benefit in view of stability of related NPs.

Table 2. Melting temperature (T_m , °C) and enthalpy of fusion (ΔH_m , J/g) of PEG and PCL blocks taken in 1° and 2° heating run for pure Fol-PEG_{1.5k}-PCL_{4k}, the two rotaxane copolymers and the precursors (ΔH_m refer to the actual weight fraction of PEG/PCL in the copolymers).

Sample	T_{m1} PEG	ΔH_{m1} PEG	T_{m1} PCL	ΔH_{m1} PCL	T_{m2} PEG	ΔH_{m2} PEG	T_{m2} PCL	ΔH_{m2} PCL
Fol-PEG _{1.5k} - PCL _{4k}	-	-	54.4	121.5	-	-	51.6	103.3
R1	-	-	57.7	196.1	-	-	53.1	135.3
R2	-	-	59.3	227.5	-	-	56.5	160.4
butynyl-PCL _{4k}			57.8	104.9			53.9	75.5
PEG _{1.5k} diol	43.4	186.9			43.1	172.7		
N ₃ -PEG _{1.5k} - PCL _{4k}	39.1	41.2	54.6	92.9	32.2	61.5	50.2	69.8

X-ray diffraction analysis

X-ray powder diffraction patterns for N₃-PEG_{1.5k}-PCL_{4k}, Fol-PEG_{1.5k}-PCL_{4k} and the two rotaxanes are shown in **Figure 6**. Peaks characteristic of α CD were not detectable in the spectrum of rotaxanes, likely due to its low amount. All samples display the reflection peaks of PCL ($2\theta = 21.4^\circ$ and 23.7°), whereas the characteristic reflection of PEG at $2\theta 19.3^\circ$ was detected only in the diffractogram of N₃-PEG-PCL copolymer. Fol-functionalized copolymers do not show evidence of PEG crystallinity. Nevertheless, formation of IC could cause a crystal modification of PEG with a consequent shift of the peak at 19.3° , which would overlap with the one of PCL at 21.4° . A similar behavior was described by Ye et al. in the case of PEG/urea inclusion complex (30). The authors suggested that PEG chains adopt a more extended conformation when included in urea channels than the conformation found in the bulk. As a matter of fact, there are no reports on the crystal structure of PEG in α CD-PEG inclusion complexes. The exact conformation of PEG chains in the complex has not yet been determined (32)

Interestingly, a new weak reflection at $2\theta 20^\circ$ was present in R1 pattern. According to literature (33) the $2\theta 20^\circ$ peak is associated to α CD crystalline organization in the channel-like structure, characteristic of polymer/CD inclusion complexes. Hence, some short α CD sequences organized in the channel-like structure are present in R1, despite the low coverage.

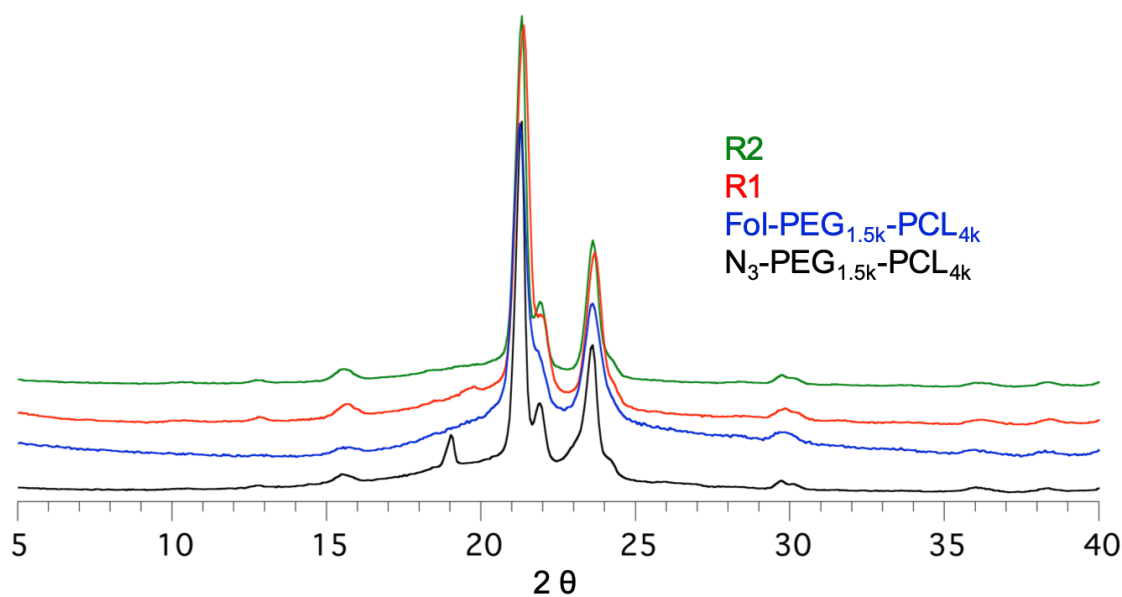


Figure 6. X-ray diffraction patterns for (black) N_3 -PEG_{1.5k}-PCL_{4k}, (blue) Fol-PEG_{1.5k}-PCL_{4k}, (red) R1 and (green) R2.

TGA analysis

The thermal stability of pure copolymer and rotaxanes was investigated by TGA. Increase in thermal stability is a striking feature for the formation of PEG- α CD inclusion complex. In fact, rotaxanes show unique thermoresistant properties, due to the supramolecular structure. The thermogravimetric curve of Fol-PEG_{1.5k}-PCL_{4k} (**Figure 7**) follows a two-step decomposition process which starts around 250°C. According to literature, PEG starts to degrade at T 280°C, which corresponds to the second stage in the curve of Fol-PEG_{1.5k}-PCL_{4k}, whereas the first stage is relative to PCL degradation. The profile of both rotaxanes shows a one stage thermal decomposition starting around 290°C for R2 and above 300°C for R1. The higher incipit of degradation of R1 with respect to R2 was attributed to the crystalline organization of threaded α CDs in the channel-like structure, as assessed by WAXD analysis, which further contributes to increase the thermal stability.

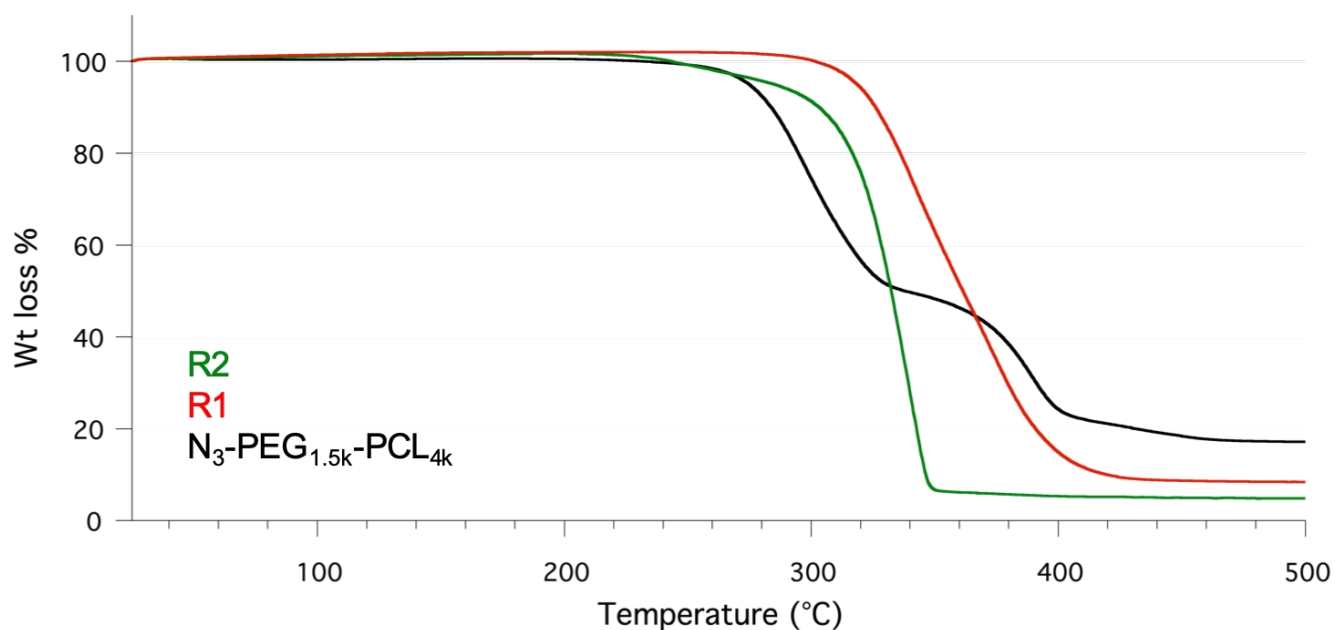


Figure 7. TGA curves of Fol-PEG_{1.5k}-PCL_{4k} and rotaxanated copolymers

Optical microscopy

Optical photos of Fol-PEG_{1.5k}-PCL_{4k}, R2 and R1 are shown in **Figure 8**. Formation of large spherulites was inhibited by the rotaxane units in R1 copolymer. This behavior is analogous to what reported in the case of a β CD/PCL inclusion complex (34). Nevertheless, in our case DSC and RX analyses did not give evidence of rotaxanation of PCL blocks. Therefore, the presence in R1 of α CD/PEG inclusion complex organized in a channel-like crystalline structure influences the morphology of PCL. It is supposed that the crystalline ICs embedded into the PCL matrix disturb the growth of spherulites and, at the same time, act as nucleation agents, giving rise to the growth of a higher number of spherulites of smaller dimension.

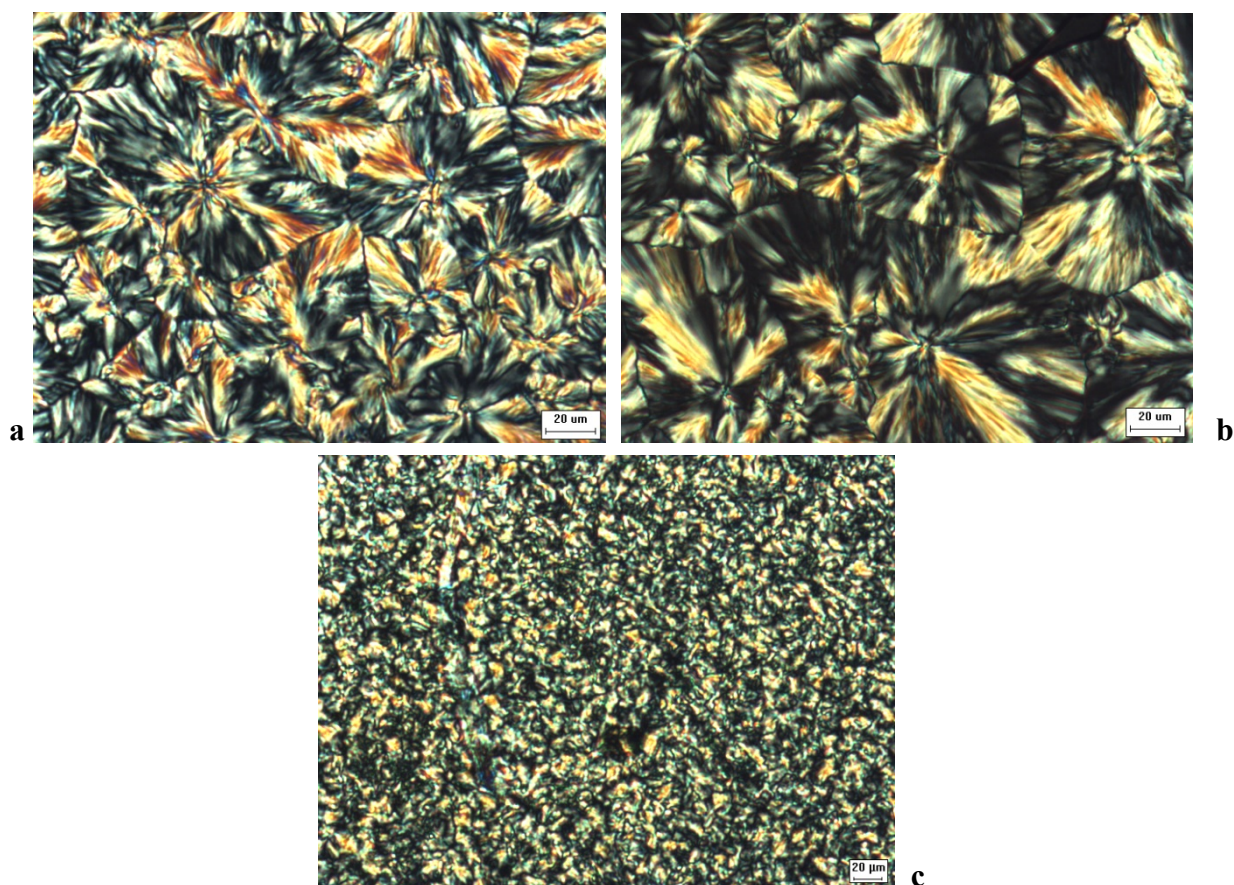


Figure 8. Comparison between photographs of FoI-PEG_{1.5k}-PCL_{4k} (a), R2 (b) and R1 (c) obtained by polarized light optical microscopy. Samples are crystallized at 48°C.

Preparation and characterization of NPs

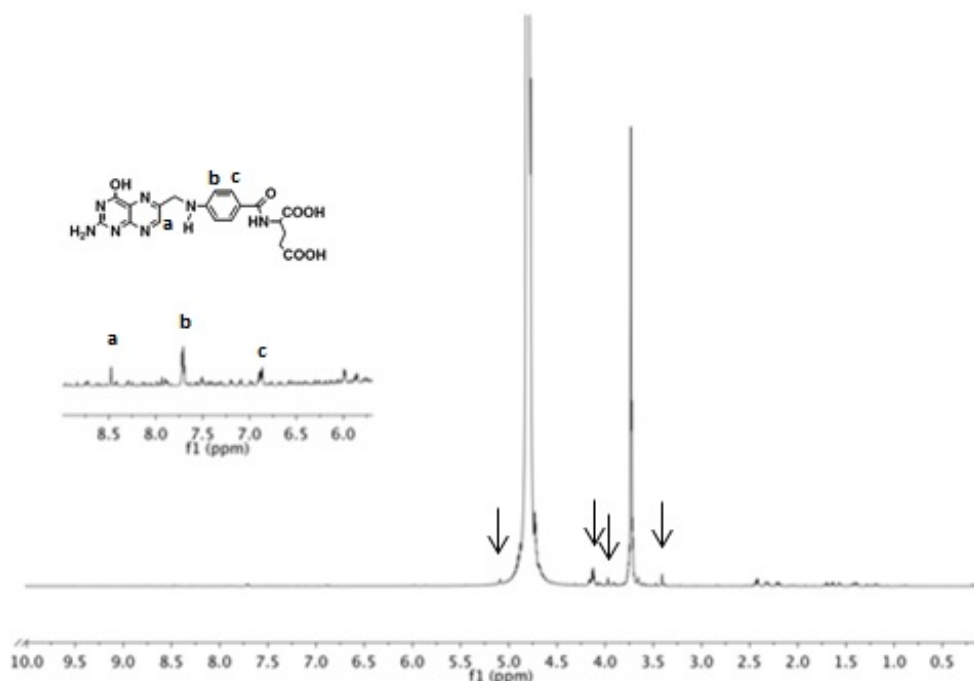
A preliminary study aimed at forming NPs suitable to deliver chemotherapeutics was carried out using R1 in mixture with mPEG_{1k}-PCL_{4k} copolymer (R2 was not considered, due to its instability in solution). NPs were prepared by solvent diffusion method (currently indicated as nanoprecipitation) from a mixture of mPEG_{1k}-PCL_{4k} with different percentages (10 and 20% by wt) of R1. Corresponding non-targeted NPs were prepared from mPEG-PCL. The hydrodynamic diameter (D_H), polydispersity index (PI) and zeta potential (ζ) of NPs are reported in **Table 3**. The extent of PEG on NPs surface was evaluated by ¹H NMR according to literature (35).

Table 3. Properties of NPs and R1-NPs. 10% and 20% refer to the amount of R1 in the mixture.

Formulation	D_H (nm) ±SD (PI)	ζ (mV) ±SD	Surface PEG (wt%)	Surface αCD (wt%)
mPEG _{1k} PCL _{4k}	85.67±0.77 (0.108)	-25.1±0.3	7.1	-
R1-NP10%	171.0±10 (0.220)	-42.3±1	5.5	84.4
R1-NP20%	167.2±10 (0.254)	-38.8±0.5	7.1	88.2

Nanoprecipitation of mPEG_{1k}-PCL_{4k} gave NPs of size below 100 nm with very low polydispersity and negative surface charge, in line with previous studies (3). Upon R1 addition, nanoparticles of higher dimension and much more negative ζ were formed. Increase of NPs dimension can be likely attributed to a slight extension of PEG chains upon rotaxanation, which increases shell thickness. As a matter of fact, Fol-NPs, which do not contain the α CD-rotaxanated copolymer, did not show any size increase (3). The higher value of ζ is suggestive of the presence of Fol moieties on the surface.

To evaluate surface PEG, ¹H NMR spectrum of R1-NP micelles in D₂O was acquired, and the amount of surface PEG was determined by the ratio with total PEG amount as determined by ¹H NMR spectrum of freeze dried R1-NPs dissolved in d₆-DMSO. The experimental amount of PEG on the surface is much lower than the theoretical value, as already found in a previous work (3). It is worth of noting, however, that no variation of surface PEG amount was detected upon R1 addition. Spectrum of R1-NPs micelles in D₂O clearly shows also the resonances relative to Fol (36) and α CD units, attesting their good exposition on the surface (**Figure 9A**). Furthermore, by comparing the ratio between the intensities of H1 signal of α CD and -CH₃ signal of mPEG-PCL as determined by the spectrum of micelles in D₂O with the corresponding ratio in the spectrum of R1-NPs dissolved in d₆-DMSO, it was also possible to estimate the percentage of α CD exposed. As shown in **Table 4**, a percentage of α CD close to 90% was found. This result is extremely important, since the full surface exposition of α CD implies a full surface exposition of folate targeting molecules. The thickness of the external hydrophilic PEG shell of NPs was evaluated too by FALT, measuring the values of NPs ζ in NaCl solutions at different concentrations. The shell thickness results higher for untargeted NPs (~5 nm), compared to R1-NP10% (~3.8 nm) and R1-NP20% (~3.3 nm), thus demonstrating that the presence of targeting moieties and their exposition on NP surface can modify the conformation of the PEG shell (**Figure 9 B**). Moreover, NPs exhibit spherical morphology and absence of aggregation phenomena, as evidenced by TEM analysis (**Figure10**)



A

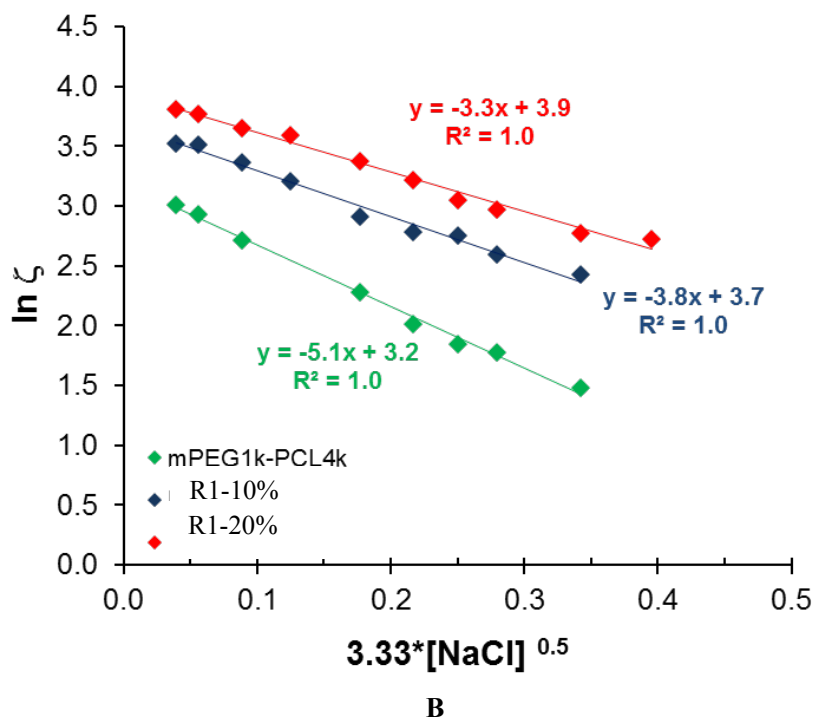


Figure 9. (A) $^1\text{H-NMR}$ spectrum in D_2O of R1-NP20%. Signals relative to αCD are indicated by arrows; signals of Fol are evidenced in the box. (B) FALT measurements. The slope of the straight line represents the thickness of the outer hydrophilic shell expressed in nm.

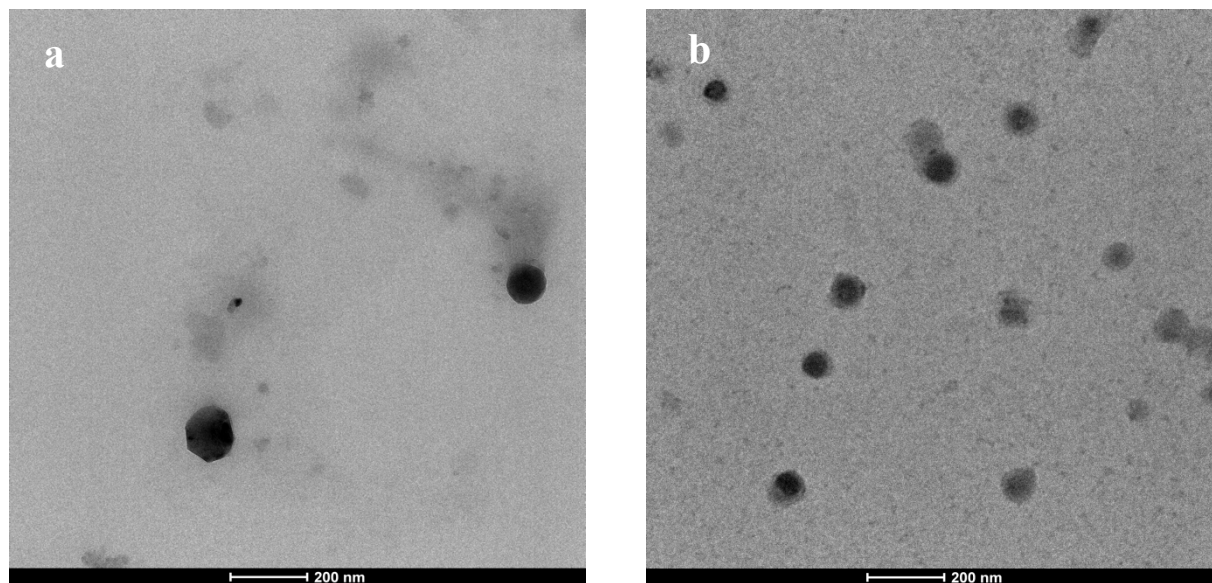


Figure 10 Representative TEM micrographs of Fol-NPs 20% (a) and R1-NPs 20% (b)

Cell uptake studies

After the deep characterization of surface properties of NPs in terms of Fol and CD exposition, PEG density and thickness, we investigated whether these NPs could bind and be internalized in KB cancer cells, in which $\text{FR}\alpha$ is over-expressed. Uptake studies were performed with fluorescent NR-loaded NPs

showing no significant variation in term of colloidal properties as compared with their unloaded counterpart. To highlight the effect of α CD/PEG rotaxane on Fol exposition, folate decorated NPs prepared from a mixture of mPEG_{1k}-PCL_{4k} with Fol-PEG_{1.5k}-PCL_{4k} (Fol-NPs) were also tested as a comparison. **Figure 11** shows the uptake of the different nanoformulations in KB cells, pre-incubated or not with 1 mM free Fol before NP addition, used as competitor to saturate the FRs over-expressed on the cell surface. As clearly visible in the graph, all Fol-decorated NPs showed a higher internalization compared to untargeted NPs, thus demonstrating the effective involvement of the targeting agent in the NP uptake. Importantly, the uptake of both R1-NP formulations was higher with respect to the corresponding Fol-NPs, confirming a better exposition of Fol on NP surface. Competition experiments showed significant reduced uptake for all Fol-decorated NPs, confirming the partial involvement of FR-mediated endocytosis on NP internalization process. In fact, since Fol-decorated NPs showed a higher internalization compared to mPEG-PCL NPs also in the competition experiment, this may suggest the involvement of additional uptake mechanisms besides FR-mediated endocytosis.

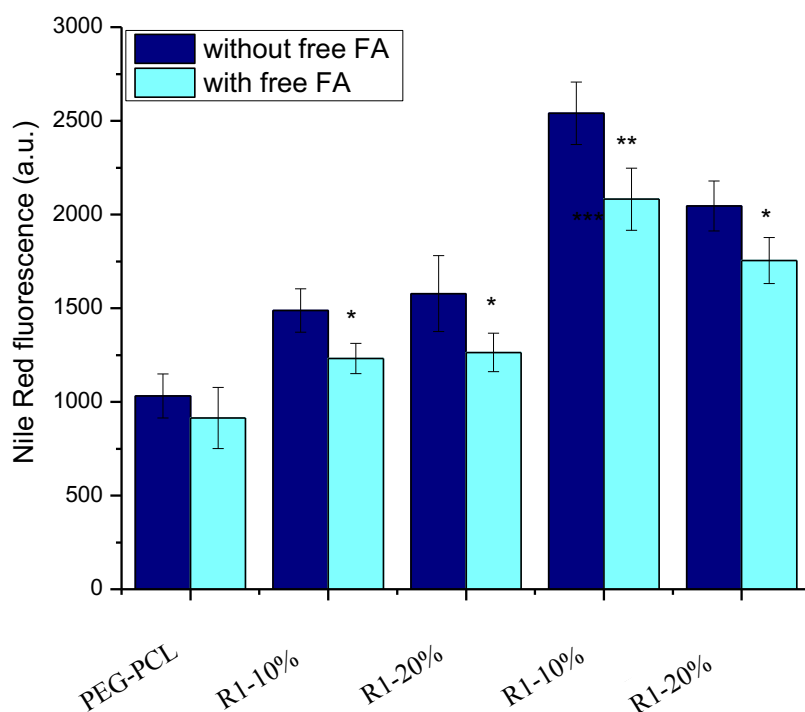


Figure 11. Flow cytometry measurement of NP uptake in KB cells incubated for 1 h with 100 μ g/mL of NR-loaded NPs. in the absence or in the presence (competition experiment) of 1 mM free fol. Data are the means of at least 2 independent experiments (mean \pm SD), carried out in triplicate. Significant different for * $p < 0.01$; ** $p < 0.001$, Student's t-test.

Conclusions

Selective complexation of PEG-PCL copolymers with α CD was successfully obtained from a α,ω -hetero bifunctional PEG pseudo-rotaxane with an original methodology, involving two different end-capping reactions to prevent α CD unthreading. Folate and butynyl-PCL (Mn 4 kDa) were bonded on PEG ends as stoppers through, respectively, nucleophilic substitution and click reaction, finally realizing a selective

rotaxanated Fol-PEG(α CD)-PCL copolymer. To the best of our knowledge, this is the first example of end-capping of a PEG pseudo-rotaxane with two different stoppers. We found that when the two end-capping reactions were carried out simultaneously (“one-step”, R1), the inclusion complex was stable in solution, as demonstrated by DOSY spectroscopy, whereas a rapid unthreading was detected in the case of rotaxane obtained by carrying out the reactions in sequence (“two-steps”, R2). This finding was ascribed to the low Folate capping efficiency achieved with the two-steps methodology. Results of DSC analysis suggested that PEG melting was shifted to higher temperatures values, which overlap with PCL melting temperature, upon Fol functionalization and α CD complexation. X-ray diffraction analysis of R1 showed that α CD inclusion complex presents the typical channel-like crystalline structure. Thermogravimetric analysis evidenced an improvement of thermal stability of copolymers upon rotaxanation. Optical microscopy showed how the morphology of PCL spherulites was strongly influenced by the presence of crystalline rotaxanated units on PEG block in R1.

Finally, in preliminary experiments of NP uptake in cancer cells over-expressing FR α , we demonstrated that the proper exposition of Fol in R1-NPs significantly improved NP internalization with respect to untargeted NPs but also with respect to Fol-decorated NPs prepared from a mixture of mPEG_{1k}-PCL_{4k} with Fol-PEG_{1.5k}-PCL_{4k}.

References

- 1 Cheung, Kevin & Ewald, Andrew. (2016). A collective route to metastasis: Seeding by tumor cell clusters. *Science*. 352. 167-169. 10.1126/science.aaf6546.
- 2 Conte, Claudia & Maiolino, Sara & Pellosi, Diogo & Miro, Agnese & Ungaro, Francesca & Quaglia, Fabiana. (2015). Polymeric Nanoparticles for Cancer Photodynamic Therapy. *Topics in current chemistry*. 370. 61-112. 10.1007/978-3-319-22942-3_3.
- 3 Venuta, Alessandro & Moret, Francesca & Dal Poggetto, Giovanni & Esposito, Diletta & Fraix, Aurore & Avitabile, Concetta & Ungaro, Francesca & Malinconico, Mario & Sortino, Salvatore & Romanelli, Alessandra & Laurienzo, Paola & Reddi, Elena & Quaglia, Fabiana. (2017). Shedding light on surface exposition of poly(ethylene glycol) and folate targeting units on nanoparticles of poly(ϵ -caprolactone) diblock copolymers: Beyond a paradigm. *European Journal of Pharmaceutical Sciences*. 111. 10.1016/j.ejps.2017.09.048.
- 4 Harada, Akira & Hashidzume, Akihito & Yamaguchi, Hiroyasu & Takashima, Yoshinori. (2009). Polymeric Rotaxanes. *Chemical reviews*. 109. 5974-6023. 10.1021/cr9000622.
- 5 Loethen, Scott & Thompson, David. (2007). Biomedical Applications of Cyclodextrin Based Polyrotaxanes. *Polymer Reviews - POLYM REV*. 47. 383-418. 10.1080/15583720701455145.
- 6 Akira Harada and Mikiharu Kamachi (1990) Complex formation between poly(ethylene glycol) and α -cyclodextrin *Macromolecules* 23, 10, 2821-2823

- 7 Simoes, Susana & Rey-Rico, Ana & Concheiro, Angel & Alvarez-Lorenzo, Carmen. (2015). Supramolecular cyclodextrin-based drug nanocarriers. *Chemical communications (Cambridge, England)*. 51. 10.1039/c4cc10388b.
- 8 Ooya, Tooru & Lee, Jaehwi & Park, Kinam. (2004). Hydrotropic Dendrimers of Generations 4 and 5: Synthesis, Characterization, and Hydrotropic Solubilization of Paclitaxel. *Bioconjugate chemistry*. 15. 1221-9. 10.1021/bc049814l.
- 9 Zhang, Lillian & Wu, Fang & Lee, Sue-Chih & Zhao, Hong & Zhang, Lei. (2014). pH-Dependent Drug-Drug Interactions for Weak Base Drugs: Potential Implications for New Drug Development. *Clinical pharmacology and therapeutics*. 96. 10.1038/clpt.2014.87.
- 10 Arisaka, Yoshinori & Yui, Nobuhiko. (2019). Polyrotaxane-based biointerfaces with dynamic biomaterial functions. *Journal of Materials Chemistry B*. 7. 10.1039/C9TB00256A.
- 11 Endres, Thomas & Beck-Broichsitter, Moritz & Samsonova, Olga & Renette, Thomas & Kissel, Thomas. (2011). Self-assembled biodegradable amphiphilic PEG-PCL-IPEI triblock copolymers at the borderline between micelles and nanoparticles designed for drug and gene delivery. *Biomaterials*. 32. 7721-31. 10.1016/j.biomaterials.2011.06.064.
- 12 Mahou, Redouan & Wandrey, Christine. (2012). Versatile Route to Synthesize Heterobifunctional Poly(ethylene glycol) of Variable Functionality for Subsequent Pegylation. *Polymers*. 4. 561-589. 10.3390/polym4010561.
- 13 Shenoy, Dinesh & Fu, Wei & Li, Jane & Crasto, Curtis & Jones, Graham & Dimarzio, Charles A. & Sridhar, Srinivas & Amiji, Mansoor. (2006). Surface functionalization of gold nanoparticles using heterobifunctional poly(ethylene glycol) spacer for intracellular tracking and delivery. *International journal of nanomedicine*. 1. 51-7. 10.2147/nano.2006.1.1.51.
- 14 Bouzide, Abderrahim & Sauvé, Gilles. (2002). Silver(I) Oxide Mediated Highly Selective Monotosylation of Symmetrical Diols. Application to the Synthesis of Polysubstituted Cyclic Ethers. *Organic letters*. 4. 2329-32. 10.1021/ol020071y.
- 15 Huang, Feihe & Gibson, Harry. (2005). Polypseudorotaxanes and Polyrotaxanes. *Progress in Polymer Science - PROG POLYM SCI*. 30. 982-1018. 10.1016/j.progpolymsci.2005.07.003.
- 16 Harada, Akira & Li, Jun & Kamachi, Mikiharu. (1994) Preparation and Characterization of a Polyrotaxane Consisting of Monodisperse Poly(ethylene glycol) and α -Cyclodextrins. *Journal of the American Chemical Society* 116 (8), 3192-3196 doi: 10.1021/ja00087a004
- 17 Ichi, Takahiro & Watanabe, Junji & Ooya, Tooru & Yui, Nobuhiko. (2001). Controllable Erosion Time and Profile in Poly(ethylene glycol) Hydrogels by Supramolecular Structure of Hydrolyzable Polyrotaxane. *Biomacromolecules*. 2. 204-10. 10.1021/bm005617n.

- 18 Ooya, Tooru & Arizono, Koichi & Yui, Nobuhiko. (2000). Synthesis and Characterization of an Oligopeptide-Terminated Polyrotaxane as a Drug Carrier. *Polymers for Advanced Technologies - POLYM ADVAN TECHNOL.* 11. 642-651. 10.1002/1099-1581(200008/12)11:8/12<642::AID-PAT15>3.0.CO;2-8.
- 19 Zhou, Yi & Wang, He & Wang, Chengxi & Li, Yueshan & Lu, Wenfeng & Chen, Shuifang & Luo, Jian-Dong & Jiang, Yongnan & Chen, Jianhai. (2012). Receptor-Mediated, Tumor-Targeted Gene Delivery Using Folate-Terminated Polyrotaxanes. *Molecular pharmaceutics.* 9. 1067-76. 10.1021/mp200315c.
- 20 Chen, Chen & Ke, Jiyuan & Zhou, X & Yi, Wei & Brunzelle, Joseph & Li, Jun & Yong, Eu-Leong & Xu, Eric & Melcher, Karsten. (2013). Structural basis for molecular recognition of folic acid by folate receptors. *Nature.* 500. 10.1038/nature12327.
- 21 Wenz, G. & Han, Bao-Hang & Mueller, A.. (2006). Cyclodextrin Rotaxanes and Polyrotaxanes. *Chemical reviews.* 106. 782-817. 10.1021/cr970027+.
- 22 Lu, Jin & Shin, Daniel & Nojima, S & Tonelli, A.E. (2000). Formation and characterization of the inclusion compounds between poly(ϵ -caprolactone)-poly(ethylene oxide)-poly(ϵ -caprolactone) triblock copolymer and α - and γ -cyclodextrin. *Polymer.* 41. 5871-5883. 10.1016/S0032-3861(99)00773-9.
- 23 Zhao, Tiejun & Beckham, Haskell. (2003). Direct Synthesis of Cyclodextrin-Rotaxanated Poly(ethylene glycol)s and Their Self-Diffusion Behavior in Dilute Solution. *Macromolecules.* 36. 10.1021/ma035513f.
- 24 Y.K. Agrawal, C.R. Sharma. (2005) *Supramolecular Assemblies and their Applications. Reviews in Analytical Chemistry*, 24 (1), 35-74. DOI: 10.1515/REVAC.2005.24.1.35
- 25 Araki, Jun & Ito, Kohzo. (2007). Recent Advances in the Preparation of Cyclodextrin-Based Polyrotaxanes and Their Applications to Soft Materials. *Soft Matter.* 3. 10.1039/b705688e.
- 26 Ito, Kohzo. (2010). Slide-ring materials using topological supramolecular architecture. *Current Opinion in Solid State and Materials Science.* 14. 28-34. 10.1016/j.cossms.2009.08.005.
- 27 Jiang, Lan & Liu, Chang & Mayumi, Koichi & Kato, Kazuaki & Yokoyama, Hideaki & Ito, Kohzo. (2018). Highly Stretchable and Instantly Recoverable Slide-Ring Gels Consisting of Enzymatically Synthesized Polyrotaxane with Low Host Coverage. *Chemistry of Materials.* 30. 10.1021/acs.chemmater.8b01208.
- 28 Zhao, Tiejun & Beckham, Haskell. (2003). Direct Synthesis of Cyclodextrin-Rotaxanated Poly(ethylene glycol)s and Their Self-Diffusion Behavior in Dilute Solution. *Macromolecules.* 36. 10.1021/ma035513f.

- 29 Bogdanov, B. & Vidts, A. & Buicke, A. & Verbeeck, Ronald & Schacht, Etienne. (1998). Synthesis and thermal properties of poly(ethylene glycol)-poly(ϵ -caprolactone) copolymers. *Polymer*. 39. 1631-1636. 10.1016/S0032-3861(97)00444-8.
- 30 Ye, Hai-Mu & Song, Yun-Yang & Xu, Jun & Guo, Baohua & Zhou, Qiong. (2013). Melting behavior of inclusion complex formed between polyethylene glycol oligomer and urea. *Polymer*. 54. 3385-3391. 10.1016/j.polymer.2013.04.026.
- 31 Liu, Jubo & Zeng, Faquan & Allen, Christine. (2007). In vivo fate of unimers and micelles of a poly(ethylene glycol)-block-poly(caprolactone) copolymer in mice following intravenous administration. *European journal of pharmaceutics and biopharmaceutics : official journal of Arbeitsgemeinschaft für Pharmazeutische Verfahrenstechnik e.V.* 65. 309-19. 10.1016/j.ejpb.2006.11.010.
- 32 Takahashi, Shoko & Yamada, Norifumi & Ito, Kohzo & Yokoyama, Hideaki. (2016). Inclusion Complex of α -Cyclodextrin with Poly(ethylene glycol) Brush. *Macromolecules*. 49. 10.1021/acs.macromol.6b01238.
- 33 Lei, Huang & Emily, Allen & Alan E. Tonelli (1998) Study of the inclusion compounds formed between α -cyclodextrin and high molecular weight poly(ethylene oxide) and poly(ϵ -caprolactone) *Polymer* 39, 20, 4857-4865 [https://doi.org/10.1016/S0032-3861\(97\)00568-5](https://doi.org/10.1016/S0032-3861(97)00568-5)
- 34 Jazkewitsch, Olga & Ritter, Helmut. (2011). Formation and Characterization of Inclusion Complexes of Alkyne Functionalized Poly(ϵ -caprolactone) with β -Cyclodextrin. Pseudo-Polyrotaxane-Based Supramolecular Organogels.. *Macromolecules*. 44. 10.1021/ma102456n.
- 35 Xu, Qingguo & Ensign, Laura & Boylan, Nicholas & Schon, Arne & Gong, Xiaoqun & Yang, Jeh-Chang & Lamb, Nicholas & Cai, Stephen & Yu, Tao & Freire, Ernesto & Hanes, Justin. (2015). Impact of Surface Polyethylene Glycol (PEG) Density on Biodegradable Nanoparticle Transport in Mucus ex Vivo and Distribution in Vivo. *ACS nano*. 9. 10.1021/acsnano.5b03876.
- 36 Yang, Xiaoqiang & Pilla, Srikanth & Grailer, Jamison & Steeber, Douglas & Gong, Shaoqin & Chen, Yinghua & Chen, Guihua. (2009). Tumor-targeting, superparamagnetic polymeric vesicles as highly efficient MRI contrast probes. *J. Mater. Chem.* 19. 5812-5817. 10.1039/B903845K.

6 Biodegradable nanoparticles based on an amine terminated polyester as a strategy to tune surface properties, protein interaction and accumulation in lung metastasis³

Introduction

Biodegradable polymer-based nanoparticles (NPs) are emerging in the treatment of several diseases, including cancer, due to the advantage that their features can be manipulated by selecting the appropriate polymer type and tuning the mode of carrier assembly.(1–3) For the rational design of NPs, the size and surface properties are of key importance to control the interactions with the body environment at the molecular, cell and tissue/organ levels.(4–8) It is widely accepted that polymeric NPs surrounded by a hydrophilic shell of polyethylene glycol (PEG) are able to evade the mononuclear phagocyte system (MPS) and to circulate for a long time once intravenously injected.(9–11) The presence of a hydrophilic fringe represents an outstanding tool also in the light of NP stability in aqueous media since aggregation phenomena are efficiently limited. Despite these advantages, PEGylation critically affects NP/cell interactions acting as a ‘steric’ barrier to NP internalization. (12)

In the context of biodegradable materials, PEGylated polyesters have been widely employed in drug delivery applications due to their biocompatibility and biodegradation to non-toxic products. (13–15) Block copolymers of PEG and poly(ϵ -caprolactone) (PCL) have gained attention due to the possibility to tune the PEG conformation on the surface. Through proper synthetic strategies, PEG–PCL copolymers with different copolymer architectures (diblock, triblock, star-shaped or branched) and hydrophilic/lipophilic balances are obtained and nanoassembled forming different delivery platforms (micelles, polymersomes, NPs, nanocapsules). This formulation versatility allows efficient entrapment of both hydrophilic and lipophilic drug cargo.¹⁴ In the case of diblock copolymers, PEG/PCL chain length and the mode of copolymer assembly are crucial to drive the PEG orientation on the surface, eventually affecting the interactions with proteins and the biological response *in vitro* and *in vivo*.^{16–18} In fact, PEG–PCL NPs were found mainly to alleviate the toxicity profile of a lipophilic chemotherapeutic cargo as compared to commercial formulations due to increased circulation time. (14)

To promote accumulation in solid tumours, and in turn to improve the therapeutic potential, pioneering studies have shown that PEGylated cationic liposomes demonstrate superior effectiveness in targeting tumour versus normal vascular networks.(19) More recently, it has been shown that PEGylated cationic NPs possess a unique ability to penetrate deeply inside tumour tissue(20,21) and, although slightly inferior in blood circulation and tumour accumulation as compared to their neutral and anionic counterparts, they are more effective in inhibiting tumour growth in subcutaneous CT26 and BX-PC3 tumour xenografts.(20) In fact, the elevated glycolysis in different cancer cell lines leads to a higher level of lactate secretion as compared to normal cells, generating negative surfaces with high affinity toward

³ The work presented in this paragraph has been published as: Biodegradable nanoparticles bearing amine groups as a strategy to alter surface features, biological identity and accumulation in a lung metastasis model

Diletta Esposito, Claudia Conte, Giovanni Dal Poggetto, Annapina Russo, Antonio Barbieri, Francesca Ungaro, Claudio Arra, Giulia Russo, Paola Laurienzo and Fabiana Quaglia

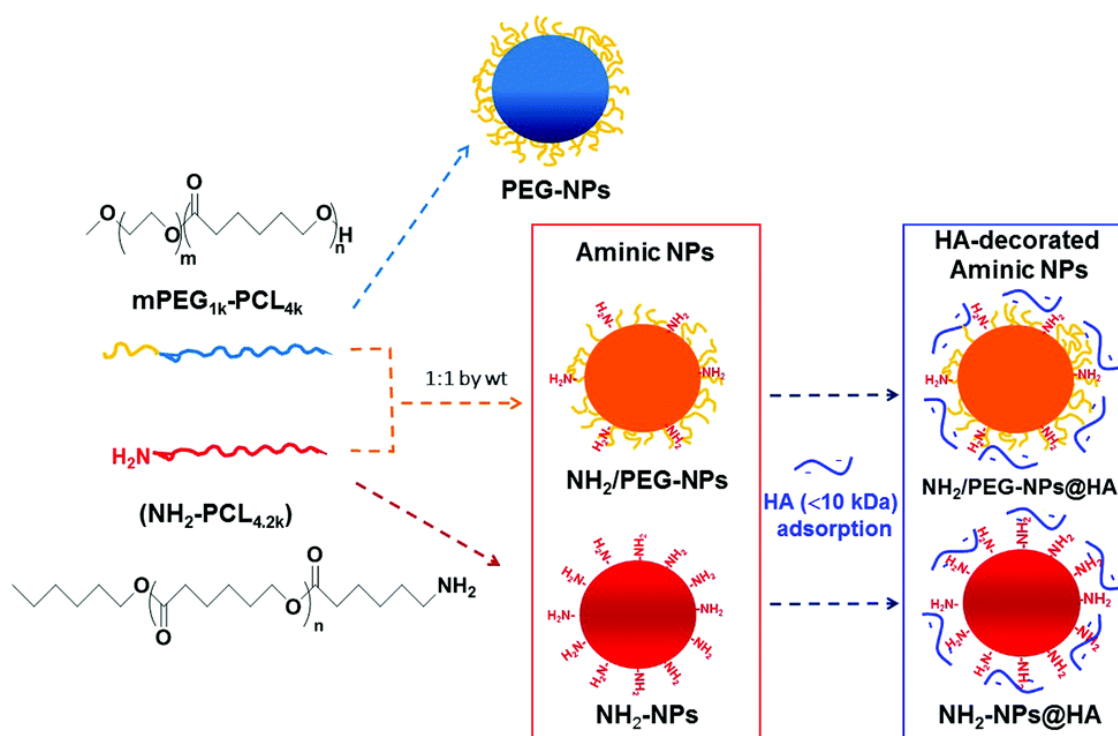
Journal of Materials Chemistry B, Issue 37, August 2018, 5922

DOI:10.1039/C8TB01330F

cationic nanocarriers. (22) This has prompted a renewed interest in developing NPs with a positive charge to expand the arsenal of nanotools for the delivery of chemotherapeutics. (23,24)

Cationic NPs are usually prepared through adsorption of cationic surfactants, polymers or phospholipids on the surface of a preformed biodegradable nanotemplate, (25) while only recently NPs prepared from amine-bearing biodegradable polymers have been proposed. (26)

In an attempt to extend the benefit of bearing a positive charge to PCL-based NPs through synthetic strategies, herein we have developed amine-functionalized NPs based on an amine terminated PCL (PCL4.2k-NH₂) and its mixture with monomethoxy-PEG-PCL (mPEG1k-PCL4k) (**Scheme 1**). Further functionalization of the amine NPs with hyaluronan (HA) has been carried out to modify the surface charge toward negative values and eventually to encourage uptake in CD44⁺ tumours through receptor-mediated endocytosis. In view of intravenous administration, the interaction of the NPs with human plasma has been investigated to acquire knowledge of their biological identity. (27,28) Subsequently, haemolysis and cytotoxicity were investigated in different lung cancer cell lines. Finally, the in vivo biodistribution of the NPs in an experimental mouse model of lung metastasis was investigated.



Scheme 1 Schematic representation of the synthesized polymers and prepared NPs. The NPs were designed to bear on their surface amine groups (NH₂-NPs) or amine/PEG groups (NH₂/PEG-NPs). To shield the amines, sodium hyaluronan (HA) was adsorbed on the surface. The PEG-NPs were also tested as a reference formulation.

Experimental

Materials

Monomethoxy-poly(ethylene glycol) with Mn 1.0 kDa (mPEG1.0k, Nanocs Inc., New York, USA) was dehydrated by azeotropic distillation with dry toluene in a Dean-Stark trap. All reagents were purchased from Sigma-Aldrich (Milan, Italy). ϵ -Caprolactone (CL) was distilled over CaH₂ under vacuum. Stannous-(2-ethylhexanoate)₂ (Sn(oct)₂), triethylamine (TEA), tosyl chloride (TsCl), triphenylphosphine

(PPh₃) and sodium azide were used without further purification. 1-Hexanol was dried according to a standard procedure. All solvents (analytical grade) were purchased from Sigma-Aldrich. N,N-Dimethylformamide (DMF) and dichloromethane (DCM) were dried before use according to standard procedures (Armarego and Chai, Purification of Laboratory Chemicals, 7th Edition). Sodium hyaluronan (HA, Mw < 10 kDa) was a kind gift from Magaldi Life S.r.l. DiD-oil was provided by Sigma-Aldrich. All other solvents were used as received.

Polymer characterization

FTIR analysis was performed with a PerkinElmer spectrometer (Paragon 500) equipped with a ZnSe attenuated total reflectance (ATR) crystal accessory. Samples were placed in direct contact with the ATR crystal and pressed with a pressure clamp positioned over the crystal/sample area to allow intimate contact between the material and the crystal. Spectra were acquired in the 4000–400 cm⁻¹ range, at a resolution of 2 cm⁻¹ (average of 20 scans). ¹H NMR spectra were recorded with a Bruker Avance DPX400 apparatus operating at 400 MHz. For GPC analysis, the samples were dissolved in THF and passed through a 0.22 μm PTFE membrane filter. Measurements were performed on an injected volume of 100 μL by using a Malvern-Viscotek GPC MAX/TDA 305 quadruple detector array equipped with a precolumn and two Phenogel columns (Phenomenex) with exclusion limits of 106 and 103 Da, respectively. The GPC instrument was used at a flow rate of 0.8 mL min⁻¹ and at a column and system temperature of 35 °C. Triple detector calibration was based on a standard of polystyrene with molecular weight 104.959 Da.

Polymer synthesis

Synthesis of monoamino-PCL (PCL_{4.2k}-NH₂)

Step 1. Synthesis of monohydroxyl-PCL (PCL_{4.2k}-OH)

1-Hexanol (100 mg, 0.98 mmol), CL (3.912 g, 34.3 mmol) and Sn(Oct)₂ (79.0 mg, 0.196 mmol) were charged in a flask under dry nitrogen. The polymerization was carried out under stirring at 120 °C for 24 h. The polymer was dissolved in 5 mL of DCM, precipitated in cold hexane, filtered and finally dried (yield 94%). ¹H-NMR (CDCl₃, δ in ppm): 1.29–1.78 (123H, m), 2.19–2.43 (74H, m), 3.92–4.21 (74H, t), 3.64 (2H, t); Mn evaluated by ¹H NMR = 4.2 kDa. Mw (GPC) = 4.2 kDa; Mw/Mn = 1.14.

Step 2. Synthesis of monotosyl-PCL (PCL_{4.2k}-OTs)

PCL_{4.2k}-OH (4.00 g, 0.955 mmol) was dissolved in 40 mL of DCM, then TEA (506 mg, 5.0 mmol) and TsCl (953 mg, 5.0 mmol) were added. The solution was stirred at room temperature for 24 h. The polymer was dissolved in 20 mL of DCM, precipitated in cold hexane, recovered and finally dried (yield 92%). ¹H-NMR (CDCl₃, δ in ppm): 1.29–1.78 (123H, m), 2.19–2.43 (74H, m), 3.92–4.21 (74H, t), 3.64 (2H, t), 7.79 (2H, d), 7.49 (2H, d), 2.43 (3H, s).

Step 3. Synthesis of monoazido-PCL (PCL_{4.2k}-N₃)

PCL_{4.2k}-OTs (3.5 g, 0.88 mmol) dissolved in 15 mL of dry DMF was charged in a flask under nitrogen, then NaN₃ (229 mg, 3.52 mmol) was added, and the mixture was stirred at 90 °C overnight. The reaction was stopped by cooling to room temperature, the solution was filtered and the DMF was removed under vacuum. The residue was dissolved in 15 mL of DCM and the solution was extracted twice with brine and

twice with water in a separating funnel. The organic phase was dried over anhydrous Na₂SO₄, concentrated and poured into cold hexane to precipitate the final polymer (yield 80%). ¹H-NMR (CDCl₃, δ in ppm): 1.29–1.78, (123H, m), 2.19–2.43, (74H, m); 3.92–4.21(74H, t), 3.64 (2H, t). FTIR diagnostic band: 2107 cm⁻¹ (N₃ stretching).

Step 4. Synthesis of PCL_{4.2k}-NH₂

PCL_{4.2k}-N₃ (2.0 g, 0.476 mmol) was dissolved in 50 mL of MeOH at 40 °C in a flask equipped with a nitrogen inlet and a refrigerator, then PPh₃ (N₃/PPh₃ molar ratio = 1/3) was added and the reaction was carried out at 40 °C overnight. The solvent was removed by rotary evaporation and the product was dissolved in 10 mL of DCM, precipitated in cold hexane and dried under vacuum (yield 94%). The occurrence of the reaction was confirmed by FTIR through the disappearance of the 2107 cm⁻¹ N₃ stretching band. ¹H-NMR (CDCl₃, δ in ppm): 1.29–1.78, (123H, m), 2.19–2.43, (74H, m); 3.92–4.21(74H, t), 3.64 (2H, t), 2.48 (2H, broad).

Preparation and characterization of NPs

PEGylated NPs (PEG-NPs), amine NPs (NH₂-NPs) and PEGylated amine NPs (NH₂/PEG-NPs) were prepared by a solvent-diffusion method. In the latter case, mPEG1k–PCL4k and PCL4.2k-NH₂ were mixed in a 1 : 1 w/w ratio. The amine NPs were further decorated with a layer of HA, thus obtaining NH₂-NPs@HA and NH₂/PEG-NPs@HA. Briefly, 10 mg of polymer was dissolved in 2 mL of acetone and added drop by drop into 4 mL of water containing 4 mg of Pluronic®F68 under stirring. Acetone was removed by rotavapor for 5 min. Then, the NPs were split into 4 Eppendorf tubes (1 mL) and immediately characterized. For the HA-decorated NPs, 100 μL of HA (4 mg mL⁻¹) was added to each tube (2 mg mL⁻¹ of NPs on the basis of yield).

Fluorescent NPs loaded with DiD-oil at 0.2% w/w were prepared too. Specifically, 20 μg of DiD-Oil was solubilized in 200 μL of MeOH and added to the polymer solution in acetone. NPs were formed as reported above. Thereafter, the NPs were washed twice with water by centrifugation at 13 000 × g for 30 min. The supernatant was finally collected, and the DiD-Oil content quantified through spectrofluorimetry at λ_{ex}/λ_{em} of 644 and 680 nm, respectively (RF-6000-Shimadzu). As a reference, a calibration curve of DiD-Oil in methanol (concentration range 0.1–5.5 μg mL⁻¹) was constructed.

The hydrodynamic diameter (DH), polydispersity index (PI) and zeta potential (ζ) of the NPs were determined on a Zetasizer Nano ZS (Malvern Instruments Ltd).

The results are reported as the mean of three separate measurements on three different batches (n = 9) ± standard deviation (SD).

Evaluation of primary amines on the NP surface

The evaluation of amine groups on the surface of the NPs was carried out through a fluorescamine assay. Briefly, a fluorescamine stock solution in DMSO was prepared (3 mg mL⁻¹) and 3 μL of this stock solution was incubated in 1 mL of NPs in water (500 μg mL⁻¹) for 15 min. Thereafter, the emission spectra at λ_{ex} = 350 nm were collected.

FALT measurements

Fixed aqueous layer thickness (FALT) was measured by monitoring the influence of ionic strength on particle surface charge. Different amounts of a NaCl stock solution at different concentrations were added

to a NP dispersion in water (0.5 mg mL^{-1}) and the ζ of the samples was measured. A plot of $\ln(\zeta)$ against $3.33 \cdot [\text{NaCl}]^{0.5}$ gives a straight line, where the slope represents the thickness of the PEG shell in nm.

Stability studies of the NPs

The stability of the NPs under physiologically-relevant conditions was assessed by dispersing a known amount of NPs (2 mg mL^{-1}) in either 10 mM phosphate buffered saline at pH 7.4 (PBS) or DMEM/FBS+ and incubating the sample at 37°C under mild stirring. The DH and ζ of the samples were taken after 30 min of incubation.

Interaction with blood components

The behaviour of the NPs in human plasma (Sigma-Aldrich) was evaluated by monitoring DH, ζ and scattering. Briefly, $500 \mu\text{L}$ of NPs (2 mg mL^{-1}) was added to $500 \mu\text{L}$ of human plasma and incubated at 37°C for different times (15 min, 24 h and 48 h). DH and ζ were evaluated as reported above, while for the scattering measurements, the absorbance of the samples at 500 nm was collected on an UV spectrophotometer (Shimadzu UV 1800). Haemolysis of human red blood cells (RBC) was evaluated on EDTA-treated human blood from healthy volunteers (after obtaining informed ethical consent). The blood samples were collected from the student health care complex at University of Napoli Federico II, Italy. The sample was centrifuged at $880 \times g$ for 5 min. The RBC pellet was diluted with 0.1 M PBS up to a concentration of 10% v/v. The RBC dispersion (0.1 mL) was added to 0.9 mL of a NP dispersion in PBS (0.5 mg mL^{-1}). The sample was incubated at 37°C for 30 minutes and centrifuged at $1000 \times g$ for 10 minutes. The supernatant was collected and analysed for haemoglobin release by spectrophotometry at 416 nm. To obtain 0 and 100% haemolysis, 0.1 mL of the RBC dispersion was added to 0.9 mL of PBS and distilled water, respectively. The degree of haemolysis was determined using the following equation: $\text{Haemolysis (\%)} = (\text{ABS} - \text{ABS}_0)/(\text{ABS}_{100} - \text{ABS}_0) \times 100$, where ABS_{100} and ABS_0 are the absorbance of the solution at 100% and 0% haemolysis, respectively.

Cell cultures and treatments

The A549 and Calu-3 cell lines were purchased from American Type Culture Collection (Rockville, MD, USA) and were authenticated by LGC Standards (Sesto San Giovanni, Italy). The cells were cultured in DMEM with glutamax (Invitrogen, Carlsbad, California) supplemented with 10% FBS, 2 mM l-glutamine and 50 U mL^{-1} penicillin–streptomycin. Treatment of the cells was performed as previously reported.²⁹

MTT assay

A549 and Calu-3 cells were seeded onto 96-well plates (2×10^4 cells per well) and incubated with NPs (concentration range $0.1\text{--}0.75 \text{ mg mL}^{-1}$) for 24, 48 and 72 h. Then, cell viability was evaluated as metabolic activity using the MTT assay. The absorbance was measured at 540 nm using a microplate reader (Labsystems Multiskan, MS).

Biodistribution in mice

The biodistribution of the NPs was tested in forty-eight weeks old nude female mice obtained from Harlan (SanPietro al Natisone, Italy). The mice ($n = 4$) were housed five per cage and maintained on a 12 h light:12 h dark cycle (lights on at 7:00 a.m.) in a temperature-controlled room ($22 \pm 2^\circ\text{C}$) and with food

and water ad libitum. The present study was approved by the Animal Ethics Committee at National Cancer Institute – Foundation “G. Pascale”, Naples – Italy, following the guidelines of Italian law (D.L. 26/2014) and in agreement with the European Union policy for experimental animal care and use (Directive 2010/63/EU). After one week of acclimation to the housing conditions, the mice were distributed into three groups (10 animals per group) and injected with 3×10^5 B16F10 murine melanoma cells via the tail vein (lung colonization model). The mice used in the experiments were anesthetized with zolazepam (50 mg kg^{-1} i.p.), xylazine (20 mg kg^{-1}) and atropine sulphate (0.04 mg kg^{-1}). All efforts were made to minimize animal suffering.

After 1 week, the mice received one intravenous administration of saline (control), PEG-NPs, NH₂/PEG-NPs or NH₂/PEG NPs@HA loaded with DiD-Oil 0.2% w/w (dispersion in saline) into the caudal vein. The NP dose was 4 mg kg^{-1} (corresponding to $8 \mu\text{g}$ DiD-Oil per kg). The mice were sacrificed 24 h post injection and the main organs were collected (liver, spleen, and lungs). Then each organ was weighed and homogenized as previously reported.²⁹ The fluorescence intensities of the homogenized tissue samples were assessed by fluorimetry on a Cary Eclipse fluorescence spectrophotometer (Varian) at λ_{ex} of 650 nm and λ_{em} of 673 nm. Results are reported as fluorescence percent of the injected dose in each organ.

Statistical analysis

Unless otherwise stated, all data are shown as mean \pm standard deviation (SD). Two-way analysis of variance (ANOVA) was applied for comparison of three or more group means (Tukey's multiple comparisons test). A p-value of <0.05 was considered statistically significant. ***, **, and * display $p < 0.001$, $p < 0.01$, and $p < 0.05$, respectively. Origin software was used for data analysis.

Results and discussion

Polymer characterization and synthesis

Monoamino-PCL was obtained by classical ROP using hexanol as an initiator. The molecular weight was controlled by the CL/initiator molar ratio by designing a target value of around 4 kDa, close to the molecular weight of the PCL block in the mPEG–PCL copolymer. The actual molecular weight was calculated by ¹H NMR analysis as the ratio between the intensity of the resonance at 3.64 δ , associated with the –CH₂–OH methylene protons, and that of the resonance at 2.31 δ , associated with the –CH₂–CO– units in the PCL chain. The experimental M_n value was 4.2 kDa, very close to the theoretical value calculated from the CL/initiator molar ratio in the feed. GPC analysis confirmed the molecular weight, with a polydispersity index of 1.14, indicating a narrow molecular weight distribution. Subsequently, PCL was modified at the terminal hydroxyl group following the same pathway already described in the literature in the case of PEG30 (**Scheme S1**, ESI[†]). Briefly, monohydroxyl-PCL was first tosylated with tosyl chloride, then monoazide-PCL was obtained by substitution with sodium azide. The azide was finally reduced to an amine with triphenylphosphine. The reduction was followed by FTIR, where the complete disappearance of the azide band at 2107 cm^{-1} indicated complete conversion (**Figure S1**, ESI[†]). The structure and purity of PCL-NH₂ and the intermediates were confirmed by ¹H NMR analysis (**Figure S2**, ESI[†]).

The mPEG–PCL diblock copolymer (mPEG_{1k}–PCL_{4k}) was synthesized according to a standard procedure widely reported in the literature. (18)

Preparation and properties of amine-bearing NPs

The NPs were designed with the aim of manipulating the amine surface density and exposing PEG for effective stabilization. The NPs were prepared by nanoprecipitation of mPEG_{1k}–PCL_{4k} and NH₂-PCL_{4.2k}, alone or in a 1 : 1 ratio by weight, thus obtaining, respectively, PEGylated NPs (PEG-NPs), amine NPs (NH₂-NPs) and PEGylated/amine NPs (NH₂/PEG-NPs). In the following step, low molecular weight HA was spontaneously adsorbed on the top of the amine NPs (NH₂-NPs@HA and NH₂/PEG-NPs@HA as illustrated in **Scheme 1**) taking advantage of electrostatic interactions.

The NP codes and their properties are reported in **Table 1** and in **Figure 1**. In all cases, NPs with good yield and low PI were obtained. Their sizes and zeta potential values in water were affected by the type of polymer employed. The PEG-NPs were below 100 nm in diameter and showed a negative ζ , whereas the amine NPs were larger with a largely positive ζ . The NPs prepared from a 1:1 mixture by wt of mPEG–PCL and NH₂–PCL had a size comparable to that of the amine NPs but with an intermediate charge, presumably due to the presence of PEG chains shielding the primary amine groups. The larger size of the amine NPs can be reasonably attributed to the poor hydrophilicity of amine PCL as compared to PEG–PCL, which slows down acetone diffusion in water during the nanoprecipitation step.

Table 1 Properties of nanoparticles

Formulation code	Size (nm \pm SD)^b	PI	ζ (mV \pm SD)^b	Yield (%)
PEG-NPs	83 \pm 2	0.1	–2.5 \pm 0.7	98
NH ₂ -NPs	120 \pm 14	0.2	+33 \pm 1.4	95
NH ₂ /PEG-NPs ^a	117 \pm 3	0.1	+9.4 \pm 4.8	97
NH ₂ -NPs@HA	178 \pm 10	0.2	–28 \pm 3.7	94
NH ₂ /PEG-NPs@HA ^a	141 \pm 3	0.1	–10 \pm 2.5	92

^a Nanoparticles prepared with a NH₂-PCL/mPEG–PCL mixture at 1 : 1 ratio by weight. ^b SD was calculated on three different batches.

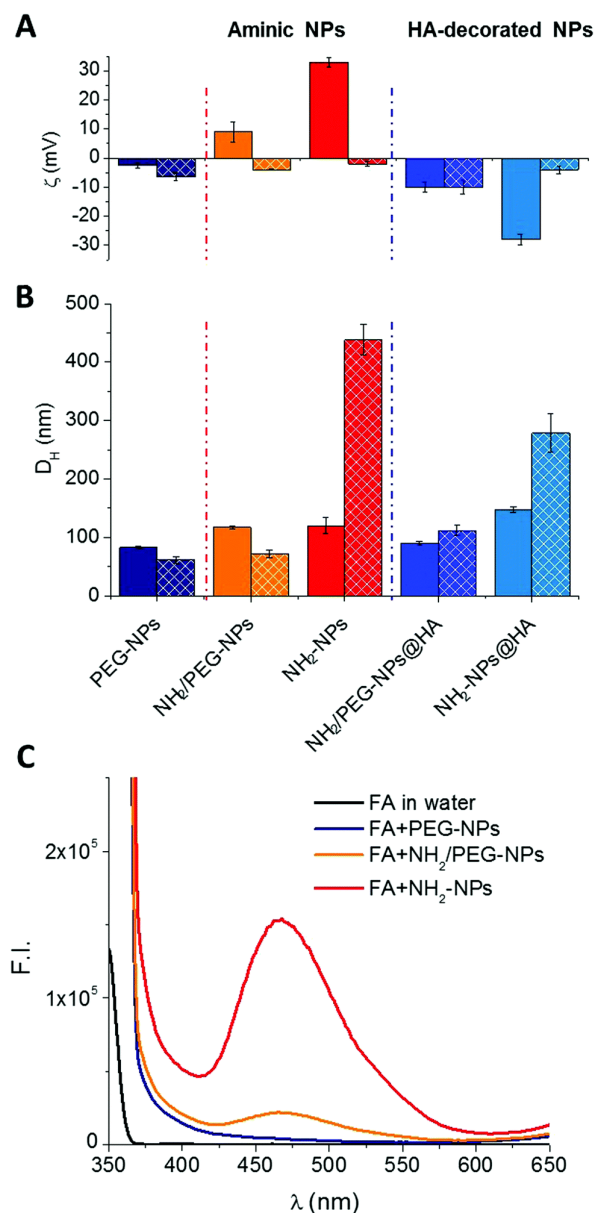


Figure 1 NP properties. (A) Zeta potential (ζ) and (B) hydrodynamic diameter (DH) of the NPs in water (full bars) and PBS at pH 7.4 (square bars). The results are the mean of three measurements obtained on three different NP batches \pm SD; (C) emission spectra (λ_{ex} 350 nm) of fluorescamine (FA) ($3 \mu\text{g mL}^{-1}$) in the presence of NPs. The F.I. maximum is dependent on the number of amine groups on the surface. The spectrum of FA is reported as a control.

The density of amino groups on the surface of the NPs was assessed by a fluorescamine-based assay (FA). Fluorescamine is a non-fluorescent molecule (ABS maximum at 350 nm) that emits fluorescence only in the presence of primary amines due to complex formation. As shown in **Figure 1C**, only the amine NPs induced FA emission due to the formation of hydrogen bonds on the NP surface, whereas no fluorescence was observed for the PEG-NPs. As expected, the number of amine groups on the surface was higher for the NH₂-NPs than the NH₂/PEG-NPs, in line with their composition and zeta potential values. These results further suggest that the amine groups on the surface are accessible also in the presence of PEG, thus giving a mixed amine/PEGylated surface.

Despite their net positive charge, cationic NPs are prone to aggregation in ion-rich media (and presumably also in biological fluids) due to perturbation of the ionic double shell.³¹ As shown in **Figure**

1B, the NH₂-NPs showed an apparent 3-fold increase of their mean size in PBS, which was limited by the presence of PEG in the NH₂/PEG-NPs. The size distribution trends (**Figure S3, ESI†**) clearly show that the NH₂-NPs severely aggregated in PBS giving rise to a new population around 2000 nm in size. To alter the ionic nanoenvironment around the NPs due to the presence of amine groups, negatively charged HA was adsorbed on their surface as recently proposed to stabilize cationic NPs.³² As shown in **Figure 1A**, HA reversed the ζ of the amine NPs from positive to negative values due to its electrostatic anchoring on the surface of the cationic NPs. HA decoration made it possible to limit the size increase in PBS only for NH₂/PEG-NPs due to the cooperative shielding effect of PEG (**Figure S3 in the ESI†**).

Fixed aqueous layer thickness measurements were performed on the PEGylated NPs to investigate the impact of composition on the orientation of the PEG/HA chains in the shell (**Figure 2**). The PEGylated NPs showed the lowest PEG thickness, whereas the NH₂/PEG-NPs were characterized by a two-fold larger thickness, thus suggesting a more extended orientation of the PEG chains on the NP shell. These results demonstrate that the presence of amino groups on the NP surface can critically affect the PEG conformation, offering a novel and additional tool to modulate the NP interface. The electrostatic interaction with HA macromolecules did not significantly alter the thickness of the hydrophilic shell, suggesting the intercalation of HA with the PEG chains.

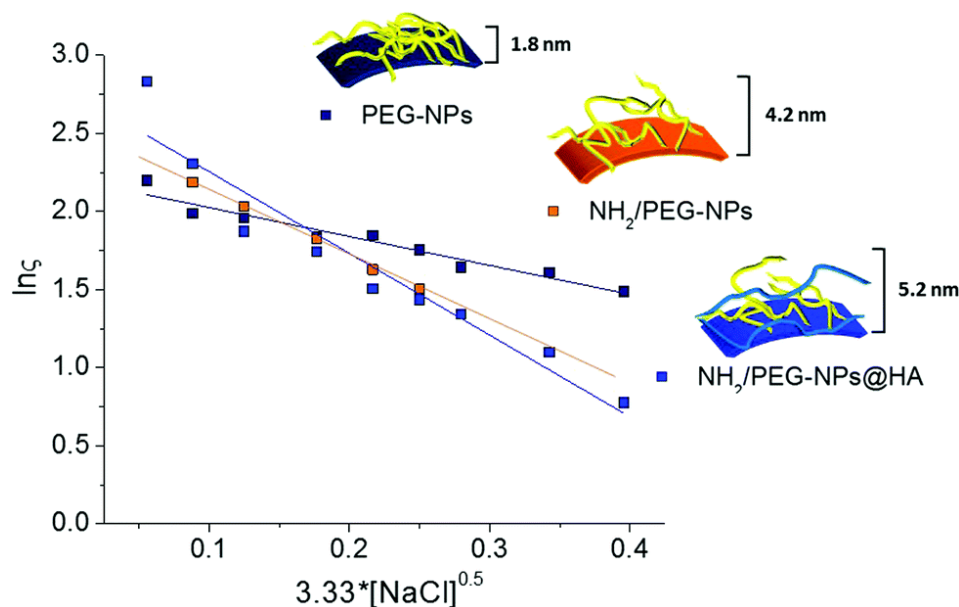


Figure 2 FALT measurements on the PEGylated NPs as assessed by monitoring zeta potential (ζ) at different NaCl concentrations (representative curves are shown). The slope of the interpolated straight line represents the thickness of the PEG shell in nm (d shell). FALT values are the mean of three measurements obtained on three different NP batches (SD was below 0.2 nm).

Interaction with blood components

To get preliminary insights into the behaviour of the NPs after i.v. injection, their interaction with human plasma over time was investigated (**Figure 3**). Indeed, the presence of ions and the formation of a protein corona may mask the surface of the NPs, imparting a specific biological identity. Consequently, these interactions should be considered, since they have a huge impact on the journey of the NPs in the body. As shown in **Figure 3A**, the amine-bearing NPs switched from net positive to negative values of ζ upon contact with plasma, which is suggestive of surface adsorption of the protein pool. Thereafter, all of the NP formulations stably displayed a negative ζ of around -10 mV. Accordingly, the DH of the amine NPs

in human plasma at 15 min slightly increased as compared to that in water, while for the HA-coated NPs, no significant change took place (**Figure 3B**). A progressive increase of size was observed in the case of the amine NPs and fully PEGylated NPs demonstrating that reorganization of the protein corona can occur over time.³³ The scattering of NP samples (**Figure 3C**) and the size distribution curves (**Figure S4, ESI†**) were not altered up to 48 h, except for the NH₂-NPs for which protein adsorption impacted remarkably on the particle-to-particle interaction, inducing aggregation. HA adsorption on the amine NPs alleviated aggregation, as shown previously for PBS. No significant effect of the NP features on the haemolysis of red blood cells was found (**Figure 3D**).

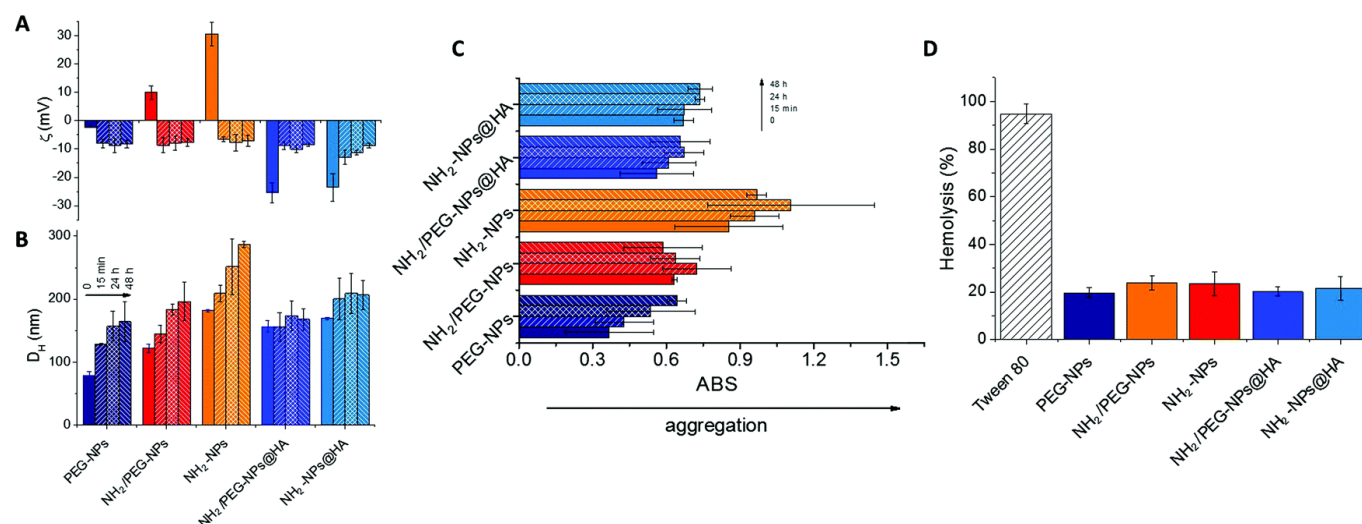


Figure 3 NP behaviour in human plasma: (A) zeta potential (ζ) and (B) hydrodynamic diameter (DH) of the NPs dispersed in human plasma at 37 °C; (C) scattering of the NPs in human plasma (ABS at 500 nm); (D) haemolytic activity of the NPs (Tween 80 is reported as a positive control). The results are the mean of three measurements obtained on three different NP batches \pm SD.

Overall, these results suggest that the biological identity of the amine NPs is far from the designed chemical identity and is remarkably affected by interactions with the plasma protein pool, as suggested previously for polyethylenimine-coated polymeric NPs and iron oxide NPs.

Based on the stability results, the PEGylated NPs (NH₂/PEG-NPs, its HA-coated counterpart and reference PEG-NPs) were selected for the following biological study. To track the NPs in cells and in vivo, fluorescent NPs loaded with DiD-Oil were prepared and characterized (**properties in ESI,† Table S1**).

Cell studies

As far as the impact of surface modification on cytotoxicity is considered, the colloidal properties (DH, PI and ζ) of the selected NPs in DMEM FBS+ were evaluated (**ESI,† Figure S5A and B**). None of the NPs tested aggregated in the medium and they all maintained a size below 250 nm. In analogy to the behaviour in human plasma, the NP surface charge switched to negative values due to electrostatic/hydrophobic adsorption of FBS proteins.

Cytotoxicity was assessed by the MTT assay on Calu-3 and A549 lung cancer cells in a range of NP concentrations upon 24, 48 and 72 h of treatment. The results in **Figure 4** show a dose- and time-dependent toxicity at the tested concentrations, which was much more evident in the Calu-3 cells (**Figure 4B**). These cells exhibited a higher sensitivity in response to NP treatment, independent of the NP composition. In fact, their viability upon exposure to the NPs decreased much more than that of the A549 cells at all tested NP concentrations. These results suggest that the NPs are presumably partially covered with FBS proteins, since their cytotoxicity is not fully attenuated as demonstrated for NPs coated with polyethyleneimine.³² These differences in sensitivity to NP treatment between cell types, which have been reported in the literature,³⁴ could be attributed to the molecular specificity of each cell type and the consequent biological response. A possible role could be played by the p53 expression levels, as we used two cell lines that express p53 (A549) or don't (Calu-3). Since it is already known that intracellular signalling pathways activated in response to cellular stress depend on the presence of p53,³⁵ it is possible to hypothesize that the differences in cell toxicity following NP treatment are due to the p53 status.

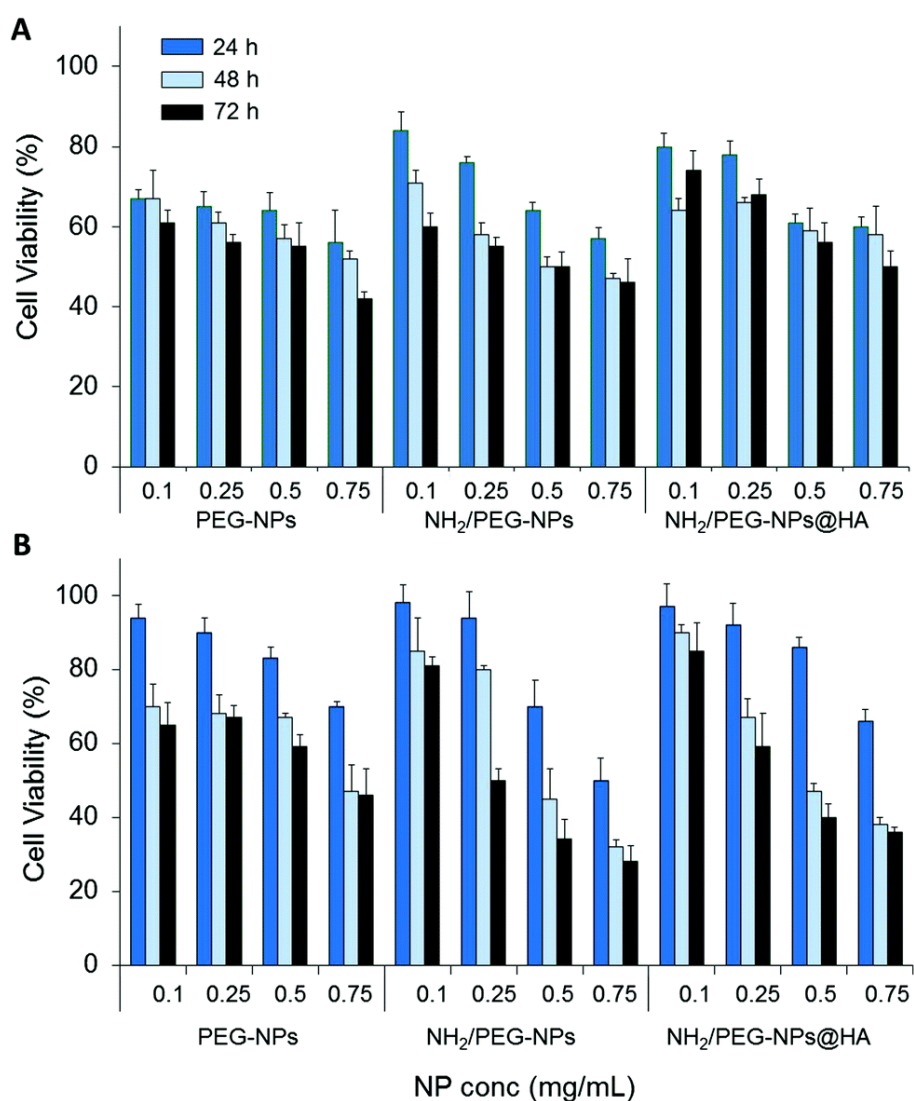


Figure 4 The viability of A549 (A) and Calu-3 (B) lung cancer cells upon exposure to increasing concentrations of NPs for 24, 48 and 72 h. After incubation, cell viability was evaluated using the MTT assay. The cell viability of the untreated control was set to 100%. The results are presented as percentage (mean \pm SEM) (n = 3) of the control cells.

HA-coated NPs can be accumulated in cancer cells overexpressing the CD44 receptor via receptor-mediated endocytosis. Since A549 cells express high levels of CD44, internalization of the non-coated and HA-coated NPs in this cell line was compared. The results (**ESI,† Figure S5C**) demonstrated no benefit of HA surface decoration, suggesting no targeting ability of the HA coating adsorbed on the NH₂/PEG-NPs and in line with the formation of a protein corona shielding HA-coated NPs/CD44 recognition.

Biodistribution in mice

After i.v. injection, the PEGylated NPs are expected to circulate for a long time, evading immune recognition and altering the biodistribution of their drug cargo. Besides size and shape, the fate of spherical PEGylated NPs is strictly dictated by their surface features, which regulate blood protein adsorption and the composition of the protein corona and drive the NPs to their final destination in the body.³⁶ It has been found that PEG–PCL NPs display different circulation times and, in turn, the dose fraction reaching the tumor in mice xenografts depends on the size and PEG surface conformation.³⁷ In fact, although designed to accumulate in solid tumours via the enhanced permeability and retention (EPR) effect, PEGylated NPs accumulate greatly in non-target organs of the MPS, i.e. the spleen and liver. This aspect is of utmost importance when targeting solid tumours in general, but much more relevant for lung metastasis since the capillary bed in the lungs is the first extravasation area that the NPs encounter after i.v. injection.³⁸

To understand the impact of the NP surface features on their lung accumulation, the biodistribution of i.v. injected NPs in a mouse model of B16F10 melanoma cell lung colonization, which is an experimental model for lung metastasis, was evaluated. DiD-Oil-loaded fluorescent NPs dispersed in saline were administered via the tail vein and the animals were sacrificed after 24 h. The spleen, liver and lungs (the target organ) were collected and processed, and their fluorescence evaluated. As clearly evidenced in **Figure 5**, the level of NPs in the MPS organs and in the lungs was strongly dependent on the NP properties. In fact, the NH₂/PEG-NPs accumulated to a higher extent in the lungs, where cancer cells are disseminated, as compared to the analogous HA-coated NPs, which preferentially distributed to the liver. This behaviour could not be due to size, since NH₂/PEG-NPs and NH₂/PEG-NPs@HA display comparable sizes. On the other hand, the smaller PEG-NPs were found in the MPS organs and lungs in comparable amounts. Thus, the presence of a cationic charge on the NPs and the switch to a new biological identity, driven by the dynamics of plasma protein fouling, may be responsible for their accumulation in the lungs and hopefully the in situ delivery of therapeutic cargo.

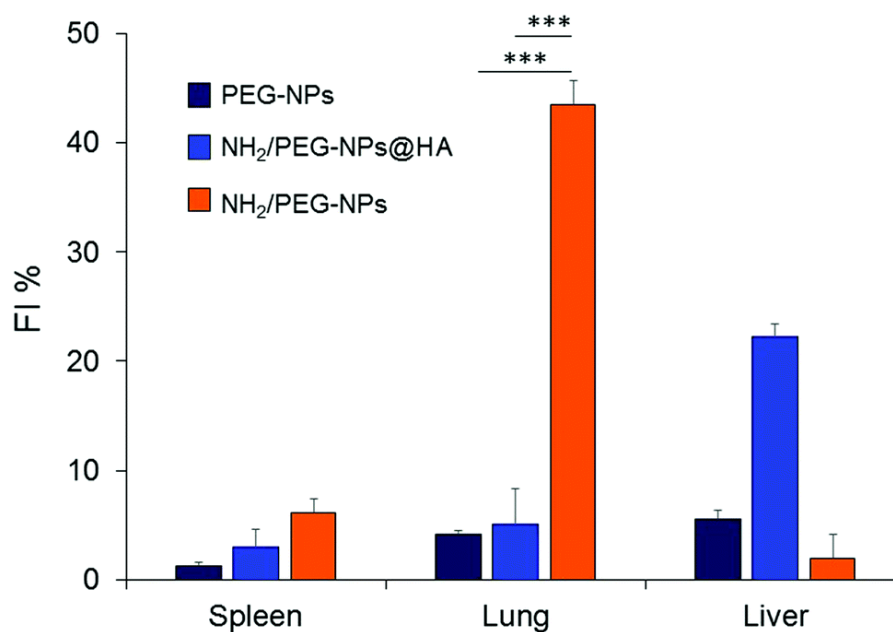


Figure 5 Quantitative *in vivo* organ distribution of intravenously injected DiD-oil-loaded NPs. Mice were i.v. injected with 3×10^5 B16F10 murine melanoma cells *via* the tail vein and treated with NPs in saline (4 mg Kg^{-1}) after 1 week (lung colonization model). The fluorescence of the treated organs was assessed at λ_{ex} of 650 nm and λ_{em} of 673 nm. The results are the mean of three measurements \pm SD

Conclusions

In this work, we have prepared a panel of polymeric PCL-based amine NPs with different composition and charge, investigating their properties both *in vitro* and *in vivo*. Size, zeta potential, shell features and interaction with proteins were remarkably affected by the presence of primary amines, PEG chains and a HA coating on the surface. The NPs were well tolerated by human red blood cells, while showing different cytotoxicity profiles against lung cancer cells. Finally, *in vivo* biodistribution studies demonstrated a much higher accumulation of cationic/PEGylated NPs at the targeted organ. Taken together, the strategy proposed here paves the way to the development of a novel class of positively-charged PEGylated NPs with great potential in the delivery of chemotherapeutics at different disease stages.

Acknowledgments

This work was supported by Italian Association for Cancer Research (IG2014#15764).

Conflicts of interest

There are no conflicts to declare.

References

1 M. S. Singh, S. N. Tammam, M. A. Shetab Boushehri and A. Lamprecht, *Pharmacological Research*, 2017, **126**, 2-30.

- 2 S. Wilhelm, A. J. Tavares, Q. Dai, S. Ohta, J. Audet, H. F. Dvorak and W. C. W. Chan, *Nature Reviews Materials*, 2016, **1**, 16014.
- 3 E. Blanco, H. Shen and M. Ferrari, *Nature Biotechnology*, 2015, **33**, 941.
- 4 N. Bertrand and J. C. Leroux, *Journal of Controlled Release*, 2012, **161**, 152-163.
- 5 N. H. Abd Ellah and S. A. Abouelmagd, *Expert Opinion on Drug Delivery*, 2017, **14**, 201-214.
- 6 N. Hoshyar, S. Gray, H. Han and G. Bao, *Nanomedicine : nanotechnology, biology, and medicine*, 2016, **11**, 673-692.
- 7 A. Verma and F. Stellacci, *Small*, 2010, **6**, 12-21.
- 8 C. Bantz, O. Koshkina, T. Lang, H.-J. Galla, C. J. Kirkpatrick, R. H. Stauber and M. Maskos, *Beilstein Journal of Nanotechnology*, 2014, **5**, 1774-1786.
- 9 J. V. Jokerst, T. Lobovkina, R. N. Zare and S. S. Gambhir, *Nanomedicine (London, England)*, 2011, **6**, 715-728.
- 10 R. Gref, A. Domb, P. Quellec, T. Blunk, R. H. Muller, J. M. Verbavatz and R. Langer, *Advanced Drug Delivery Reviews*, 2012, **64**, 316-326.
- 11 R. Gref, M. Lück, P. Quellec, M. Marchand, E. Dellacherie, S. Harnisch, T. Blunk and R. H. Müller, *Colloids and Surfaces B: Biointerfaces*, 2000, **18**, 301-313.
- 12 S. Mishra, P. Webster and M. E. Davis, *European Journal of Cell Biology*, 2004, **83**, 97-111.
- 13 C. Conte, I. d'Angelo, A. Miro, F. Ungaro and F. Quaglia, *Current topics in medicinal chemistry*, 2014, **14**, 1097-1114.
- 14 P. Grossen, D. Witzigmann, S. Sieber and J. Huwyler, *Journal of Controlled Release*, 2017, **260**, 46-60.
- 15 K. Zhang, X. Tang, J. Zhang, W. Lu, X. Lin, Y. Zhang, B. Tian, H. Yang and H. He, *Journal of controlled release : official journal of the Controlled Release Society*, 2014, **183**, 77-86.
- 16 F. Ungaro, C. Conte, L. Ostacolo, G. Maglio, A. Barbieri, C. Arra, G. Misso, A. Abbruzzese, M. Caraglia and F. Quaglia, *Nanomedicine-Nanotechnology Biology and Medicine*, 2012, **8**, 637-646.
- 17 C. Conte, I. Fotticchia, P. Tirino, F. Moret, B. Pagano, R. Gref, F. Ungaro, E. Reddi, C. Giancola and F. Quaglia, *Colloids Surf B Biointerfaces*, 2016, **141**, 148-157.

- 18 A. Venuta, F. Moret, G. Dal Poggetto, D. Esposito, A. Fraix, C. Avitabile, F. Ungaro, M. Malinconico, S. Sortino, A. Romanelli, P. Laurienzo, E. Reddi and F. Quaglia, *Eur J Pharm Sci*, 2018, **111**, 177-185.
- 19 R. B. Campbell, D. Fukumura, E. B. Brown, L. M. Mazzola, Y. Izumi, R. K. Jain, V. P. Torchilin and L. L. Munn, *Cancer Research*, 2002, **62**, 6831.
- 20 B. Chen, W. Le, Y. Wang, Z. Li, D. Wang, L. Ren, L. Lin, S. Cui, J. J. Hu, Y. Hu, P. Yang, R. C. Ewing, D. Shi and Z. Cui, *Theranostics*, 2016, **6**, 1887-1898.
- 21 H.-X. Wang, Z.-Q. Zuo, J.-Z. Du, Y.-C. Wang, R. Sun, Z.-T. Cao, X.-D. Ye, J.-L. Wang, K. W. Leong and J. Wang, *Nano Today*, 2016, **11**, 133-144.
- 22 G. Wang, Y. Chen, P. Wang, Y. Wang, H. Hong, Y. Li, J. Qian, Y. Yuan, B. Yu and C. Liu, *Acta Biomaterialia*, 2016, **29**, 248-260.
- 23 Q. Sun, T. Ojha, F. Kiessling, T. Lammers and Y. Shi, *Biomacromolecules*, 2017, **18**, 1449-1459.
- 24 T. Stylianopoulos, K. Soteriou, D. Fukumura and R. K. Jain, in *Annals of Biomedical Engineering*, 2013, vol. 41, pp. 68-77.
- 25 E. Bilensoy, *Expert Opinion on Drug Delivery*, 2010, **7**, 795-809.
- 26 A. Reisch, A. Runser, Y. Arntz, Y. Mély and A. S. Klymchenko, *ACS nano*, 2015, **9**, 5104-5116.
- 27 G. Caracciolo, O. C. Farokhzad and M. Mahmoudi, *Trends in biotechnology*, 2017, **35**, 257-264.
- 28 J. Lazarovits, Y. Y. Chen, E. A. Sykes and W. C. Chan, *Chemical communications*, 2015, **51**, 2756-2767.
- 29 A. Russo, S. Maiolino, V. Pagliara, F. Ungaro, F. Tatangelo, A. Leone, G. Scalia, A. Budillon, F. Quaglia and G. Russo, *Oncotarget*, 2016, **7**, 79670-79687.
- 30 R. Mahou and C. Wandrey, *Polymers*, 2012, **4**, 561.
- 31 T. L. Moore, L. Rodriguez-Lorenzo, V. Hirsch, S. Balog, D. Urban, C. Jud, B. Rothen-Rutishauser, M. Lattuada and A. Petri-Fink, *Chemical Society Reviews*, 2015, **44**, 6287-6305.
- 32 S. Maiolino, A. Russo, V. Pagliara, C. Conte, F. Ungaro, G. Russo and F. Quaglia, *J Nanobiotechnology*, 2015, **13**, 29.
- 33 G. J. Pillai, M. M. Greeshma and D. Menon, *Colloids and Surfaces B: Biointerfaces*, 2015, **136**, 1058-1066.

34 S. Lanone, F. Rogerieux, J. Geys, A. Dupont, E. Maillot-Marechal, J. Boczkowski, G. Lacroix and P. Hoet, *Particle and Fibre Toxicology*, 2009, **6**, 14-14.

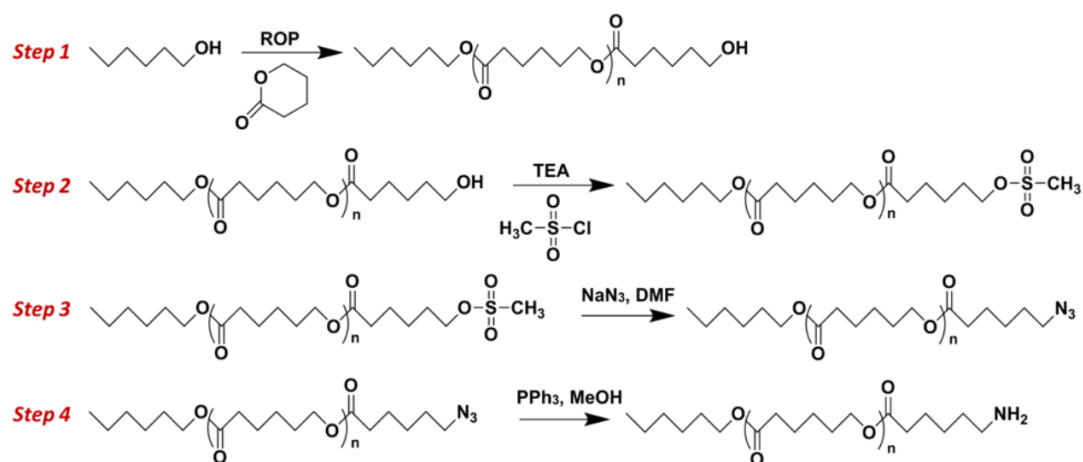
35 A. Russo and G. Russo, *International Journal of Molecular Sciences*, 2017, **18**, 140.

36 H. R. Lakkireddy and D. Bazile, *Advanced Drug Delivery Reviews*, 2016, **107**, 289-332.

37 X. J. Du, J. L. Wang, W. W. Liu, J. X. Yang, C. Y. Sun, R. Sun, H. J. Li, S. Shen, Y. L. Luo, X. D. Ye, Y. H. Zhu, X. Z. Yang and J. Wang, *Biomaterials*, 2015, **69**, 1-11.

38 J. L. Perry, K. G. Reuter, J. C. Luft, C. V. Pecot, W. Zamboni and J. M. DeSimone, *Nano letters*, 2017, **17**, 2879-2886.

Supplementary materials



Scheme S1. Synthetic strategy for PCL-NH₂.

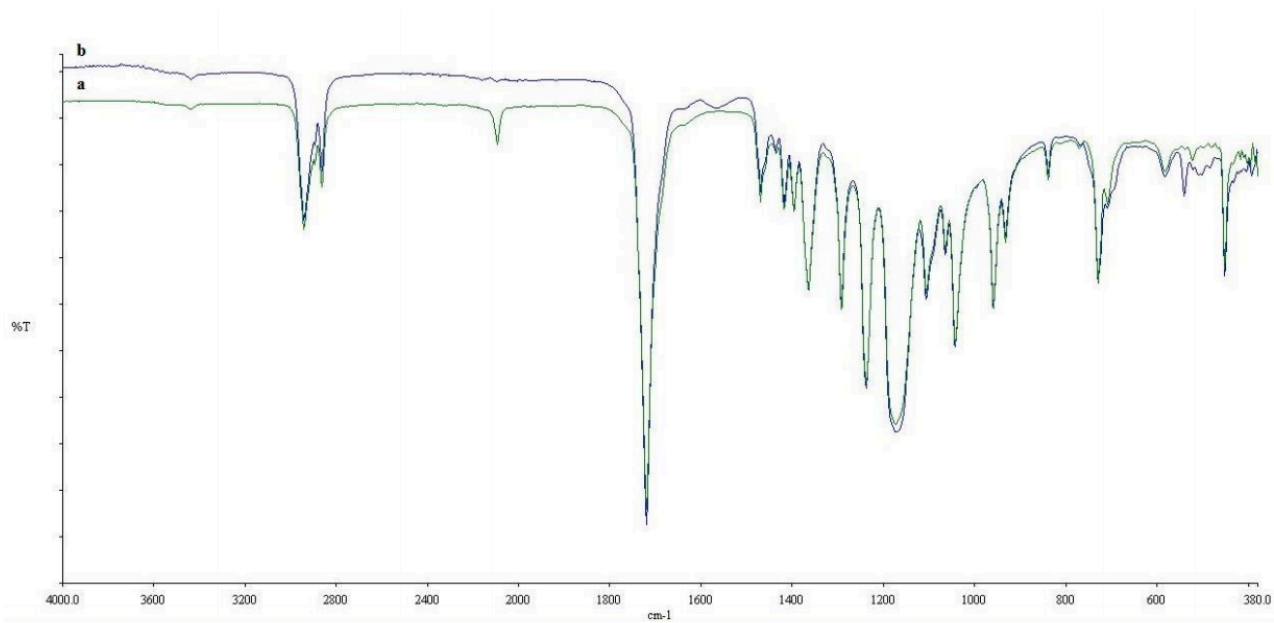


Figure S1. FTIR spectra of PCL-N₃ (a) and PCL-NH₂ (b)

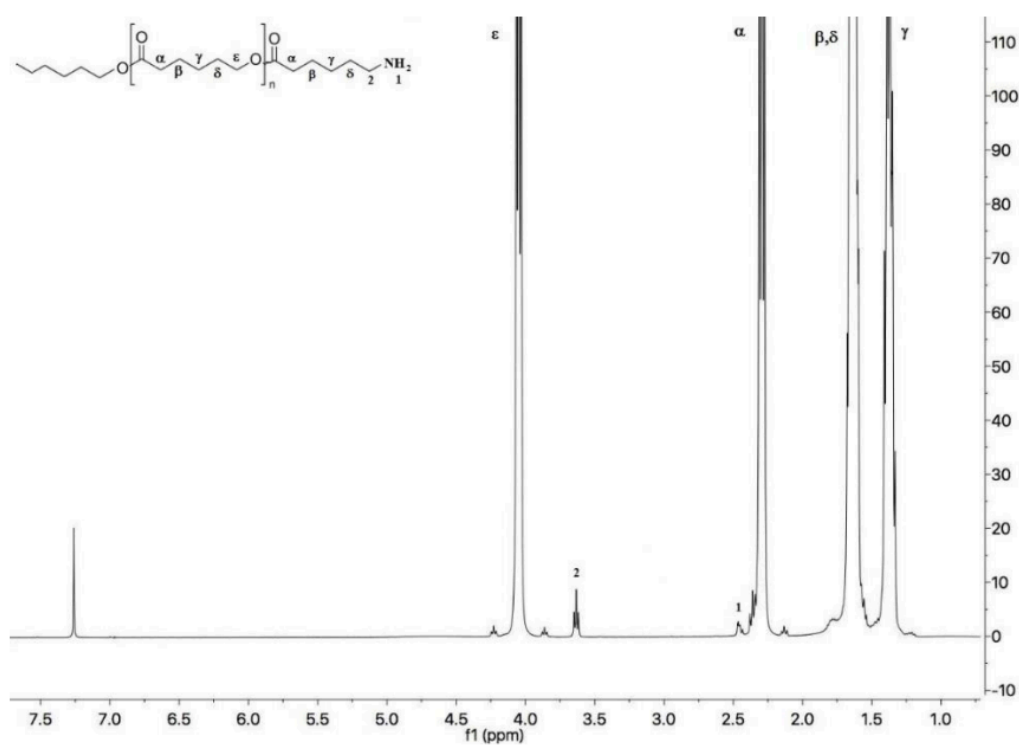


Figure S2. ¹H NMR spectrum of PCL-NH₂ (solvent: CDCl₃)

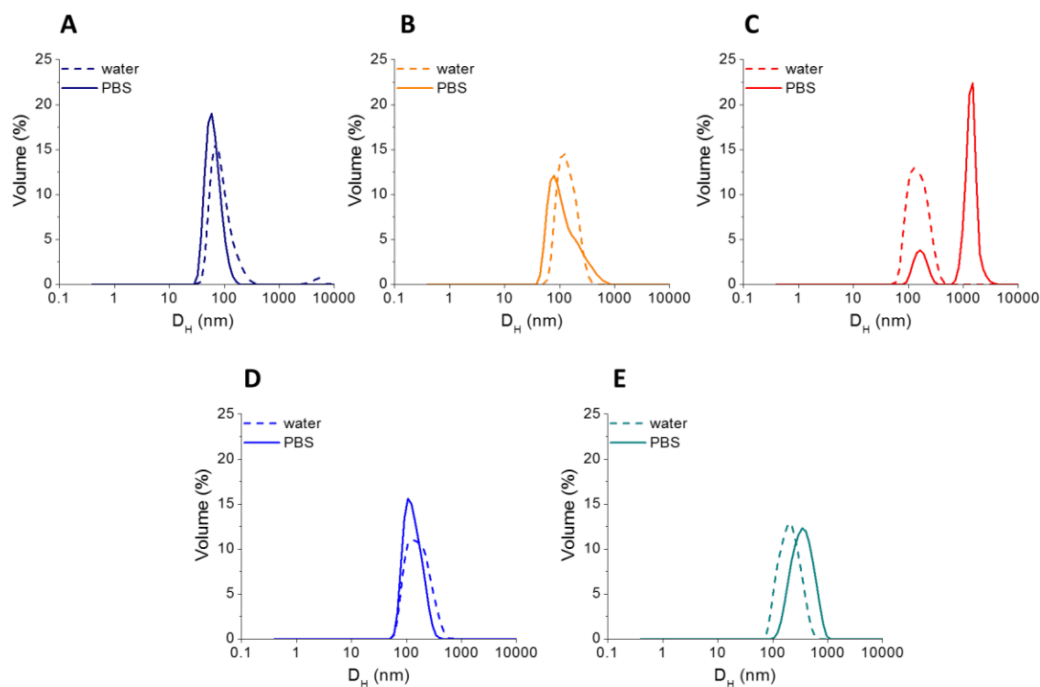


Figure S3. Distribution curves of PEG-NPs (A), NH₂/PEG-NPs (B), NH₂-NPs (C), NH₂/PEG-NPs@HA (D) and NH₂-NPs@HA (E) in water and in PBS pH 7.4 after 30 minutes of incubation at 37 °C.

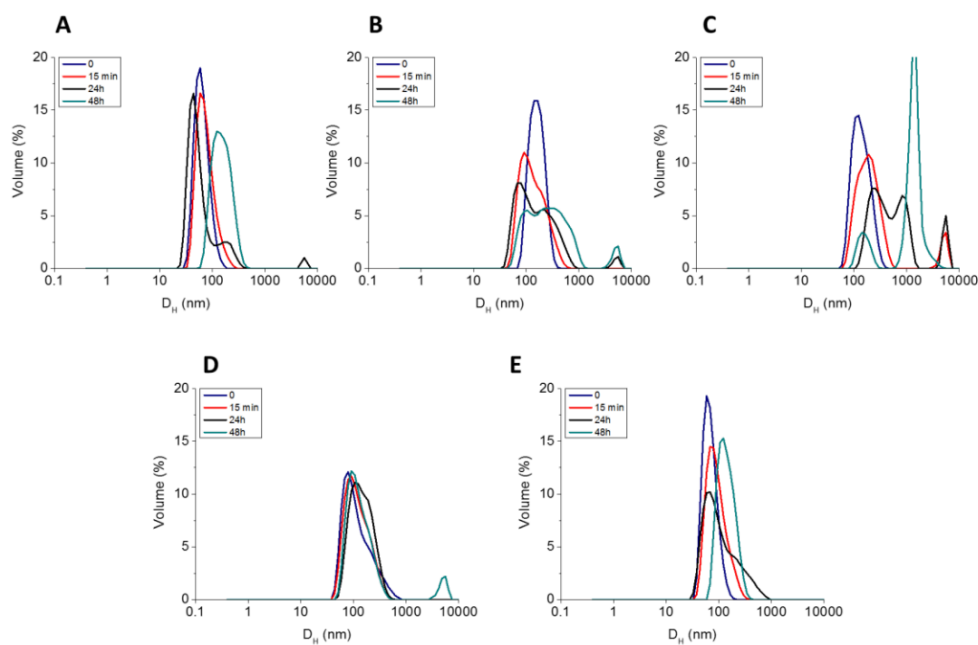


Figure S4. Distribution curves of PEG-NPs (A), NH₂/PEG-NPs (B), NH₂-NPs (C), NH₂/PEG-NPs@HA (D) and NH₂-NPs@HA (E) in human plasma along time.

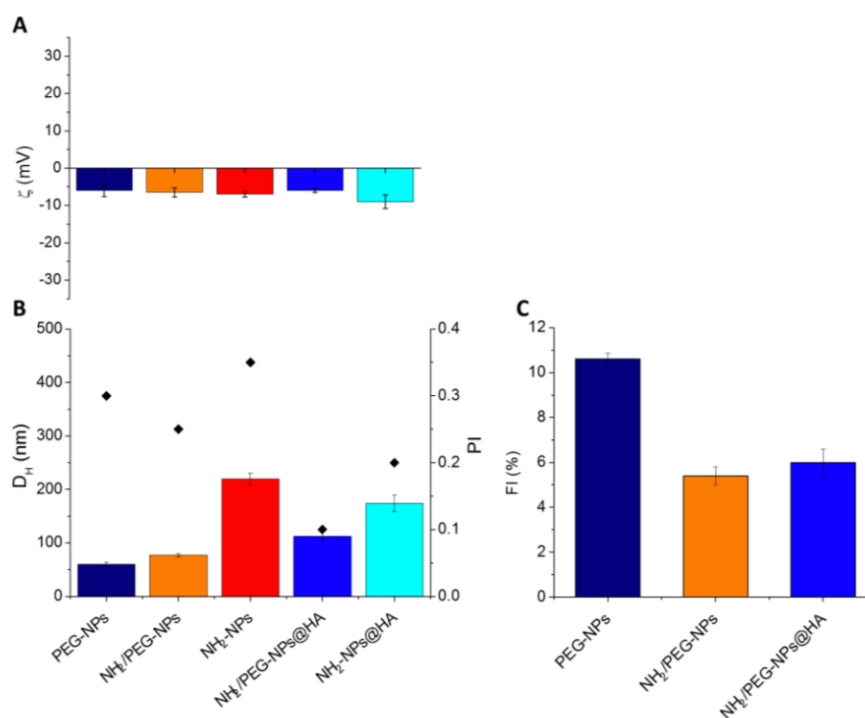


Figure S5. NPs properties in DMEM+FBS. A) Zeta potential (ζ); B) mean diameter (D_H); C) uptake of DiD-Oil loaded NPs in A549 cells after 4 h ($[NPs]=0.5$ mg/mL). Results are the mean of three measurements obtained on three different NP batches.

Table S1. Properties of Did-Oil loaded nanoparticles

Formulation code	Size (nm \pm SD)	PI	ζ (mV \pm SD)	Actual load mg Did-Oil/100 mg NPs	Encaps. Eff (%)
Did-Oil/PEG-NPs	119 \pm 8	0.2	-8 \pm 4	0.19	95
Did-Oil/NH ₂ /PEG-NPs ^a	121 \pm 12	0.2	+8 \pm 3	0.19	95
Did-Oil/NH ₂ /PEG-NPs@HA	124 \pm 11	0.1	-12 \pm 4	0.20	98

^aNH₂-PCL/mPEG-PCL ratio was 1:1 by weight

7 Surface Exposure of PEG and Amines on Biodegradable Nanoparticles as a Strategy to Tune Their Interaction with Protein-Rich Biological Media ⁴

Introduction

Polyethylene glycol (PEG)-coated biodegradable nanoparticles (NPs) based on amphiphilic block copolymers are earning increased attention in the nanodelivery field due to their complete degradability in the body, ease of processing, and synthesis scalability. Owing to their core-shell structure, the hydrophobic inner compartment can host single or multiple drug(s), protects the payload from the harsh environment in the body, and ensures sustained release. On the other hand, the hydrophilic outer shell can be tailored toward deliberate interactions with the biological environment, besides providing superior physical stability to the entire manufacturing process (1,2). The effects of PEGylation are closely related to the PEG molecular weight, the number of PEG chains located on NP surface, and the corresponding orientation (brush/mushroom), each of which can be affected by the preparation method (3,4).

For nanomedical approaches that imply intravenous NP administration, PEGylation is the most common strategy to extend their half-life, since the hydrophilic PEG fringe hinders adsorption of opsonin on NP surface, thus avoiding prompt recognition by the mononuclear phagocyte system (5,6). PEGylation is also useful for improving NP transport through protein-rich gel barriers in the body (7,8). Precise PEG physico-chemical properties and conformation on the particle surface are needed to effectively evade interaction with mucin and facilitate NP transport through mucus-covered epithelial barriers.

One of the drawbacks of PEGylated NPs is that cell internalization is impaired, which decreases the delivery of the drug payload to intracellular targets. To overcome poor cell uptake, the preeminent strategy is the decoration of NPs with ligands that target receptors on the cell surface, thereby allowing for internalization via receptor-mediated endocytosis (9). Recently, we have explored the modification of the surface features of biodegradable PEGylated NPs made of poly(ϵ -caprolactone) (PCL) in view of their application as a drug delivery platform. The introduction of amine groups on the surface, which imparts a positive charge to NPs, could in fact become an additional tool to expand the possibility to manipulate NP properties and their interaction with the bioenvironment. Advantages of cationic NPs are mainly related to their unique ability to penetrate deeply inside tumor tissue (10,11) and bacterial biofilms, which could expand the arsenal of nanotools for the delivery of drugs through different routes (12,13). Despite their potential, the strategies proposed thus far to build cationic NPs are limited, mainly relying on the adsorption of cationic surfactants, polymers, or phospholipids on the surface of preformed biodegradable nanotemplates (14). Only recently, NPs prepared from ammonia-terminated (15) and amine-terminated biodegradable polymers have been reported (16). Envisaging an application of amine-bearing NPs in cancer, we demonstrated that size, surface charge, shell thickness, and interaction with the human serum of these NPs were remarkably affected by the presence of PEG chains on the surface (16).

⁴The work presented in this paragraph has been published as: Surface Exposure of PEG and Amines on Biodegradable Nanoparticles as a Strategy to Tune Their Interaction with Protein-Rich Biological Media
Claudia Conte, Giovanni Dal Poggetto, Benjamin J. Swartzwelter, Diletta Esposito, Francesca Ungaro, Paola Laurienzo, Diana Boraschi and Fabiana Quaglia
Nanomaterials, Volume 9, September 2019, 1354
<https://doi.org/10.3390/nano9101354>

In terms of interactions with the biophase, it is expected that manipulation of the NP chemical identity would result in dramatic variations to its biological behaviour. In fact, interaction with the biological environment results in the formation of a biomolecular corona around NPs, which drives their in vivo behavior, cytotoxicity, immunotoxicity and activity (17,18). Proteins are key players in this phenomenon and the presence/absence of protein–NP interactions should not be overlooked. For instance, the great majority of NPs tested in cell cultures comes in contact with a protein-rich medium (e.g., protein from fetal bovine serum-FBS), which can get adsorbed on their surface, thereby changing their properties. This aspect is often poorly addressed or ignored when interpreting biological data. Consequently, linking chemical identity to biological behavior becomes unreliable, making the design of NPs with a particular delivery requirement a challenging task.

To fully understand the interaction of the amine-functionalized NPs with biological systems, we have developed a panel of amine-functionalized PEGylated NPs with different PEG lengths, and assessed their properties with specific regard given to their surface features, their behavior in protein solutions, their ability to permeate through gel-like barriers (tumor extracellular matrix and artificial mucus), and finally both their uptake by human innate immune cells as well as capacity to induce an inflammatory reaction (19).

Materials and Methods

Materials

Monomethoxy-polyethylene glycol with Mn 1.0 kDa (mPEG1.0k, Nanocs Inc., New York, NY, USA) and Mn 2.0 kDa (mPEG2.0k, Sigma-Aldrich, Milan, Italy) were dehydrated by azeotropic distillation with dry toluene in a Dean-Stark trap. Stannous-(2-ethylhexanoate)₂ (Sn(oct)₂), triethylamine (TEA), tosyl chloride (TsCl), triphenylphosphine (PPh₃), 1,4-butanediol, sodium azide and PEG5K-PCL5K were purchased from Sigma-Aldrich (Milan, Italy). ϵ -caprolactone (CL) (Sigma-Aldrich, Milan, Italy) was distilled over CaH₂ under vacuum. All solvents (analytical grade) were purchased from Sigma-Aldrich (Milan, Italy). N,N-dimethylformamide (DMF) and dichlorometane (DCM) were dried before use. Sodium chloride (NaCl), potassium chloride (KCl), calcium chloride (CaCl₂), sodium acetate (NaH₃C₂O₂), sodium bicarbonate (NaHCO₃), sodium citrate dihydrate, magnesium chloride hexahydrate (MgCl₂·6H₂O), sodium sulfate (Na₂SO₄), disodium phosphate (Na₂HPO₄), poloxamer 188 (Pluronic® F68), Human Serum Albumin (HSA), Type II porcine mucin, ECM gel from Engelbreth-Holm-Swarm murine sarcoma, diethylenetriaminepentaacetic acid (DPTA), RPMI 1640 amino acids solution, and egg yolk emulsion (microbiology) were purchased from Sigma-Aldrich (Milan, Italy). 3,3'-Dioctadecyloxycarbocyanine perchlorate (DiO) and 1,1'-Dioctadecyl-3,3,3',3'-tetramethylindocarbocyanine perchlorate (DiI) were purchased from Thermo Fisher Scientific (Monza, Milan, Italy).

Polymer Synthesis

Synthesis of Diamine-PCL (NH₂-PCL_{4k}-NH₂)

Step 1. Synthesis of PCL diol (HO-PCL_{4k}-OH).

1,4-butanediol (500 mg, 5.55 mmol), CL (22.49 g, 197 mmol), and SnOct₂ (449 mg, 1.1 mmol) were added in a flask under dry nitrogen. The polymerization was carried out under stirring at 120 °C for 24 h. The product was dissolved in 20 mL of DCM and precipitated in cold hexane; the polymer was collected and dried under vacuum. ¹H NMR (CHCl₃, δ in ppm): 1.29–1.78 (123H, m), 2.19–2.43 (74H, m), 3.92–4.21 (74H, t), 3.64 (4H, t) (Mn evaluated by ¹H NMR = 4344 dalton).

Step 2. Synthesis of ditosyl-PCL (Ts-PCL_{4k}-Ts).

HO-PCL_{4k}-OH (4.0 g, 0.92 mmol) was dissolved in 40 mL of DCM, then TEA (506 mg, 5.0 mmol) and TsCl (953 mg, 5.0 mmol) were added. The reaction was carried out under stirring at room temperature for 24 h. The polymer was dissolved in 15 mL of DCM and precipitated in cold hexane, then collected and dried under vacuum. ¹H NMR (CHCl₃, δ in ppm): 1.29–1.78 (123H, m), 2.19–2.43 (74H, m), 3.92–4.21(74H, t), 7.79 (4H, d), 7.49 (4H, d), 2.43 (6H, s).

Step 3. Synthesis of diazide-PCL (N₃-PCL_{4k}-N₃).

Ts-PCL_{4k}-Ts (1.0 g, 0.66 mmol) was dissolved in 15 mL of dry DMF, then NaN₃ (214 mg, 3.3 mmol) was added and the mixture was stirred overnight at 90 °C under nitrogen stream. The reaction mixture was then cooled down to room temperature and filtered, and DMF was removed under vacuum. The crude product was dissolved in 10 mL of DCM and washed twice with brine and twice with water in a separating funnel. The organic phase was dried over anhydrous Na₂SO₄, concentrated, poured into cold hexane, and the precipitated polymer was dried under vacuum. FTIR diagnostic band: 2107 cm⁻¹ (N₃ stretching) ¹H NMR (CHCl₃, δ in ppm): 1.29–1.78, (123H, m), 2.19–2.43, (74H, m); 3.92–4.21(74H, t).

Step 4. Synthesis of diamine-PCL (NH₂-PCL_{4k}-NH₂).

N₃-PCL_{4k}-N₃ (2.0 g) was dissolved in 50 mL of MeOH at 40 °C in a flask equipped with a nitrogen inlet and refrigerator, then PPh₃ (N₃/PPh₃ molar ratio = 1/3) was added and the reaction was carried out at 100 °C overnight. After removing the solvent by rotary evaporation, the polymer was dissolved in 10 mL of DCM, precipitated in cold hexane, collected, and finally dried under vacuum. The occurrence of the reaction was confirmed by FTIR through disappearance of the 2097 cm⁻¹ N₃ stretching band. ¹H NMR (CDCl₃, δ in ppm): 1.29–1.78, (123H, m), 2.19–2.43, (74H, m); 3.92–4.21(74H, t), 3.64 (4H, t), 2.48 (4H, broad). GPC analysis: Mw 4.8 kDa; Mn 4.2 kDa; Mw/Mn 1.1.

Polymer Characterization

FTIR analysis was performed with a Perkin-Elmer spectrometer (Paragon 500, Norwalk, CT, USA) equipped with a ZnSe attenuated total reflectance (ATR) crystal accessory. ¹H NMR spectra were recorded with a Bruker Avance DPX400 apparatus (Billerica, MA, USA) operating at 400 MHz at 25 °C and 128 NS. GPC analysis was performed using a Malvern-Viscotek GPC-MAX/TDA 305 quadruple detector array (Malvern, UK) equipped with a precolumn and two Phenogel columns (Phenomenex, Torrance, CA, USA) with exclusion limits of 106 and 103, respectively. THF solutions (100 μL) were filtered (PTFE 0.22 μm) and analyzed at a flow rate of 0.8 mL/min and a temperature of 35 °C. Calibration was based on a standard of polystyrene (Mw 104,959 Da).

Preparation and Characterization of Nanoparticles

PEGylated and amine/PEGylated NPs were prepared by the solvent-diffusion method. In particular, we prepared PEG-NPs series (PEG1K-PCL4K, PEG2K-PCL4K, and PEG5K-PCL5K), amine-NPs (NH₂-

PCL4k-NH₂), and amine/PEG-NPs (NH₂-PCL4k-NH₂ mixed with either PEG1K-PCL4K or PEG2K-PCL4K or PEG5K-PCL5K at 1:1 w/w ratio). Briefly, 10 mg of polymers were dissolved in 2 mL of acetone and added dropwise in 4 mL of water containing 4 mg of Pluronic® F68 as surfactant (0.1% w/v) under stirring. Acetone was removed under vacuum (5 min). Finally, the NP dispersion was transferred and stored in Eppendorf tubes at a final NP concentration of 2.5 mg/mL. NPs were tested shortly after preparation.

Fluorescent NPs giving FRET (FRET-NPs) were prepared by nanoprecipitation as described above with minor modifications. DiO ($\lambda_{\text{ex}} = 488 \text{ nm}$, $\lambda_{\text{em}} = 505 \text{ nm}$) and DiL ($\lambda_{\text{ex}} = 543 \text{ nm}$, $\lambda_{\text{em}} = 575 \text{ nm}$) were selected as FRET pair. Briefly, 100 μL from each DCM stock solution of DiO and DiL (1 mg/mL) were transferred to a clean vial and left to evaporate for 30 min until a colorless film was formed. Then, the copolymer solution in acetone was added. Nanoprecipitation was carried out as reported above. After preparation, NPs were filtered (RC 0.45 μm) to remove any free dye molecules. DiL and DiO loading inside NPs was assessed by dissolving 1 mg of freeze-dried NPs in 1 mL of DCM under stirring for 1 h. Samples were analyzed for DiO and DiL quantification by UV spectrophotometry at 488 and 543 nm, respectively. The concentration of DiL and/or DiO was calculated by means of a standard calibration curve derived for DCM solutions of the specific dye at known concentrations (0.5–60 $\mu\text{g/mL}$). Potential interference from DiL on DiO absorbance and vice versa were assessed by spiking a DiO solution in DCM with different amounts of DiL, or a DiL solution in DCM with different amount of DiO. To verify a possible interference of copolymers on DiL/DiO quantitative analysis, a weighted amount of unloaded NPs was dissolved in DCM and analyzed under the same conditions reported for the dyes.

The hydrodynamic diameter (DH), polydispersity index (PI), and zeta potential (ζ) of NPs were determined on a Zetasizer Nano ZS (Malvern Instruments Ltd.). Results are reported as the mean of three separate measurements of three different batches ($n = 9$) \pm standard deviation (SD).

Pluronic® F68 associated to NPs was assessed by quantitative ¹H NMR. After preparation, NPs were centrifuged at 2300 \times g for 20 min and the supernatant containing unabsorbed surfactant was lyophilized. The obtained solid was dissolved in D₂O and analyzed by ¹H NMR. The quantitative determination of Pluronic® F68 was achieved by comparing the integral of –CH₃ protons at 1.23 ppm in the samples with the corresponding signal of a spectrum of pure Pluronic® F68 of a known concentration (2 mg/mL). The amount of Pluronic® F68 absorbed on the NP surface was determined indirectly by the difference between the initial amount of Pluronic® F68 (4 mg) and the calculated amount of residual Pluronic® F68 in solution.

Stability studies of NPs as prepared (0.5 mg/mL) were conducted over a 24-h time span by monitoring size, ζ , and scattering (absorbance at 500 nm on a UV-1800 spectrophotometer, Shimadzu Corporation, Tokyo, Japan).

Evaluation of NP Surface Features

Fixed aqueous layer thickness (FALT) measurements were based on the approximation of the Gouy–Chapman theory and carried out by monitoring the influence of ionic strength on the particle surface (20,21). Different amounts of NaCl stock solutions at different concentrations were added to an NP dispersion in water (0.5 mg/mL), and ζ of the samples was measured. A plot of $\ln(\zeta)$ against $3.33 \cdot [\text{NaCl}]^{0.5}$ results in a straight line, where the slope represents the thickness of the PEG shell in nm.

The amount of PEG on the NP surface was evaluated through ¹H NMR. Spectra were recorded for either NPs dispersed in D₂O (5 mg/mL) or dissolved in CDCl₃ (5 mg/mL). The amount was calculated by comparing the integral of the –CH₂– resonance at 3.6 ppm of PEG in D₂O with the corresponding signal

in CDCl₃. The -CH₂- integral relative to PEG was calculated considering the contribution of -CH₂- from Pluronic® F68:

$$\text{int. CH}_2(\text{PEG}) = \text{int. CH}_2(\text{total}) - 8 \times \text{int. CH}_2(\text{Plur})$$

where $8 \times \text{int. CH}_2(\text{Plur})$ was obtained from a pure Pluronic® F68 spectrum (ratio -CH₃/CH₂ = 1/8).

Interactions with Proteins

Interaction of NPs with HSA or mucin was assessed by fluorescence spectroscopy, DLS measurements and turbidimetry analyses. For interaction with HSA, 200 μL of NPs (2.5 mg/mL) were mixed with 100 μL of HSA stock solution in water (2 mg/mL) and 700 μL of water. The final concentrations of NPs and HSA in the samples were 500 and 200 μg/mL, respectively. For interaction with mucin, mucin powder was dispersed in water (0.16% w/v) and stirred overnight. Then, the dispersion was centrifuged at 2300× g for 20 min and the supernatant collected. Thereafter, 200 μL of NPs were mixed with 250 μL of mucin dispersion and water up to a final volume of 1 mL. The final concentrations of NPs and mucin in these samples were 500 μg/mL and 0.04% w/v, respectively (22). Control samples of HSA, mucin, and NPs were run as a control.

Fluorescence spectroscopy was used to assess the ‘quenching’ effect of NPs on the ability of certain residues of the protein to emit light. Following preparation, the samples were incubated at RT for 1 h. Then, the emission spectra were acquired (Ex = 278 nm) (RF-6000, Shimadzu Corporation, Tokyo, Japan) (3). At different time points (0, 4, and 24 h), size, ζ potential, and scattering were measured as described above.

Permeation of NPs through Gel-Like Barriers

The capacity of NPs to cross artificial mucus (AM) and a tumor ECM was investigated. The transport experiment was carried out by placing either artificial mucus (AM) (for composition, see SI) or ECM gel (from a murine sarcoma) in the upper chambers of Transwell®-12 well plates (12 mm diameter, polyester membranes with a 3.0 μm pore size), applying NPs, and monitoring the amount of NPs that diffused into the lower chamber (23). For transport through the AM, the lower chamber was filled with 1 mL of simulated interstitial lung fluid (SILF) (for composition, see Supplementary Information (SI)). For transport through the ECM gel, the lower chamber was filled with 1 mL of 0.01 M PBS (phosphate buffer saline, NaCl 0.138 M, KCl 0.0027 M), pH 7.4 at 25 °C. FRET-NPs (0.1 mL, 2.5 mg/mL) were placed on the top of gel layer (0.3 mL) and maintained at RT. At 0, 1, 4, and 24 h, the medium in the lower chamber was collected and the fluorescence emission spectra recorded at λ_{Ex} = 488 and 543 nm to determine the FRET efficiency ratio and the NP concentration, respectively.

To calculate the NP concentration in SILF and PBS, a calibration curve of DiL emission intensity at Ex = 543 nm against different known concentrations of NPs was generated for each formulation. FRET efficiency was calculated for DiO λ_{ex} = 488 nm emission spectra using the following equation (24):

$$\text{FRET efficiency} = \frac{\text{Intensity at } \lambda_{\text{em}} = 575 \text{ nm}}{\text{Intensity at } \lambda_{\text{em}} = 575 \text{ nm} + \text{Intensity at } \lambda_{\text{em}} = 505 \text{ nm}}$$

The stability of FRET-NPs in SILF and PBS was monitored until 24 h through the DLS measurements.

NP Interaction with Human Immune Cells

Monocyte Isolation

Human primary blood monocytes were isolated from healthy donors with informed consent. Briefly, peripheral blood mononuclear cells were separated from freshly obtained whole blood by gradient density centrifugation on Ficoll-Paque PLUS (GE healthcare, Bio-Sciences AB, Uppsala, Sweden). CD14 receptor-positive monocytes were further isolated by magnetic cell sorting using CD14 microbeads following the manufacturer's protocol (Miltenyi Biotec, Bergisch-Galdbach, Germany). Cell viability was assessed by trypan blue dye exclusion and determined to be >98%.

NP Uptake

Freshly isolated CD14⁺ monocytes were seeded in 24-well plates (Corning® Costar®; Corning Inc. Life Sciences, Oneonta, NY, USA) at 2×10^5 cells/well in 0.5 mL of Phenol Red-free RPMI 1640 medium (GIBCO by Life Technologies, Paisley, UK) supplemented with 5% heat-inactivated pooled human AB serum (Sigma-Aldrich) and 50 µg/mL gentamicin sulfate (GIBCO). After 24 h at 37 °C, the cells were washed and exposed for 2 h to 50 µg/mL of DiL-loaded NPs (NPs pre-treated for 1 h with 70% HSA). The extracellular media were then collected and the fluorescence intensity of DiL was measured at $\lambda_{ex}/\lambda_{em} = 543/575$ nm in a microplate reader (Cytation 3 imaging reader, Biotek, Winooski, VT, USA). The concentration of NPs in the extracellular compartment was calculated by means of a standard calibration curve derived for NP dispersions in the cell medium at known concentrations (0.5–50 µg/mL). For confocal microscopy, monocytes were seeded on glass cover slips and treated as described above. Following NP incubation, cells were fixed for 20 min in 3.7% formaldehyde, washed 3 times with PBS, and cover slips were mounted on slides with Vectashield mounting medium containing 4',6-diamidino-2-phenylindole (Vector Laboratories Inc., Burlingame, CA, USA). Confocal microscopy was conducted using a Zeiss LSM 700 confocal microscope.

Monocyte Activation

Isolated monocytes were seeded in 24-well culture plates at 5×10^5 cells/well in 1 mL of RPMI 1640 medium supplemented with 5% heat-inactivated human AB serum and 50 µg/mL gentamicin sulfate. Cells were exposed to NPs (pre-treated for 1 h with 10% human AB serum) ± 1 ng/mL LPS from *Escherichia coli* (*E. coli*, serotype O55:B5, Sigma-Aldrich) for 1 h. The concentration of NPs incubated in each well was calculated based upon the NP surface area as indicated in **Table S1**. After 24 h of incubation, supernatants were collected and frozen at -20 °C until use. Activation was assessed as release in the supernatant of the inflammatory/defensive cytokines Interleukin-1 beta (IL-1 β) and Tumor Necrosis Factor alpha (TNF α), measured by ELISA with commercially available kits (DuoSet ELISA, R&D Systems, Minneapolis, MN, USA) following the manufacturer's instructions.

Results and discussion

Synthesis and Characterization of the Polymers

The mPEG-PCL diblock copolymers were synthesized by classical ROP polymerization, using mPEG-OH of different molecular weights as an initiator. Theoretical molecular weights were in agreement with the values found by GPC and determined by ¹H NMR (M_n of PCL block was calculated from the ratio between intensities of the resonance associated to -O-CH₃ protons of mPEG end groups at 3.36 ppm and

–CH₂–CO– units in the PCL chain at 2.31 ppm) (**Table S2**). Diamine-PCL (H₂N-PCL-NH₂) was synthesized according to the scheme reported in **Figure 1a**.

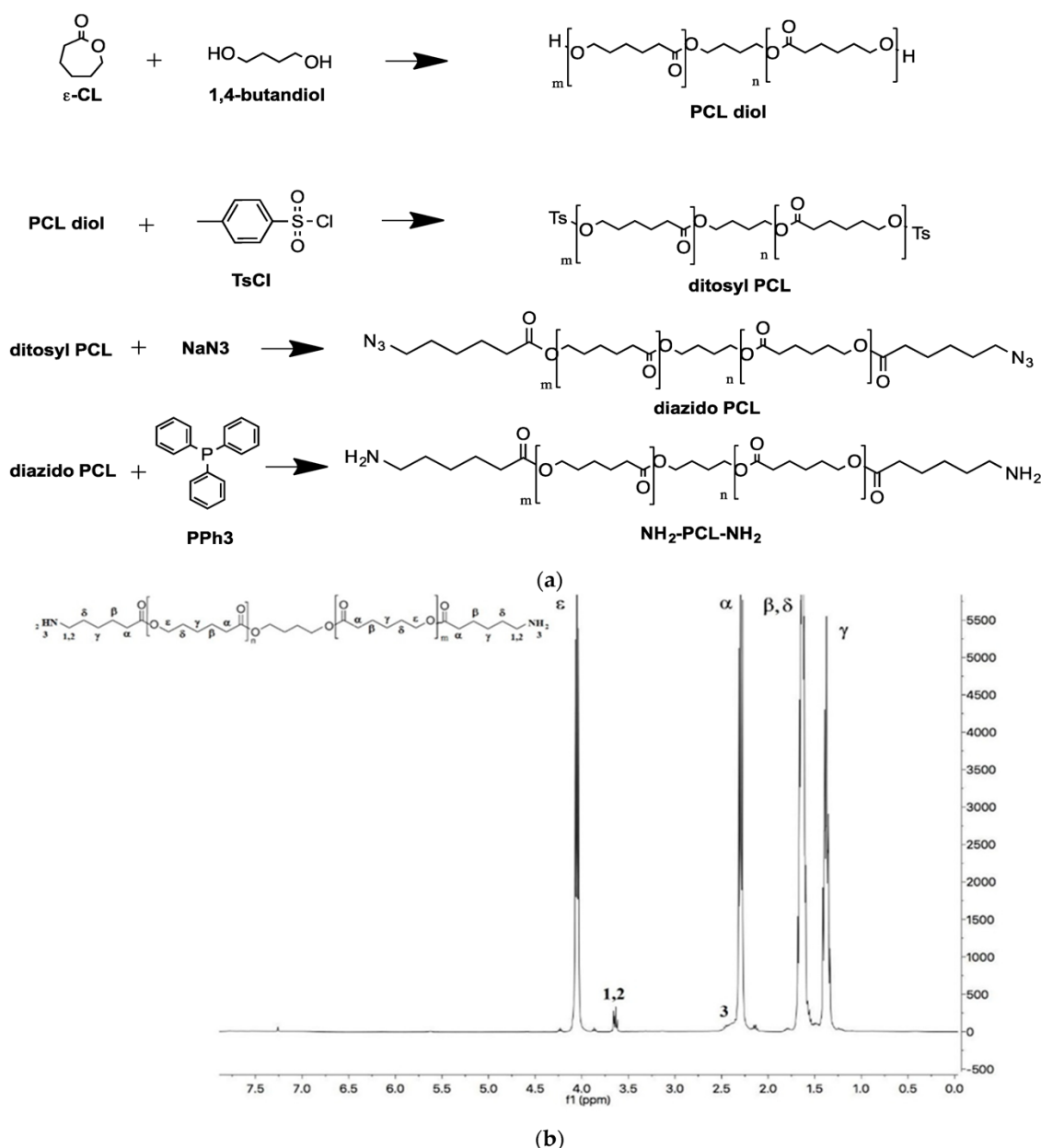


Figure 1. (a) Steps for the synthesis of NH₂-PCL-NH₂. (b) 1H NMR spectrum of NH₂-PCL-NH₂ in CDCl₃.

Full conversion of azide end-groups of N₃-PCL-N₃ precursor to amines was checked by FTIR through disappearance of the azide band at around 2100 cm⁻¹ (**Figure S1**). The structure of the final polymer was confirmed by 1H -NMR as reported in **Figure 1b**.

Nanoparticle Properties

A panel of core-shell NPs was obtained from 1:1 mixtures of NH₂-PCL-NH₂ and PEG-PCL (amine/PEG-NPs), and single NH₂-PCL-NH₂ (Amine-NPs) or PEG-PCL (PEG-NPs) mixtures as shown in **Figure 2**. PEGs of different molecular weights were employed in the study (1, 2, 5 kDa) while PCL moiety remained fixed (~4 kDa).

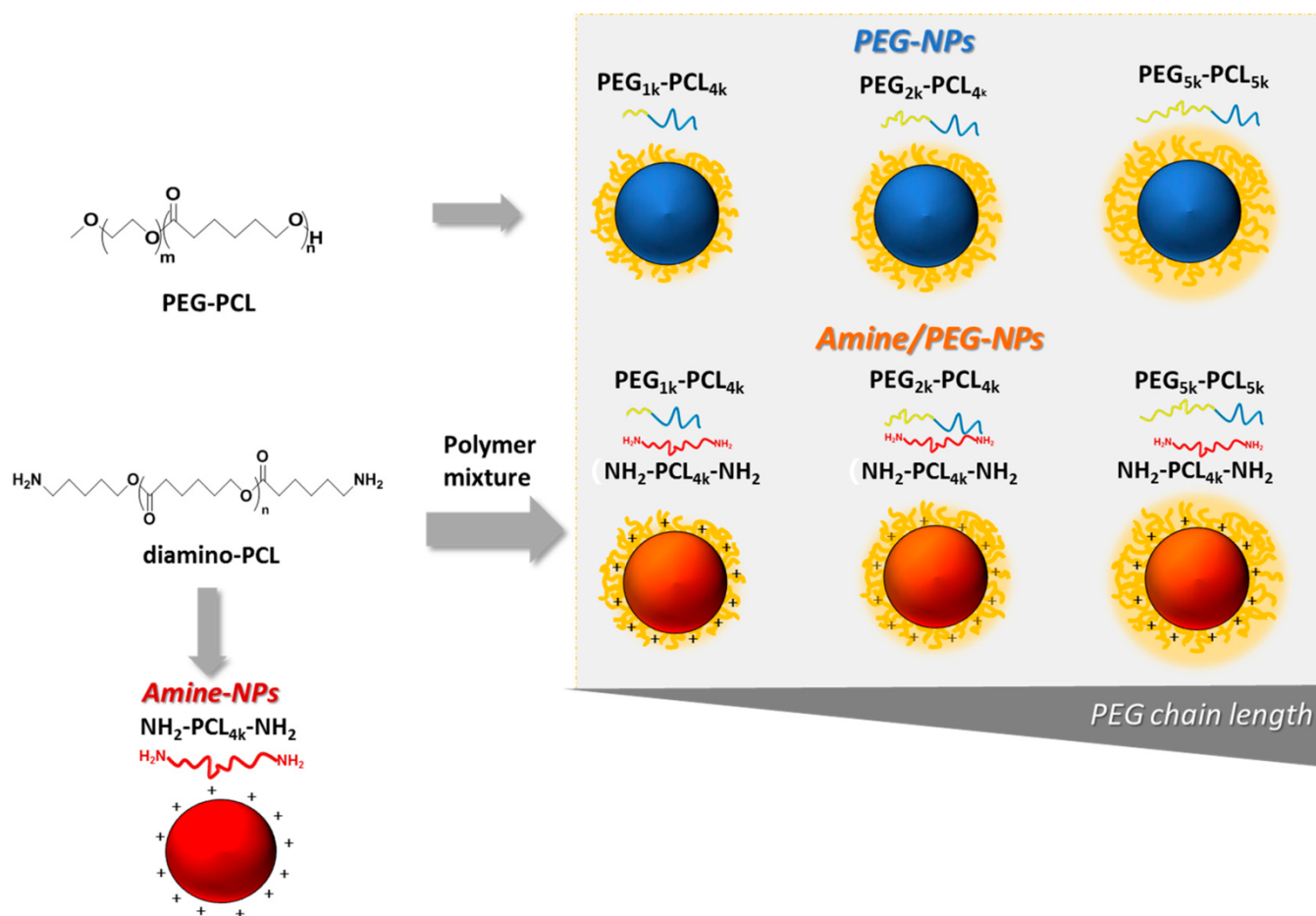


Figure 2. Schematic representation of nanoparticles tested in the study.

Pluronic® F68 was needed to fabricate amine-bearing NPs with good yields yet avoiding their premature aggregation. For comparison purposes, its use was extended to all the formulations tested. Indeed, poloxamer was associated to all the types of PEGylated NPs and its surface amount decreased as PEG MW increased (**Table 1**). NPs had an average size below 150 nm and a monomodal distribution, a finding also supported by the low PI values (**Table 1**). The increase of PEG MW in the copolymer decreased DH for both PEG-NPs and amine/PEG-NPs. A positive ζ was observed in the amine-bearing variants, which was decreased in the amine/PEG series, especially at increasing PEG MW. As expected, PEG-NPs had a negative ζ .

Table 1. Colloidal properties of NPs. Values are expressed as mean \pm SD of three different batches.

	Code	Composition	Yield (%)	Poloxamer ² (mg)	D _H ³ (nm \pm SD)	PI ³	ζ ⁴ (mV \pm SD)
PEG-NPs	PEG _{1K} -NPs	PEG _{1K} -PCL _{4K}	80	2.2	78 \pm 0.3	0.224	-10.2 \pm 2.0
	PEG _{2K} -NPs	PEG _{2K} -PCL _{4K}	95	1.3	44 \pm 1.3	0.160	-17.1 \pm 1.6
	PEG _{5K} -NPs	PEG _{5K} -PCL _{5K}	98	1.9	44 \pm 3.6	0.175	-7.4 \pm 1.9
Amine-NPs	Am-NPs	NH ₂ -PCL _{4K} -NH ₂	82	-	134 \pm 0.3	0.128	34.3 \pm 1.3
Amine/PEG-NPs ¹	Am/PEG _{1K} -NPs	NH ₂ -PCL _{4K} -NH _{2k}	93	2.4	121 \pm 2.8	0.191	28.6 \pm 1.0
	Am/PEG _{2K} -NPs	PEG _{1K} -PCL _{4K} -NH ₂ -PCL _{4K} -NH ₂	95	1.0	99 \pm 5.9	0.257	20.0 \pm 2.3

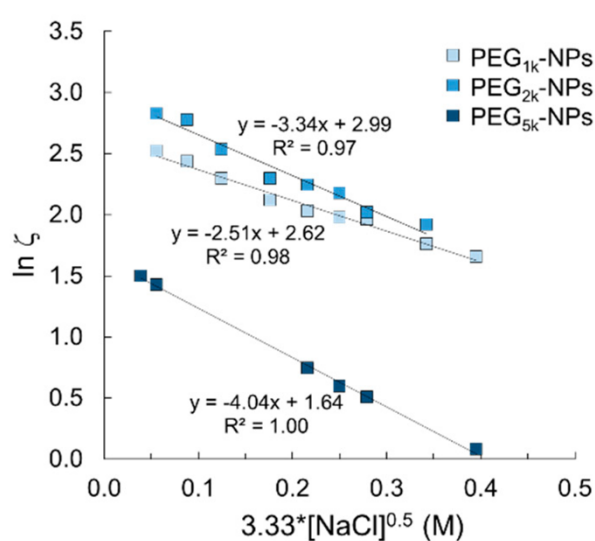
	PEG _{2K} -PCL _{4K}					
	NH ₂ -PCL _{4K} -					
Am/PEG _{5K} -NPs	NH ₂	98	1.2	94 ± 6.8	0.250	21.3 ± 2.4
	PEG _{5K} -PCL _{5K}					

¹: Copolymer mixture was 1:1 by wt.; ²: Pluronic[®] F68 associated to NPs was derived from the amount found in the medium after NPs preparation. Quantitative ¹H NMR measurements were taken as described in 2.4.; ³: D_H and PI were measured in water by DLS; ⁴: ζ measures the electrophoretic mobility of NPs.

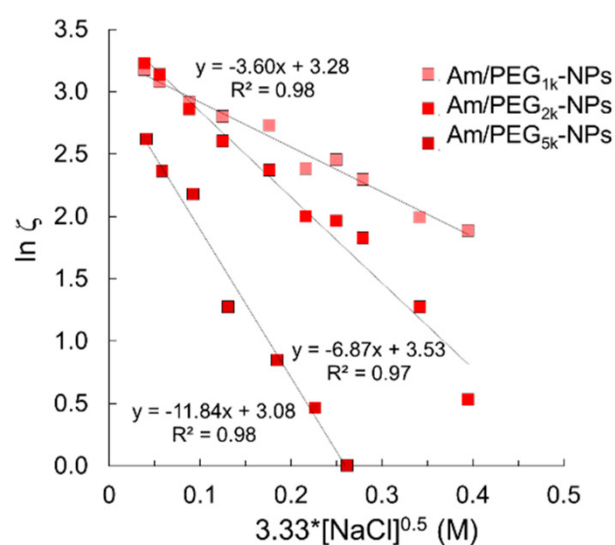
The short-term stability of NPs in water was observed up to 24 h by monitoring scattering, D_H, and ζ (**Figure S2a,b**). Scattering analysis of NPs suggested that no aggregation occurred over 4 h due to negligible changes in absorbance values at 500 nm and ζ. Amine-NPs and Am/PEG1K-PCL4K NPs showed an increase of D_H values and large fluctuations of ζ after 24 h while the other NPs showed no significant differences in D_H. Size distribution curves in water (**Figure S2c**) clearly highlight that PEG1K is not able to confer satisfactory colloidal stability to Am/PEG1k-NPs in analogy to PEG1k-NPs. Overall, these results indicate that NPs should be tested within 4 h of preparation. From a clinical perspective, freeze-drying of the NPs dispersion, likely in the presence of a cryoprotectant, is needed to ensure suitable shelf-life and storage stability.

Extent of Nanoparticle PEGylation

Fixed aqueous layer thickness (FALT) of the outer shell of NPs was determined by measuring ζ as a function of the sodium chloride concentration at pH values of 7.0 where primary amines are expected to be ionized. As reported in **Figure 3**, the slope value of the linear regression line obtained plotting log ζ vs sodium chloride concentration gives the shell thickness (nm) for each NPs type. As expected, shell thickness increased as PEG MW increased. Interestingly, Am-PEG-NPs displayed thicker aqueous layers as compared with the corresponding PEG-NPs counterparts (11.8 nm for Am/PEG5K-NPs vs. 4.0 nm for PEG5K-NPs). The shell thickness for amine/PEG-NPs increased with respect to the increasing PEG chain length, as was the case for the PEG-NPs. However, the increase across the series was greatest for the amine/PEG-NPs. The extent of the shell thickness increase for amine/PEG-NPs was steeper and more profound.



(a)



(b)

Figure 3. Fixed aqueous layer thickness (FALT) measurements for (a) PEG-NPs and (b) Am/PEG-NPs.

The amount of PEG on the surface of NPs was assessed by quantitative ¹H NMR (**Table 2**). As can be seen, NPs exposed much less PEG than expected, suggesting that during nanoprecipitation, PEG chains are entangled in the PCL core. This result confirms that the preparation method has a major impact on the PEGylation extent, and also on the conformation of the flexible hydrophilic cloud on the NPs surface.

Table 2. Shell thickness of NPs and percentage of PEG on NPs surface.

Type	Shell Thickness ¹ (nm)	Surface PEG ² (wt %)
PEG _{1K} -NPs	2.5 ± 0.4	3
PEG _{2K} -NPs	3.4 ± 0.8	11
PEG _{5K} -NPs	4.0 ± 0.2	5
Am/PEG _{1K} -NPs	3.5 ± 0.2	2
Am/PEG _{2K} -NPs	6.8 ± 1.2	4
Am/PEG _{5K} -NPs	11.8 ± 0.9	2

¹: Slope of the regression line of FALT analysis in **Figure 3**; ²: Surface PEG calculated by ¹H NMR as described in 2.5.

Nanoparticle Interactions with Proteins in Solution

Physical properties of NPs, such as size, shape and surface composition, strongly affect the interaction with proteins in complex media, which can alter the chemical identity of NPs and in turn their biological fate. HSA is a dysopsonic protein that can extend NP circulation time (25) and its mode of interaction with NPs can impact cell uptake (26). On the other hand, mucin is a barrier protein that is relevant in the case of NP interactions with mucosal surfaces. Thus, we studied HSA and mucin interaction with the panel of NPs fabricated through the combination of fluorescence spectroscopy, turbidimetry and size measurements.

Protein adsorption onto the nanoparticles, which can affect their stability over time, was monitored by measuring the absorbance value (at $\lambda = 500$ nm) of NPs dispersions in the presence of HSA and mucin, over time (**Figure S3**). As the proteins adsorb onto the NPs, light scattering occurs, which changes the absorbance value over time. As can be seen in **Figure S3**, only Am-NPs suffered from stability issues in the presence of proteins, showing a tendency to increase the scattering of light over time, whereas no significant effect was found for the PEGylated series.

Figure 4 a,b show the fluorescence emission spectra of HSA in the absence and in the presence of NPs upon excitation at 278 nm. The black spectrum shows the typical dual band fluorescence spectrum of HSA, which reflects the contribution of the tyrosine (λ_{em} ca 310 nm) and tryptophan (λ_{em} ca 340 nm) fluorogenic centers. This strong emission is quenched upon addition of PEG-PCL NPs simply due to static quenching effects arising by the massive aggregation of HSA on the NPs (3). This result suggests that: (i) A PEG shell is unable to prevent NP–protein hydrophobic interactions; (ii) Am-NPs adsorb HSA, presumably due to electrostatic interactions, and (iii) amine-PEG NPs interact with HSA through combined hydrophobic/electrostatic interaction. These results are in line with those found for a series of PEGylated cationic liposomes that adsorbed human plasma proteins depending on PEG length (27).

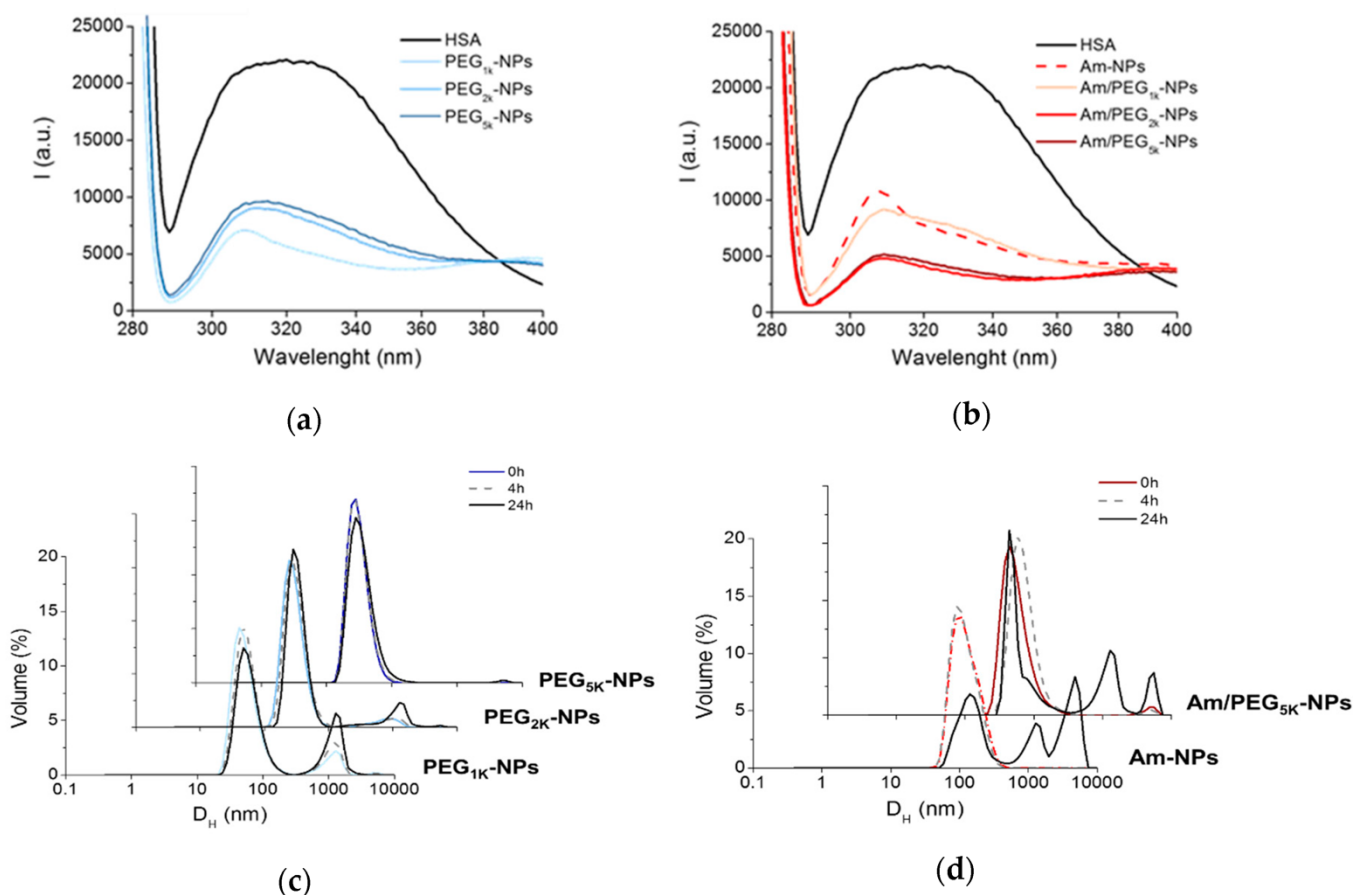


Figure 4. Interaction of NPs with proteins. Fluorescence emission spectra of HSA (0.2 mg/mL) at Ex = 278 nm in the presence of PEG-NPs (a) and Am-NPs or Am/PEG-NPs (b) (NPs = 0.5 mg/mL). Spectrum of free HSA is reported as control. Representative size distribution curves of PEG-NPs (c) and Am-NPs or Am/PEG-NPs (d) incubated in HSA (0.2 mg/mL) (NPs = 0.5 mg/mL).

Particle size in the presence of proteins was monitored over time using DLS, as shown in **Figure 4 c,d**. PEG-NPs experienced a high degree of protection from aggregation, especially for the PEG5k variant (**Figure 4c**). On the contrary, amine-bearing NPs showed a completely different behavior, exhibiting a fast and time-dependent aggregation that even a PEG5k copolymer was unable to hamper. These data demonstrate that PEGylated NPs are only partly capable of shielding HSA interaction, presumably due to the low amount of surface PEG and marginal effect of the adsorbed poloxamer.

As far as mucin interaction is concerned, its interaction with cationic NPs has been routinely used to achieve mucoadhesion (28). Nevertheless, precise tuning of PEG grafting density and molecular weight is considered a strategic approach to minimize mucoadhesion and in turn promote NPs transport through a mucus layer (7).

Mucoadhesive behavior of NPs can be estimated on the basis of an increased absorbance at 500 nm (29), while interactions between mucin and positively charged NPs can be monitored by size measurements (8). There was little quenching of mucin fluorescence in the presence of all NPs (**Figure S4**), suggesting that mucin was not significantly interacting with the NPs. As shown in **Figure 5a**, scattering in water increased only for Am-NPs, suggesting that such an interaction with the protein occurs. Nevertheless, ζ was unchanged for PEG-NPs and switched to negative values for all amine-bearing NPs. These results indicate that mucin negative chains adsorb onto positive Am-NPs via electrostatic interactions between opposite charges, which are not shielded by the concurrent presence of PEG chains. As evidenced by the

corresponding size curves in **Figure 5 c,d**, the increase of PEG length is increasingly effective in ensuring satisfactory stability while avoiding interactions between NPs. Thus, PEG length and its surface conformation remains the main determinant for regulating behavior at the interface also for amine-modified NPs (8).

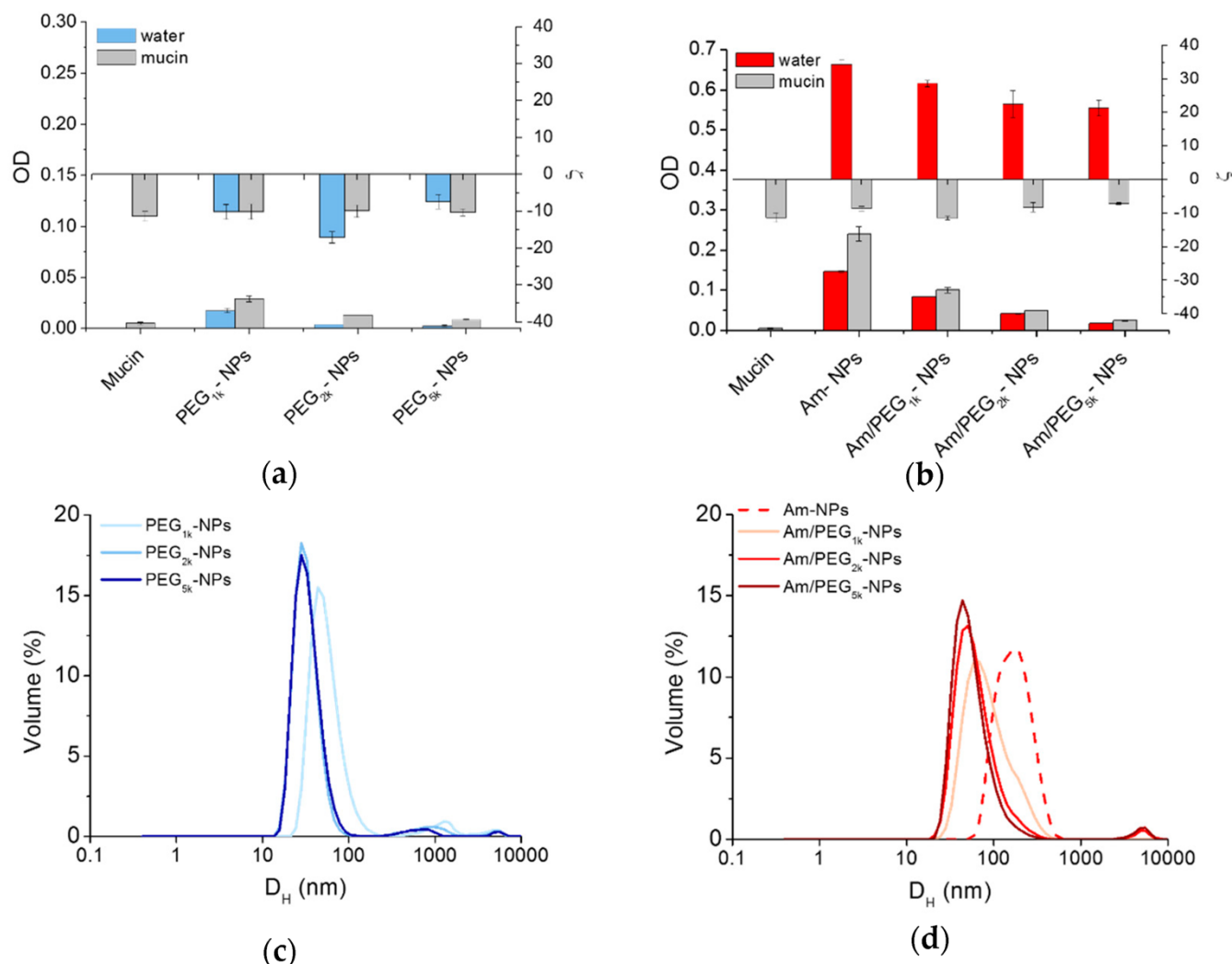


Figure 5. Interaction of NPs with mucin. Scattering of PEG-NPs (a) or Am-NPs and Am/PEG-NPs (b) in water or in a mucin water dispersion (0.08% w/v) (NPs = 0.5 mg/mL). Data are an average of triplicate measurements \pm SD. Representative size distribution curves of PEG-NPs (c) or Am-NPs and Am/PEG-NPs (d) in a mucin water dispersion (0.08% w/v) (NPs = 0.5 mg/mL).

Permeation through Protein-Rich Gels

To ascertain if the developed NPs permeated differently through protein-rich gel-like barriers, we focused on a tumor ECM, which could mimic tumor stroma, and artificial mucus, which is representative of the bronchial secretion.

For this experiment, FRET NPs were developed. FRET is a mechanism describing energy transfer between two light-sensitive molecules, a donor chromophore and an acceptor. The efficiency of this energy transfer is inversely proportional to the sixth power of the distance between the donor and acceptor, making FRET extremely sensitive to small changes in distance. Measurement of FRET

efficiency is a useful tool for determining if two fluorophores are released from an NP system and to monitor its disassembly in different biological conditions, in vitro and in vivo (23,30). As donor and acceptor chromophores, we selected the hydrophobic dyes DiO ($\lambda_{ex/em}$ is 488/505 nm) and DiL ($\lambda_{ex/em}$ at 543/575 nm), respectively, since the DiO emission spectrum overlaps well with the DiL absorption spectrum. **Figure 6a** reports the emission spectra of PEG5k-NPs loaded with DiO/DiL as a representative FRET formulation in both water and DCM. Upon excitation of NPs in water at 488 nm, DiO emission at 505 nm is quenched due to FRET, and DiL emission is enhanced. When NPs are dissolved in DCM, DiO emission is restored and DiL emission is depressed since no FRET occurs. Mean particle size was doubled only in FRET-based PEG-NPs while ζ of all NPs types were comparable to their unloaded counterparts (cfr DH and ζ in **Table 1** and **Table S3**). NP stability and constant FRET efficiency in the acceptor medium was demonstrated for all NP formulations (**Figure S5**); a fundamental prerequisite for the validation of results in transport experiments.

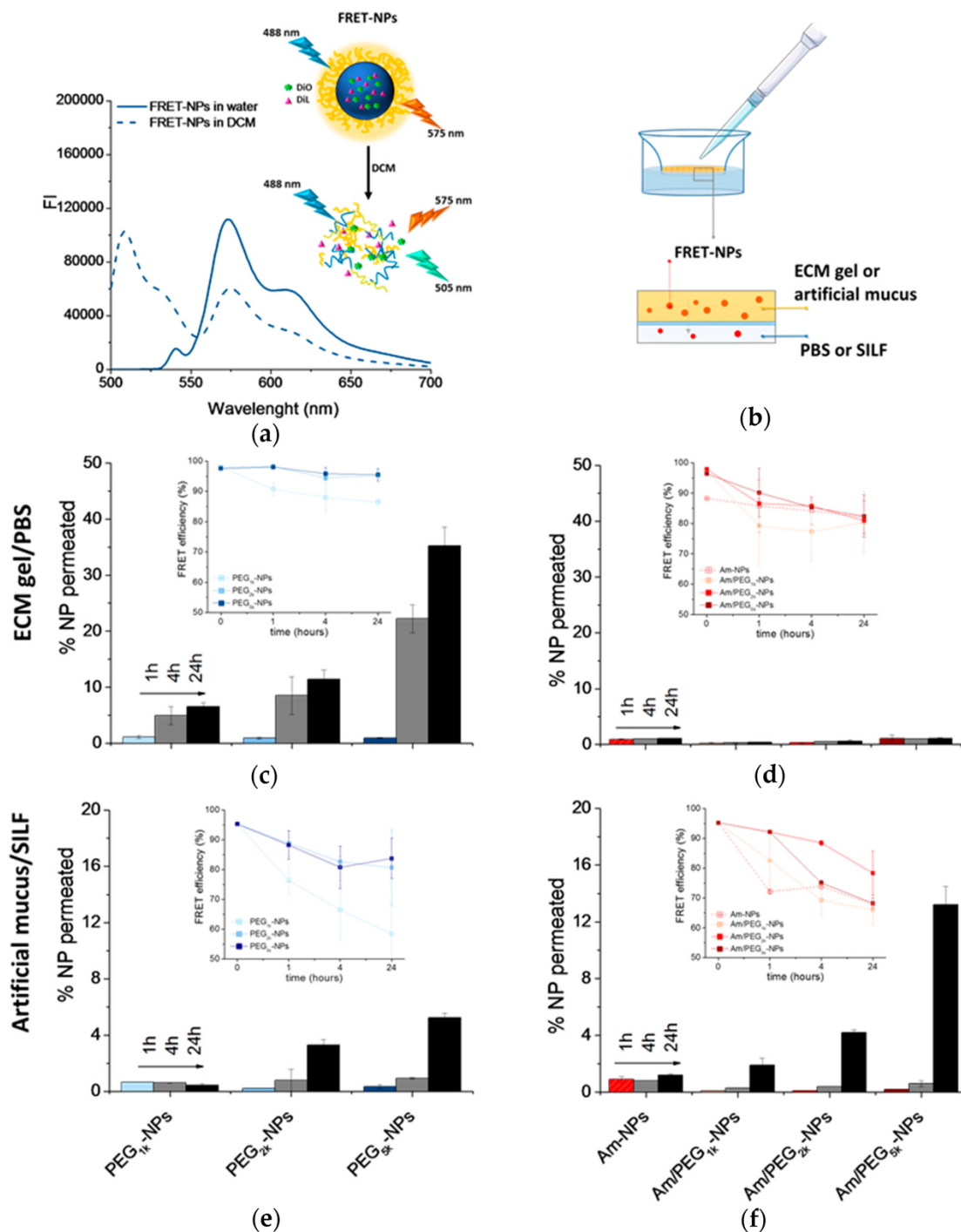


Figure 6. Permeation of NPs through protein-rich gels over time. For this experiment, NPs were loaded with DiO/DiL as a FRET pair. (a) Emission spectra collected after DiO excitation ($\lambda_{ex} = 488$ nm) of DiO/DiL-loaded PEG5k-NPs dispersed in water or dissolved in DCM. (b) Set-up of the transport experiment. Amount of DiO/DiL-loaded PEG-NPs (c,e) and amine-NPs and amine/PEG-NPs (d,f) found in the acceptor chamber after crossing the ECM gel (c,d) and artificial mucus (e,f). The amount of NPs in the acceptor medium was evaluated by monitoring DiL emission ($\lambda_{ex} = 543$ nm). In the inset, FRET efficiency is reported. Data are an average of triplicate measurements \pm SD.

The percentage of NPs permeated through the ECM or mucin over time was evaluated according to the set-up described in **Figure 6b**. At different time points, the NP amounts in the acceptor chamber were evaluated by measuring DiL emission ($\lambda_{ex} = 543$ nm). As reported in **Figure 6c**, PEG-NPs showed a

time-dependent transport through the ECM gel, with the extent of permeation clearly increasing as PEG MW increased. On the contrary, Am-NPs and Am/PEG-NPs did not show any capability to permeate through the ECM gel (**Figure 6d**). In the case of artificial mucus, we found that increasing PEG MW allowed an increase of NP penetration for both PEG-NPs (**Figure 6d**), and very surprisingly, this was also the case for Am/PEG-NPs (**Figure 6e**). In fact, the amount of transported Am/PEG5k-NPs was higher than that corresponding to PEG5k-NPs, highlighting that the presence of amine groups coupled with long PEG chains could even facilitate transport. Nevertheless, independently of the PEG MW, Am/PEG-NPs did not show any aggregation in SILF over time, as confirmed by DLS measurements (**Figure S6**). It is worth noting that permeation of Am-NPs was affected by their poor stability in both PBS (**Figure S5**) and SILF (**Figure S6**).

Emission spectra of DiL collected at DiO excitation (**Figure S7**) allowed calculation of the FRET efficiency according to the equation reported previously (insets in **Figure 6c–e**). A FRET efficiency higher than 80% for all the samples at different time points demonstrated that the fluorescence emission is due to intact fluorescent NPs and that only a limited contribution from FRET pair leaching occurred.

Uptake and Immune Activation

The innate immune system is the first to come in contact with NPs entering the body. For this reason, we investigated both the uptake and immunostimulatory capacity of our synthesized NPs in human primary monocytes, which are the main innate immune cells.

The extent of NP uptake by human monocytes was assessed by measuring the fluorescence of DiL in the extracellular compartment of cells, after exposing them to NPs for 2 h. The extent of NP uptake by human monocytes (**Figure 7a** and **Figure S8**) was roughly related to PEG length in the copolymer (greater PEG length results in lower uptake) following a very general rule for PEGylated systems, while the presence of amine groups on NPs surface had no impact.

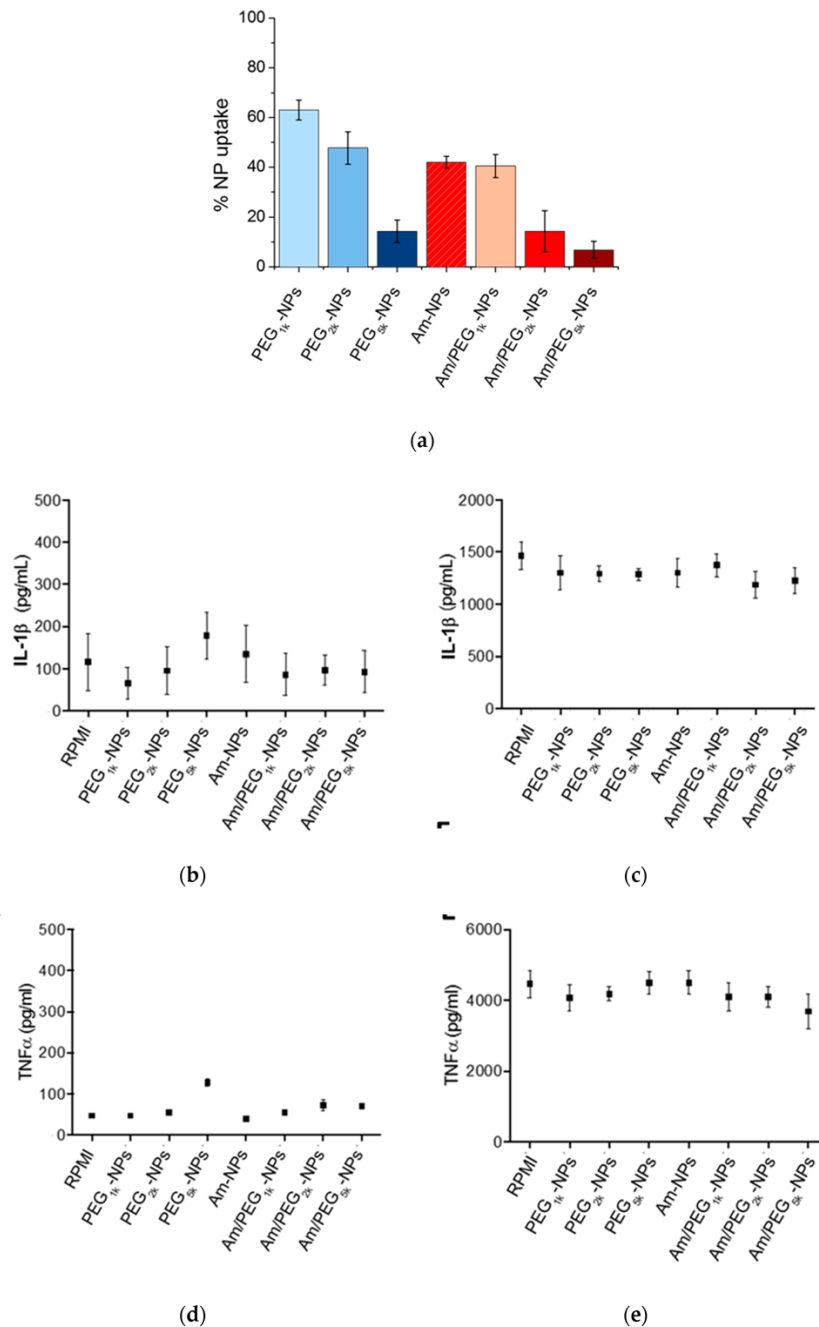


Figure 7. Uptake and inflammatory response to NPs by human monocytes. (a) Quantification of NPs taken up by monocytes after 2 h incubation. Production of IL-1 β (b,c) and TNF α (d,e) by human monocytes after 24 h of incubation with NPs as assessed by an ELISA kit. Panels (c,e) refer to LPS stimulated monocytes. Results represent mean \pm SEM, n = 2.

The production of IL-1 β and TNF α , which are indicators of inflammatory effects, was assessed using a commercially available ELISA kit following 24 h of NP incubation (**Figure 7 b,d**). In no cases were the levels of IL-1 β or TNF α markedly elevated or suppressed compared to background cytokine production. To assess whether the NPs may modulate induced innate immune responses, cells were additionally stimulated with the gram-negative bacterial molecule lipopolysaccharide (LPS), in the presence and absence of each NP formulation (**Figure 7 c,e**). LPS stimulation resulted in elevated production of IL-1 β and TNF α , a phenomenon that was not altered toward either increased or suppressed production in the presence of the NPs (19).

Conclusions

In this work, we prepared a panel of amine-functionalized PEGylated NPs (amine/PEG-NPs) with different PEG-chain lengths and evaluated their surface properties compared to corresponding PEG-NPs. The interaction of the NPs with human proteins, such as serum albumin and mucin, was studied using fluorescence spectroscopy, DLS, and turbidimetry analysis. The results demonstrated that amine-bearing NPs interacted strongly with proteins, and that this was found to be dependent on PEG length and surface charge. Furthermore, differences in their ability to permeate through protein-rich biological barriers were also found. Amine/PEG-NPs were unable to cross the ECM but were able to be transported through mucus, with transport facilitated by increasing MWs of PEG. Finally, the interaction of the different NP types with human innate immune cells (primary blood monocytes) was also studied. Cell uptake was found to decrease with increasing PEG MW and overall surface charge. Independently of uptake, NPs not were found to induce an inflammatory response, nor were they observed to interfere with a normal defensive reaction to bacterial agents, thereby demonstrating high tolerability. In conclusion, we demonstrated that PEGylation extent and the presence of amine groups on the NP surface are key elements that affect NP behavior in biological environments.

Funding: This research was funded by Italian Association for Cancer Research (IG2014 n.15764)” and “the EU H2020 project PANDORA (GA n. 671881)”.

Acknowledgments: B.J.S. and D.B. were supported by the EU H2020 project PANDORA (GA n. 671881). D.B. was also supported by the Cluster project MEDINTECH of the Italian Ministry of University and Research. The authors thank the Morpho-Functional Analysis and Bioimaging Unit of the Stazione Zoologica Anton Dohrn for assistance with confocal microscopy.

References

- 1 Grossen, P.; Witzigmann, D.; Sieber, S.; Huwyler, J. PEG-PCL-based nanomedicines: A biodegradable drug delivery system and its application. *J. Controll. Release* **2017**, *260*, 46–60, doi:10.1016/j.jconrel.2017.05.028.
- 2 Conte, C.; d’Angelo, I.; Miro, A.; Ungaro, F.; Quaglia, F. PEGylated polyester-based nanoncologicals. *Curr. Top. Med. Chem.* **2014**, *14*, 1097–1114.
- 3 Venuta, A.; Moret, F.; Dal Poggetto, G.; Esposito, D.; Fraix, A.; Avitabile, C.; Ungaro, F.; Malinconico, M.; Sortino, S.; Romanelli, A.; et al. Shedding light on surface exposition of poly(ethylene glycol) and folate targeting units on nanoparticles of poly(epsilon-caprolactone) diblock copolymers: Beyond a paradigm. *Eur. J. Pharm. Sci.* **2018**, *111*, 177–185, doi:10.1016/j.ejps.2017.09.048.
- 4 Quaglia, F.; Ostacolo, L.; De Rosa, G.; La Rotonda, M.I.; Ammendola, M.; Nese, G.; Maglio, G.; Palumbo, R.; Vauthier, C. Nanoscopic core-shell drug carriers made of amphiphilic triblock and star-diblock copolymers. *Int. J. Pharm.* **2006**, *324*, 56–66, doi:10.1016/j.ijpharm.2006.07.020.

- 5 Harris, J.M.; Chess, R.B. Effect of pegylation on pharmaceuticals. *Nat. Rev. Drug Discov.* **2003**, *2*, 214–221, doi:10.1038/nrd1033.
- 6 Swierczewska, M.; Lee, K.C.; Lee, S. What is the future of PEGylated therapies? *Expert Opin. Emerg. Drugs* **2015**, *20*, 531–536, doi:10.1517/14728214.2015.1113254.
- 7 Xu, Q.; Ensign, L.M.; Boylan, N.J.; Schon, A.; Gong, X.; Yang, J.C.; Lamb, N.W.; Cai, S.; Yu, T.; Freire, E.; et al. Impact of Surface Polyethylene Glycol (PEG) Density on Biodegradable Nanoparticle Transport in Mucus ex Vivo and Distribution in Vivo. *ACS Nano* **2015**, *9*, 9217–9227, doi:10.1021/acsnano.5b03876.
- 8 Huckaby, J.T.; Lai, S.K. PEGylation for enhancing nanoparticle diffusion in mucus. *Adv. Drug Deliv. Rev.* **2018**, *124*, 125–139, doi:10.1016/j.addr.2017.08.010.
- 9 Shen, Z.; Nieh, M.-P.; Li, Y. Decorating Nanoparticle Surface for Targeted Drug Delivery: Opportunities and Challenges. *Polymers* **2016**, *8*, 83, doi:10.3390/polym8030083.
- 10 Chen, B.; Le, W.; Wang, Y.; Li, Z.; Wang, D.; Ren, L.; Lin, L.; Cui, S.; Hu, J.J.; Hu, Y.; et al. Targeting Negative Surface Charges of Cancer Cells by Multifunctional Nanoprobes. *Theranostics* **2016**, *6*, 1887–1898, doi:10.7150/thno.16358.
- 11 Wang, H.-X.; Zuo, Z.-Q.; Du, J.-Z.; Wang, Y.-C.; Sun, R.; Cao, Z.-T.; Ye, X.-D.; Wang, J.-L.; Leong, K.W.; Wang, J. Surface charge critically affects tumor penetration and therapeutic efficacy of cancer nanomedicines. *Nano Today* **2016**, *11*, 133–144, doi:10.1016/j.nantod.2016.04.008.
- 12 Sun, Q.; Ojha, T.; Kiessling, F.; Lammers, T.; Shi, Y. Enhancing Tumor Penetration of Nanomedicines. *Biomacromolecules* **2017**, *18*, 1449–1459, doi:10.1021/acs.biomac.7b00068.
- 13 Stylianopoulos, T.; Soteriou, K.; Fukumura, D.; Jain, R.K. Cationic nanoparticles have superior transvascular flux into solid tumors: Insights from a mathematical model. *Ann. Biomed. Eng.* **2013**, *41*, 68–77.
- 14 Bilensoy, E. Cationic nanoparticles for cancer therapy. *Expert Opin. Drug Deliv.* **2010**, *7*, 795–809, doi:10.1517/17425247.2010.485983.
- 15 Reisch, A.; Runser, A.; Arntz, Y.; Mély, Y.; Klymchenko, A.S. Charge-Controlled Nanoprecipitation as a Modular Approach to Ultrasmall Polymer Nanocarriers: Making Bright and Stable Nanoparticles. *ACS Nano* **2015**, *9*, 5104–5116, doi:10.1021/acsnano.5b00214.
- 16 Esposito, D.; Conte, C.; Dal Poggetto, G.; Russo, A.; Barbieri, A.; Ungaro, F.; Arra, C.; Russo, G.; Laurienzo, P.; Quaglia, F. Biodegradable nanoparticles bearing amine groups as a strategy to alter surface features, biological identity and accumulation in a lung metastasis model. *J. Mater. Chem. B* **2018**, *6*, 5922–5930, doi:10.1039/C8TB01330F.

- 17 Monopoli, M.P.; Åberg, C.; Salvati, A.; Dawson, K.A. Biomolecular coronas provide the biological identity of nanosized materials. *Nat. Nanotechnol.* **2012**, *7*, 779, doi:10.1038/nnano.2012.207.
- 18 Corbo, C.; Molinaro, R.; Parodi, A.; Toledano Furman, N.E.; Salvatore, F.; Tasciotti, E. The impact of nanoparticle protein corona on cytotoxicity, immunotoxicity and target drug delivery. *Nanomedicine* **2016**, *11*, 81–100, doi:10.2217/nnm.15.188.
- 19 Boraschi, D.; Italiani, P.; Palomba, R.; Decuzzi, P.; Duschl, A.; Fadeel, B.; Moghimi, S.M. Nanoparticles and innate immunity: New perspectives on host defence. *Semin. Immunol.* **2017**, *34*, 33–51, doi:10.1016/j.smim.2017.08.013.
- 20 Shi, B.; Fang, C.; Pei, Y. Stealth PEG-PHDCA niosomes: Effects of Chain Length of PEG and Particle Size on Niosomes Surface Properties, In Vitro Drug Release, Phagocytic Uptake, In Vivo Pharmacokinetics and Antitumor Activity. *J. Pharm. Sci.* **2006**, *95*, 1873–1887, doi:10.1002/jps.20491.
- 21 Abdelbary, A.A.; Li, X.; El-Nabarawi, M.; Ellassasy, A.; Jasti, B. Effect of fixed aqueous layer thickness of polymeric stabilizers on zeta potential and stability of aripiprazole nanosuspensions. *Pharm. Dev. Technol.* **2013**, *18*, 730–735, doi:10.3109/10837450.2012.727001.
- 22 Ungaro, F.; d'Angelo, I.; Coletta, C.; d'Emmanuele di Villa Bianca, R.; Sorrentino, R.; Perfetto, B.; Tufano, M.A.; Miro, A.; La Rotonda, M.I.; Quaglia, F. Dry powders based on PLGA nanoparticles for pulmonary delivery of antibiotics: Modulation of encapsulation efficiency, release rate and lung deposition pattern by hydrophilic polymers. *J. Controll. Release* **2012**, *157*, 149–159, doi:10.1016/j.jconrel.2011.08.010.
- 23 Conte, C.; Mastrotto, F.; Taresco, V.; Tchoryk, A.; Quaglia, F.; Stolnik, S.; Alexander, C. Enhanced uptake in 2D-and 3D-lung cancer cell models of redox responsive PEGylated nanoparticles with sensitivity to reducing extra- and intracellular environments. *J. Controll. Release* **2018**, *277*, 126–141, doi:10.1016/j.jconrel.2018.03.011.
- 24 Wan, F.; Nylander, T.; Klodzinska, S.N.; Foged, C.; Yang, M.; Baldursdottir, S.G.; Nielsen, H.M. Lipid Shell-Enveloped Polymeric Nanoparticles with High Integrity of Lipid Shells Improve Mucus Penetration and Interaction with Cystic Fibrosis-Related Bacterial Biofilms. *ACS Appl. Mater. Interfaces* **2018**, *10*, 10678–10687, doi:10.1021/acsami.7b19762.
- 25 Takeuchi, T.; Kitayama, Y.; Sasao, R.; Yamada, T.; Toh, K.; Matsumoto, Y.; Kataoka, K. Molecularly Imprinted Nanogels Acquire Stealth In Situ by Cloaking Themselves with Native Dysopsonic Proteins. *Angew. Chem. Int. Ed.* **2017**, *56*, 7088–7092, doi:10.1002/anie.201700647.
- 26 Fleischer, C.C.; Payne, C.K. Nanoparticle-cell interactions: Molecular structure of the protein corona and cellular outcomes. *Acc. Chem Res.* **2014**, *47*, 2651–2659, doi:10.1021/ar500190q.
- 27 Pozzi, D.; Colapicchioni, V.; Caracciolo, G.; Piovesana, S.; Capriotti, A.L.; Palchetti, S.; De Grossi, S.; Riccioli, A.; Amenitsch, H.; Laganà, A. Effect of polyethyleneglycol (PEG) chain length on the bio-

nano-interactions between PEGylated lipid nanoparticles and biological fluids: From nanostructure to uptake in cancer cells. *Nanoscale* **2014**, *6*, 2782–2792, doi:10.1039/C3NR05559K.

28 Prego, C.; Torres, D.; Alonso, M.J. The potential of chitosan for the oral administration of peptides. *Expert Opin. Drug Deliv.* **2005**, *2*, 843–854, doi:10.1517/17425247.2.5.843.

29 D'Angelo, I.; Casciaro, B.; Miro, A.; Quaglia, F.; Mangoni, M.L.; Ungaro, F. Overcoming barriers in *Pseudomonas aeruginosa* lung infections: Engineered nanoparticles for local delivery of a cationic antimicrobial peptide. *Colloids Surf. B Biointerfaces* **2015**, *135*, 717–725, doi:10.1016/j.colsurfb.2015.08.027.

30 Chen, H.T.; Kim, S.W.; Li, L.; Wang, S.Y.; Park, K.; Cheng, J.X. Release of hydrophobic molecules from polymer micelles into cell membranes revealed by Forster resonance energy transfer imaging. *Proc. Natl. Acad. Sci. USA* **2008**, *105*, 6596–6601, doi:10.1073/pnas.0707046105.

Supplementary materials

Preparation of media for transport experiments

Artificial mucus

For the experiment, 5 mL of artificial mucus (AM) were prepared by initially solubilising 20 mg of DNA from calf thymus in 3 mL of purified water followed by the addition of 25 μ L of sterile egg yolk emulsion, 25 mg of type II porcine mucin, 30 μ L of DPTA stock solution (1 mg/mL), 25 mg NaCl, 11 mg KCl and 0.1 mL of RPMI. The volume was made up to 5 mL with purified water and allowed to mix until a cloudy uniform dispersion was obtained (16).

Simulated Interstitial Lung Fluid

A 100 mL aliquot of Simulated Interstitial Lung Fluid (SILF) contains 600 mg of NaCl, 30 mg of KCl, 15.7 mg of disodium phosphate (Na_2HPO_4), 7.1 mg of sodium sulfate (Na_2SO_4), 27.1 mg of calcium chloride (CaCl_2), 57.4 mg of sodium acetate ($\text{NaH}_3\text{C}_2\text{O}_2$), 260.2 mg of sodium bicarbonate (NaHCO_3), 9.8 mg of sodium citrate dihydrate and 29.4 mg of hydrated magnesium chloride ($\text{MgCl}_2 \cdot 6\text{H}_2\text{O}$).

Table S1. Concentration of NPs employed to study macrophage interaction. The calculation accounted for the volume and surface area of each type of particle.

Samples	NP size (nm)	Conc. ($\mu\text{g/mL}$)
PEG _{1k} -NPs	70	25.0
PEG _{2k} -NPs	45	16.1
PEG _{5k} -NPs	45	16.1
Am-NPs	130	46.4
Am/PEG _{1k} -NPs	120	42.9
Am/PEG _{2k} -NPs	100	35.7
Am/PEG _{5k} -NPs	100	35.7

Table S2. Theoretical and experimental molecular weights of synthesized PEG-PCL copolymers.

Copolymer	Mn (Da) ¹ (theoretical)	Mn (Da) ¹ (experimental)	Mn (Da) ²	Mw (Da) ²	PDI ² (Mw/Mn)
mPEG _{1k} -PCL _{4k}	5104	5446	5059	6737	1.32
mPEG _{2k} -PCL _{4k}	6104	5789	6194	8420	1.35

¹ Calculated or experimentally evaluated on the basis of OH/ ϵ -CL molar ratio ($M_n = 114,14 \times ([\epsilon\text{-CL}]/[\text{mPEG}]) \times \text{conversion } \epsilon\text{-CL} + M_n \text{ of mPEG}$); ² Determined by GPC.

Table S3. Properties of FRET NPs.

Type	DH (nm \pm SD)	PI	ζ (mV \pm SD)	Encaps. eff DiO (%)	Encaps. eff DiL (%)
PEG _{1k} -NPs	165.8 \pm 11.9	0.249	-8.3 \pm 2.0	70	62
PEG _{2k} -NPs	95.8 \pm 26.2	0.410	-15.3 \pm 2.7	76	55
PEG _{5k} -NPs	124.2 \pm 19.4	0.257	-9.4 \pm 0.7	100	100
Am-NPs	134.4 \pm 0.3	0.128	34.3 \pm 1.3	81	83
Am/PEG _{1k} - NPs	137.1 \pm 6.7	0.109	30.1 \pm 1.3	62	83
Am/PEG _{2k} - NPs	131.8 \pm 22.6	0.158	29.5 \pm 4.1	83	100
Am/PEG _{5k} - NPs	112.3 \pm 1.6	0.154	22.1 \pm 3.2	70	100

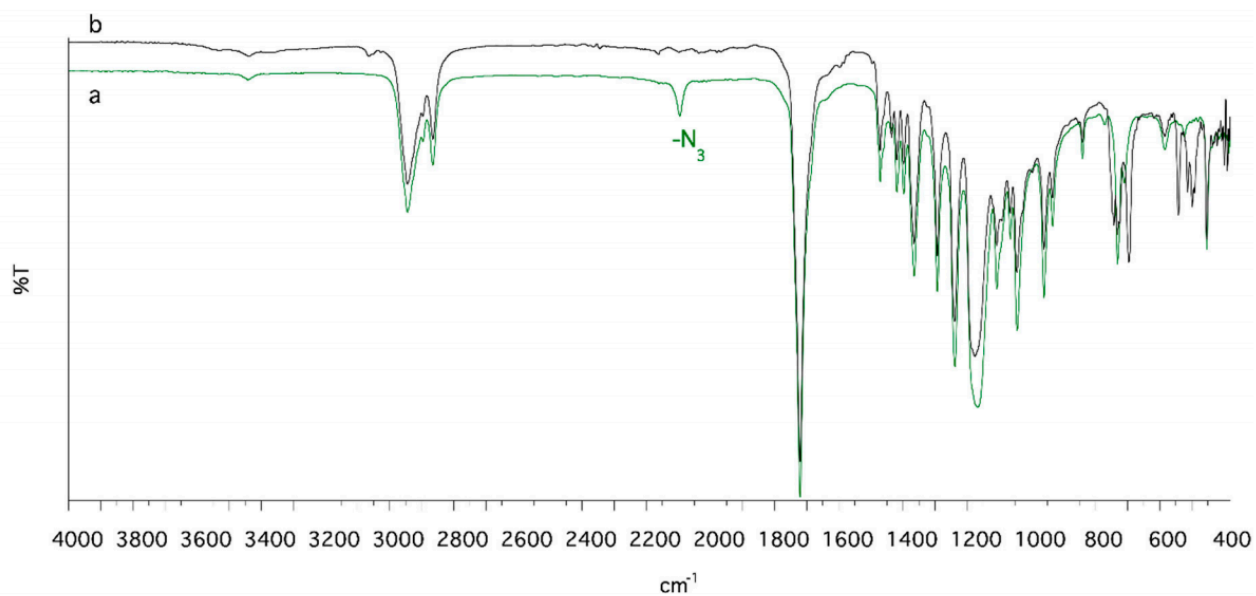


Figure S1. FTIR spectra of $\text{N}_3\text{-PCL}_{4k}\text{-N}_3$ (a) and $\text{H}_2\text{N-PCL}_{4k}\text{-NH}_2$ (b). Spectra were acquired at a resolution of 2 cm^{-1} (average of 20 scans).

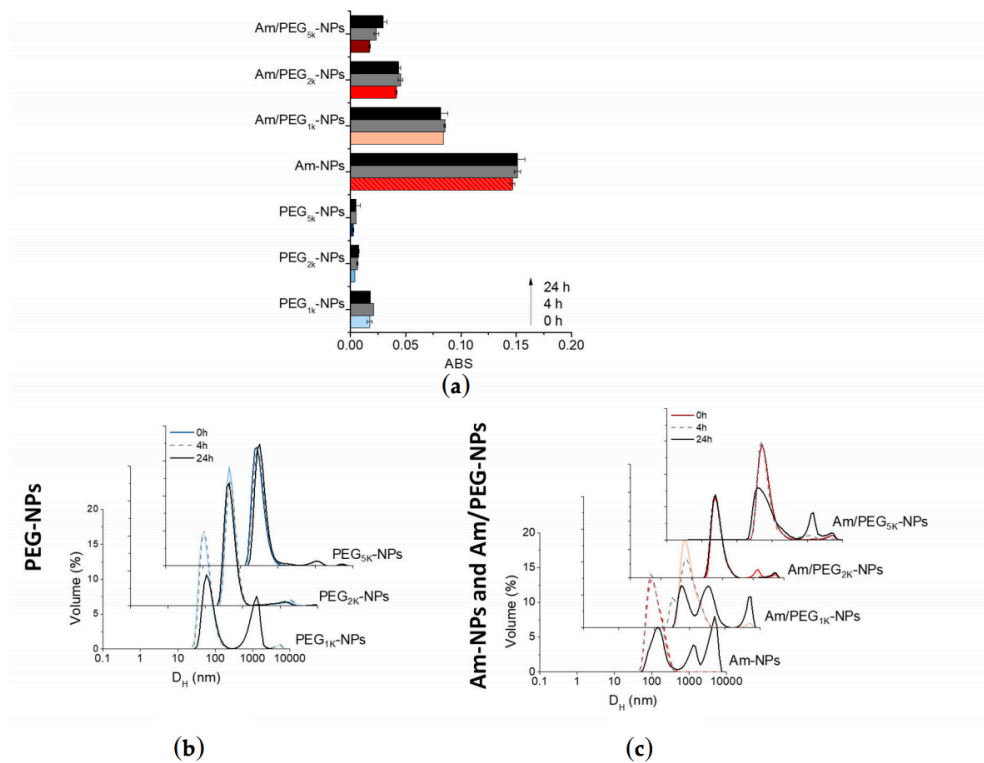


Figure S2. NP stability over 24 h assessed through (a) scattering of NPs sample at $\lambda=500$ nm and representative size distribution curves of PEG-NPs (b) and Am-NPs and Am/PEG-NPs (c). NP concentration was 0.5 mg/mL. Data are reported as an average of duplicate experiments \pm SD.

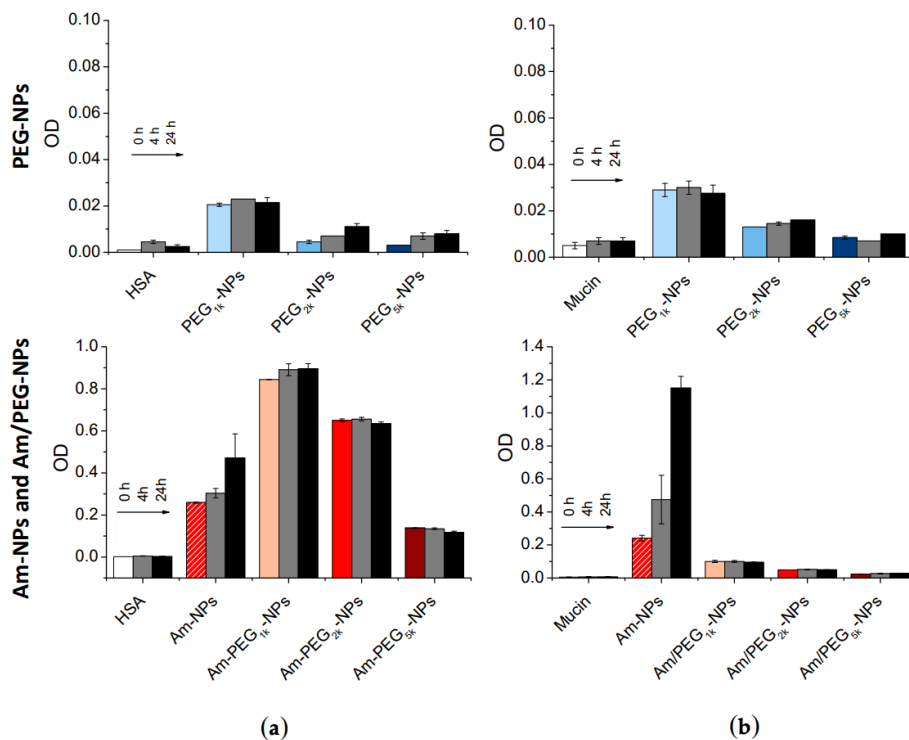


Figure S3. Scattering of NPs sample at $\lambda=500$ nm in the presence of a) HSA or b) mucin. PEG-NPs (top); Am-NPs and Am/PEG-NPs (bottom). NPs=0.5 mg/mL, HSA=0.2 mg/mL, mucin=0.08% w/w. Data are reported as an average of duplicate experiments \pm SD. .

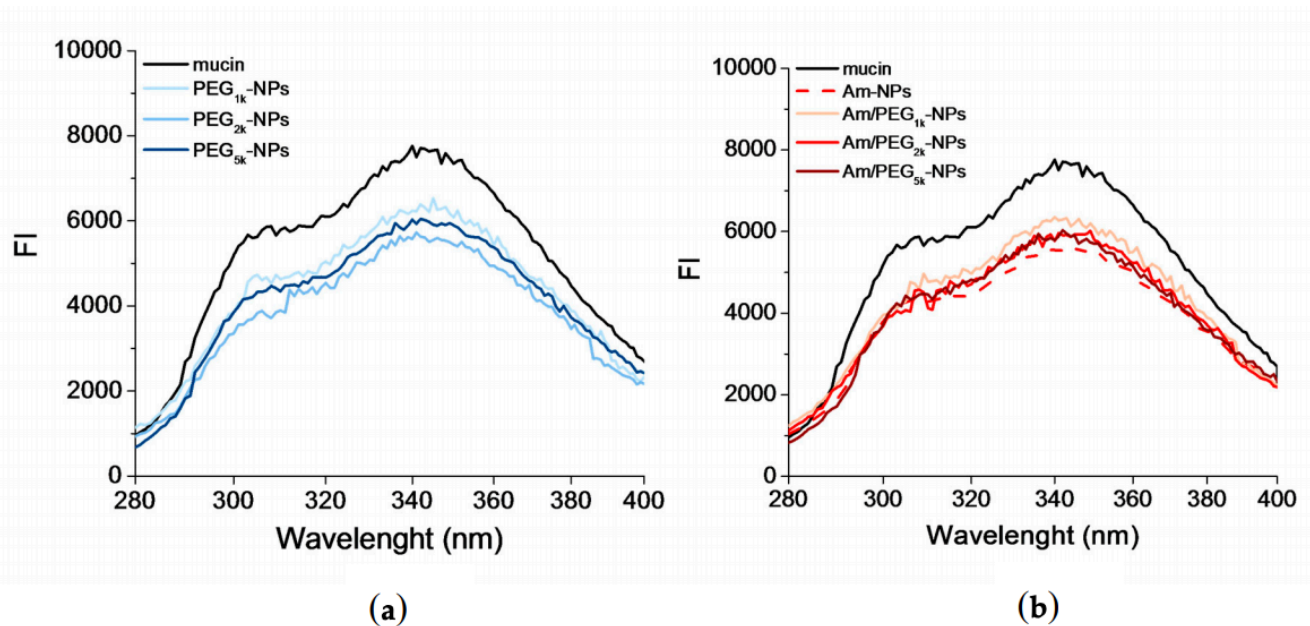


Figure S4. Fluorescence spectra of mucin (0.08%) in the presence of NPs (0.2 mg/mL); (a) PEG-NPs and (b) Am-NPs and Am/PEG-NPs. Spectrum of free mucin is reported as control.

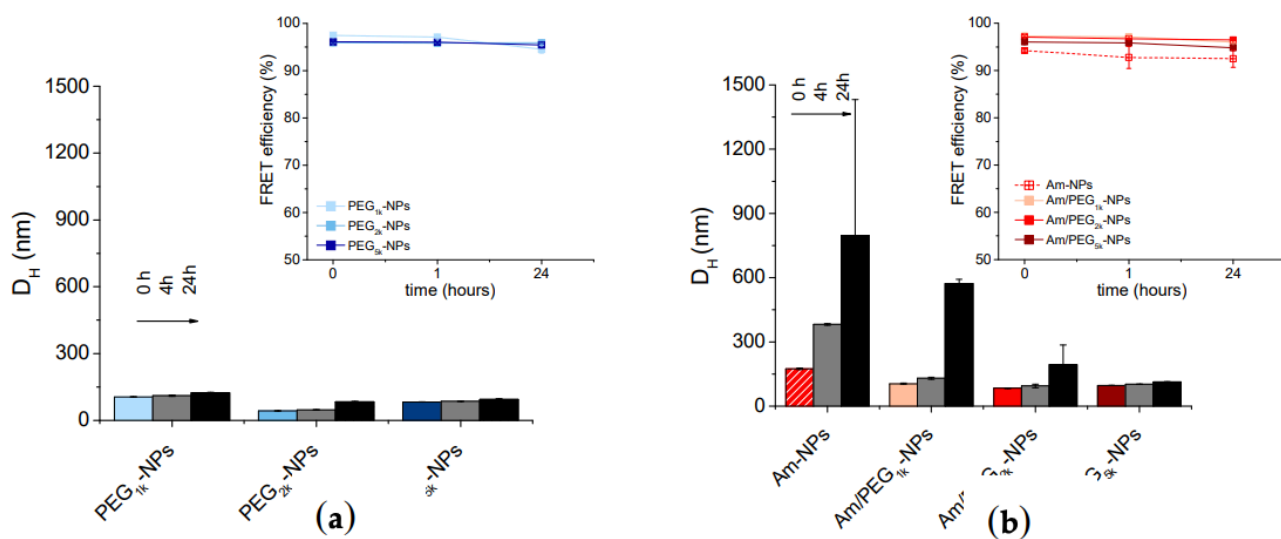


Figure S5. Stability of PEG-NPs (a) or Amine-NPs and Amine/PEG-NPs (b) in PBS at pH 7.4 along time. In the inset FRET efficiency of NPs along time is reported. NP concentration was 0.5 mg/mL. Data are reported as an average of duplicate experiments \pm SD. .

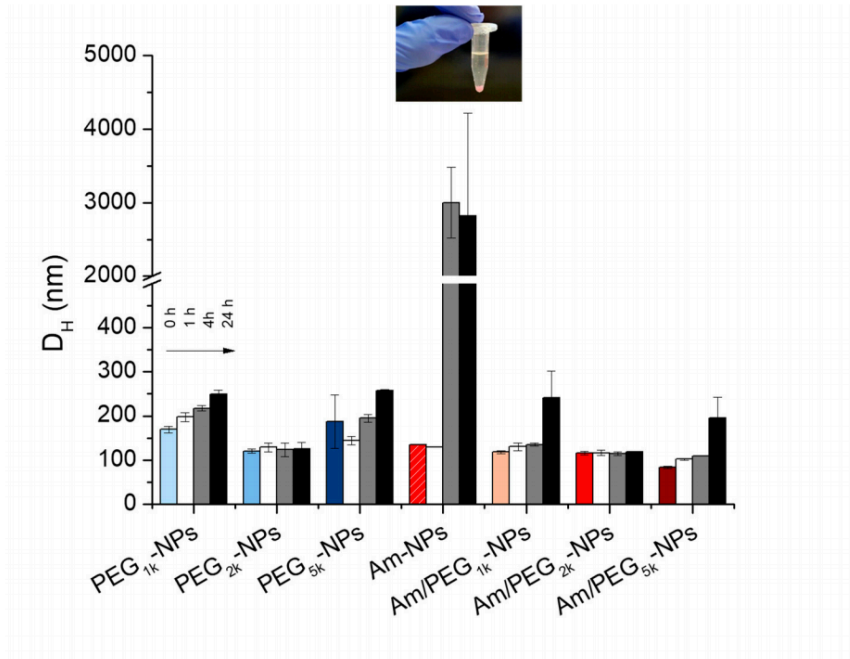


Figure S6. Stability of NPs in SILF at pH 7.4 up to 24 h. NP concentration was 0.5 mg/mL. Data are reported as an average of duplicate experiments \pm SD.

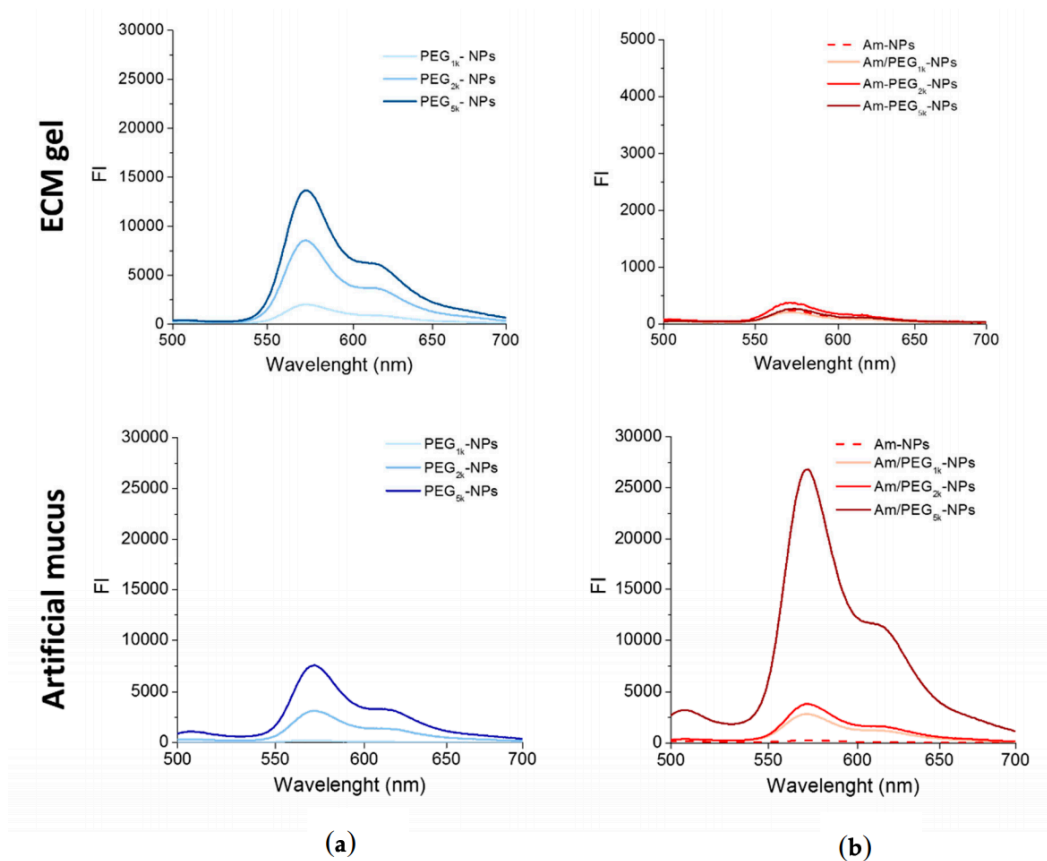


Figure S7. Emission spectra collected at $\lambda_{ex} = 488$ nm (DiO excitation) of PEG-NPs (a) and Am-NPs and Am/PEG-NPs (b) loaded with DiO/DiL permeated through an ECM gel and an artificial mucus.

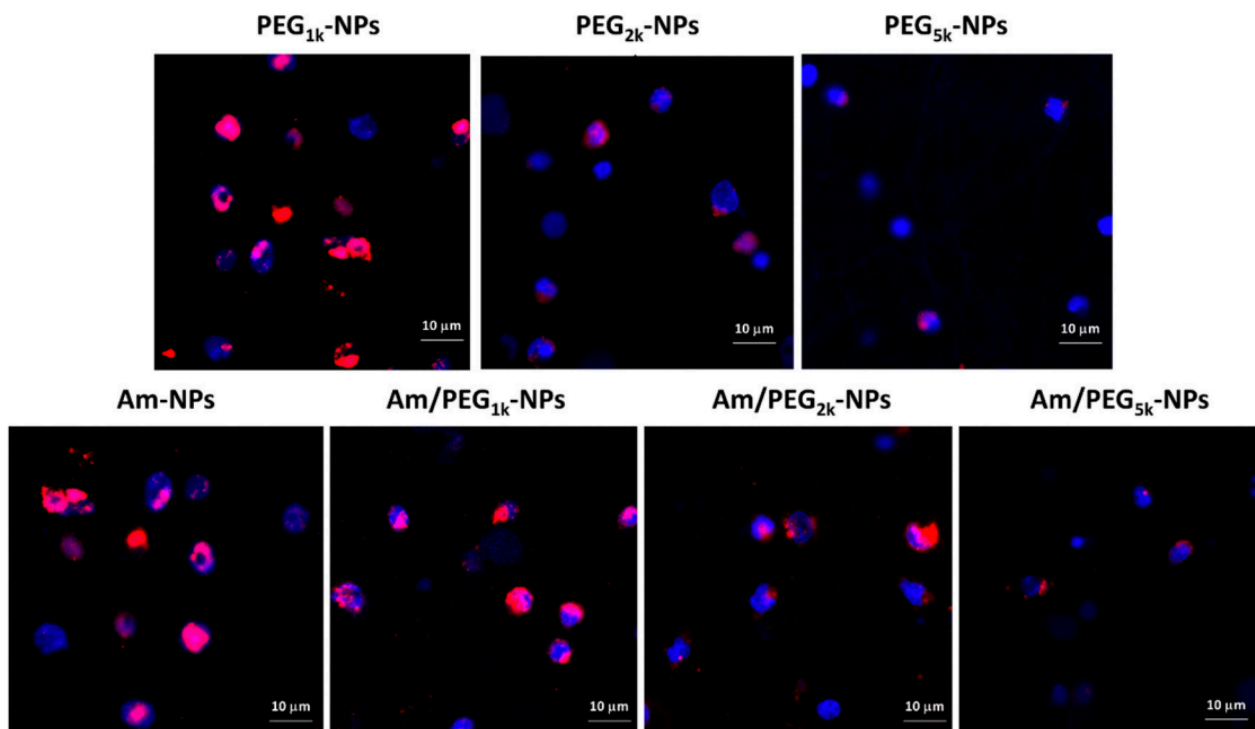


Figure S8. Confocal images of human monocytes after incubation with DiL-loaded NPs 50 μ g/mL at 37°C for 2 h. Images were acquired at $\lambda_{\text{exc}} = 543$ nm and spectral filter LP 560 nm for DiL detection.

Zen 2009 image Software was used for image processing. Blue, DAPI-stained cell nuclei; red, DiL showing the NP uptake.

8 Terpolymers for combined therapy of cancer

Introduction

Small interfering RNA (siRNA) has emerged as one of the most advanced and versatile therapeutic agent for various diseases such as viral infections, hereditary diseases and tumors (1-2). siRNA exhibits in general a high specificity and a low non-specific toxicity, can be easily introduced into cells with high efficiency, numerous libraries targeting the entire human genome are available, chemical modifications are possible to reduce off-target effects. Anyway, siRNA cannot be administered directly because it will be rapidly degraded, its internalization is underprivileged due to its negative charge, and it may induce inflammatory response. Among delivery systems, viral or non-viral vectors have been studied for siRNA delivery. Notwithstanding high efficiency of viral vectors, these are limited by production cost and safety issues. Recently, non-viral vectors and in particular cationic polymers have received growing interests due to many advantages compared with their viral counterparts including improved safety, easy to produce, virtually no limitation in loading, and low immune responses.

As drawback carrier-induced toxicity must be taken in consideration. Usually, in order to condense siRNA, polycations are required to have high molecular weights and high charge densities, which are often associated with acute and/or long-term toxicity. Recently, different low cytotoxic carriers composed by biodegradable polycations such as poly(b-amino esters)s, bio reducible poly(amido-amine)s (3) have been explored to deliver siRNA into cells. Notably, Wang and coworkers reported that cationic degradable micelles self-assembled from amphiphilic tri-block copolymer PEG-b-poly(3-caprolactone)-b-poly(2-aminoethylethylene phosphate) mediated efficient siRNA delivery(3).

Cationic nanoparticles (NPs) are particularly appealing because they have the potential to simultaneously deliver genes and hydrophobic anti-cancer drugs (4). The co-delivery of paclitaxel and an interleukin-12-enco-ded plasmid DNA from self-assembled cationic core-shell nanoparticles have shown to efficiently suppress cancer growth in a 4T1mouse breast cancer model (5). Triblock copolymers were designed on the basis of the following reasons: (i) PDMAEMA has received a lot of attention for gene delivery due to its relatively low toxicity, (ii) combination of biodegradation and low molecular weight PDMAEMA will further reduce their in vitro and in vivotoxicity, (iii) formation of NPs may result in largely improved siRNA condensation ability and thereby transfection activity, (iv)NPs are one of the most efficient nano-carriers for hydrophobic anti-cancer drugs, and (v) they can be conveniently prepared with controlled macromolecular structures and molecular weights by ATRP.

In this work amphiphilic triblock copolymers composed by PEG-pDMAEMA-PCL have been synthesized through the following scheme. (**Figure 1**)

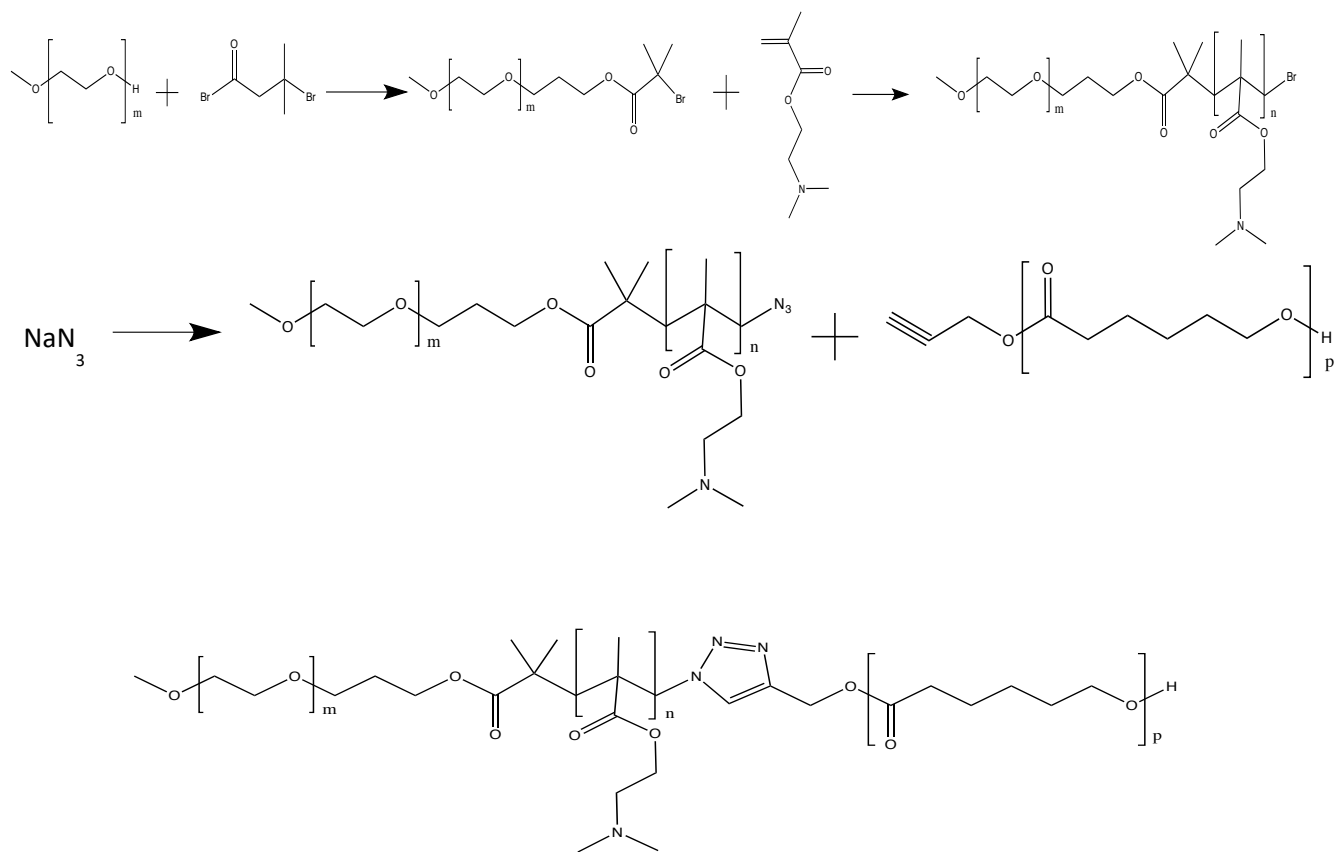


Figure 1

Experimental Section

Materials and Methods

Poly(ethylene glycol) methyl ether (mPEG) with M_n 2 kDa and 5kDa (PEG2k and PEG5k Sigma-Aldrich, Milan, Italy) were dehydrated by azeotropic distillation with dry toluene in a Dean-Stark trap. ϵ -Caprolactone (ϵ -CL) was dried over CaH_2 and distilled under vacuum before use. 3-butyn-1-ol was dried with molecular sieves (3\AA). Tin(II) 2-ethylhexanoate ($\text{Sn}(\text{Oct})_2$), 2-(dimethylamino)ethyl methacrylate (DMAEMA), α -bromoisobutyryl bromide (α -BIBB), triethylamine (TEA), 2,2'-Bipyridyl (bPy), Copper(I) Bromide, Sodium Azide were purchased from Sigma-Aldrich and used as received. Copper wires (Carlo Erba, Milan, Italy) were treated with H_2SO_4 for 10 minutes prior to use, repeatedly washed with water and methanol, and finally dried under vacuum in an oven for 20 minutes at 60°C . Dimethylformamide (DMF), methanol, diethyl ether, methanol were purchased from Sigma-Aldrich. Dimethyl sulfoxide (DMSO), tetrahydrofuran (THF), chloroform (CHCl_3), acetone were from Romil. Petroleum ether, Dichloromethane (DCM), n-hexane were from Titolchimica. All listed solvents were of HPLC grade. Chloroform-d was from ARMAR Chemicals. Sodium hydrogen carbonate (NaHCO_3) and docetaxel (DTX) were purchased from Alfa Aesar. Silica Gel high-purity grade, pore size 60\AA ,

230-400 mesh particle size, 40-63 μm particle size and Aluminium oxide active neutral 150 mesh, 58 Å (Al_2O_3) were from Sigma-Aldrich. THF and DMF were dried over 3 Å molecular sieves (20 % m/v).

Synthesis of terpolymers

PEG-pDMAEMA-PCL block copolymers with different blocks length were synthesized through ATRP (atom transfer radical polymerization) and CuAAC.

Synthesis of mPEG-pDMAEMA copolymer

Synthesis of Macroinitiator (mPEG-Br)

The ATRP macroinitiator was prepared by reaction of mPEG with α -BIBB. As example, mPEG_{2k}-OH (10 mmol) was dissolved in 150 ml of anhydrous THF. The solution was then cooled in an ice bath and TEA (50 mmol) was added under stirring, followed by the addition of α -BIBB (25 mmol). The reaction was allowed to warm up to room temperature and left under argon overnight. The resulting bromine salt was removed by filtration, then the solvent was removed under vacuum. The residual yellow oil was re-dissolved in DCM and washed three times with a saturated NaHCO_3 solution. The organic layer was separated, dried over sodium sulphate anhydrous and filtered, then the solvent removed under vacuum. The yellow oil was precipitated in cold hexane to get a white powder. The product was evaluated by ^1H NMR. To obtain the mPEG_{5k}-Br macroinitiator, the procedure was identical to the one described above maintaining the molar ratio between the reactants.

NMR mPEG_{2k}-Br: δ 4.31 (t), 3.64 (s), 3.37 (s), 1.93 (s) (Y%: 83)

NMR mPEG_{5k}-Br: δ 4.31 (t), 3.64 (s), 3.37 (s), 1.93 (s) (Y%: 92)

Polymerization of DMAEMA initiated by mPEG-Br via ATRP

In a typical reaction, under flux of argon the macroinitiator (for ex., mPEG_{2k}-Br, 3.34 mmol) was dissolved in 12 ml of anhydrous THF in a round bottom flask then bPy (3.34 mmol) and CuBr (3.34 mmol) were added. The flask was placed into an oil bath at room temperature, then DMAEMA (85.00 mmol) was added. The temperature was increased to 60 °C. The reaction was stopped after 6 h. After cooling, the solution was passed through a column filled with neutral aluminum oxide. THF was removed under vacuum and the yellow oil was precipitated in cold hexane to get the final product as a powder. To obtain the mPEG_{5k}-pDMAEMA₁₄₉₃₄, the procedure was identical to the one described above maintaining the molar ratio between the reactants except for DMAEMA with molar ratio with macroinitiator was 50:1

NMR

mPEG_{2k}-pDMAEMA₅₆₆₀-Br ^1H NMR δ 4.06 (d), 3.84 – 3.78 (m), 3.64 (d), 3.37 (s), 2.57 (d), 2.36 – 2.22 (m), 1.82 (s), 1.05 (s), 0.96 – 0.81 (m). Y%: 80

mPEG_{5k}-pDMAEMA₁₄₉₃₄-Br ^1H NMR δ 4.07 (t), 3.87 – 3.73 (m), 3.63 (s), 3.37 (s), 2.55 (d), 2.27 (s), 1.81 (s), 1.00 (d), 0.89 (s). Y%: 93

B) Synthesis of PEG-pDMAEMA-PCL

Synthesis of mPEG-pDMAEMA-N₃

In a general reaction mPEG-pDMAEMA-Br (1.59 mmol) was dissolved in 10 ml of anhydrous DMF. Sodium azide (7.98 mmol) was added under stirring. The reaction was carried out for 2 days at 90 °C under Argon. The DMF was removed by vacuum distillation. The solid product was dissolved in DCM and passed through a dropping funnel filled with silica. The DCM was removed under vacuum and the recovered yellow oil was precipitated into cold hexane to get a white powder. Confirmation of substitution was followed by NMR (**Figure 2**).

NMR

mPEG_{2k}-pDMAEMA₅₆₆₀-N₃ ¹H NMR δ 4.06 (d), 3.84 – 3.78 (m), 3.64 (d), 3.37 (s), 2.57 (d), 2.36 – 2.22 (m), 1.94 (s), 1.82 (s), 1.42 (m), 1.05 (s), 0.96 – 0.81 (m). Y%: 77

mPEG_{5k}-pDMAEMA₁₄₉₃₄-N₃ ¹H NMR δ 4.07 (t), 3.87 – 3.73 (m), 3.63 (s), 3.37 (s), 2.55 (d), 2.27 (s), 1.93 (s), 1.81 (s), 1.42 (m), 1.00 (d), 0.89 (s). Y%: 94

Synthesis of mPEG-pDMAEMA-PCL by CuAAC

mPEG-pDMAEMA-N₃ (0.39 mmol) was dissolved in DMSO (18 mL). Cu⁰ (1.49 mg) was added to the stirred solution, followed by the addition of butynyl-PCL₇₅₀ (0.489 mol). The reaction mixture was stirred at 78 °C for 3 days. Solid Cu and DMSO were removed, the obtained solid was dissolved in THF and passed through neutral aluminium oxide. The copolymer was precipitated in methanol and recovered by centrifugation. The product was dried under vacuum, then further purified by dissolution in DCM followed by precipitation in cold hexane. The final product, a powder, was characterized by NMR.

mPEG_{2k}-pDMAEMA₅₆₆₀-PCL₇₅₀ δ 4.06 (d), 3.84 – 3.78 (m), 3.64 (d), 3.37 (s), 2.57 (d), 2.36 – 2.22 (m), 1.82 (s), 1.05 (s), 0.96 – 0.81 (m) Y%: 76

mPEG_{2k}-pDMAEMA₅₆₆₀-PCL₄₀₀₀ δ 4.06 (d), 3.84 – 3.78 (m), 3.64 (d), 3.37 (s), 2.56 (d), 2.36 – 2.22 (m), 1.82 (s), 1.05 (s), 0.96 – 0.81 (m) Y%: 84

mPEG_{5k}-pDMAEMA₁₄₉₃₄-PCL₇₅₀ δ 4.07 (t), 3.87 – 3.73 (m), 3.63 (s), 3.37 (s), 2.55 (d), 2.27 (s), 1.93 (s), 1.81 (s), 1.42 (m), 1.00 (d), 0.89 (s). Y%: 88

mPEG_{5k}-pDMAEMA₁₄₉₃₄-PCL₄₀₀₀ δ 4.05 (t), 3.87 – 3.73 (m), 3.63 (s), 3.37 (s), 2.57 (d), 2.27 (s), 1.93 (s), 1.81 (s), 1.42 (m), 1.00 (d), 0.89 (s). Y%: 87

Characterization of polymers

¹H NMR spectra were recorded on a Bruker DRX-400 nuclear magnetic resonance instrument, using CDCl₃ as solvent. Chemical shifts are expressed in parts per million, ppm(δ).

Fourier transform infrared (FT-IR) spectra were obtained using a PerkinElmer Spectrum 100 spectrometer, equipped with a diamond single reflection ATR unit.

Gel permeation chromatography (GPC) was used to measure the molecular weight. For GPC analysis, samples were dissolved in THF and passed through a 0.22μm PTFE membrane filter. Measurements were performed on an injected volume of 100μL by using a Malvern-Viscotek GPC MAX/TDA 305 quadruple detector array equipped with a pre-column and two Phenogel columns (Phenomenex) with exclusion limits 10⁶ and 10³ respectively. The GPC instrument was used at a

flow rate of 0.8 mL/min and at columns and system temperature of 35 °C. Triple detectors calibration was based on a standard of polystyrene with molecular weight 104,959 Da.

Critical micelle concentration (CMC) of the copolymers was determined by a fluorescence method using pyrene as probe. Briefly, copolymers were poured in water, heated at 60°C, and stirred for 24 h. The dispersion was cooled at room temperature and filtered to eliminate undissolved polymer. Polymer solubility was assessed by weight after sample lyophilization. A pyrene solution in acetone was added in 2-mL flasks to provide a final concentration of 6×10^{-7} M. Acetone was evaporated and replaced with aqueous polymer solutions at concentrations ranging from 0.38 to 950 µg/mL. Samples were heated at 65°C for 1 h, cooled at room temperature and analyzed at 25°C with a Shimadzu RF-1501 spectrofluorimeter. The emission wavelength was set at 390 nm.

NPs preparation

mPEG_{2k}-pDMAEMA₅₆₆₀-PCL₇₅₀ (SSS), mPEG_{2k}-pDMAEMA₅₆₆₀-PCL₄₁₆₁ (SSL), mPEG_{5k}-pDMAEMA₁₄₉₃₄-PCL₄₁₆₁ (LLL) and mPEG_{5k}-pDMAEMA₁₄₉₃₄-PCL₇₅₀ (LLS) copolymers were employed to prepare unloaded, DTX-loaded and combined siRNA/DTX-loaded NPs by a solvent diffusion technique. Briefly, 5 mg of copolymer was dissolved in 1 mL of acetone and added dropwise in water (2 mL) under magnetic stirring (400 rpm). After solvent evaporation, NPs were filtered through 0.22 µm RC Phenex® filters (Phenomenex, USA). NPs loaded with DTX were prepared according to the procedure reported above by co-dissolving DTX with the copolymer (10% w/w) in the organic phase. For siRNA-loaded NPs, after preparation NP dispersion was mixed with a scramble siRNA (50 µmol siRNA solution) in N/P ratio of 0.25, 0.50, 1, 2, 5, 10 and 20. In order to allow siRNA adsorption on NP surface, the dispersions were stirred for 15 minutes at room temperature.

Yield of NP production process was evaluated on an aliquot of NP dispersion by weighting the solid residue after freeze-drying. Results are expressed as the ratio of the actual NP weight to the theoretical polymer weight $\times 100$.

NPs characterization

Hydrodynamic diameter (DH), polydispersity index (PI) and zeta potential (ζ) of NPs were determined on a Zetasizer Nano Z (Malvern Instruments Ltd). Results are reported as mean DH of three separate measurements of three different batches ($n = 9$) \pm standard deviation (SD). The morphology of the NPs was examined by transmission electron microscopy (TEM). Samples were imaged using a JEOL 2100F FEG-TEM electron microscope. A few drops were added onto a copper grid and allowed to dry in air. NPs were negatively stained with 2% phosphotungstic acid solution.

To determine the stability of NPs under simulated physiologic conditions, 0.1 mL of NPs dispersion was added to 0.9 mL of PBS pH 7.4 or 5.5 (NPs conc: 0.25 mg/mL) and incubated at 37 °C. Size measurements of the samples were taken by dynamic light scattering on a Zetasizer Nano ZS after 1hr, 3hr and 24hr of incubation.

Surface PEG was evaluated through NMR comparing the integrals of PEG in samples dissolved in CDCl₃ and NPs suspended in D₂O maintaining the machine parameters.

DTX loading and release

DTX loading inside NPs was assessed by placing 1 mg of freeze-dried NPs in 1 mL of THF and filtering the samples through a 0.45 μm filter (Phenomenex, USA). DTX was analyzed by HPLC using a Shimadzu (Japan) apparatus equipped with a LC-10ADvp pump, a SIL-10ADvp autoinjector, a SPD-10Avp UV-Vis detector and a C-R6 integrator. The analysis was performed using a Juppiter 5 μm , C18 column (250 x 4.6 mm, Å) (Phenomenex, USA). The mobile phase was a 55:45 (v/v) mixture of water with 0.1% TFA and acetonitrile pumped at a flow rate of 1 mL min^{-1} . The UV detector was set at 227 nm. A calibration curve for DTX in ethanol was plotted in the concentration range of 2–200 $\mu\text{g mL}^{-1}$.

The release of DTX was determined on 1.25 mg of NPs dispersed in 0.5 mL of 10 mM phosphate buffer containing NaCl (137 mM) and KCl (2.7 mM) at pH 7.4 (PBS) at 37°C in a dialysis bag immersed in an external phase (5 mL) of the same medium. At predetermined times, 1 mL aliquots of the sample were collected and then analyzed by HPLC to evaluate the actual loading of DTX in NPs. The results are expressed as % release \pm SD of three experiments.

siRNA adsorption

The loading of siRNA associated with NPs was confirmed by agarose gel retardation assays. siRNA-loaded NPs containing 1 μg of siRNA depending on the different N/P ratio, were loaded on 2% agarose gel in Tris-Acetate-EDTA (TAE) buffer and subjected to electrophoresis for 45 min at 60 V. siRNA bands were stained with ethidium bromide and finally visualized with an UV illuminator.

PEGylation extent of NPs

Fixed aqueous layer thickness (FALT) of NPs was measured by monitoring the influence of ionic strength on zeta potential (ζ). Different amounts of NaCl stock solutions were added to NPs dispersed in water (500 $\mu\text{g mL}^{-1}$) and ζ of the samples measured. The plot of $\ln \zeta$ against $3.33[\text{NaCl}]^{0.5}$ gives a straight line where the slope represents the thickness of the shell in nm.

^1H NMR was carried out on NPs aqueous dispersions to evaluate the amount of PEG on the surface. Spectra were recorded for either nanoparticles dispersed in D_2O or nanoparticles dissolved in CDCl_3 (2.5 mg/mL).

Result and Discussion

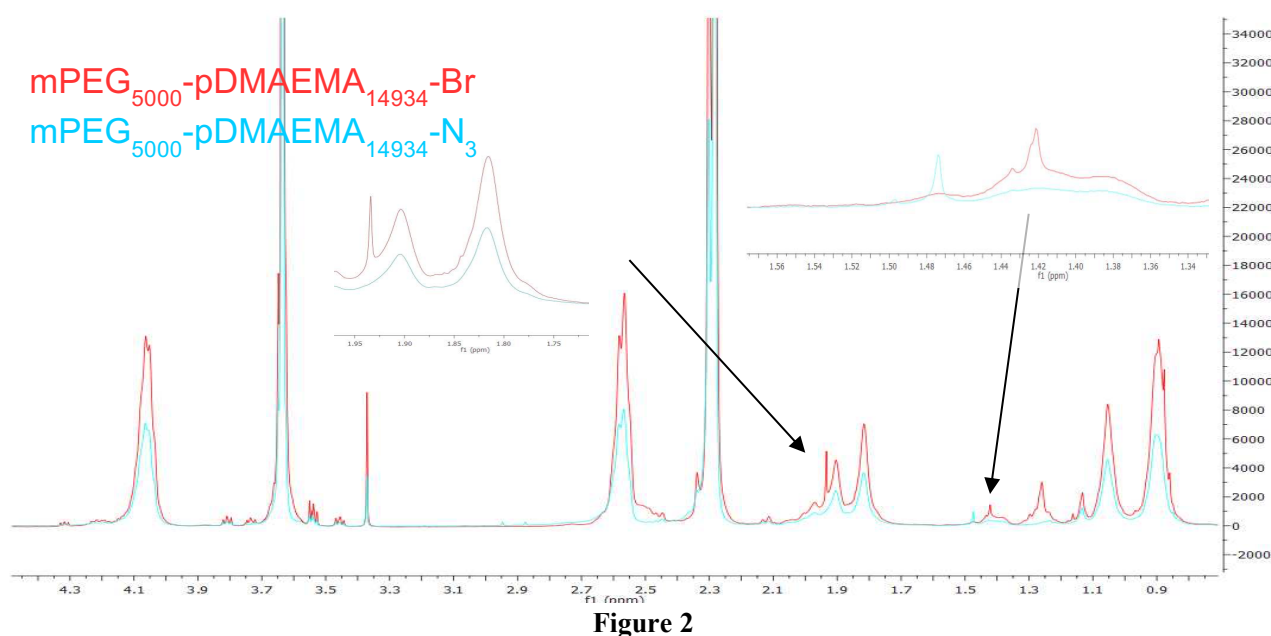
Synthesis and characterization of copolymers

Examples of amphiphilic copolymers containing pDMAEMA as hydrophilic cationic block are reported in literature (6-7). In case of mPEG-PCL-pDMAEMA triblock copolymers (8), the authors found that, for this specific block sequence, when pDMAEMA chain is longer than PEG chain the copolymer aggregates to form polymeric vesicles, in which pDMAEMA block is segregated to the outer surface, whereas PEG block is segregated inside the PCL wall. In the present work, the block sequence was changed to mPEG-pDMAEMA-PCL, in order to yield micelles with a PCL hydrophobic core and a PEG/pDMAEMA corona. The presence of hydrophilic PEG chains to the surface of the particle is welcome to stabilize NPs and impart stealth property, whereas the cationic pDMAEMA block, along to form complex with siRNA, minimizes aggregation phenomena thanks to electrostatic repulsion. Hydrophobic molecules, as DTX, can be encapsulated inside the PCL core, whereas siRNA is absorbed on NP cationic surface. Thus, NPs from triblock copolymers with

this specific block sequence have the dual function to transport DXT and siRNA for a combined anticancer therapy.

Copolymers were synthesized by a combination of techniques: i) quantitative conversion of –OH terminal group of mPEG to bromoisobutyrate, to obtain the macroinitiator (mPEG-Br); ii) polymerization of DMAEMA block via ATRP; iii) conversion of -Br terminal group on pDMAEMA block to azide group (mPEG-pDMAEMA-N₃); iv) ring-opening polymerization of ε-CL initiated by 3-butyn-1-ol (butynyl-PCL); v) click reaction between mPEG-pDMAEMA-N₃ and butynyl-PCL. The sequence of reactions is reported in **Figure 1**.

The first step of synthesis guarantees the presence of a functional group suitable as ATRP initiator. The second step, the pDMAEMA polymerization through ATRP, promises a well-defined control over the block length and, as a consequence, the desired hydrophilic/hydrophobic ratio and amount of amino groups for positive charge surface. The third step of synthesis, substitution of Br by -N₃, allows in the successive step the possibility to conjugate through CuAAC a PCL bearing an alkyne functionality. The evidence of success of step iii was confirmed by NMR **Figure 2**.



The signals highlighted by the arrows show the difference of the new introduced functionality. (9)

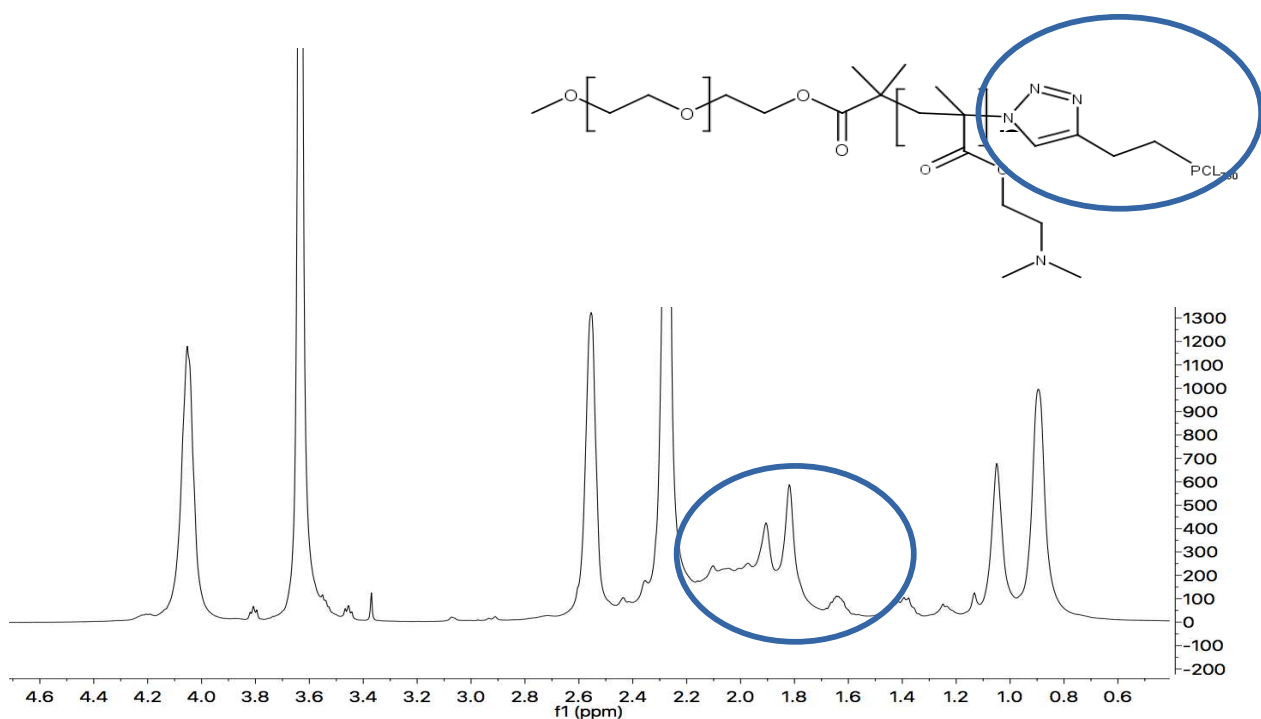


Figure 3

In the fourth step, alkyne-PCL was successfully conjugated to diblock copolymer as confirmed through NMR. **Figure 3**

Four different copolymers with different block length were synthesized (**Table 1**). pDMAEMA block length was set higher than PEG chain in all copolymers, to favor siRNA complexation. Two different molecular weights of PEG-pDMAEMA blocks were studied (named short-short and long-long), keeping constant the PEG-pDMAEMA ratio (around 1:3). Different molecular weights of PCL block were also examined, namely 750 and 4000 Da, to study the characteristics and stability of micelles as a function of PCL length.

Table 1. Molecular weights of copolymers (Da)

Copolymer	Code*	Mn (NMR)	Mn (GPC)	Mw (GPC)	PDI
mPEG _{2k} pDMAEMA _{5.6k} PCL ₇₅₀	PEG _S -pDMAEMA _S -PCL _S	8386	8597	11237	1.30
mPEG _{2k} pDMAEMA _{5.6k} PCL _{4k}	PEG _S -pDMAEMA _S -PCL _L	11832	11978	16870	1.41
mPEG _{5k} pDMAEMA _{15k} PCL ₇₅₀	PEG _L -pDMAEMA _L -PCL _S	20684	20982	25998	1.24
mPEG _{5k} pDMAEMA _{15k} PCL _{4K}	PEG _L -pDMAEMA _L -PCL _L	23934	24285	32543	1.34

*s=short, L=long

Preparation and characterization of loaded-unloaded Nanoparticles

NPs were prepared through solvent diffusion method, also referred as nanoprecipitation, since formation of the NPs is instantaneous and needs only one step so it has the advantage of rapid and easy operation to increase the scale of NP production. Colloidal properties of NPs in terms of size (DH), polydispersity index (PDI), CMC, zeta potential (ζ), yield, loading and entrapment efficiency of DTX are reported in **Table 2**.

Table 2 Properties of unloaded and DTX-loaded Nanoparticles

Formulation	Copolymer	CMC (mg/ml)	DTX (% w/w)	DH (nm \pm SD)	PD I	Zeta Potential (mV \pm SD ^a)	Yield (%)	DTX Actual loading (mg/100 mg NPs)	DTX entrapment efficiency (%)
SSS-NPs	PEG _S -pDMAEMA _S -PCL _S	0.11	-	48 \pm 11	0.5	+12 \pm 2	82	-	-
DTX/SSS-NPs	PEG _S -pDMAEMA _S -PCL _S	-	10	50 \pm 10	0.4	+10 \pm 2	80	7.7	21 \pm 10
SSL-NPs	PEG _S -pDMAEMA _S -PCL _L	0.017	-	94 \pm 3	0.1	+22 \pm 2	72	-	-
DTX/SSL-NPs	PEG _S -pDMAEMA _S -PCL _L	-	10	103 \pm 5	0.1	+26 \pm 8	75	9.5	81 \pm 12
LLS-NPs	PEG _L -pDMAEMA _L -PCL _S	0.55	-	73 \pm 12	0.5	+9 \pm 0.1	82	-	-
DTX/LLS-NPs	PEG _L -pDMAEMA _L -PCL _S	-	10	64 \pm 13	0.4	+11 \pm 0.5	85	6.5	80 \pm 12
LLL-NPs	PEG _L -pDMAEMA _L -PCL _L	0.05	-	69 \pm 5	0.1	+11 \pm 2	80	-	-
DTX/LLL-NPs	PEG _L -pDMAEMA _L -PCL _L	-	10	79 \pm 7	0.1	+13 \pm 3	79	3.2	32 \pm 5

NPs were obtained in high yield and in case of SSL and LLS with high entrapment efficiency without the help of any surfactant with a maximum size of 103 nm and PDI less than 0.5, while the ζ was positive as commonly found for NPs exposing pDMAEMA. Interestingly, CMC values decrease of one order of magnitude comparing SSS-SSL and LLS-LLL.

The size of DTX loaded NPs was unmodified as commonly happens to loaded NPs, even in high entrapment efficiency cases (LLL and SSL). The release of DTX from NPs was evaluated in 10 mM PBS, pH 7.4 at 37 °C through the dialysis method. (**Figure 3**)

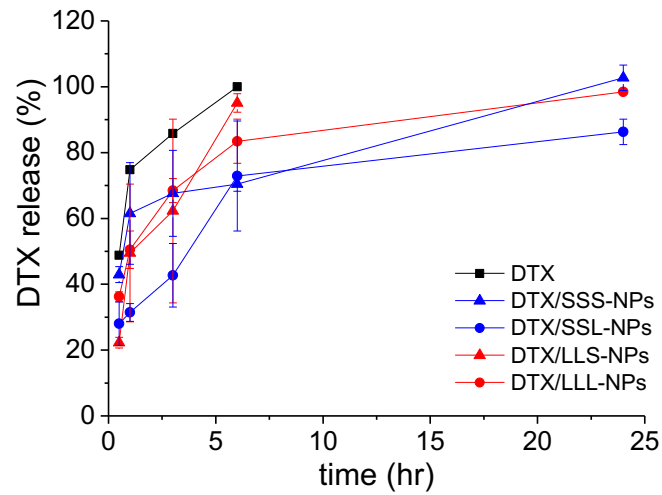


Figure 3

The figure above shows a trend for LLS comparable to free DTX, while for other formulations complete release was achieved over 3h. These results are in line with short-term stability evaluations performed at pH 7.4 and 5.5. **(Figure 4)**

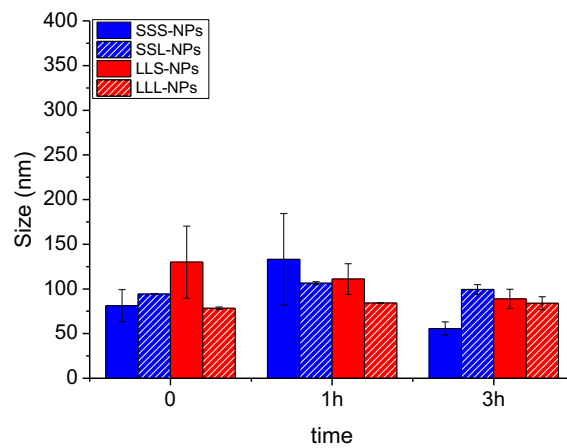
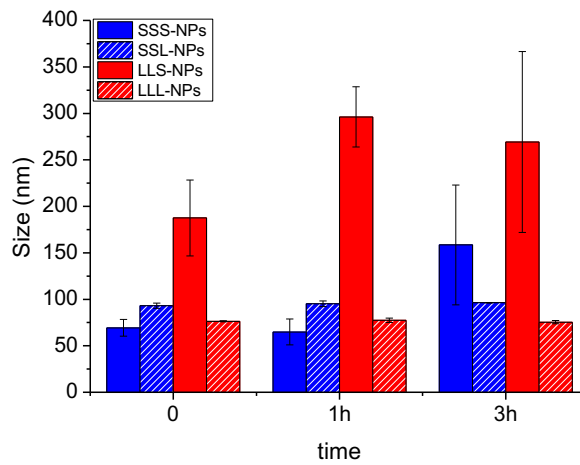


Figure 4

LLS sample shows a significant increase in size at pH 7.4 after 1h while the same behavior was not observed at pH 5.5. This may be attribute in case of pH 7.4 to a not well-balanced ratio between hydrophilic/hydrophobic blocks while at pH 5.5 to a more compact conformation comparing size at zero time.

Extent of Nanoparticle PEGylation

Fixed aqueous layer thickness (FALT) of the outer shell of NPs was determined by measuring ζ as a function of the NaCl concentration at pH values of 7. As reported in **Figure 5**, the slope value of the linear regression line obtained plotting $\log \zeta$ vs NaCl concentration gives the shell thickness (nm) for each NPs type. Shell thickness increased as hydrophilic/hydrophobic block ratio increase. The amount of PEG on the surface of NPs was assessed by quantitative NMR (**Table 3**). As can be seen, NPs exposed much less PEG when PCL₇₅₀ is used compared to NPs where PCL₄₀₀₀ is present. This trend is likely to be attributed to the insufficient PCL core.

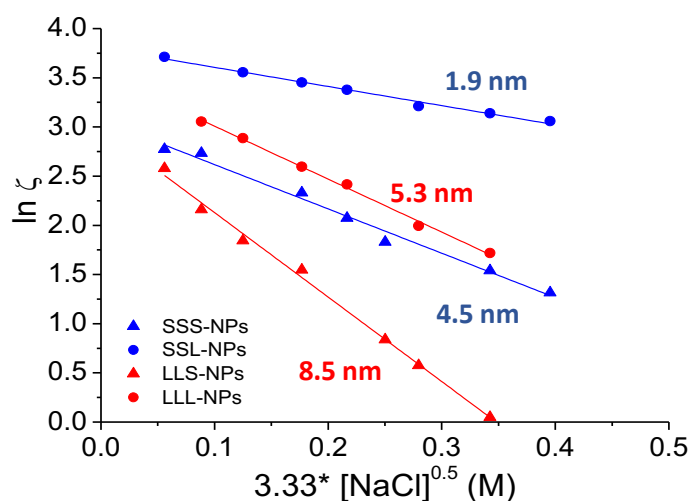


Figure 5

Table 3

<i>Formulation</i>	<i>Shell thickness (nm)</i>	<i>PEGylation rate (%)</i>
SSS-NPs	4.5	40
SSL-NPs	1.9	99
LLS-NPs	8.5	25
LLL-NPs	5.3	99

siRNA adsorption

The binding assay was analyzed by agarose gel electrophoresis, a technique used to separate macromolecules (such as DNA and RNA) based on their size and charge.

A range of polymer/siRNA weight ratio is loaded into the wells of an agarose gel and a current of 60V for 45 min is applied. siRNA bands were visualized using an ultra violet (UV) imaging system. The negatively charged complex migrates toward the anode during electrophoresis

Results showed (**Figure 6**) that the positive charge density of the polymers should be neutralized by the negative siRNA charges; the complete neutralization is achieved studying the so-called N/P ratio.

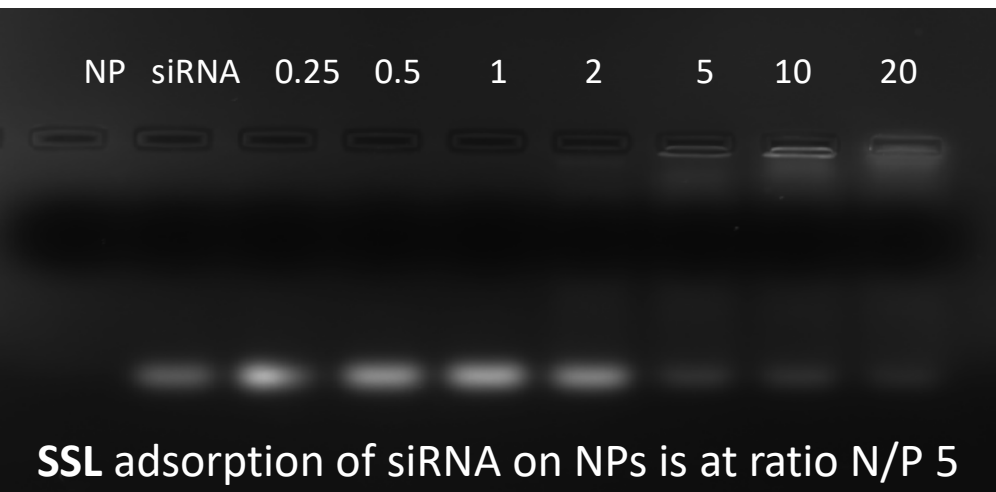
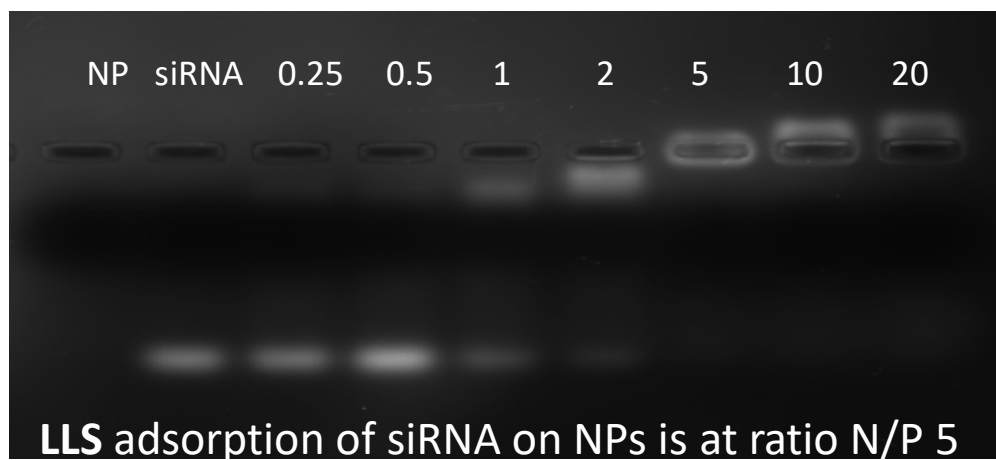
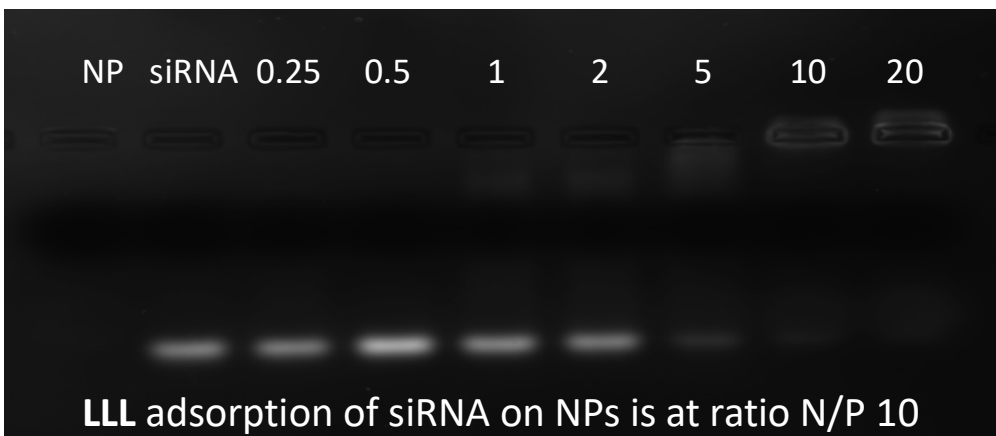
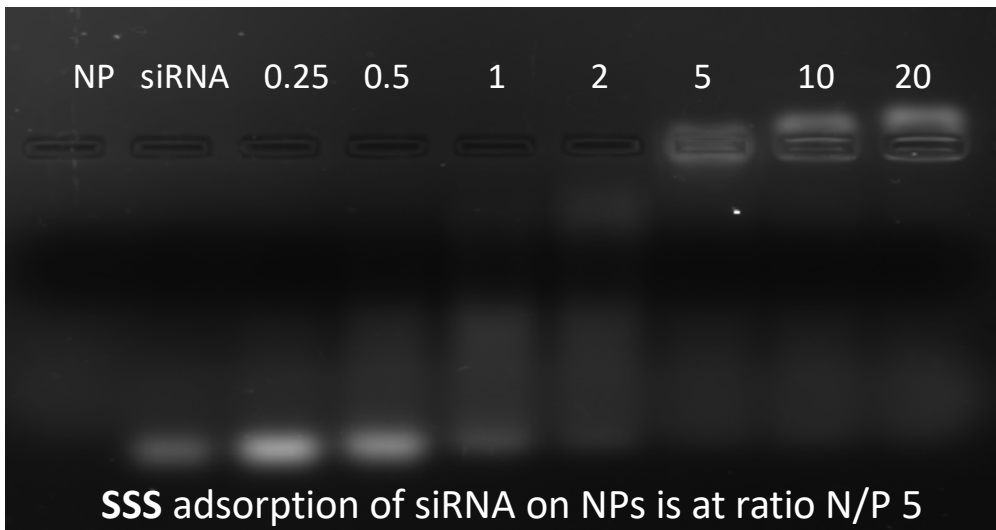


Figure 6

Conclusions

In conclusion, hereby is reported the successful synthesis of triblock copolymers made of PEG-pDMAEMA-PCL able to form NPs. The presence of the pDMAEMA block allows the complexation with siRNA on the NP surface. The hydrophilic/hydrophobic ratio play an important role in all aspects of final NPs (CMC, DH, FALT, PEG exposure and siRNA complexation). DTX loaded NPs showed good results in terms of DH, release and stability.

Reference

- 1 Mahmoodi Chalbatani G, Dana H, Gharagouzloo E, et al. Small interfering RNAs (siRNAs) in cancer therapy: a nano-based approach. *Int J Nanomedicine*. 2019;14:3111–3128. Published 2019 May 2. doi:10.2147/IJN.S200253
- 2 Guo W, Chen W, Yu W, Huang W, Deng W. Small interfering RNA-based molecular therapy of cancers. *Chin J Cancer*. 2013;32(9):488–493. doi:10.5732/cjc.012.10280
- 3 Liu, Ye & Wu, Decheng & Ma, Yuexia & Tang, Guping & Wang, Shu & He, Chaobin & Chung, Tai-Shung & Goh, Suathong. (2003). Novel poly(amino ester)s obtained from Michael addition polymerizations of trifunctional amine monomers with diacrylates: Safe and efficient DNA carriers. *Chemical communications (Cambridge, England)*. 9. 2630-1. 10.1039/B309487A.
- 4 Qi, Ruogu & Hu, Xiuli & Yan, Leshan & Chen, Xuesi & Huang, Yubin & Jing, Xiabin. (2011). Synthesis of biodegradable cationic triblock copolymer mPEG-PCL-PLL for siRNA delivery. *Journal of controlled release : official journal of the Controlled Release Society*. 152 Suppl 1. e167-8. 10.1016/j.jconrel.2011.08.067.
- 5 Dai, S.. (2015). Natural cationic polymers for advanced gene and drug delivery. *RSC Polymer Chemistry Series*. 2015. 557-582.
- 6 Wang, Y., Gao, S., Ye, W. et al. Co-delivery of drugs and DNA from cationic core-shell nanoparticles self-assembled from a biodegradable copolymer. *Nature Mater* 5, 791–796 (2006) doi:10.1038/nmat1737
- 7 Bruce, Carl & Javakhishvili, Irakli & Fogelström, Linda & Carlmark, Anna & Hvilsted, Søren & Malmström, Eva. (2014). Well-defined ABA- and BAB-type block copolymers of PDMAEMA and PCL. *RSC Advances*. 4. 25809-25818. 10.1039/c4ra04325a.
- 8 Li, Zhibiao & Yin, Hui & Zhang, Zhongxing & Liu, Kerh & Li, Jun. (2012). Supramolecular Anchoring of DNA Polyplexes in Cyclodextrin-Based Polypseudorotaxane Hydrogels for Sustained Gene Delivery. *Biomacromolecules*. 13. 3162-72. 10.1021/bm300936x.
- 9 Ward, Mark & Georgiou, Theoni. (2010). Thermoresponsive Terpolymers Based on Methacrylate Monomers: Effect of Architecture and Composition. *Journal of Polymer Science Part A: Polymer Chemistry*. 48. 775 - 783. 10.1002/pola.23825.

10 Bruce, Carl & Javakhishvili, Irakli & Fogelström, Linda & Carlmark, Anna & Hvilsted, Søren & Malmström, Eva. (2014). Well-defined ABA- and BAB-type block copolymers of PDMAEMA and PCL. RSC Advances. 4. 25809-25818. 10.1039/c4ra04325a.

9 Conclusions

The work here presented provides a wide investigation of synthesis and characterization of amphiphilic PEG-PCL block copolymers for the fabrication of NPs bearing different functionality on their surface, and evaluation of cellular uptake and biological activity of surface decorated NPs.

In a first part new synthetic strategies were proposed to conjugate and improve surface exposure of folic acid and aFLT1, in order to enhance respectively NPs active targeting and antiangiogenic properties. This was achieved by varying the PEG length bearing the functionalites and through the introduction of polyrotaxane, with the possibility of imparting an unfolded conformation to PEG chains, reaching an improved internalization.

The second part focuses on synthesis and characterization of PCL bearing amine groups in order to tune NPs superficial charge. NPs realized in this way showed an improved internalization and trafficking through different kind of biological barriers. In vivo distribution studies proved higher accumulation of these NPs at specific organs. The results demonstrated moreover a reliance of PEG length and surface charge.

The last part focuses on triblock copolymers containing a pDMAEMA cationic block able to complex siRNA. These terpolymers were studied for a dual therapy combining siRNA complexed on NPs surface and a hydrophobic anticancer drug loaded in NPs core. Preliminary results showed a strong dependence of hydrophilic/hydrophobic ratio on NPs properties and siRNA complexation.